The Vibro-Acoustic Modelling and Analysis of Damage Mechanisms in Paper

David Kao

A thesis submitted in partial fulfilment of

the requirements of the University of Greenwich for

the degree of Doctor of Philosophy

April 2006

To Yuling and My Family

Abstract

This thesis investigates the use of the acoustic emission (AE) monitoring technique for use in identifying the damage mechanisms present in paper associated with its production process. The microscopic structure of paper consists of a random mesh of paper fibres connected by hydrogen bonds. This implies the existence of the two damage mechanisms of interest, the failure of a fibre/fibre bond and the failure of a fibre.

The majority of this work focuses on the development of a novel hybrid mathematical model which couples the mechanics of the mass/spring model to the acoustic wave propagation model for use in generating the acoustic signal emitted by complex structures of paper fibres under strain. A discussion of the coupling method is presented and the model is then analysed using a simple plucked fibre as a test case with a comparison between the numerical and experimental results.

The hybrid mathematical model is then used to simulate small fibre networks aimed at providing information on the acoustic response of each damage mechanism. To do this the mass/spring model must successfully simulate the response of the fibre structure when undergoing a fibre/fibre bond failure or a fibre failure. This can be achieved by dynamically manipulating the mass and spring elements of the fibre structure. The simulated AEs from the two damage mechanisms are then analysed using a Continuous Wavelet Transform (CWT) to provide a two dimensional time/frequency representation of the signal. From the CWT certain features of the AEs can be attributed to each damage mechanism and as such a criteria for the time and frequency properties of each damage mechanism can

be formulated. This criterion provides the basis for identifying the damage mechanisms present in the experimental data.

The final contribution of this thesis is the investigation of training an intelligent classifier which can dynamically identify the AEs from the two damage mechanisms. This is achieved by converting the time and frequency criteria for each damage mechanisms into a set of features for the training of a Self-Organising Map (SOM). The significant step in this analysis is the method for the extraction of the features from the CWT of the AE.

This work successfully combines four different scientific areas, paper physics, acoustic emission technology, data analysis and computational modelling to provide an insight into the micro-mechanics of paper. The most significant contribution of this work is the development of the hybrid model which has the ability to generate the acoustic response of a paper fibre structure undergoing two different damage processes. This alone has provided a significant insight into the micro-mechanics of paper to allow for the identification of the two damage mechanisms when the AEs are analysed with the CWT. Other contributions include the method used for the extraction of relevant features from the CWT to enable the training of a SOM for identifying the type of damage mechanism the AE originated from.

Acknowledgements

Firstly, I would like to thank my supervisors, Dr. Deryn Graham and Prof. Koulis Pericleous for their advice and encouragement during my PhD studies. In particular, I am grateful for the freedom given by both to explore and follow topics of the research that were of most interest. I would like to make a special mention to Dr. Choi-Hong Lai whose encouragement during the initial development of the numerical model was much appreciated. I would also like to thank Prof. Brian Knight for his support and input into my research. Finally, I must acknowledge the European Union Fifth Frame Program for funding this research and providing me with the opportunity to interact with and travel to other European institutions.

Contents

List of Figures

List of Tables

Nomenclature

AE	Acoustic Emission
BEM	Boundary Element Method
BLAS	Basic Linear Algebra Subprograms
CWT	Continuous Wavelet Transform
DFT	Discrete Fourier Transform
EqIC	Equilibrium Initial Condition
FDTD	Finite Difference Time Domain
FEM	Finite Element Method
FP5	European Union Fifth Frame Program
FFT	Fast Fourier Transform
FVM	Finite Volume Method
LAPACK	Linear Algebra Package
ODE	Ordinary Differential Equation
PCA	Principal Component Analysis
PSD	Power Spectral Density
SEM	Scanning Electron Microscope
SHO	Simple Harmonic Oscillator
SOM	Self-Organising Map
SPL	Sound Power Level
STFT	Short Time Fourier Transform
StIC	Stretching Initial Condition
WD	Wigner Distribution
WT	Wavelet Transform

Preface

The work presented in this thesis contributes to the EU project QLK5-CT-2002-00772 AEP [2], a European Union Fifth Frame Program (FP5). The purpose of the FP5 project is to investigate the microscopic behaviour of paper under mechanical loading with a view to developing new and value added paper products. To achieve this, the Acoustic Emission (AE) monitoring technique is used for detecting and recording damage ranging from a single fibre or fibre/fibre bond failure to details on the macroscopic level. The objective of this work is to develop a method to identify the type of damage mechanism from the acoustic emission generated.

This project requires a multi-disciplinary team comprising of four partners with experience in paper science[1,3], acoustic emission[4], data analysis[2] and computational modelling[2].

The preface provides an overview of the FP5 project as a whole and will provide a brief description of the different stages of the experimental process, with Chapter 1 providing an overview of the work contained in this thesis.

---

[1]**Partner 1:** Mid Sweden University, Sundsvall, Sweden. **Team Leader:** Prof. Per Gradin

[2]**Partner 2:** University of Greenwich, Greenwich, UK. **Team Leader:** Dr. Deryn Graham

[3]**Partner 3:** Norwegian Pulp and Paper Research Institute (PFI), Trondheim, Norway. **Team Leader:** Dr. Per Nygard

[4]**Partner 4:** Vallen-Systeme, Munich, Germany. **Team Leader:** Mr. Hartmut Vallen

Paper Production and Paper Structure

To understand the structure of paper and the subsequent damage mechanisms, it is important to know the basic principles of paper making. Paper is made from trees which consist of millions of fibres which are categorised in to two types: hardwood and softwood. Hardwood trees such as oak are made up of very short fibres whilst softwood trees, such as spruce are made up of long fibres. It is these fibres which are the basic ingredient for paper. The paper making process begins by first harvesting the trees into logs which are then processed into wood chips. The fibres are then extracted from the wood chips using a technique called 'pulping' which comes in two varieties, mechanical pulping and chemical pulping. Mechanical pulping uses a machine to beat the wood chips so that the fibres can be extracted, where as chemical pulping uses a chemical to separate the fibres. Both methods result in a solution of fibres that contains 80% water. This solution is then compressed which reduces the water content to around 65% and then dried to remove the rest of the water. This results in a mesh of fibres otherwise known as paper.

As the fibres are initially extracted into a watery solution, the orientation of the fibres has no definitive direction. As this solution dries, hydrogen bonds form between the fibres acting like a glue, creating a fibre/fibre bond. The resulting fibre structure is random by nature, with the strength of each fibre/fibre bond proportional to its bonded area. Therefore, there exist two obvious damage mechanisms; the failure of a fibre/fibre bond and the failure of a fibre, with the partial failure of a fibre/fibre bond as a third damage mechanism. Figure 1 shows a scanning electron microscope (SEM) picture of the surface of copy paper.

Generation of the Acoustic Emissions

Consider a force applied to the material such that only elastic deformation occurs. Releasing this force will cause the material to return to its original state due to the potential strain

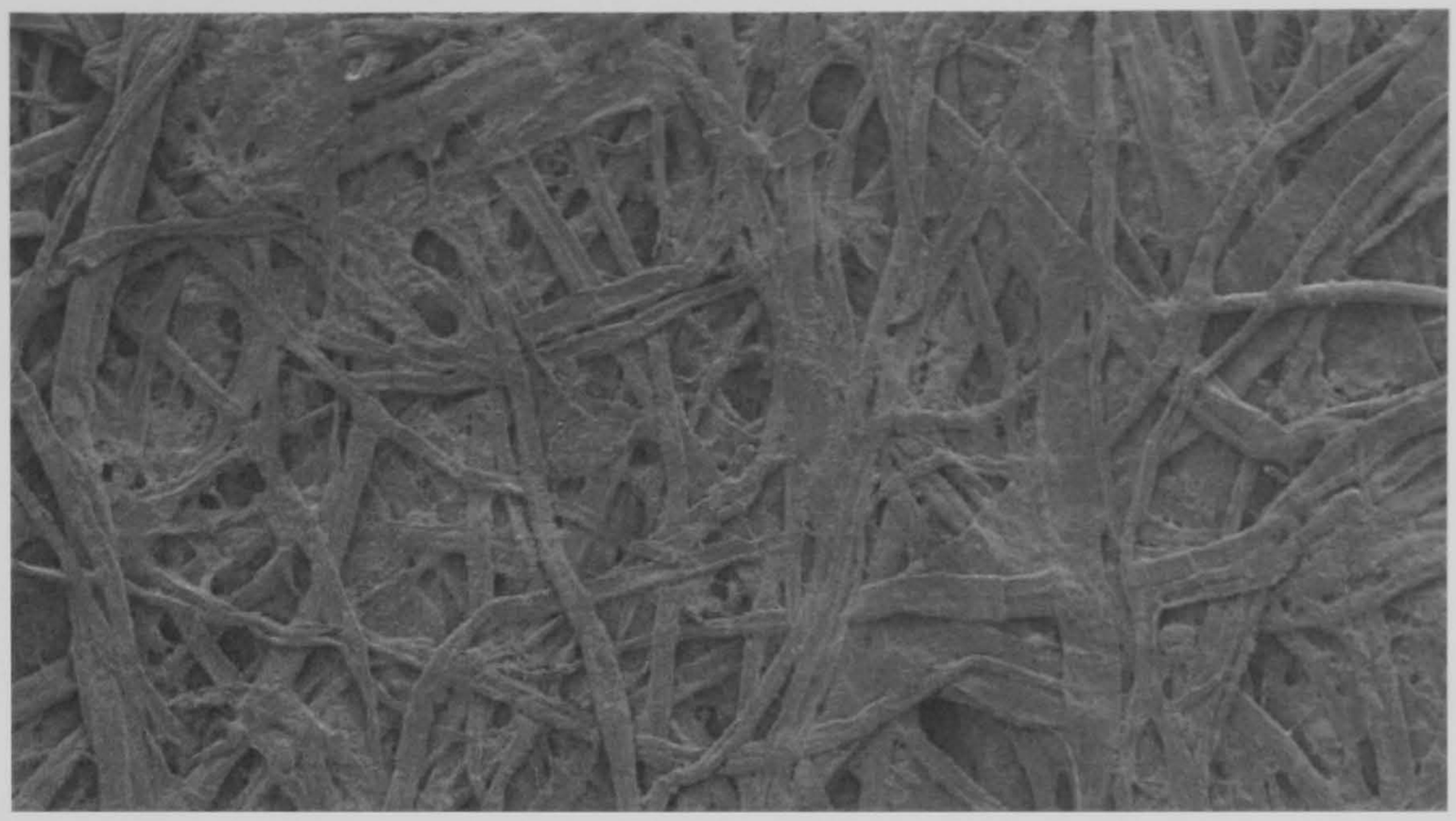

Figure 1: The Surface of Copy Paper [1]

energy in the material. Increasing the force applied to the material will cause plastic deformation to occur. When this force is released the material does not return to its original state. Figure 2 shows a typical stress/strain curve for a generic material.

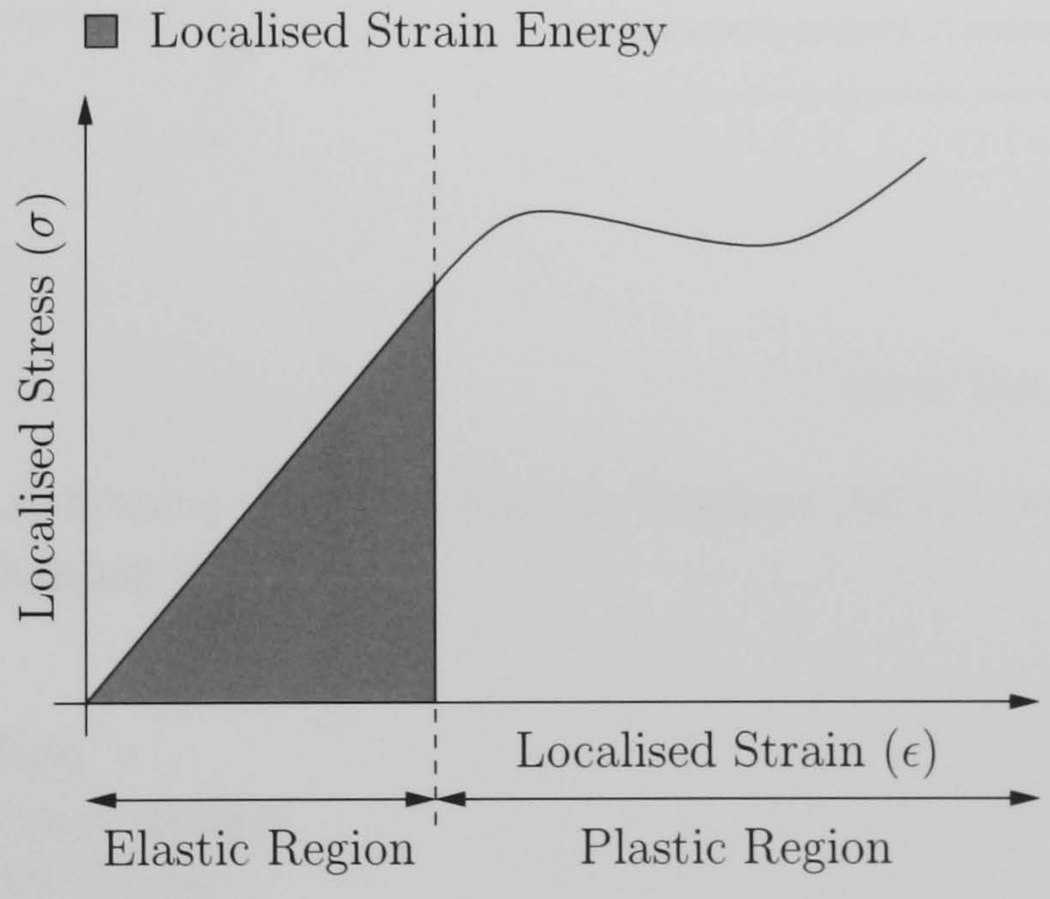

Figure 2: Stress/Strain Curve of a Generic Material

Consider the straining of a fibre/fibre bond. At the moment of failure the stored strain energy local to the fibre/fibre bond is instantaneously released as elastic energy caused by the relaxation of the damaged fibre/fibre bond. The elastic energy is then transmitted through the paper and is recorded on the surface using an acoustic emission sensor.

Therefore, it is assumed that one damage mechanism is the source of one AE.

A similar process also occurs with the failure of a fibre, but the properties of the AE produced by a fibre failure is assumed to be noticeably different to an AE produced from a fibre/fibre bond failure. To be able to identify the AEs generated from a particular damage mechanism it is critical that certain mechanical tests be devised so that the AEs generated from the paper under load are predominantly one failure type. Figure 3 shows the Z-Test and Shear Test which are thought to produce predominantly fibre/fibre bond failures as the fibres are orientated in the plane of the paper. Figure 4 shows the Zero Span Test which, if the span length is less than the average fibre length, will generate AEs from fibre failures.

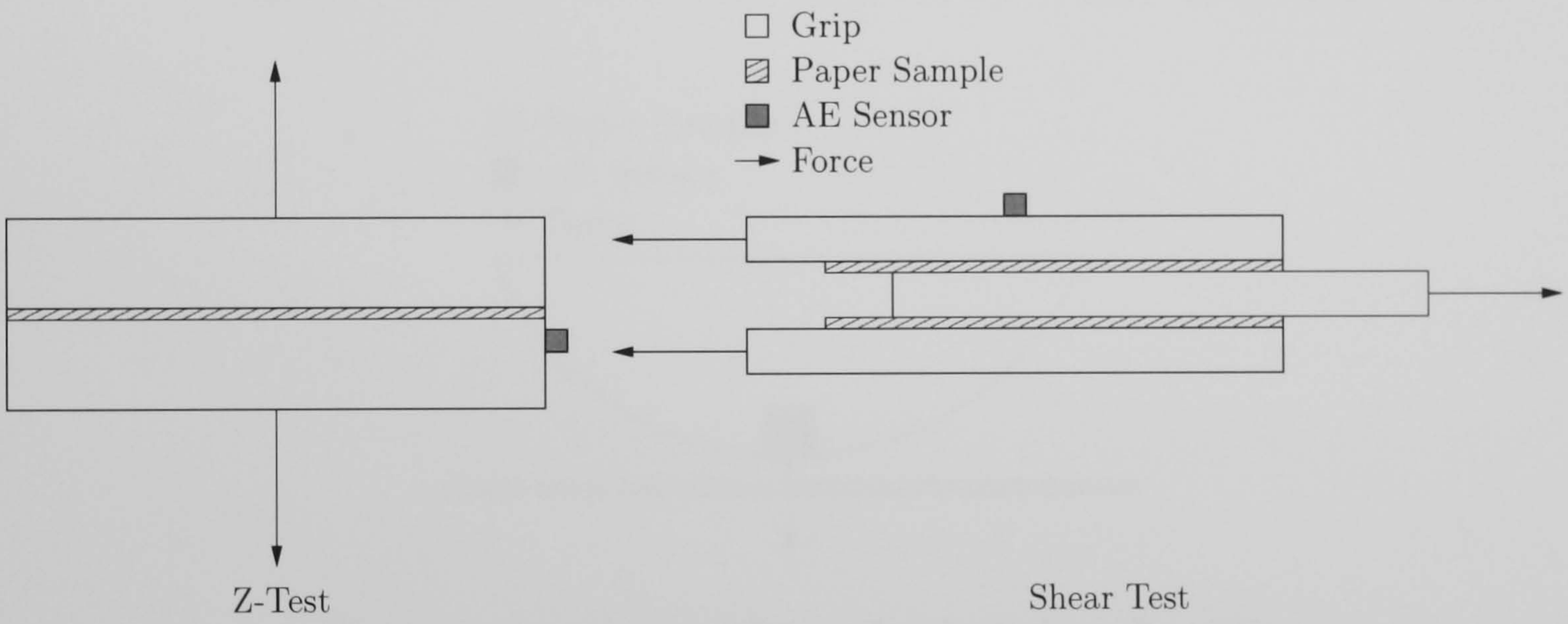

Figure 3: The Z-Test and Shear Test Designed to Produce AEs from the Fibre/Fibre Bond Failure Damage Mechanism [2]

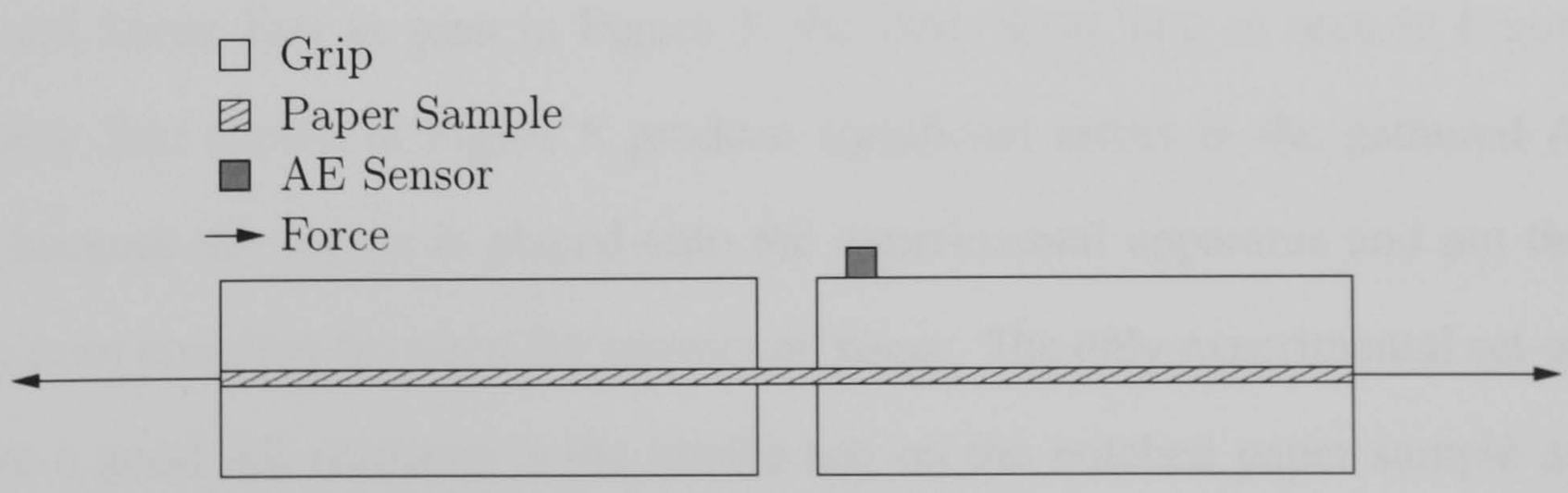

Figure 4: The Zero Span Test Designed to Produce AEs from the Fibre Failure Damage Mechanism [2]

Once the data has been obtained from these three experiments, a third set of experi-

ments will be run which will contain AEs produced from both damage mechanisms. This will be used to see whether the damage mechanism can be identified from the AEs. These tests can be seen in Figures 5 and 6 where the paper sample undergoes uni-axial and bi-axial loading respectively.

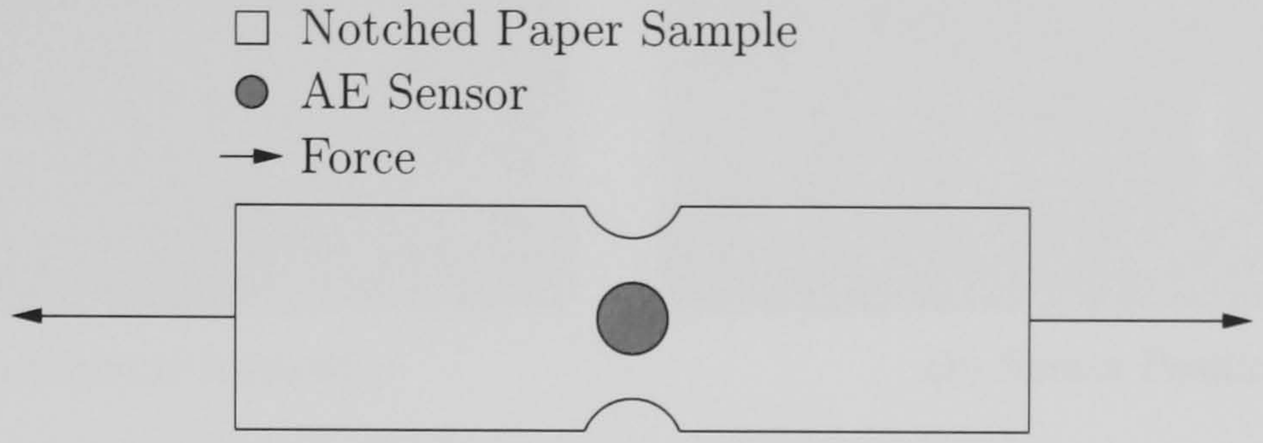

Figure 5: Experimental Set-up for the Notched Paper Sample [2]

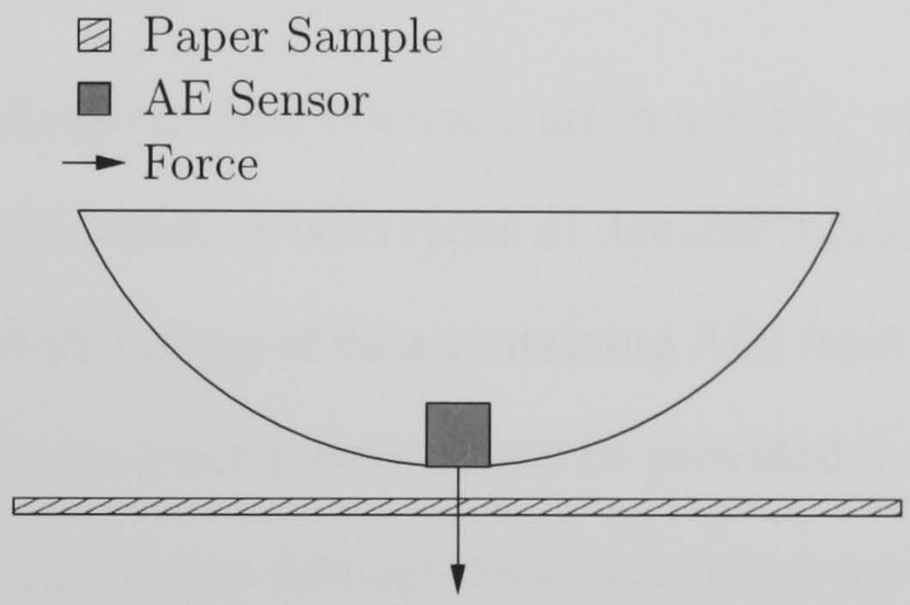

Figure 6: Experimental Set-up for the Sphere Test [2]

Having defined the mechanical tests, it was decided that the AE sensor placement for Z-Test and Shear Test as seen in Figure 3, the Zero Span Test as seen in Figure 4 and the Sphere Test shown in Figure 6 produce significant errors in the gathered AE data. This is because the sensor is placed onto the experimental apparatus and not the paper, giving a poor coupling between the sensor and paper. The only experimental set-up which will give a good AE response is the tensile test on the notched paper sample as shown in Figure 5. Figures 7(a) and 7(b) show the apparatus used for the experiments and one possible configuration of the sensor positions.

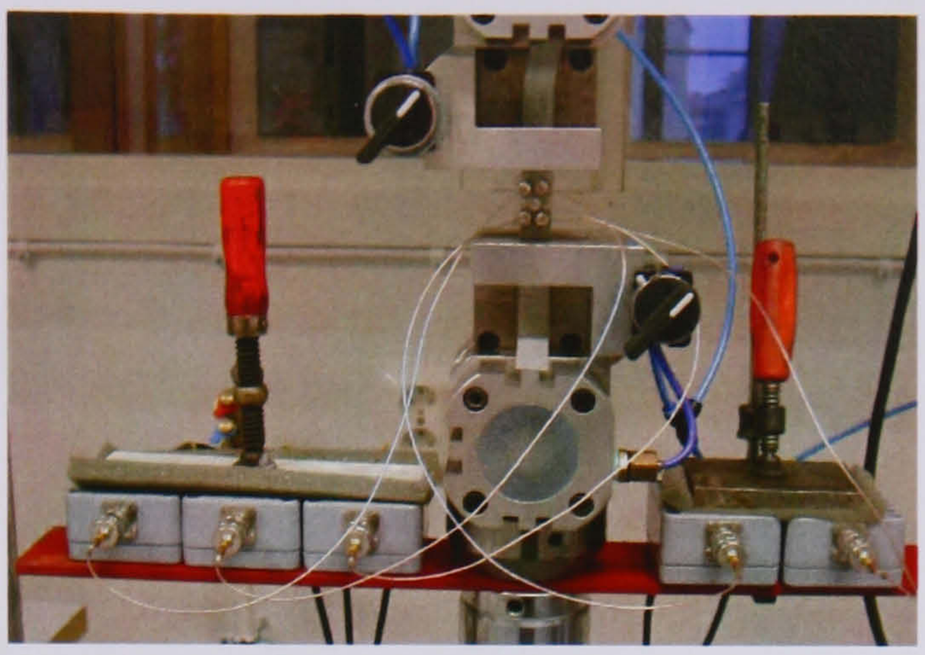

(a) Experimental Apparatus

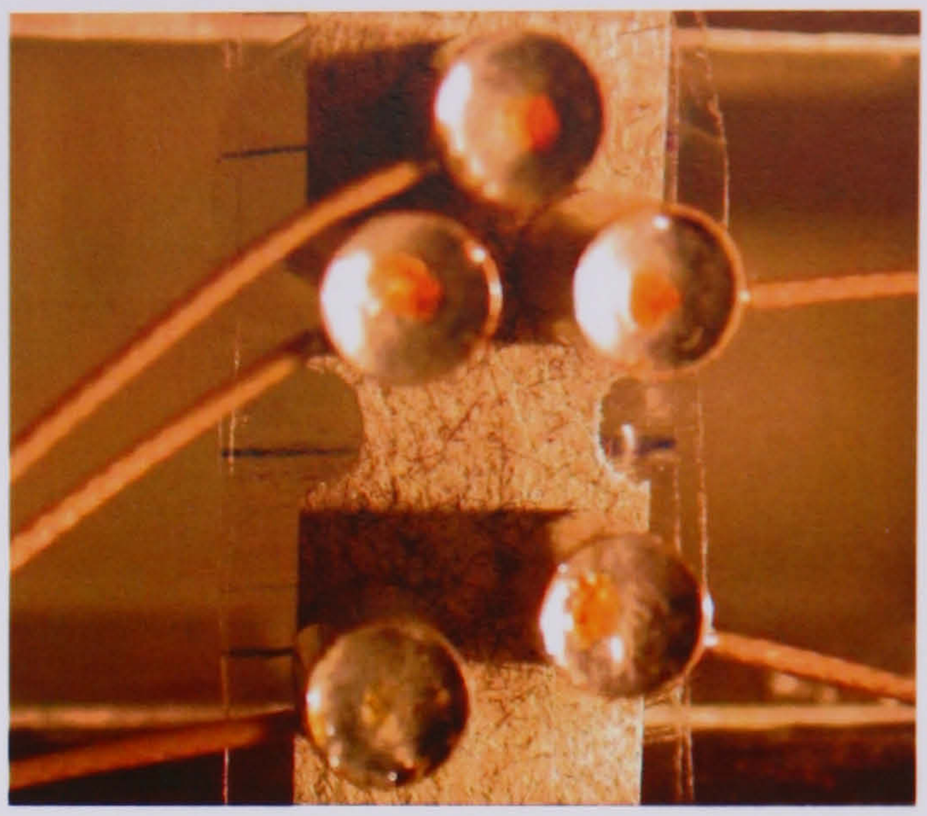

(b) Sensor Positions

Figure 7: Typical Experimental Set-up [2]

Data Analysis to Identify the Damage Mechanisms in Paper

It is clear that the experimental data obtained are not ideal, as only one experimental set-up is provided which will contain both types of damage mechanisms. It was originally proposed that the three distinct types of data containing AEs from fibre/fibre bond failures, fibre failures and both damage mechanisms would be provided for analysis. If this was the case, the task of identifying the two damage mechanisms would have been much simpler and could have been limited to an exercise in data analysis.

This is not the case, as the experimental data was found to contain AEs from two different damage mechanisms, with no information known about the effects each damage mechanism has on the AE. Standard data analysis techniques may result in two distinct AE fingerprints, but determining which fingerprint is associated with a particular damage mechanism would be difficult. This situation requires a deeper understanding of the microscopic nature of paper which must be investigated using a numerical model.

Chapter 1

Introduction

1.1 Thesis Introduction

It is clear that there is a need for an alternative method to provide information on the acoustic properties of the two types of damage mechanism present in paper. The work contained in this thesis focuses on the development of a numerical model and its use in helping to identify the damage mechanisms in paper. To do this a hybrid vibro-acoustic model is described which simulates the vibration of a fibre structure using the mass/spring and couples this movement to the acoustic wave equation to generate the resulting AE. The hybrid model is able to simulate the two damage mechanisms by dynamic manipulation of the mass/spring elements.

Using the hybrid model to simulate the two damage mechanisms will provide an insight into the relationship between the movement of the fibre structure caused by the damage process and the resulting AE. This thesis will explore the role the material properties of the paper fibres have on the frequency content of the AE, which will result in the use of the Continuous Wavelet Transform (CWT) as the primary analysis technique. The CWT allows the visualisation of certain features of the AEs, allowing the identification of the damage mechanism it was generated from.

These features provide the information required to proceed with the analysis of the experimental data. Subsequently, a Self-Organising Map (SOM) is used to show the potential for the automatic classification of the AEs using the features extracted from the CWT.

1.2 Thesis Contributions

The main objective of this research is to answer the following question:

> ***Is it possible to identify two of the damage mechanisms present in paper, the fibre/fibre bond failure and the fibre failure, using an acoustic emission monitoring technique?***

From the outset of this project, it was clear that the experimental data, provided by the partners of the EU project QLK5-CT-2002-00772 AEP [2], would not provide enough information relating to the microscopic nature of the paper to classify the AEs from the two types of damage mechanisms. A numerical model able to simulate the AE generated from the different damage mechanisms is needed to provide a starting point for the analysis of the experimental data. The major contribution of this thesis is the development of a numerical model able to simulate the movement of a microscopic fibre structure that results in the generation of an AE. The model can also dynamically manipulate the microscopic fibre structure to simulate a fibre/fibre bond failure or a fibre failure.

Several smaller contributions resulted from the development of the numerical model:

- ***Using the CWT to define an acoustic fingerprint for the failure of a fibre/fibre bond.***

- ***Using the CWT to define an acoustic fingerprint for the failure of a fibre.***

- ***Evidence that the frequency of the AEs decreases as the damage in the paper increases.***

Previous research using the AE monitoring technique with respect to paper has focused primarily on using the number of acoustic events detected [3], or the amplitude of the recorded AE events [4]. This thesis presents work that uses the time/frequency representation of the AE and provides an understanding of the link between the fibre network and the properties of the generated AE. This work shows the potential of the AE monitoring technique for detecting and identifying the damage mechanisms in paper and provides the basis for further research in this area.

1.3 Thesis Outline

The remainder of this thesis is structured as follows:

Chapter 2 reviews the available literature in the relevant subject areas. These areas are: the mechanical properties of paper, the AE monitoring technique, the analysis of the AE data and the numerical modelling of paper.

Chapter 3 describes the development of the hybrid numerical model used in simulating the acoustic response from the two types of damage mechanisms. This includes the derivation from first principles of the mass/spring model used in simulating the movement of the fibre structure. A detailed analysis of the mass/spring model is then presented, including a discussion on the advantages of an implicit formulation over an explicit one, followed by comments on the importance of applying physically correct initial conditions to the fibres. The mass/spring model is then tested using a single fibre. The acoustic wave equation, used to predict the resulting AE, is derived from first principles. The application of non-reflecting boundary conditions is then considered, followed by the modelling approach for different types of acoustic sources. The acoustic wave equation is then tested

using a single oscillation of a sine wave and a continuous sine wave. This chapter also includes a discussion on the optimal coupling of the mass/spring model to the acoustic wave equation. Finally, the hybrid model is tested by comparing the numerical predictions of a plucked rubber band and a plucked paper fibre to measurements.

Chapter 4 introduces a relationship between the frequency of the generated AEs to the material properties of a paper fibre. This is followed by an explanation of the assumptions used when modelling the paper fibre structure. The numerical model is then used to simulate the AEs generated from a single fibre, a fibre/fibre bond failure in a 3x3 Cartesian mesh, and a fibre failure from 2x1 fibre structure. These numerical results are analysed using the CWT and compared to similar experimental results, resulting in a set of criteria used to identify between the two damage mechanisms. This chapter also provides evidence that the frequency content of the experimental AEs decreases as the amount of damage increases in the paper.

Chapter 5 uses the criteria obtained from Chapter 4 to extract the features from the CWT of a typical AE. The criteria are also used to manually classify a set of experimental AEs, of which 10% of these AEs are then used to train a SOM. The remainder of the experimental AEs are then classified by the SOM, with the results showing a good potential for the SOM to automatically identify the damage mechansims.

Chapter 6 presents the conclusions of the advances made in this research and discusses ideas for future work. The appendices include an example of the input file used for the hybrid model along with the CWTs of all the AEs from the experimental data of a typical notched paper sample.

Chapter 2

Literature Review

2.1 Overview

The literature review presented here covers four diverse scientific disciplines required to identify the damage mechanisms in paper, namely, paper physics, acoustic emission technology, data analysis and computational modelling. The literature available for each field of research is vast, but there has been very little work carried out where these four areas have been used in conjunction with one another. This thesis forms the basis of research in this specialist topic and, as such, there is a shortage of highly relevant literature to review.

Section 2.2 reviews the current work in the paper physics field with particular interest in any research which can supplement the development of the numerical model. This section will also review any previous research that has used the AE monitoring technique on paper. Section 2.3 will provide a synopsis of current uses of the AE monitoring technique with Section 2.4 providing a review of current methods for analysing the recorded AEs. Finally, Section 2.5 will provide a review of the suitable numerical models available for simulating the micro-mechanics of paper.

2.2 Mechanical Properties of Paper

As the bulk of this thesis is dedicated to the development of a numerical model for use in identifying the two damage mechanisms in paper, the review of the literature in the paper physics field will focus on research that will complement the development of the model. This leads to a single topic of interest, the mechanical properties of paper which encompasses research on the microscopic structure of the paper, the fibre/fibre bond damage mechanism and the fibre failure damage mechanism.

Much research has been undertaken to investigate the microscopic structure and mechanical properties of paper. Niskanen [5] provides a good overview of the subject area, in particular the pre-rupture process of paper and is the source of most references stated on this topic. Corte and Kallmes [6] proposed a theory for the random geometry of two-dimensional fibre networks which showed good agreement with the geometric properties of thin paper sheets. The experimental work undertaken by Corte [3, 7] allowed the detection of individual fibre/fibre bond failures, with each failure generating an audible acoustic event. The number of fibre/fibre bond failures required for the paper to fracture as predicted by the statistical model [6] was similar to the number of acoustic events generated from the experiment. If this is correct, it is plausible to assume that *one damage event in the paper produces one acoustic emission.*

Page *et al.* [8,9] also studied individual fibre bonds under strain in normal paper sheets in contrast to the thin sheets studied by Corte. Page *et al.* found that only partial failure of the fibre/fibre bonds occurs before fracture of the paper specimen. It was observed in these partially damaged fibre/fibre bonds the irregularity in their bonded areas. As the bonded areas have an irregular shape, the stress within the bond is not uniform, which causes certain regions within the bond to fail first [5]. This partial failure causes a redistribution of the stress in the fibre structure so that the fibre/fibre bond does not fail completely. This work suggests that there is a possible third damage mechanism present, the partial failure

of a fibre/fibre bond. However, as the proposed numerical model will only represent a two dimensional fibre structure, then the work by Corte indicates that the numerical model need only consider the *fibre/fibre bond failure* and *fibre failure* damage mechanisms.

Uesaka *et al.* [10] provide an overview of the fibre/fibre bonding process and a detailed discussion of the strength of a fibre/fibre bond. Uesaka states that a fibre/fibre bond will only form if the fibre surfaces are brought close enough together and if the conditions on the surface of the fibres are conducive to bonding. This work at present has had little use for determining the strength of the fibre/fibre bond as the model is in its infancy, but as the model evolves this property will be required.

The work undertaken by Seth and Page [11] proposes that the *stress/strain curve of paper is independent of the fibre structure and can be described by the average properties of the fibre*. This is a very important result as it simplifies the modelling process. Instead of generating a system of fibres with properties calculated from a particular statistical distribution, it is possible to use the average values of these properties.

Seth [11] and Jayne [12] have shown that *perfect fibres*, which have no defects such as crimps, kinks and micro-compressions, *behave linearly and elastically*. The perfect fibres are most likely to exist in the middle layers of the paper sheet, protected from damage during the papermaking process by the fibres in the surface layers. This bodes well for the modelling process as the mass/spring paradigm is ideally suited for simulating perfect fibres.

To summarise from the perspective of the numerical model; if the simulated fibre structure is two-dimensional, then only two damage mechanisms are present, fibre/fibre bond failure and fibre failure. Expanding the fibre structure to a third dimension introduces a third damage mechanism, the partial failure of a fibre/fibre bond, which will occur more regularly than the fibre/fibre bond failure. If two fibres overlap, there is not necessarily a fibre/fibre bond between them. Also, if the fibres are assumed to be perfect, then they can

be approximated by an elastic spring. Finally, the properties of each simulated fibre can be approximated by the average properties of the fibres without affecting the stress/strain curve of the paper.

2.3 Acoustic Emission Monitoring Technique

Acoustic emission monitoring is used in a broad range of practical applications, from condition monitoring, and fault diagnostics of engines, gearboxes, in biomedical applications such as heart murmurs, in ship sonars, in geological and seismic surveys, in fault detection of medical components by ultrasonic inspection and many other applications [13–19]. An introduction to the fundamentals of AE is given by Holroyd [13] and Vallen Systeme [20] with Wu [21] providing an overview of the technique applied to concrete.

The first use of the AE monitoring technique with respect to paper was performed by Corte [3] in the 1960's. The technique was used to count the number of acoustic events generated when a thin paper sheet was placed under load until fracture occurred. Corte showed an agreement between the experimental results and a statistical model of paper fracture [6]. In recent years, Yamauchi *et al.* [4] have carried out AE experiments on paper in an attempt to distinguish between a fibre/fibre bond failure and a fibre failure. To achieve this, a method involving the amplitude distribution of the acoustic events was used.

More recent applications of AE technology include the monitoring of damage in spruce [22], light weight coated paper [23] and isotropic paper sheets [24]. Houle [25] and Salminen [26] also monitored the damage progression in paper and used the AEs to show that the acoustic energy obeys a power law distribution similar to that of earthquakes. Figure 2.1 shows that this relationship can also be found in the experimental data generated from this FP5 project. The exponent $\beta = 1.30$ agrees with the results by Minozzi *et al.* [27] and by Salminen [26]. Note that the tail in power law distribution is due to the finite size of

the paper sample and is common in this type of analysis.

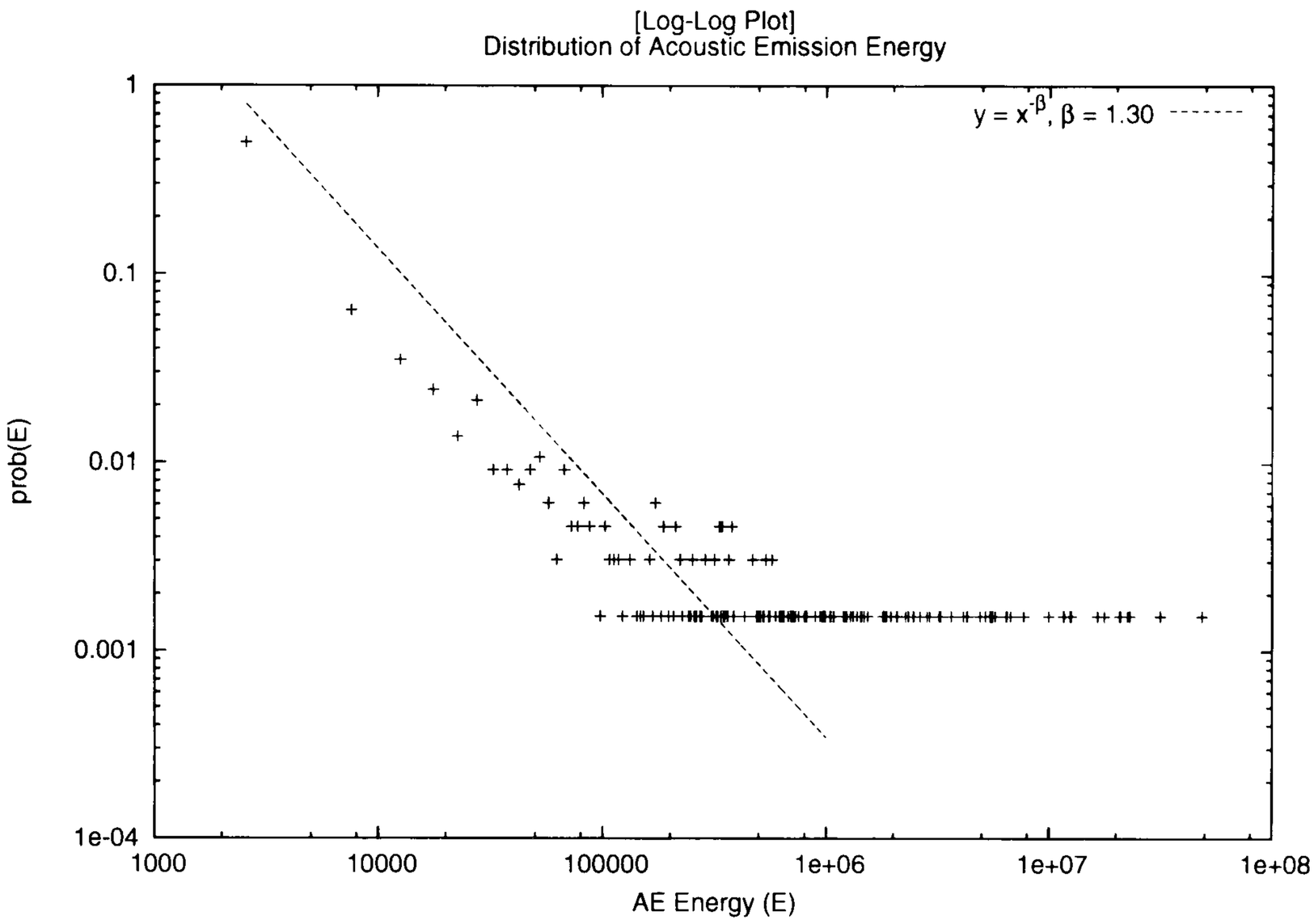

Figure 2.1: Distribution of AE Energy

Most of the literature uses the traditional AE monitoring technique which only records the number of AE events, peak levels and acoustic energies. This only provides data on the existence of a damage event, with no attempt to characterise the damage mechanism from the AE transient. The literature is very sparse regarding the analysis of AE transients from the damage mechanisms in paper. Johnson [28–33] has reported on work involving the AE transients generated from damage mechanisms in composite laminates. The approach used by Johnson can be applied to this project, as the composite laminate material is similar to paper as it has glass fibres embedded in it. Hamstad [34] has also used AE as a tool for identifying the source of damage within aluminium, however, the author could not show a unique and consistent relationship between the damage mechanism and the AE.

To summarise, the AE monitoring technique has seen wide success when used as a tool for detecting damage in certain materials. More recent uses of the technology for locating the source of the damage has shown varying degrees of success, depending on

the material being examined. However, very little work has been attempted at identifying the type of damage occurring in the material, in particular where paper is concerned. The work presented here hopes to lay the foundation for future work in this area.

2.4 Analysis of the Acoustic Emission Data

Methods for analysing the AE data to distinguish between a fibre/fibre bond failure and a fibre failure fall into two main categories; the extraction of features from the AE signal and the analysis of these features. A typical AE waveform has several properties or features defining its behaviour. Standard time domain features include the maximum amplitude of the signal, the duration of the signal and the time taken to reach the maximum amplitude, known as the rise time, as suggested by Vallen-Systeme [20]. In the frequency domain, features include the dominant frequency of the AE, the power of the dominant frequency and total power of the signal.

The standard method for extracting the frequency from a stationary signal (a signal where the frequency does not change with time) is the Fast Fourier Transform (FFT) [35–37]. In non-stationary signals, the Short Time Fourier Transform (STFT) [38], the Wigner Distribution (WD) [39, 40] and the Wavelet Transform (WT) [41–43] are used. The STFT, WD and WT all produce essentially the same results, representing the signal as a two-dimensional contour map of frequency against time, with varying degrees of time/frequency resolution. The WT was chosen as the preferred method as it overcomes the time/frequency resolution problem of the STFT and because of this it has generated much interest in the research community in recent times.

The mathematical theory of the WT is discussed by Kaiser [41], Chui [42] and Young [43], with Torrence [44] providing a more practical approach to wavelet analysis and supplying the wavelet transform software on-line [45]. AGU-Vallen is another freely available software tool for calculating the WT and is provided by Vallen-Systeme [46], having been

developed in corroboration with Takemoto [47] and Suzuki [48]. Hamstad [49] provides a brief overview of the software's functionality. Commercially available WT software is available from Clecom Software known as AutoSignal [50] and the Wavelet Toolbox in Matlab from Mathworks [51].

In the AE field, wavelets have been used in determining the location of damage in materials such as metal plates [18, 52] and composite laminates [53], and in structures [54, 55]. However, for this work, recurrent time-frequency patterns will be extracted from the wavelet analysis to help in classifying the AEs from different damage mechanisms [34, 56, 57]. Currently, no such work has been carried out on the AEs generated from paper.

Having extracted the required features from a set of AE signals, various methods can be called upon to analyse the data. Such methods include Principal Component Analysis (PCA) [58] and Self-Organising Maps (SOM) [59]. Once the data is processed by the PCA or SOM, the AEs from a particular damage mechanism will cluster together and will therefore be identifiable. If this is to be achieved, some of the features extracted from the AE must be dependent on the damage mechanism, so intelligent extraction of the features is required. To do this, a numerical model must be developed to ascertain which features of the AE are important.

2.5 The Numerical Modelling of Paper

It is clear a numerical model that can generate an AE from the movement of a complex structure of fibres would be a valuable tool to aid the identification of the AEs generated from the two selected damage mechanisms in paper. The modelling techniques used must be able to satisfy the following criteria.

- The ability to model the movement of a complex structure of fibres.

- The ability to handle the dynamic changes in the fibre structure caused by the damage mechanisms.

- The ability to generate an AE from the resulting movement.

Current numerical schemes for vibro-acoustic systems are almost exclusively based on Finite (FEM) and Boundary (BEM) Element Methods as they provide easy coupling of the vibro-acoustic equations. Sample applications of these methods are those by Ohayon and Soize [60], Grosveld [61] and Jarvinen [62] and commercial software is available for this methodology [63–65]. The FEM and BEM model the vibration of a continuous surface and couple this movement to the acoustic wave equation to generate the acoustic radiation. In contrast, this work requires the movement of the paper structure to be simulated from a microscopic level at which there is no continuous surface to model; instead the surface comprises a number of interconnected fibres, therefore two dimensional element methods cannot be applied to this problem, but it is possible to use beam elements.

It has been decided to approximate the paper fibres to a series of masses and springs, a technique known as the mass/spring or lumped mass system, rather than implement a FEM using beam elements. The reason for this as stated by Bourguignon [66], is that mass/spring models are able to generate dynamic behaviours in the fibre mesh, such as the two damage mechanisms, whereas FEMs are more suited to a static mesh. However, it is important to note that the formulation of the mass/spring model assumes that the springs have no bending stiffness. The bending stiffness of a typical paper fibre is defined as EI where E is the Young's modulus of the paper fibre and $I = \frac{Lt^3}{12}$ is the moment of inertia for a rectangular beam, where L and t are the fibre length and fibre thickness respectively. Using the material properties given in Table 4.1 for an average fibre, the bending stiffness EI = 1.92E-10 Pa m^4 $\approx= 0$, showing that the mass/spring model is a suitable approximation for the paper fibre structure. As reported by Seth [11] and Jayne [12], a perfect paper fibre has a similar behaviour to that of the springs in a mass/spring

model. The mass/spring model has seen extensive use in the area of real-time animation of cloth [67–74], hair [75,76] and is an integral part of game physics engines [77,78]. The mass/spring model is thought to be an ideal candidate for modelling the movement of the paper fibre structure as it can model the motion of the fibres in a thin paper sheet at a lower computational cost than using beam elements. There are software packages available that use the mass/spring paradigm, both free [79] and commercial [80, 81], but they do not provide the flexibility needed to model the damage mechanisms in thin paper sheets.

Much of the literature available on the mass/spring model focuses on its application in the animation and gaming industries, which often sacrifice accuracy for graphics speed. Baraff's ground breaking work [68] paved the way for the real-time simulation of cloth by solving the mass/spring model using an implicit formulation. The implicit formulation, in contrast with the explicit version as used by Provot [67], is unconditionally stable when a first-order accurate Euler approximation is used. This means that no matter what size time step is used, the motion of the mass/spring system is stable, which is desirable for the method's application in real-time animation. However, for physical simulations, a first order accurate approximation is poor, considering the fourth order accurate explicit Runge-Kutta method [82] is an available alternative. The work presented in this thesis will comment on the accuracy of the mass/spring model when applied to the vibration of the microscopic structure of paper.

The mass/spring model has also seen use in the area of music synthesis [83–86], which further qualifies it for use in generating AEs for this work. However, all implementations of the mass/spring model for music synthesis fix the positions of the masses in a plane and only allow the mass to move perpendicular to this plane. This enables the acoustic wave to be recorded directly from the mass/spring model. Similarly, Minozzi *et al.* [27] use a dynamic lattice model, where the motion of the lattice is restricted to one dimension, to directly generate the AEs from the fracture process. In contrast, the model presented in this

thesis allows the two-dimensional movement of the masses in the plane, which requires the coupling of the acoustic wave equation to generate the acoustic wave. For completeness, it should be noted that the mass/spring model is used for approximating strings where the properties of the string are lumped to certain points. An alternative approximation exists where the string is discretised so that its properties are distributed across its length, leading to a set of partial differential equations that can be solved numerically using standard techniques [87]. However, this method was rejected as there is no obvious approach for implementing the damage mechanisms in thin paper sheets.

The final topic that must be discussed is the acoustic propagation of the AEs generated from the vibrating mass/spring model. Wave propagation is defined by the Continuity equation and the Navier-Stokes equations. These equations can be found in standard texts on the subject [88, 89]. Popular methods for the numerical solution of these equations include the Finite Element Method (FEM) [90–92], the Finite Volume Method (FVM) [93] and the Finite Difference Time Domain (FDTD) method [94].

As the model is being developed for a specific need, a high degree of flexibility is required that the commercial codes available to the author [95–97] cannot provide. Therefore, the FDTD method will be used for its ease of implementation. The work done by Zakaria [94] will be used as the basis for the acoustic wave propagation portion of the model. The Continuity equation and Navier-Stokes equations can be combined to form the wave equation [98]. The wave equation is very well documented and its numerical solution is detailed in standard numerical texts [82].

However, most standard texts do not cover the application of non-reflecting boundary conditions of the wave equation. Non-reflecting boundary conditions are required for this work, so that the finite acoustic domain can model free-field sound radiation. To do this, the method proposed by Reynold [99] is used, as implemented by Zakaria [94]. Alternative non-reflecting boundary conditions are available [100–102] but the selected method will

be shown to be adequate for this study.

This discussion has so far covered the means for propagating a wave over a finite computational domain. The generation of the acoustic wave is now discussed. The movement of the mass/spring model is the required source function for the acoustic wave equation. The literature on this subject is very sparse and, as a result, no previous work could be found. Therefore, a study was undertaken to determine how the mass/spring model could be coupled to the acoustic wave equation. It is known that the mass/spring model is able to provide the velocities and positions of each mass. Corle [103] defined the source term for an inhomogeneous acoustic wave equation that accounts for the presence of solid boundaries. Using this definition, it is possible with the knowledge that all vibrating structures produce a dipole source [104], to accurately couple the mass/spring model to the acoustic wave equation.

Chapter 3

The Numerical Model

3.1 Overview

This chapter will discuss the numerical techniques used in modelling the damage mechanisms present in paper. This involves developing a hybrid model which uses the mass/spring paradigm to calculate the movement of the fibre structure coupled with the acoustic wave equation to generate the resulting AE. The mass/spring model was chosen for its ability to approximate very simple structures like the simple harmonic oscillator to more complex structures like a 3x3 Cartesian mesh. More importantly, the mass/spring model can be dynamically manipulated to simulate damage mechanisms of paper. A discussion of this can be found in Chapter 4 as this chapter will only provide details of the basic use of the mass/spring model.

In Section 3.2.1, the mass/spring model is derived from first principles, including details of the implementation of Poisson's ratio (Section 3.2.2), which must be taken in to account for materials with a high degree of elasticity. The mass/spring model can be simplified to two first order ordinary differential equations (ODE), which can be solved by explicit or implicit methods. Three explicit and one implicit method are investigated, namely the explicit Euler (Section 3.2.3), the fourth order Runge-Kutta (RK4) (Section

3.2.4) and the Velocity Verlet (Section 3.2.5) methods for the explicit methods, and the implicit Euler (Section 3.2.6) is the implicit method. The explicit Euler was considered for its simplicity, ease of implementation and is a standard benchmark for comparison with other ODE solvers. The RK4 method was considered as it incorporates a multi-step method and is widely used due to its stability and speed. The Velocity Verlet method is discussed as it is the only method which solves for the acceleration of the mass elements in the mass/spring model, rather than solving for the velocity. The implicit Euler method was considered as it is the simplest implicit method to implement.

Finding a suitable solver for the mass/spring model is only one part of the achieving an accurate numerical solution. The initial conditions of the mass/spring model must be given much consideration and care. A detailed discussion of the initial conditions can be found in Section 3.2.8. This leads to the identification of two types of initial conditions, the Equilibrium Initial Condition (EqIC) and the Stretching Initial Condition (StIC), which handle the initial disturbance of the fibre structure and the stretching of the fibre structure respectively.

Having described the implementation of the mass/spring model, Section 3.3.1 discusses the use of the acoustic wave equation which can be formulated into the acoustic pressure wave equation (Section 3.3.2) or the particle velocity wave equation (Section 3.3.3). Section 3.3.4 presents the use of non-reflecting boundary conditions when using the second and fourth order accurate numerical solvers of the wave equation. Section 3.3.5 provides a study of the acoustic fields generated by a single monopole, dipole and quadrupole source. This is needed to validate the wave equation solvers against the standard analytical test cases. Section 3.3.6 completes the analysis of the acoustic propagation model by presenting test cases of the acoustic wave equation using sinusoidal pulses for monopole and dipole sources.

This completes the individual analysis of the two numerical models, with Section 3.4.1

formulating an accurate method for coupling the mass/spring model to the acoustic wave equation. The hybrid model is then tested using a simple harmonic oscillator with the results shown in Section 3.4.4. Finally, the hybrid model is used to simulate the vibration of a rubber band and a paper fibre, comparing the numerical results with their experimental counterparts, with the results shown in Section 3.5.

3.2 Mass/Spring (Lumped) Model

3.2.1 Derivation of the Mass/Spring Model

Consider the mass/spring model unit cell:

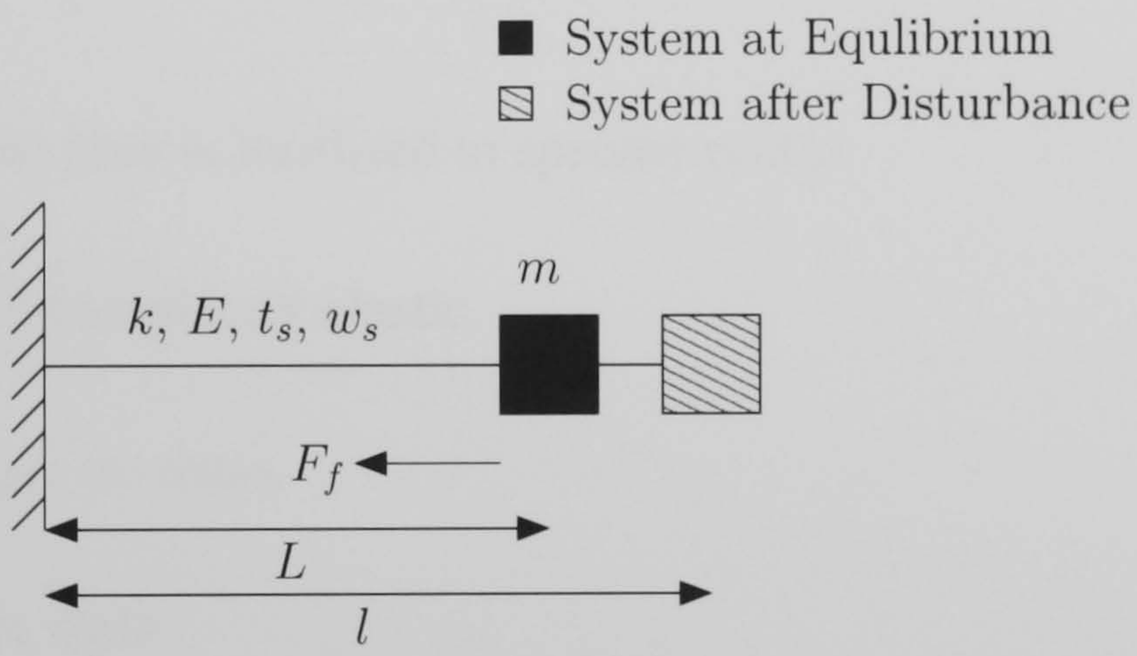

Figure 3.1: Mass/Spring Model Unit Cell

where:

x	Position of the Mass
m	Mass's Mass
F_f	Friction Force on the Mass
k	Stiffness of the Spring
E	Young's Modulus of the Spring
t_s	Thickness of the Spring
w_s	Width of the Spring
L	Equilibrium Length of the Spring
l	Length of the Spring

Before the derivation can proceed, there are certain assumptions associated with the mass/spring model.

- The mass of the fibre is localised to specific points.
- The springs are completely elastic.
- The springs have no mass.
- The springs are rigid.

The force F_s exerted by the spring on to the mass is given by Hooke's Law.

$$F_s = -k(l - L) \tag{3.2.1}$$

The frictional force F_f can be defined as proportional to the velocity of the mass.

$$F_f = -b\frac{dx}{dt} \tag{3.2.2}$$

where b is known as the frictional damping coefficient.

Applying Newton's Second Law, the sum of the forces acting on a rigid body is equal to the body's mass times its acceleration.

$$m\frac{d^2x}{dt^2} = F_s + F_f \tag{3.2.3}$$

$$m\frac{d^2x}{dt^2} + k(l - L) + b\frac{dx}{dt} = 0 \tag{3.2.4}$$

The spring stiffness can be calculated as follows [105]:

$$k = \frac{Et_s w_s}{L} \tag{3.2.5}$$

For the general two-dimensional case, where there are several springs connected to each node, the equations of motion become:

$$m_i\frac{d^2x_i}{dt^2} + \sum_j k_{ij}(l_{ij} - L_{ij})cos(\theta_{ij}) + b_i\frac{dx_i}{dt} = 0 \tag{3.2.6a}$$

$$m_i\frac{d^2y_i}{dt^2} + \sum_j k_{ij}(l_{ij} - L_{ij})sin(\theta_{ij}) + b_i\frac{dy_i}{dt} = 0 \tag{3.2.6b}$$

where:

i Mass Index

j Neighbouring Mass Index

ij Spring Connecting Masses i and j

Equation 3.2.6 can be expressed in vector form as:

$$m_i\frac{d^2\mathbf{r}_i}{dt^2} + \sum_j k_{ij}(||\mathbf{r}_j - \mathbf{r}_i|| - L_{ij})\frac{\mathbf{r}_j - \mathbf{r}_i}{||\mathbf{r}_j - \mathbf{r}_i||} + b_i\frac{d\mathbf{r}_i}{dt} = 0 \tag{3.2.7}$$

where:

$\mathbf{r}$ $[x, y]$ - Mass Position Vector

$||\mathbf{r}_j - \mathbf{r}_i||$ l_{ij} - Length of the Spring Connecting Masses i and j

$\frac{\mathbf{r}_j - \mathbf{r}_i}{||\mathbf{r}_j - \mathbf{r}_i||}$ $[\cos(\theta_{ij}), \sin(\theta_{ij})]$

3.2.2 Poisson's Ratio

The simple mass/spring model assumes that the cross-sectional area of the springs remain constant, independent of the amount by which they are displaced from equilibrium. This is an incorrect assumption as it neglects the influence of Poisson's Ratio, defined as the ratio of the transverse contracting strain to the longitudinal extension strain in the direction of the stretching force. Simply put, as the spring is stretched its width contracts, which in turn changes the cross-sectional area.

Poisson's ratio (ν) can be expressed as:

$$\nu = -\frac{\epsilon_{trans}}{\epsilon_{long}} \tag{3.2.8}$$

The strain (ϵ) in any dimension i can be calculated by:

$$\epsilon_i = \frac{\Delta i}{i}$$

For a fibre of length L, thickness t and width w, Poisson's ratio can be expressed as:

$$\nu = -\frac{\Delta t L}{\Delta L t} = -\frac{\Delta w L}{\Delta L w}$$

Express the above equation in terms of Δt and Δw to get:

$$\Delta t = -\frac{\nu \Delta L t}{L}$$

$$\Delta w = -\frac{\nu \Delta L w}{L}$$

The change in cross-sectional area can be calculated as:

$$A = (t + \Delta t)(w + \Delta w)$$

which can be expressed as:

$$A = \left(t - \frac{\nu \Delta L t}{L}\right)\left(w - \frac{\nu \Delta L w}{L}\right) \tag{3.2.9}$$

The model uses Equation 3.2.9 to account for the change in the cross-sectional area due to the stretching of the system under load.

3.2.3 Explicit Euler Method

The simplest explicit numerical solver for a first order ordinary differential equation (ODE) is the first order explicit Euler method. As Equation 3.2.7 is a second order ODE, the Euler method cannot be applied directly to produce a solution. However Equation 3.2.7 can be simplified to two first order ODEs as shown below:

$$\frac{d\mathbf{u}_i}{dt} = -\sum_j \frac{k_{ij}}{m_i}(||\mathbf{r}_j - \mathbf{r}_i|| - L_{ij})\frac{\mathbf{r}_j - \mathbf{r}_i}{||\mathbf{r}_j - \mathbf{r}_i||} - \frac{b_i}{m_i}\mathbf{u}_i \tag{3.2.10a}$$

$$\frac{d\mathbf{r}_i}{dt} = \mathbf{u}_i \tag{3.2.10b}$$

Using the explicit Euler method (refer to [82] for a derivation of the algorithm), the two time differentials can be approximated to:

$$\frac{d\mathbf{u}}{dt} = \frac{\mathbf{u}^{n+1} - \mathbf{u}^n}{\Delta t} \tag{3.2.11a}$$

$$\frac{d\mathbf{r}}{dt} = \frac{\mathbf{r}^{n+1} - \mathbf{r}^n}{\Delta t} \tag{3.2.11b}$$

Therefore, Equation 3.2.10 becomes:

$$\mathbf{u}_i^{n+1} = \mathbf{u}_i^n - \Delta t \left(\sum_j \frac{k_{ij}}{m_i} (||\mathbf{r}_j^n - \mathbf{r}_i^n|| - L_{ij}) \frac{\mathbf{r}_j^n - \mathbf{r}_i^n}{||\mathbf{r}_j^n - \mathbf{r}_i^n||} + \frac{b_i}{m_i} \mathbf{u}_i^n \right) \tag{3.2.12a}$$

$$\mathbf{r}_i^{n+1} = \mathbf{r}_i^n + \Delta t \mathbf{u}_i^{n+1} \tag{3.2.12b}$$

Algorithm 1 shows the pseudocode for the explicit Euler method, with Algorithm 2 showing the pseudocode for calculating the internal forces acting on each mass.

Algorithm 1 The Explicit Euler Method

Require: $\mathcal{F}(i, \mathbf{r})$ (see Algorithm 2)

```
I ← Number of Masses
N ← Number of Iterations
for n = 0 to N do
    for i = 0 to I do
        u_i ← u_i − (Δt/m_i)(F(i, r) + b_i r_i)
        r_i ← r_i + Δt u_i
    end for
end for
return r, u
```

Algorithm 2 $\mathcal{F}(i, \mathbf{r})$ - Calculates Internal Forces on Mass i

```
J ← Number of Neighbouring Masses
F ← 0
for j = 0 to J do
    L_ij ← Original Length of Spring
    k_ij ← Stiffness of Spring
    F ← F + (k_ij/m_i)(||r_j − r_i|| − L_ij)(r_j − r_i)/||r_j − r_i||
end for
return F
```

Before the system can be solved using the explicit Euler method, a stability analysis [106] must be performed to ascertain a stable time step. Consider the two first order ODEs of the mass/spring unit cell.

$$\frac{dx}{dt} - u = 0 \tag{3.2.13a}$$

$$\frac{du}{dt} + \frac{k}{m}x + \frac{b}{m}u = 0 \tag{3.2.13b}$$

The above two equations can be shown in matrix form as:

$$\begin{bmatrix} \frac{dx}{dt} \\ \\ \frac{du}{dt} \end{bmatrix} = \begin{bmatrix} 0 & 1 \\ \\ -\frac{k}{m} & -\frac{b}{m} \end{bmatrix} \begin{bmatrix} x \\ \\ u \end{bmatrix} \tag{3.2.14}$$

Using a first order forward difference approximation, Equations 3.2.13 become:

$$x^{n+1} = x^n + \Delta t u^n \tag{3.2.15a}$$

$$u^{n+1} = u^n - \Delta t \frac{k}{m} x^n - \Delta t \frac{b}{m} u^n \tag{3.2.15b}$$

which can be expressed in matrix form as:

$$\begin{bmatrix} x^{n+1} \\ \\ u^{n+1} \end{bmatrix} = \begin{bmatrix} 1 & \Delta t \\ \\ -\Delta t \frac{k}{m} & 1 - \Delta t \frac{b}{m} \end{bmatrix} \begin{bmatrix} x^n \\ \\ u^n \end{bmatrix} \tag{3.2.16}$$

where P, known as the amplification matrix, is given as:

$$P = \begin{bmatrix} 1 & \Delta t \\ \\ -\Delta t \frac{k}{m} & 1 - \Delta t \frac{b}{m} \end{bmatrix} \tag{3.2.17}$$

A stable time step can be calculated by finding the roots of $|P|$, which are given as:

$$|P| = \Delta t^2 k - \Delta t b + m = 0 \tag{3.2.18}$$

Therefore, the stability criteria for the mass/spring unit cell are defined as:

$$\Delta t \leq \frac{b \pm \sqrt{b^2 - 4km}}{2k} \tag{3.2.19}$$

The smallest positive eigenvalue must be used as the time step size Δt, to ensure the

system is conditionally stable.

3.2.4 The Fourth Order Runge-Kutta Method

The fourth order Runge-Kutta method (RK4) is similar to the explicit Euler method as it solves ODEs of the form.

$$\frac{dx}{dt} = f(t, x)$$

The formulae for the RK4 method are given below (refer to Cheney [82] for a description of the algorithm).

$$x^{n+1} = x^n + \frac{1}{6}(K_1 + 2K_2 + 2K_3 + K_4) \tag{3.2.20}$$

where:

$$\begin{aligned} K_1 &= \Delta t f(t, x) \\ K_2 &= \Delta t f\left(t + \frac{1}{2}\Delta t, x + \frac{1}{2}K_1\right) \\ K_3 &= \Delta t f\left(t + \frac{1}{2}\Delta t, x + \frac{1}{2}K_2\right) \\ K_4 &= \Delta t f(t + \Delta t, x + K_3) \end{aligned}$$

Henrici [107] and Ralston [108] give a full derivation of the RK4 formulae. The equation of motion for the mass/spring model as given in Equation 3.2.10 can be written as.

$$\frac{d\mathbf{u}_i}{dt} = f(t, \mathbf{u}_i, \mathbf{r}) \quad \text{where:} \quad f(t, \mathbf{u}_i, \mathbf{r}) = -\sum_j \frac{k_{ij}}{m_i}(||\mathbf{r}_j - \mathbf{r}_i|| - L_{ij})\frac{\mathbf{r}_j - \mathbf{r}_i}{||\mathbf{r}_j - \mathbf{r}_i||} - \frac{b_i}{m_i}\mathbf{u} \tag{3.2.21a}$$

$$\frac{d\mathbf{r}_i}{dt} = g(t, \mathbf{u}_i) \quad \text{where:} \quad g(t, \mathbf{u}_i) = \mathbf{u}_i \tag{3.2.21b}$$

Algorithm 3 shows the pseudocode for the RK4 method.

Algorithm 3 The Fourth Order Runge-Kutta Method

Require: $\mathcal{F}(i, \mathbf{r})$ (see Algorithm 2)

$I \leftarrow$ Number of Masses
$N \leftarrow$ Number of Iterations
for $n = 0$ to N **do**
  for $i = 0$ to I **do**
    $K_{1\mathbf{u}_i} \leftarrow \Delta t(\mathcal{F}(i, \mathbf{r}) - \frac{b}{m_i}\mathbf{u}_i)$
    $K_{1\mathbf{r}_i} \leftarrow \Delta t\mathbf{u}_i$
  end for
  for $i = 0$ to I **do**
    $K_{2\mathbf{u}_i} \leftarrow \Delta t(\mathcal{F}(i, \mathbf{r} + \frac{1}{2}K_{1\mathbf{r}}) - \frac{b}{m_i}(\mathbf{u}_i + \frac{1}{2}K_{1\mathbf{u}_i}))$
    $K_{2\mathbf{r}_i} \leftarrow \Delta t(\mathbf{u}_i + \frac{1}{2}K_{1\mathbf{r}_i})$
  end for
  for $i = 0$ to I **do**
    $K_{3\mathbf{u}_i} \leftarrow \Delta t(\mathcal{F}(i, \mathbf{r} + \frac{1}{2}K_{2\mathbf{r}}) - \frac{b}{m_i}(\mathbf{u}_i + \frac{1}{2}K_{2\mathbf{u}_i}))$
    $K_{3\mathbf{r}_i} \leftarrow \Delta t(\mathbf{u}_i + \frac{1}{2}K_{2\mathbf{r}_i})$
  end for
  for $i = 0$ to I **do**
    $K_{4\mathbf{u}_i} \leftarrow \Delta t(\mathcal{F}(i, \mathbf{r} + K_{3\mathbf{r}}) - \frac{b}{m_i}(\mathbf{u}_i + K_{3\mathbf{u}_i}))$
    $K_{4\mathbf{r}_i} \leftarrow \Delta t(\mathbf{u}_i + K_{3\mathbf{r}_i})$
  end for
  for $i = 0$ to I **do**
    $\mathbf{u}_i \leftarrow \mathbf{u}_i + \frac{1}{6}(K_{1\mathbf{u}} + 2K_{2\mathbf{u}} + 2K_{3\mathbf{u}} + K_{4\mathbf{u}})$
    $\mathbf{r}_i \leftarrow \mathbf{r}_i + \frac{1}{6}(K_{1\mathbf{r}} + 2K_{2\mathbf{r}} + 2K_{3\mathbf{r}} + K_{4\mathbf{r}})$
  end for
end for
return $\mathbf{r}, \mathbf{u}$

3.2.5 The Velocity Verlet Method

Consider the general equation of motion for a mass/spring system as shown in Equation 3.2.7, which can be written in terms of displacement $\mathbf{r}$, velocity $\mathbf{u}$ and acceleration $\mathbf{a}$.

$$m_i\mathbf{a}_i + \sum_j k_{ij}(||\mathbf{r}_j - \mathbf{r}_i|| - L_{ij})\frac{\mathbf{r}_j - \mathbf{r}_i}{||\mathbf{r}_j - \mathbf{r}_i||} + b_i\mathbf{u}_i = 0 \tag{3.2.22}$$

where:

$$\mathbf{a}_i = \frac{d^2\mathbf{r}_i}{dt^2}$$
$$\mathbf{u}_i = \frac{d\mathbf{r}_i}{dt}$$

The Velocity Verlet method as described by Eberly [78] and Ercolessi [109] is a variant of the Verlet method [110] with the formulae stated below.

$$\mathbf{r}_i^{n+1} = \mathbf{r}_i^n + \mathbf{u}_i^n \Delta t + \frac{1}{2}\mathbf{a}_i^n \Delta t^2 \tag{3.2.23a}$$

$$\mathbf{u}_i^{n+\frac{1}{2}} = \mathbf{u}_i^n + \frac{1}{2}\mathbf{a}_i^n \Delta t \tag{3.2.23b}$$

$$\mathbf{a}_i^{n+1} = -\sum_j \frac{k_{ij}}{m_i}(||\mathbf{r}_j^{n+1} - \mathbf{r}_i^{n+1}|| - L_{ij})\frac{\mathbf{r}_j^{n+1} - \mathbf{r}_i^{n+1}}{||\mathbf{r}_j^{n+1} - \mathbf{r}_i^{n+1}||} - \frac{b_i}{m_i}\mathbf{u}_{i+\frac{1}{2}} = 0 \tag{3.2.23c}$$

$$\mathbf{u}^{n+1} = \mathbf{u}_i^{n+\frac{1}{2}} + \frac{1}{2}\mathbf{a}_i^{n+1} \Delta t \tag{3.2.23d}$$

where Equation 3.2.23c is simply Equation 3.2.22. Algorithm 4 shows the pseudocode for the Velocity Verlet method.

Algorithm 4 The Velocity Verlet Method

Require: $\mathcal{F}(i, \mathbf{r})$ (see Algorithm 2)

1: $I \leftarrow$ Number of Masses
2: $N \leftarrow$ Number of Iterations
3: **for** $i = 0$ to I **do**
4: $\quad \mathbf{r}_i \leftarrow \mathbf{r}_i + \mathbf{u}_i \Delta t + \frac{1}{2}\mathbf{a}_i \Delta t^2$
5: $\quad \mathbf{u}_i \leftarrow \mathbf{u}_i + \frac{1}{2}\mathbf{a}_i \Delta t$
6: $\quad \mathbf{a}_i \leftarrow \mathcal{F}(i, \mathbf{r}) - \frac{b}{m_i}\mathbf{u}_i$
7: $\quad \mathbf{u}_i \leftarrow \mathbf{u}_i + \frac{1}{2}\mathbf{a}_i \Delta t$
8: **end for**
9: **return** r, u, a

3.2.6 Implicit Euler Method

The simplest implicit numerical solver for a first order ODE is the first order accurate implicit Euler method. The explicit Euler method uses a forward difference to approximate the two time differentials, but the implicit Euler approximates the two time differentials with a backward difference which leads to the following discretised form of Equation 3.2.10. For a full derivation of the implicit Euler method, refer to the work by Baraff and Witkin [68].

$$\mathbf{u}_i^{n+1} = \mathbf{u}_i^n - \Delta t\left(\sum_j \frac{k_{ij}}{m_i}(||\mathbf{r}_j^n - \mathbf{r}_i^n|| - L_{ij})\frac{\mathbf{r}_j^{n+1} - \mathbf{r}_i^{n+1}}{||\mathbf{r}_j^n - \mathbf{r}_i^n||} + \frac{b_i}{m_i}\mathbf{u}_i^{n+1}\right) \tag{3.2.24a}$$

$$\mathbf{r}_i^{n+1} = \mathbf{r}_i^n + \Delta t\mathbf{u}_i^{n+1} \tag{3.2.24b}$$

Equation 3.2.24a can be simplified to give:

$$\mathbf{u}_i^{n+1} = \mathbf{u}_i^n - \Delta t\left(\sum_j \frac{k_{ij}}{m_i}\left(1 - \frac{L_{ij}}{||\mathbf{r}_j^n - \mathbf{r}_i^n||}\right)(\mathbf{r}_j^{n+1} - \mathbf{r}_i^{n+1}) + \frac{b_i}{m_i}\mathbf{u}_i^{n+1}\right) \tag{3.2.25}$$

Given that $\mathbf{u}^{n+1} = \Delta\mathbf{u} + \mathbf{u}^n$ and $\mathbf{r}^{n+1} = \Delta\mathbf{r} + \mathbf{r}^n$, Equations 3.2.25 and 3.2.24b can be expressed in matrix form as:

$$\Delta\mathbf{u} = -\Delta t M^{-1} f(\Delta\mathbf{r} + \mathbf{r}^n, \Delta\mathbf{u} + \mathbf{u}^n) \tag{3.2.26a}$$

$$\Delta\mathbf{r} = \Delta t(\Delta\mathbf{u} + \mathbf{u}^n) \tag{3.2.26b}$$

where:

$$f(\Delta\mathbf{r}+\mathbf{r}^n,\Delta\mathbf{u}+\mathbf{u}^n)=\sum_j k_{ij}\left(1-\frac{L_{ij}}{||\mathbf{r}_j^n-\mathbf{r}_i^n||}\right)(\Delta\mathbf{r}_j+\mathbf{r}_j^n-\Delta\mathbf{r}_i-\mathbf{r}_i^n)+b_i(\Delta\mathbf{u}_i+\mathbf{u}_i^n) \tag{3.2.27}$$

Equation 3.2.27 is non-linear and can be approximated to a linear equation by applying a first order Taylor expansion as shown below:

$$f(\Delta\mathbf{r}+\mathbf{r}^n,\Delta\mathbf{u}+\mathbf{u}^n)=\mathbf{f}^n+\frac{\partial\mathbf{f}^n}{\partial\mathbf{r}}\Delta\mathbf{r}+\frac{\partial\mathbf{f}^n}{\partial\mathbf{u}}\Delta\mathbf{u}$$

Therefore by substituting in the linear approximation, Equation 3.2.26 becomes:

$$\Delta\mathbf{u}=-\Delta t M^{-1}\left(\mathbf{f}^n+\frac{\partial\mathbf{f}^n}{\partial\mathbf{r}}\Delta\mathbf{r}+\frac{\partial\mathbf{f}^n}{\partial\mathbf{u}}\Delta\mathbf{u}\right) \tag{3.2.28a}$$

$$\Delta\mathbf{r}=\Delta t(\Delta\mathbf{u}+\mathbf{u}^n) \tag{3.2.28b}$$

Substituting in $\Delta\mathbf{r}=\Delta t(\Delta\mathbf{u}+\mathbf{u}^n)$ into Equation 3.2.28a to get:

$$\Delta\mathbf{u}=-\Delta t M^{-1}\left(\mathbf{f}^n+\frac{\partial\mathbf{f}^n}{\partial\mathbf{r}}\Delta t(\Delta\mathbf{u}+\mathbf{u}^n)+\frac{\partial\mathbf{f}^n}{\partial\mathbf{u}}\Delta\mathbf{u}\right)$$

Re-arrange the above equation to get:

$$\left(I+\Delta t M^{-1}\frac{\partial\mathbf{f}^n}{\partial\mathbf{u}}+\Delta t^2 M^{-1}\frac{\partial\mathbf{f}^n}{\partial\mathbf{r}}\right)\Delta\mathbf{u}=-\Delta t M^{-1}\left(\mathbf{f}^n+\Delta t\frac{\partial\mathbf{f}^n}{\partial\mathbf{r}}\mathbf{u}^n\right) \tag{3.2.29}$$

where I is the identity matrix. To solve for $\Delta\mathbf{u}$, $\mathbf{f}^n$, $\frac{\partial\mathbf{f}^n}{\partial\mathbf{r}}$ and $\frac{\partial\mathbf{f}^n}{\partial\mathbf{u}}$ must be evaluated. These are shown below as stated by Choi [69]:

$$\mathbf{f}_i^n=\sum_j k_{ij}\left(1-\frac{L_{ij}}{||\mathbf{r}_j^n-\mathbf{r}_i^n||}\right)(\mathbf{r}_j^n-\mathbf{r}_i^n)+b_i\mathbf{u}_i^n \tag{3.2.30a}$$

$$\frac{\partial \mathbf{f}_i^n}{\partial \mathbf{r}_j} = k_{ij}\frac{(\mathbf{r}_j^n - \mathbf{r}_i^n)(\mathbf{r}_j^n - \mathbf{r}_i^n)^T}{(\mathbf{r}_j^n - \mathbf{r}_i^n)^T(\mathbf{r}_j^n - \mathbf{r}_i^n)} + k_{ij}\left(1 - \frac{L_{ij}}{\|\mathbf{r}_j^n - \mathbf{r}_i^n\|}\right)\left(I - \frac{(\mathbf{r}_j^n - \mathbf{r}_i^n)(\mathbf{r}_j^n - \mathbf{r}_i^n)^T}{(\mathbf{r}_j^n - \mathbf{r}_i^n)^T(\mathbf{r}_j^n - \mathbf{r}_i^n)}\right) \tag{3.2.30b}$$

$$\frac{\partial \mathbf{f}_i^n}{\partial \mathbf{u}_j} = b_i I \tag{3.2.30c}$$

Equation 3.2.29 has the from $A\mathbf{x} = \mathbf{b}$ and can be solved using a host of different techniques. To be able to choose a suitable solver, it is important to note that A on first inspection is a sparse symmetric positive definite matrix, ideally suited for the Conjugate Gradient solver. However, it is possible to manipulate the inverted mass matrix M^{-1} so that certain masses remain fixed throughout the simulation. To fix mass i, the two corresponding entries in M^{-1} must be set to 0. This destroys the symmetry exhibited by A and causes the Conjugate Gradient method to fail when the system has a large number of fixed points.

To overcome this problem, the BiConjugate Gradient solver as documented by Press *et al.* [37] is used as shown in Algorithm 6, with Algorithm 5 describing the Implicit Euler method. Finally, the structure of the matrices involved in the Implicit Euler method for a 9 mass fibre can be seen in Figure 3.2. Of particular interest is Figure 3.2(a) which highlights the non-symmetric nature of A.

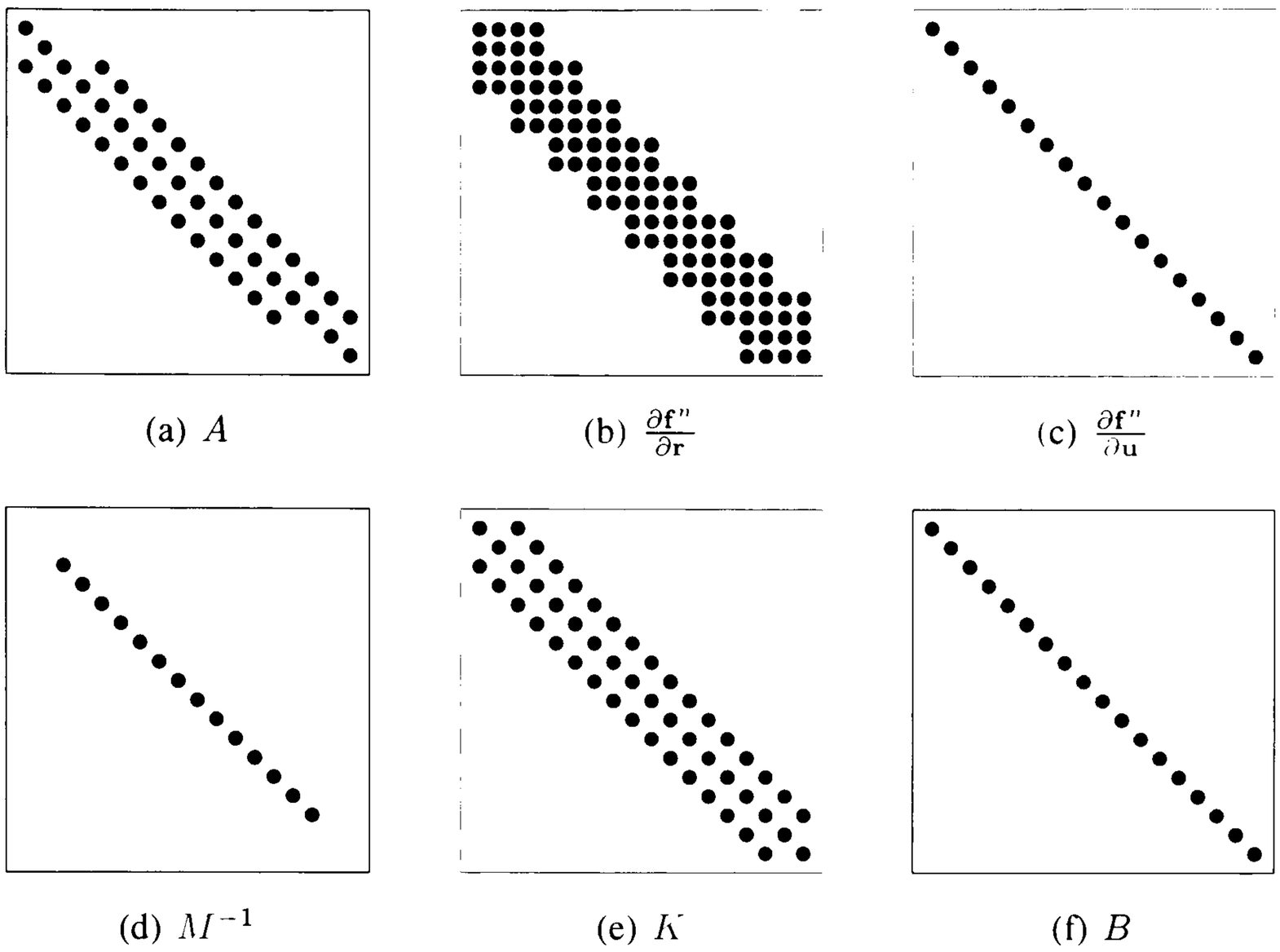

(a) A (b) $\frac{\partial \mathbf{f}''}{\partial \mathbf{r}}$ (c) $\frac{\partial \mathbf{f}''}{\partial \mathbf{u}}$

(d) M^{-1} (e) K (f) B

Figure 3.2: Structure of the Important Matrices

Algorithm 5 Time Implicit Euler Method

Require: $\mathcal{B}(A, \mathbf{x}^n, \mathrm{b})$ (see Algorithm 6)

$N \leftarrow$ Number of Iterations
$B \leftarrow$ Populate Damping Matrix
$I \leftarrow$ Populate Identity Matrix
for $n = 0$ to N **do**
  $M^{-1} \leftarrow$ Populate Mass Matrix
  $K \leftarrow$ Populate Stiffness Matrix
  $\frac{\partial \mathbf{f}^n}{\partial \mathbf{r}} \leftarrow$ Populate Matrix of Spring Force Vector
  $\frac{\partial \mathbf{f}^n}{\partial \mathbf{u}} \leftarrow$ Populate Matrix of Damping Force Vector
  $A \leftarrow I - \Delta t^2 M^{-1} \frac{\partial \mathbf{f}^n}{\partial \mathbf{r}} - \Delta t M^{-1} \frac{\partial \mathbf{f}^n}{\partial \mathbf{u}}$
  $\mathbf{b} \leftarrow \mathbf{f}^n + \Delta t \frac{\partial \mathbf{f}^n}{\partial \mathbf{u}}$
  $\Delta \mathbf{u} \leftarrow \mathcal{B}(A, \Delta \mathbf{u}, \mathbf{b})$
  $\Delta \mathbf{r} \leftarrow \Delta t(\Delta \mathbf{u} + \mathbf{u})$
  $\mathbf{u} \leftarrow \Delta u + \mathbf{u}$
  $\mathbf{r} \leftarrow \Delta r + \mathbf{r}$
end for

Algorithm 6 $\mathcal{B}(A, \mathbf{x}^{n-1}, \mathrm{b})$ - Preconditioned BiConjugate Gradient Solver

$t \leftarrow$ Tolerance Level
$\mathbf{r}^{n-1} \leftarrow \mathbf{b} - A\mathbf{x}^{n-1}$
$\tilde{\mathbf{r}}^{n-1} \leftarrow \mathbf{r}^{n-1}$
while $\mathbf{r}^{n} - \mathbf{r}^{n-1} > t$ **do**
    Solve $M\mathbf{z}^{n-1} = \mathbf{r}^{\mathbf{n-1}}$, M - Preconditioner
    Solve $M^{T}\tilde{\mathbf{z}}^{n-1} = \tilde{\mathbf{r}}^{\mathbf{n-1}}$
    $\rho^{n-1} \leftarrow \mathbf{z}^{\mathbf{n-1}^{\mathbf{T}}}\tilde{\mathbf{r}}^{\mathbf{n-1}}$
    if $\rho^{n-1} = 0$ **then**
        Exit - Method Fails
    end if
    if $n = 1$ **then**
        $\mathbf{p}^{n} \leftarrow \mathbf{z}^{n-1}$
        $\tilde{\mathbf{p}}^{n} \leftarrow \tilde{\mathbf{z}}^{n-1}$
    else
        $\beta \leftarrow \frac{\rho^{n-1}}{\rho^{n-2}}$
        $\mathbf{p}^{n} \leftarrow \mathbf{z}^{n-1} + \beta\mathbf{p}^{n-1}$
        $\tilde{\mathbf{p}}^{n} \leftarrow \tilde{\mathbf{z}}^{n-1} + \beta\tilde{\mathbf{p}}^{n-1}$
    end if
    $\alpha \leftarrow \frac{\rho^{n-1}}{\tilde{\mathbf{p}}^{n^{T}} A\mathbf{p}^{n}}$
    $\mathbf{x}^{n} \leftarrow \mathbf{x}^{n-1} + \alpha\mathbf{p}^{n}$
    $\mathbf{r}^{n} \leftarrow \mathbf{r}^{n-1} - \alpha A\mathbf{p}^{n}$
    $\tilde{\mathbf{r}}^{n} \leftarrow \tilde{\mathbf{r}}^{n-1} - \alpha A^{T}\tilde{\mathbf{p}}^{n}$
end while
return $\mathbf{x}^{n}$

3.2.7 Comparison of the Numerical Methods

This section will compare the differences in the results obtained from the explicit Euler, RK4 and Velocity Verlet methods from two test cases, the simple harmonic oscillator and the 5 mass fibre. Each simulation will provide statistics on the execution time along with plots of the displacements and velocities of the central mass.

Simple Harmonic Oscillator (SHO)

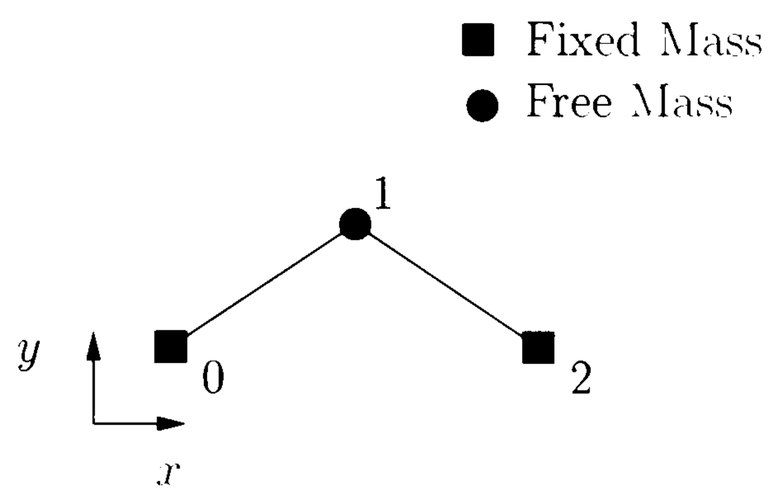

Figure 3.3: Simple Harmonic Oscillator

Table 3.1 states the model parameters and initial conditions of the simple harmonic oscillator with Table 3.2 providing the simulation statistics.

Model Parameters	
Δt	0.01 s
b	0.00 kg/s
m	0.20 kg
E	1.00 Pa
t	1.00 m
w	0.25 m
L	0.25 m
ν	0.00

Initial Conditions			
Mass	$\mathbf{r}^0$ (m)	$\Delta\mathbf{r}^0$ (m)	$\mathbf{u}^0$ (m/s)
0	[-0.55, 0.00]	[0.00, 0.00]	[0.00, 0.00]
1	[0.00, 0.00]	[0.00, 0.10]	[0.00, 0.00]
2	[0.55, 0.00]	[0.00, 0.00]	[0.00, 0.00]

Table 3.1: Model Parameters and Initial Conditions for a Simple Harmonic Oscillator

	Explicit Euler	RK4	Velocity Verlet	Implicit Euler
Order of Accuracy	1	4	4	1
Time Taken (s)	2.574	2.669	2.687	0.102
Time Step (s)	0.01	0.01	0.01	0.50
Number of Iterations	10000	10000	10000	200
Time/Iteration (ms)	0.257	0.267	0.269	0.510

Table 3.2: Simple Harmonic Oscillator Simulation Statistics

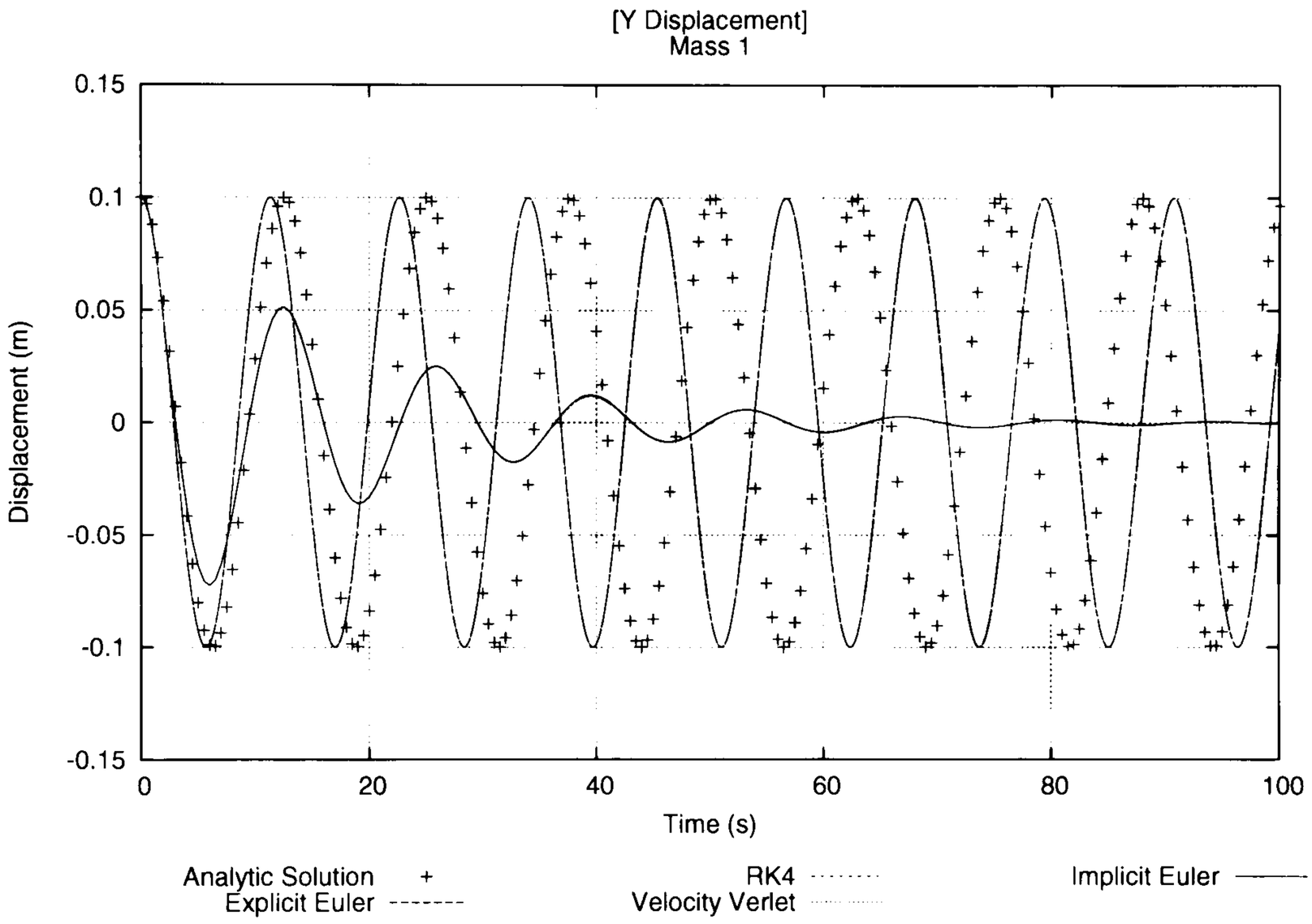

(a) Y Displacements

Figure 3.4: Results for the Simple Harmonic Oscillator

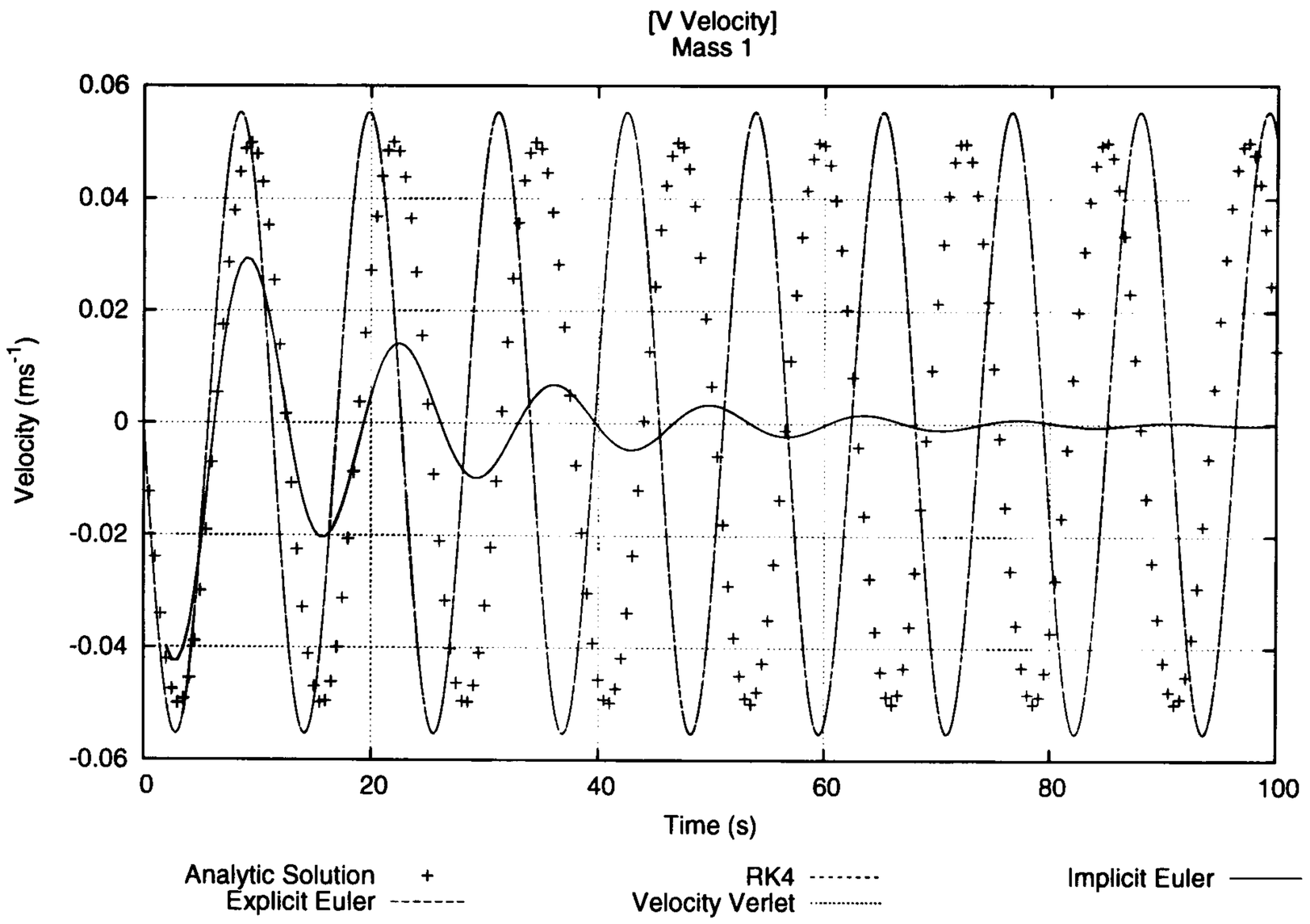

(b) V Velocity

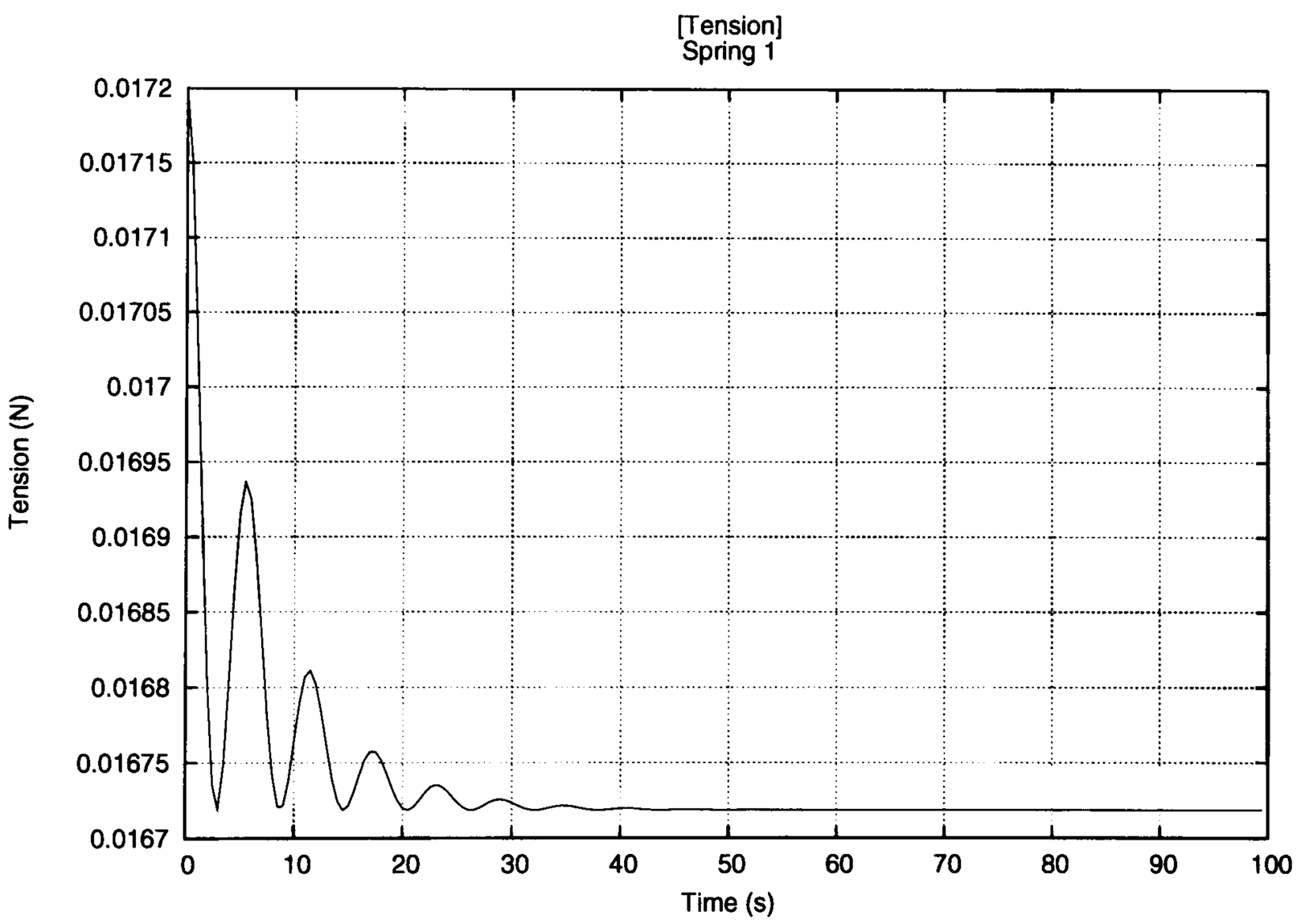

(c) Tension

Figure 3.4: Results for the Simple Harmonic Oscillator

5 Mass Fibre

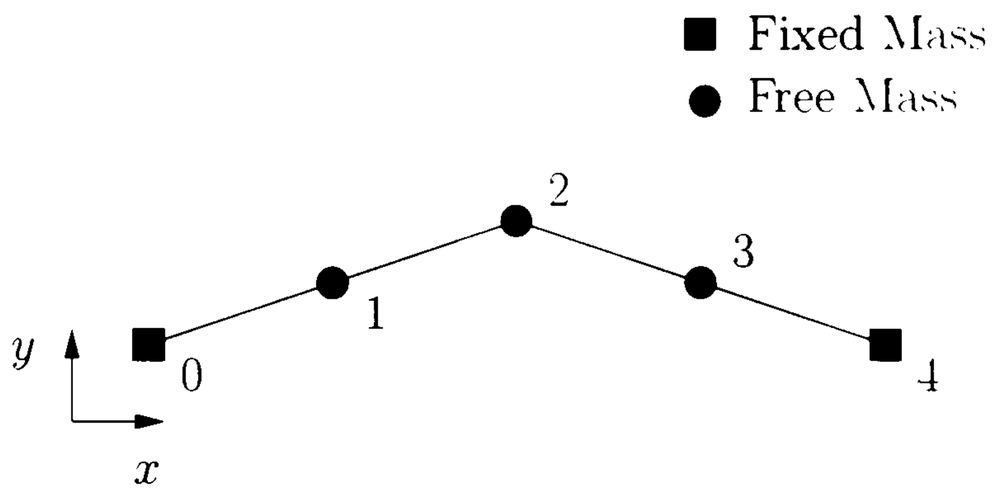

Figure 3.5: 5 Mass Fibre

Table 3.3 states the model parameters and initial conditions of the 5 mass fibre with Table 3.4 providing the simulation statistics.

Model Parameters	
Δt	0.01 s
b	0.00 kg/s
m	0.20 kg
E	1.00 Pa
t	1.00 m
w	0.25 m
L	0.25 m
ν	0.00

Initial Conditions			
Mass	$\mathbf{r}^0$ (m)	$\Delta\mathbf{r}^0$ (m)	$\mathbf{u}^0$ (m/s)
0	[-0.55, 0.00]	[0.00, 0.00]	[0.00, 0.00]
1	[-0.275, 0.00]	[0.00, 0.05]	[0.00, 0.00]
2	[0.00, 0.00]	[0.00, 0.10]	[0.00, 0.00]
3	[0.275, 0.00]	[0.00, 0.05]	[0.00, 0.00]
4	[0.55, 0.00]	[0.00, 0.00]	[0.00, 0.00]

Table 3.3: Model Parameters and Initial Conditions for a 5 Mass Fibre

	Explicit Euler	**RK4**	**Velocity Verlet**	**Implicit Euler**
Order of Accuracy	1	4	4	1
Time Taken (s)	3.656	3.810	4.086	0.204
Time Step (s)	0.01	0.01	0.01	0.50
Number of Iterations	10000	10000	10000	200
Time/Iteration (ms)	0.366	0.381	0.409	1.020

Table 3.4: 5 Mass Fibre Simulation Statistics

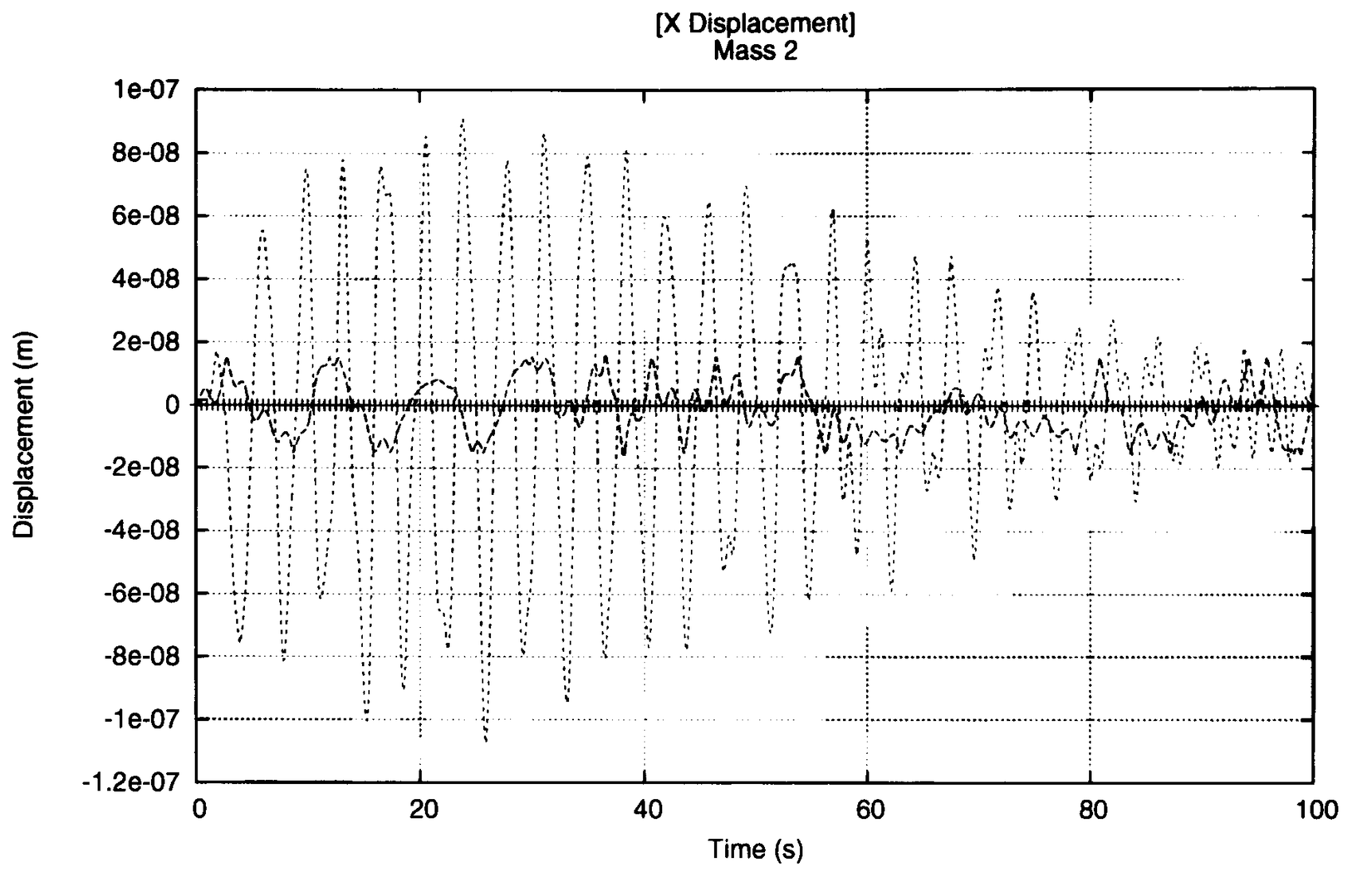

(a) X Displacements

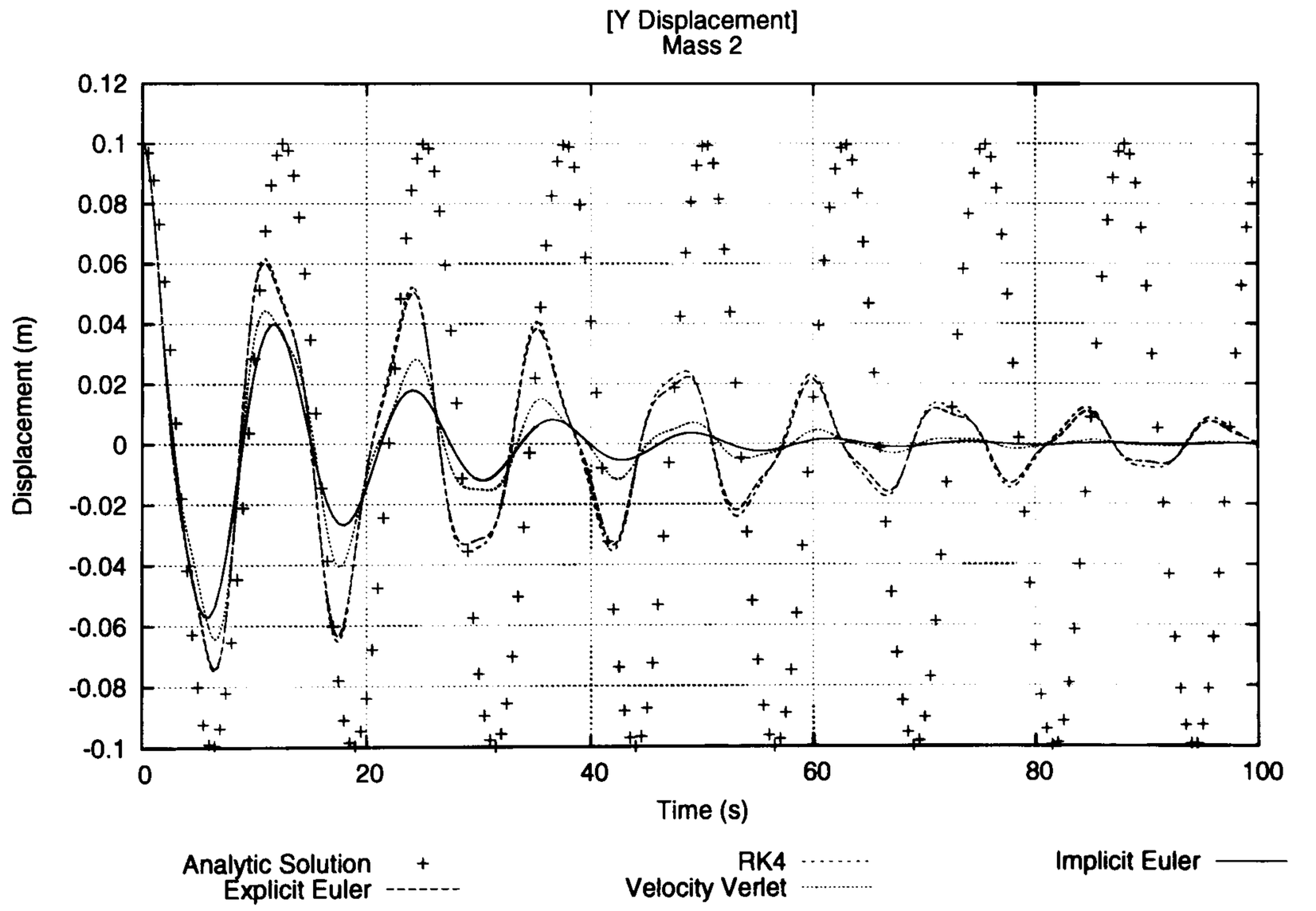

(b) Y Displacements

Figure 3.6: Results for the 5 Mass Fibre

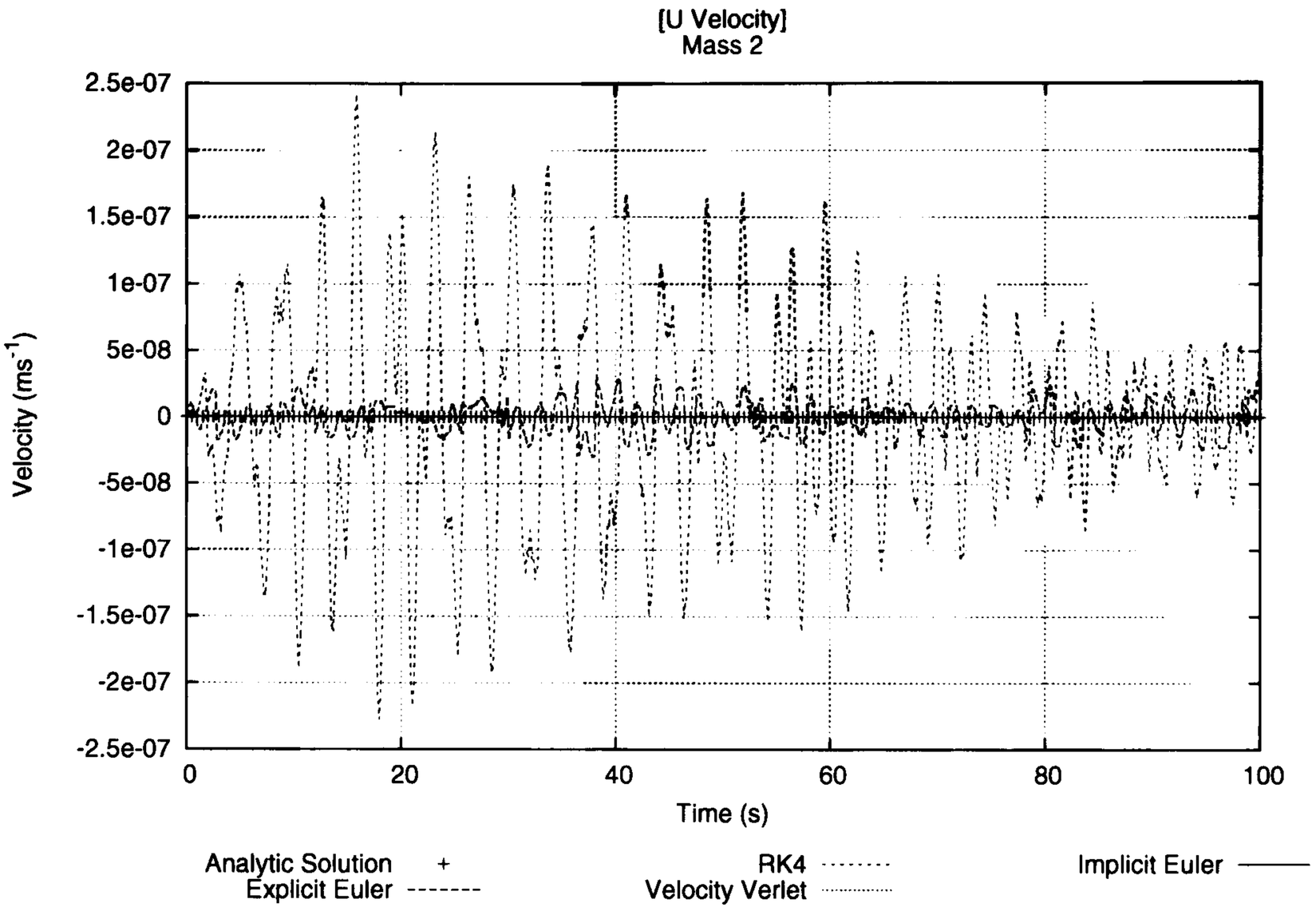

(c) U Velocity

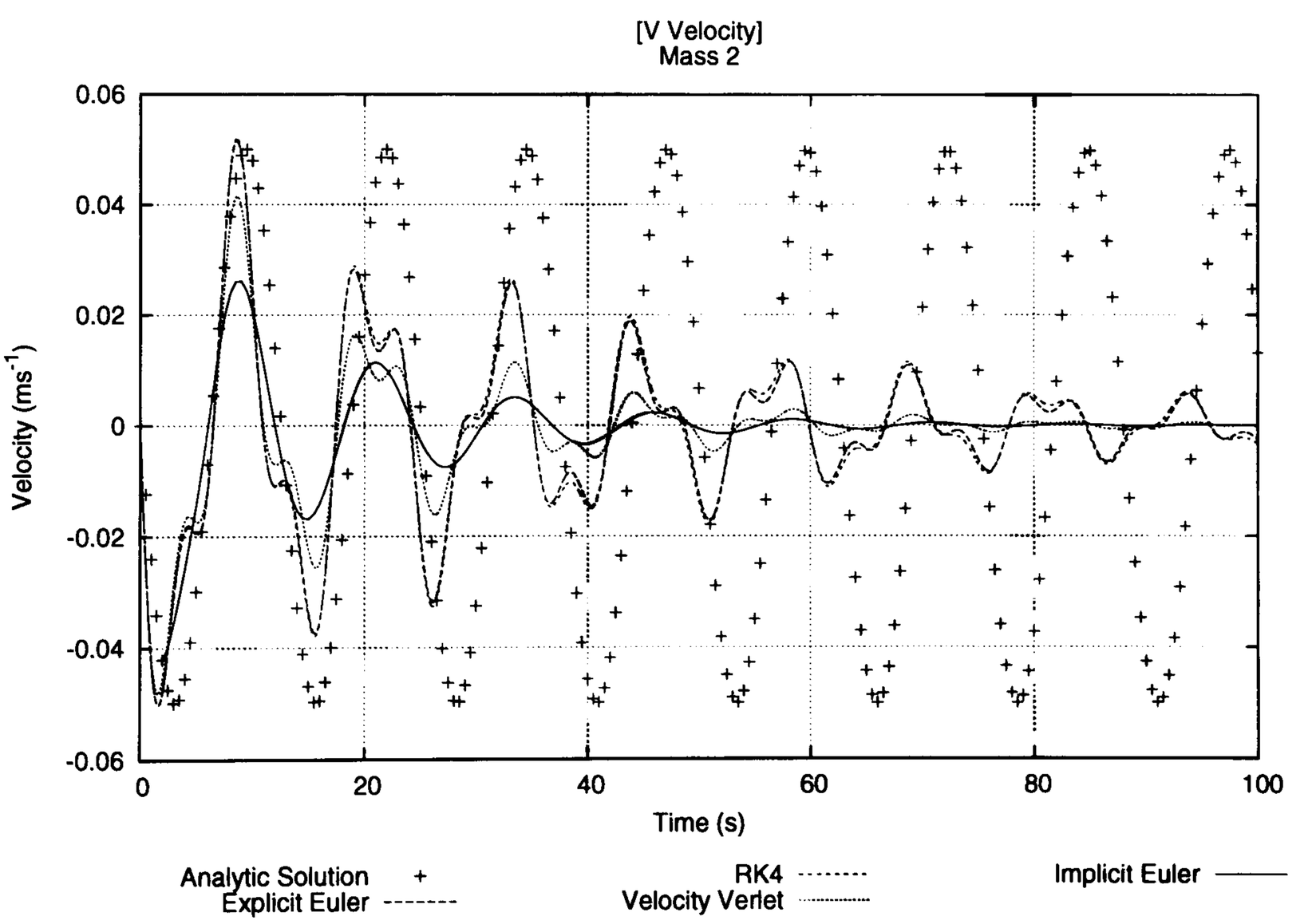

(d) V Velocity

Figure 3.6: 5 Mass Fibre Results

Discussion of Results

It is clear from Figure 3.4 that the solution of the SHO using the explicit methods do not incur any significant artificial numerical damping. The explicit methods also cause the SHO to oscillate at a slightly higher stationary frequency to that of the analytic solution. In contrast, the solution of the SHO using the implicit Euler method does initially oscillate at the same frequency as the analytic solution, but intrinsic to the implicit method is an artificial damping factor.

Figure 3.4 shows that the SHO oscillates at a non-stationary frequency when solved with the implicit Euler. This is because the implicit Euler method accurately simulates the effect of the decreasing tension in the springs as shown in Figure 3.4(c). Rossing [104] states that the frequency produced by a vibrating string is dependent on the tension within the string and the linear density of the string. Therefore, as the average tension within the spring decreases, due to the artificial damping, the frequency of oscillation will also decrease. It is clear that for the SHO example, the implicit Euler method reproduces the correct frequency characteristics of the SHO but does not correctly represent the time domain characteristics of the SHO as the motion is artificially damped compared to the analytical solution [104]. Although there is no physical damping present in the SHO, there is physical damping present in the paper fibre structure. Section 3.2.9 discusses the relationship between the artificial damping present in the implicit Euler method and the physical damping seen in the experimental data, from which it is possible to conclude that the implicit Euler method is the correct solver to use.

The results for the 5 mass fibre given in Figure 3.6 show that the three explicit solvers develop waveforms which depart from the harmonic analytical solution. They display unwanted dispersion characteristics, whilst the implicit Euler solver produces physically correct results. A damping coefficient b has been applied to the explicit methods to produce better behaved solutions. Even with this measure in place, the results were dispersive.

However, the implicit Euler method once again produces the correct results.

The 5 mass fibre is a general case where any given mass is connected to at least one other free mass causing a non-linear term in the internal forces of the system as shown in Equation 3.2.7. The equation is written in full with the non-linear term highlighted for convenience.

$$m_i \frac{d^2\mathbf{r}_i}{dt^2} + \left[\sum_j k_{ij}(\mathbf{r}_j - \mathbf{r}_i)\right] - \left[\sum_j k_{ij} L_{i,j} \frac{\mathbf{r}_j - \mathbf{r}_i}{||\mathbf{r}_j - \mathbf{r}_i||}\right] + b_i \frac{d\mathbf{r}_i}{dt} = 0$$

where, $\left[\sum_j k_{ij} L_{i,j} \frac{\mathbf{r}_j - \mathbf{r}_i}{||\mathbf{r}_j - \mathbf{r}_i||}\right]$ is the non-linear term. This leads to a 'stiff' system which is defined by Cartwright [111] as:

"*If a numerical method is forced to use, in a certain interval of integration, a step length which is excessively small in relation to the smoothness of the exact solution in that interval, then the problem is said to be 'stiff' in that interval.*"

Definition 3.1: A 'Stiff' System

Table 3.4 shows that a stable time step for the 3 explicit methods is $\Delta t = 0.01$, but Equation 3.2.19 states that for the 5 mass fibre a value of $\Delta t \leq 0.44$ should provide a numerically stable system. This highlights that the mass/spring model is indeed a set of 'stiff' equations. The solution is to use an implicit solver which is unconditionally stable for any given time step, although the time step must be small enough so that resolution of the results is not effected.

Tables 3.2 and 3.4 also show the time per iteration of each of the four methods. The explicit methods all have comparable speeds, but the implicit method is far more computationally expensive. This can be expected as the method requires generating a sparse matrix at every iteration. Although each iteration of the implicit method may take longer to run, less iterations are needed compared to the explicit methods, due to a larger time step being used, meaning less time is need to run a simulation.

To conclude, the implicit Euler method provides the fastest solution time with the most

accurate results as it overcomes the difficulties associated with a 'stiff' system at the cost of introducing an artificial damping factor to the solution. This artificial damping factor is discussed in Section 3.2.9 and with careful selection of the simulation time step does not effect the validity of the solution. Unless otherwise stated, the implicit Euler method will be the default solver for the mass/spring simulations in this research.

3.2.8 Initial Conditions

The mass/spring system is an example of an initial value problem and in its simplest form can be expressed as.

$$\frac{dx_i}{dt} = f(u_i)$$
$$\frac{du_i}{dt} = g(x_i, u_i)$$
$$x_i^0 = \alpha; \quad u_i^0 = \beta$$

where:

α Initial Value of the Displacement x_i

β Initial Value of the Velocity u_i

The initial values α and β are important in achieving a physically realistic model. This section includes two examples where the system is started at rest ($\mathbf{u}_i^0 = 0 \forall i$). In the first example, the end masses and the central mass are clamped at $t = 0$, resulting in 5 (x, y) constraints. In the second example, 5 masses are clamped at $t = 0$, resulting in 9 (x, y) constraints.

Fibre with a Single Starting Constraint

Figure 3.7(a) shows the fibre at $t = 0$. This is modelled as an assembly of 21 equally spaced masses connected by 20 springs. The end masses are clamped in x and y throughout the simulation. The central mass is constrained in y at $t < 0$. At $t = 0$ this single constraint is removed. Table 3.5 list the model parameters and initial conditions used for this example.

Model Parameters	
Δt	0.01 s
b	0.00 kg/s
m	1/21 kg
E	1.00 Pa
t	1.00 m
w	0.25 m
L	0.05 m
ν	0.00

Initial Conditions			
Mass	$\mathbf{r}^0$ (m)	$\Delta\mathbf{r}^0$ (m)	$\mathbf{u}^0$ (m/s)
0	[-0.50, 0.00]	[0.00, 0.00]	[0.00, 0.00]
10	[0.05, 0.00]	[0.00, 0.10]	[0.00, 0.00]
20	[0.60, 0.00]	[0.00, 0.00]	[0.00, 0.00]

Table 3.5: Model Parameters and Initial Conditions for a Fibre with a Single Starting Constraint

Figures 3.7(b-f) show the resulting motion of the fibre. Figure 3.7(g) shows the y displacements of masses 2, 4, 6, 8 and 10, where mass 10 is the central mass of the fibre. The y displacements show simple harmonic motion which is to be expected showing that the motion of this fibre is physically correct. There is no x displacement in masses due to the symmetry of the system.

Fibre with Multiple Starting Constraints

Figure 3.8(a) shows the fibre with a different initial condition at $t = 0$. This is again modelled by an assembly of 21 equally spaced masses connected by 20 springs. The end masses are clamped as before. The central mass is again constrained in y at $t < 0$, in addition masses 9 and 11 are also are constrained at $x = 0$ and $y = 0$ at $t < 0$. At $t = 0$, the constraints on masses 9, 10 and 11 are removed. Table 3.6 list the model parameters

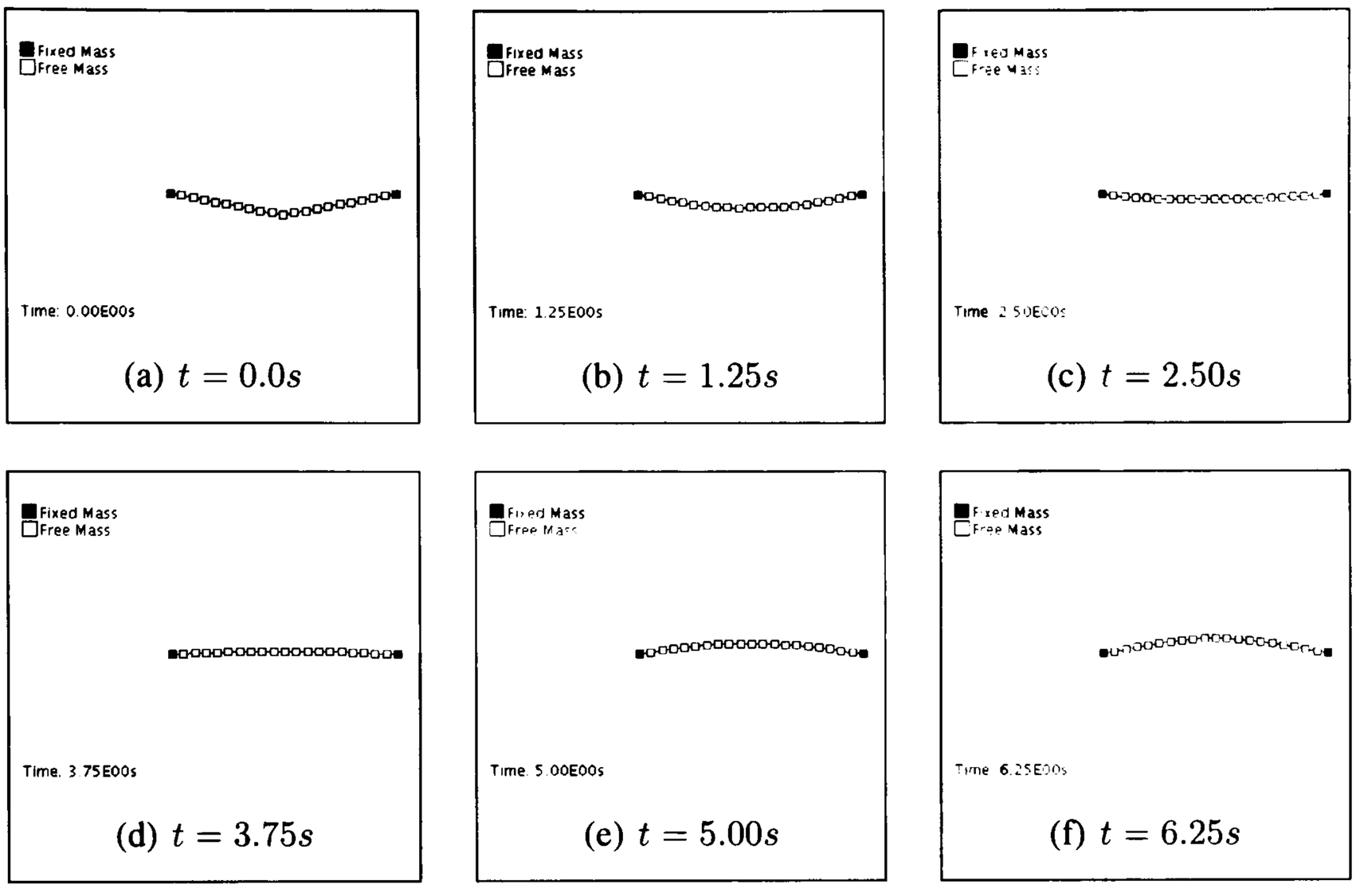

(a) $t = 0.0s$ (b) $t = 1.25s$ (c) $t = 2.50s$

(d) $t = 3.75s$ (e) $t = 5.00s$ (f) $t = 6.25s$

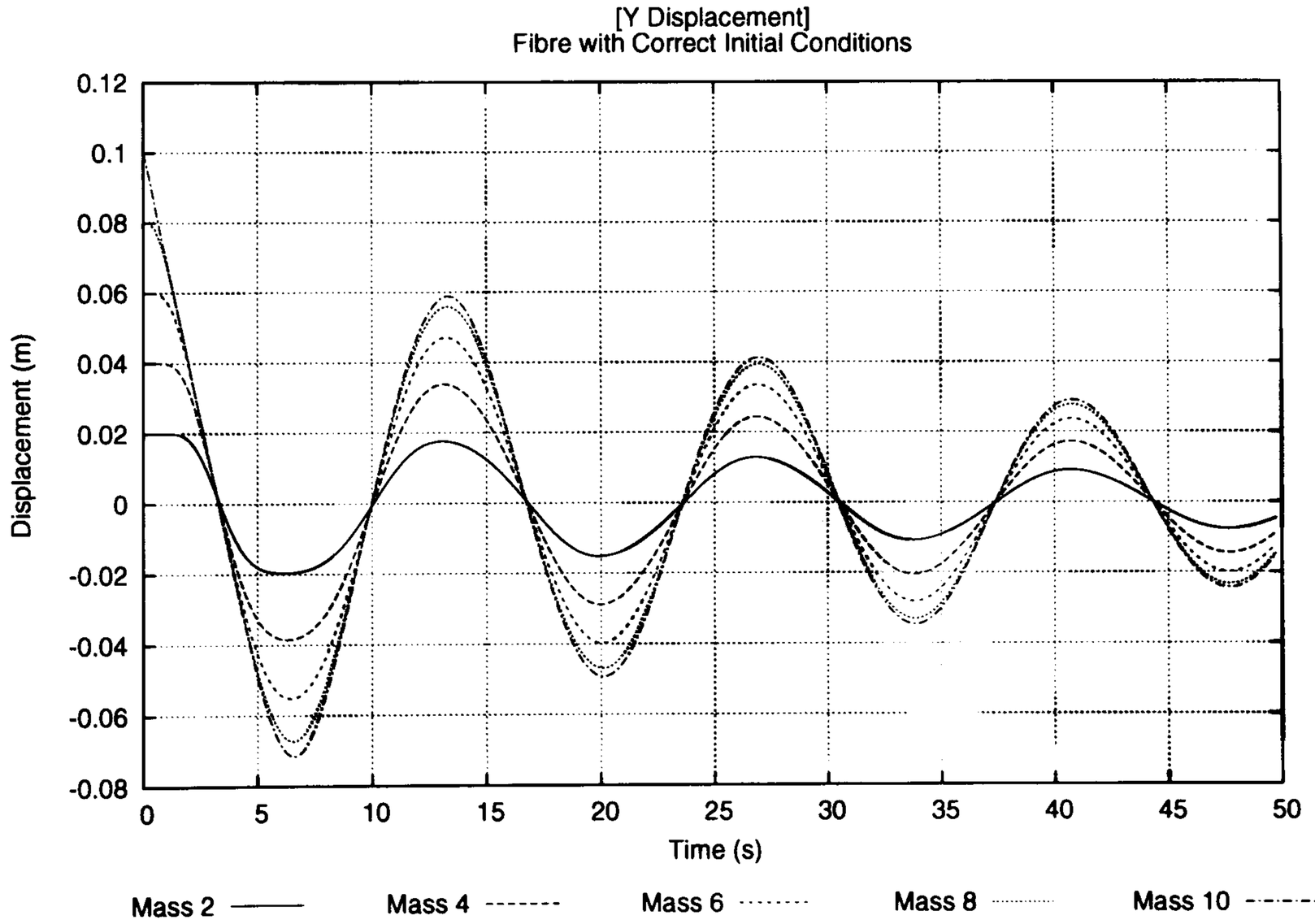

(g) Y Displacement of Masses

Figure 3.7: Results of a Fibre with Correct Initial Conditions

and initial conditions used for this example.

Model Parameters	
Δt	0.01 s
b	0.00 kg/s
m	1/21 kg
E	1.00 Pa
t	1.00 m
w	0.25 m
L	0.05 m
ν	0.00

Initial Conditions			
Mass	$\mathbf{r}^0$ (m)	$\Delta\mathbf{r}^0$ (m)	$\mathbf{u}^0$ (m/s)
0	[-0.50, 0.00]	[0.00, 0.00]	[0.00, 0.00]
9	[-0.005, 0.00]	[0.00, 0.00]	[0.00, 0.00]
10	[0.05, 0.00]	[0.00, 0.10]	[0.00, 0.00]
11	[0.105, 0.00]	[0.00, 0.00]	[0.00, 0.00]
20	[0.60, 0.00]	[0.00, 0.00]	[0.00, 0.00]

Table 3.6: Model Parameters and Initial Conditions for a Fibre with Multiple Starting Constraints

Figures 3.8(b-f) show the resulting motion of the fibre when solved using an explicit method. Figure 3.8(g) shows the y displacements of masses 2, 4, 6, 8 and 10. The masses exhibit a more complex motion, which can be explained by the excitation of high-frequency modes. The predicted displacement seen in Figure 3.8(f) are asymmetric, indicating that numerical errors have contaminated the prediction.

Figures 3.9(b-f) show the resulting motion of the fibre when solved using the implicit method. Figure 3.9(g) shows the y displacements of masses 2, 4, 6, 8 and 10. The masses exhibit high frequency oscillations with the overall motion resembling the sinusoidal motion of the fibre with a single starting constraint.

It is clear that the explicit methods are more prone to developing some numerical error when resolving high-frequency oscillations. In contrast, the implicit method is able to predict high-frequency symmetrical modes with a lower numerical error. The resulting motion of the fibre is numerically correct for the initial conditions used.

Algorithm to Calculate Initial Conditions

Figures 3.7, 3.8 and 3.9 show how vital it is to supply the mass/spring model with a realistic initial condition. Finding such an initial condition for a single fibre example is

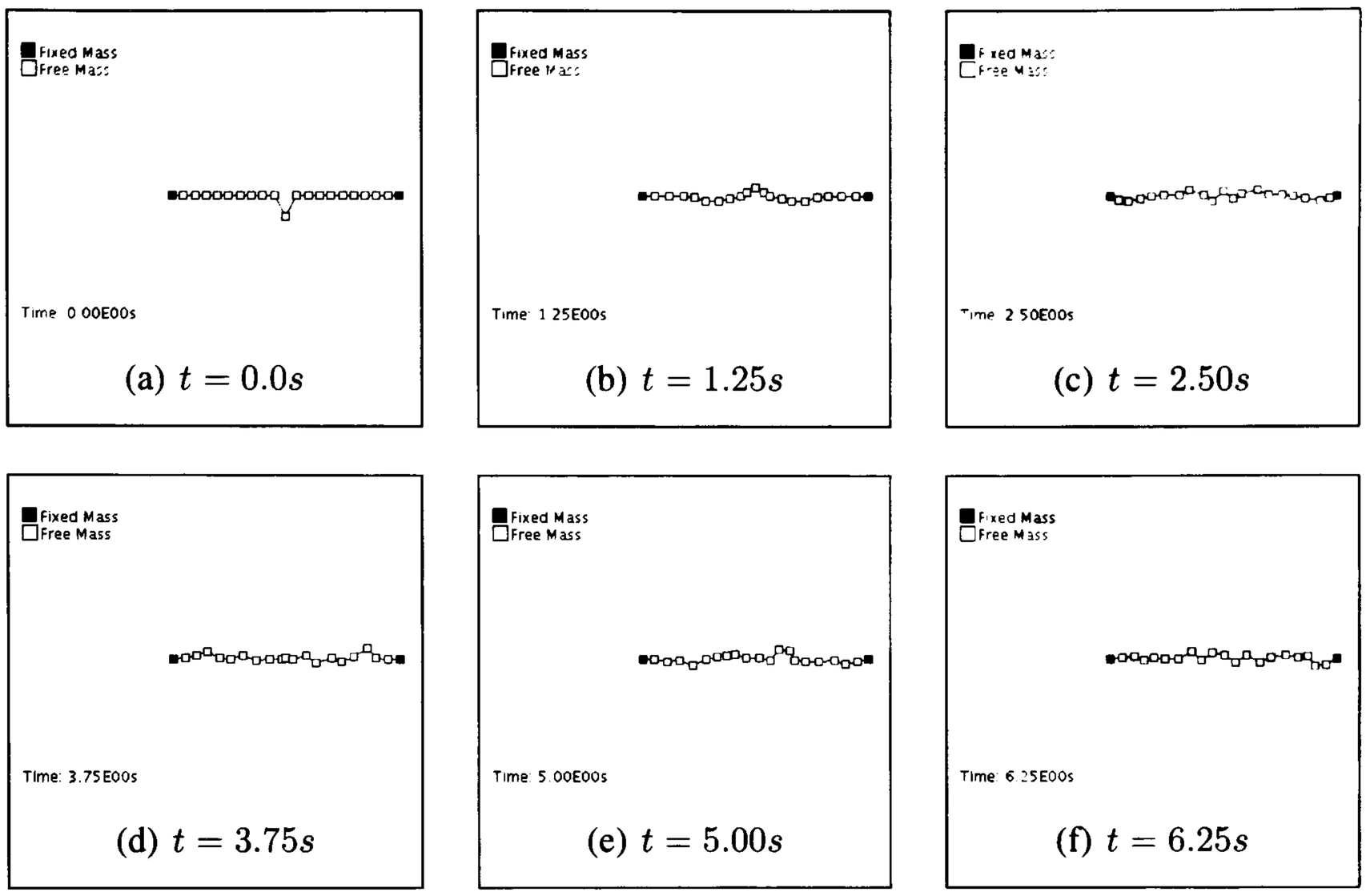

(a) $t = 0.0s$ (b) $t = 1.25s$ (c) $t = 2.50s$

(d) $t = 3.75s$ (e) $t = 5.00s$ (f) $t = 6.25s$

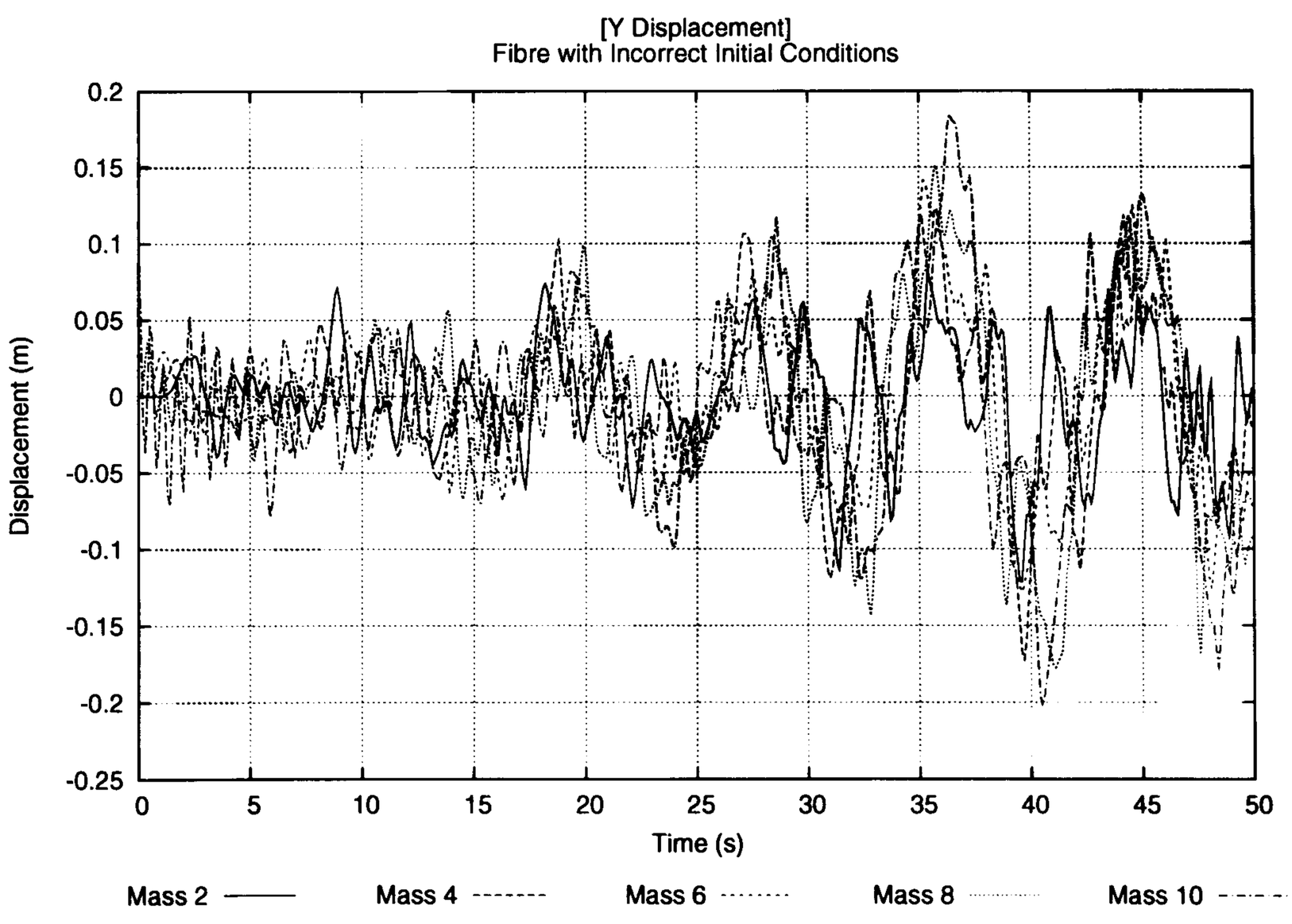

(g) Y Displacement of Masses

Figure 3.8: Results of a Fibre with Incorrect Initial Conditions when solved using an Explicit Method

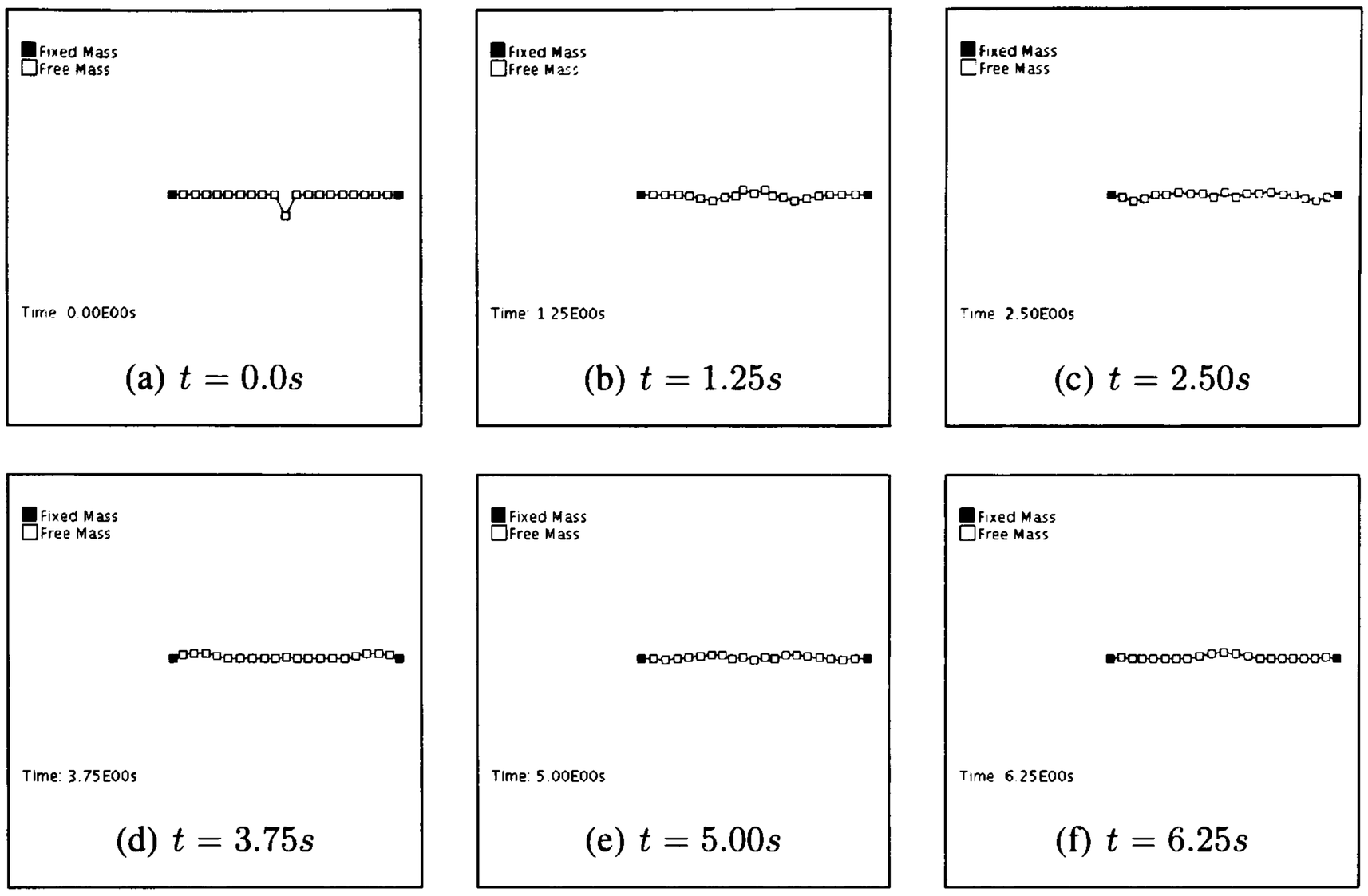

(g) Y Displacement of Masses

Figure 3.9: Results of a Fibre with Incorrect Initial Conditions when solved using an Implicit Method

a trivial task, but consider the slightly more complex example of two connected fibres as shown in Figures 3.11 and 3.13.

Algorithm 7 describes the process of calculating the initial conditions. The algorithm requires that any mass with an initial condition must have its mass set to infinity. This fixes the mass to the displacement specified by the initial condition. The system is then solved iteratively using an explicit method such as the explicit Euler, RK4 or Velocity Verlet methods until a new equilibrium is reached. Once this equilibrium is reached, any mass attached to an EqIC will have its mass set to its original value, allowing it to move freely. The masses attached to a StIC will remain fixed to represent a constant load on the system.

It is important to note that the algorithm gradually increases the damping coefficient b from 0 to the value of critical damping b_c. This damping coefficient has no relationship to the physical damping that will act on the system as the motion of the system is yet to be modelled. Algorithm 7 simply calculates the initial condition of each mass in the model by minimising the potential energy within the system. If no damping were applied to the system, the potential energy in the system would continually oscillate and never reach the new equilibrium. Therefore, an artificial damping factor must be introduced to dissipate the kinetic energy in the system. If the damping coefficient were to increase too quickly, the system would reach a false equilibrium as shown by Figure 3.10. The model will actually let the system vibrate under no damping for 10000 iterations before gradually increasing the damping factor by 0.001% each subsequent iteration, or until a suitable convergence criterion is satisfied. This will allow the system to reach a sensible equilibrium and seems to work well in practice.

Figure 3.11 highlights the first type of initial condition, a displacement from the equilibrium, referred to as an EqIC. The model is designed so that the initial condition of the system can be calculated from a single initial displacement. The simulation shown in

Algorithm 7 Calculating the Initial Conditions

Require: $\mathcal{R}(\mathbf{r}, \mathbf{u})$ (Fourth Order Runge-Kutta method, see Algorithm 3)

```
I ← Number of Masses
for i = 0 to I do
    if Initial Condition == TRUE then
        δr_i ← Displacement of Mass i
        r_i ← r_i + δr_i
        if Initial Condition == EqIC then
            m_i^0 ← m_i
        end if
        m_i ← ∞
    end if
end for
while System is Changing do
    r, u ← I(r, u)
    if b > 0 AND b < b_c (b_c - Critical Damping) then
        b ← b + δb
    end if
end while
if Initial Condition == EqIC then
    m_i ← m_i^0
end if
```

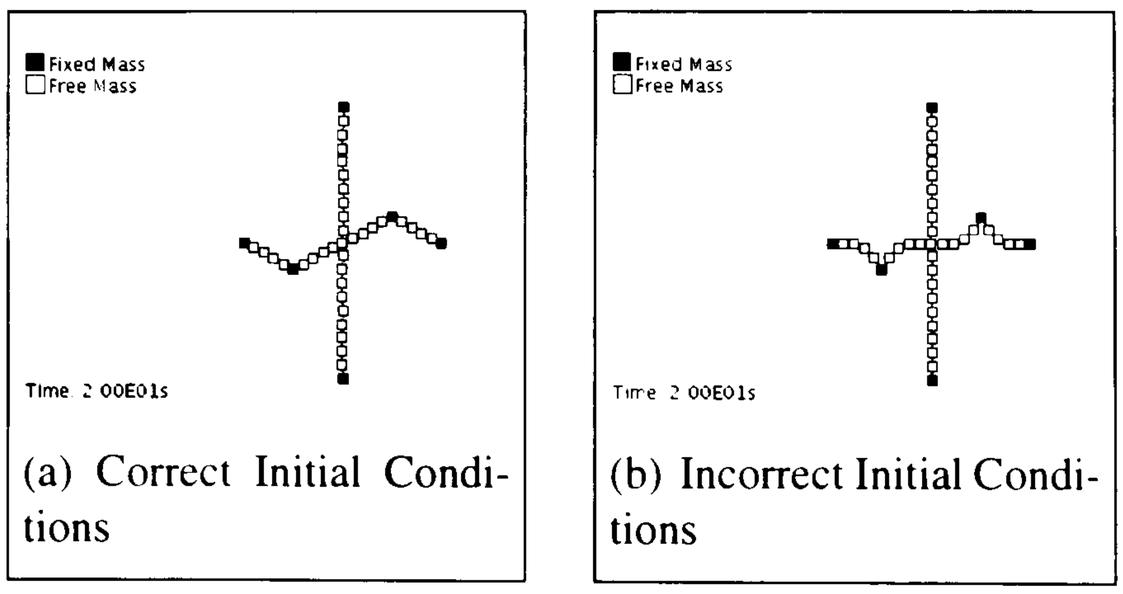

(a) Correct Initial Conditions

(b) Incorrect Initial Conditions

Figure 3.10: Over Damping Resulting in a False Equilibrium

Figure 3.7 applies this method.

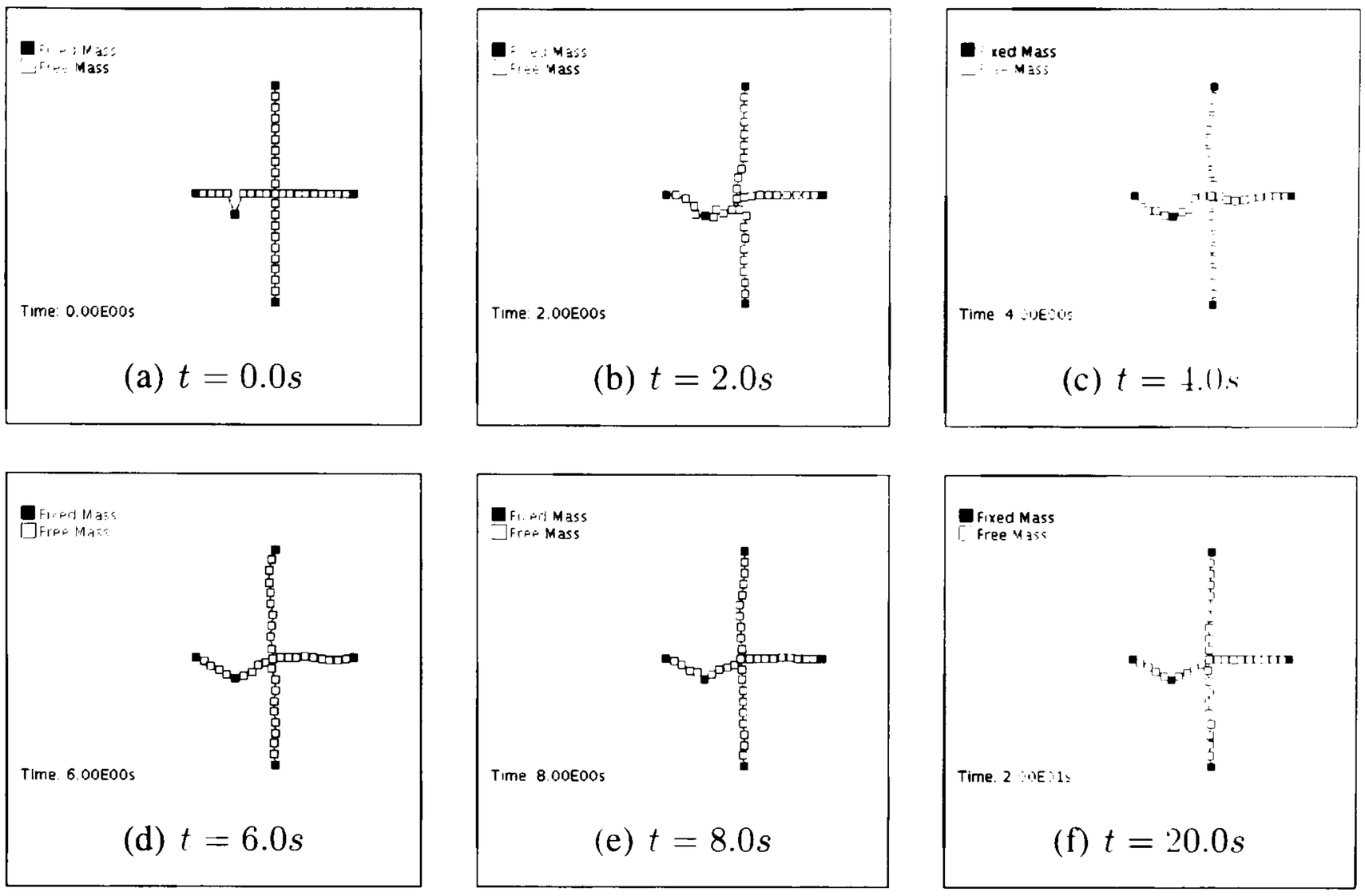

Figure 3.11: Initial Condition of a Two Fibre System from a Single Displacement

The model is also able to apply multiple EqICs as shown by Figure 3.12. The second type of initial condition highlighted by Figure 3.13 is used to stretch the system and is referred to as the StIC.

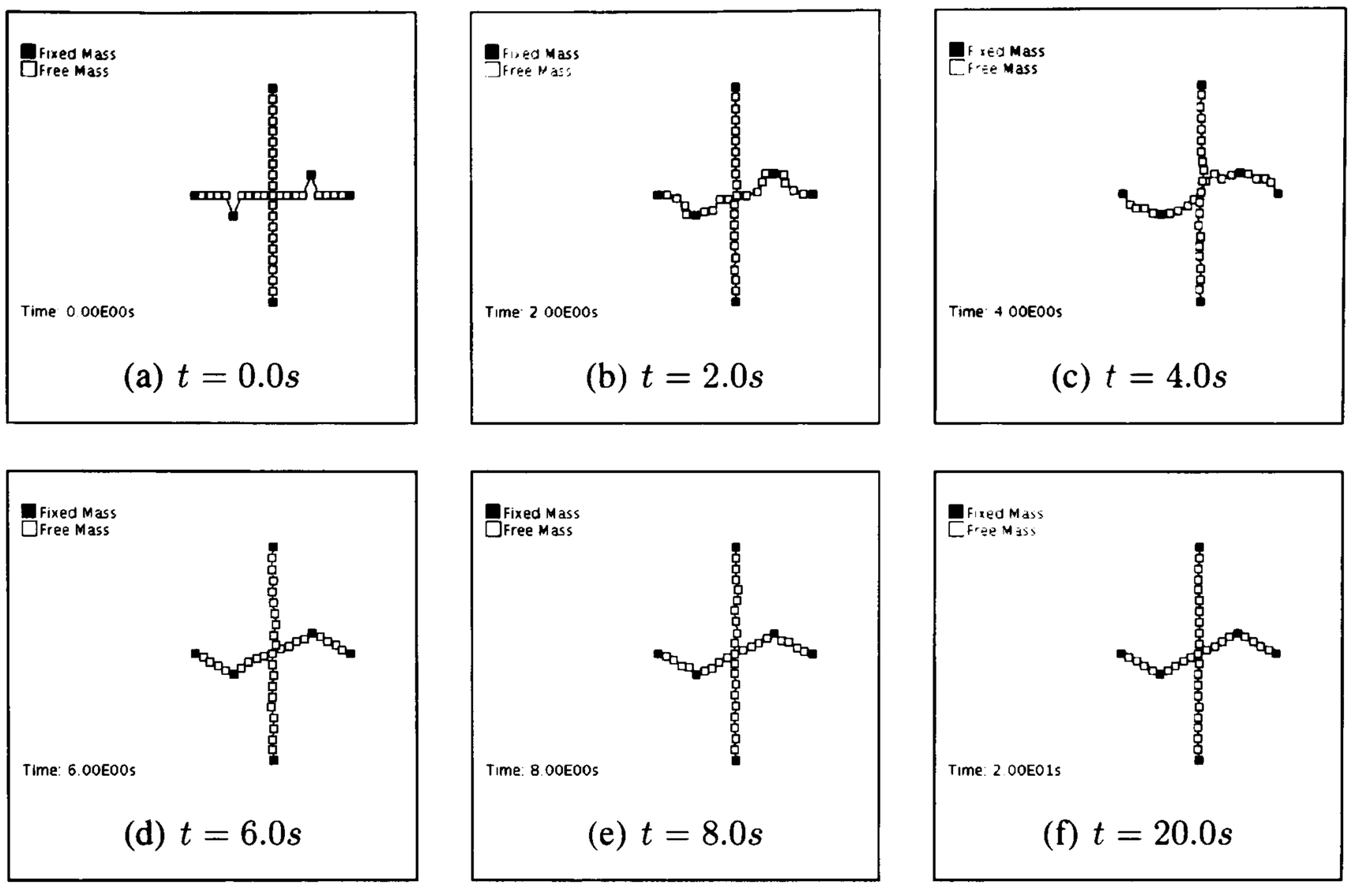

Figure 3.12: Initial Condition of a Two Fibre System from Multiple Displacements

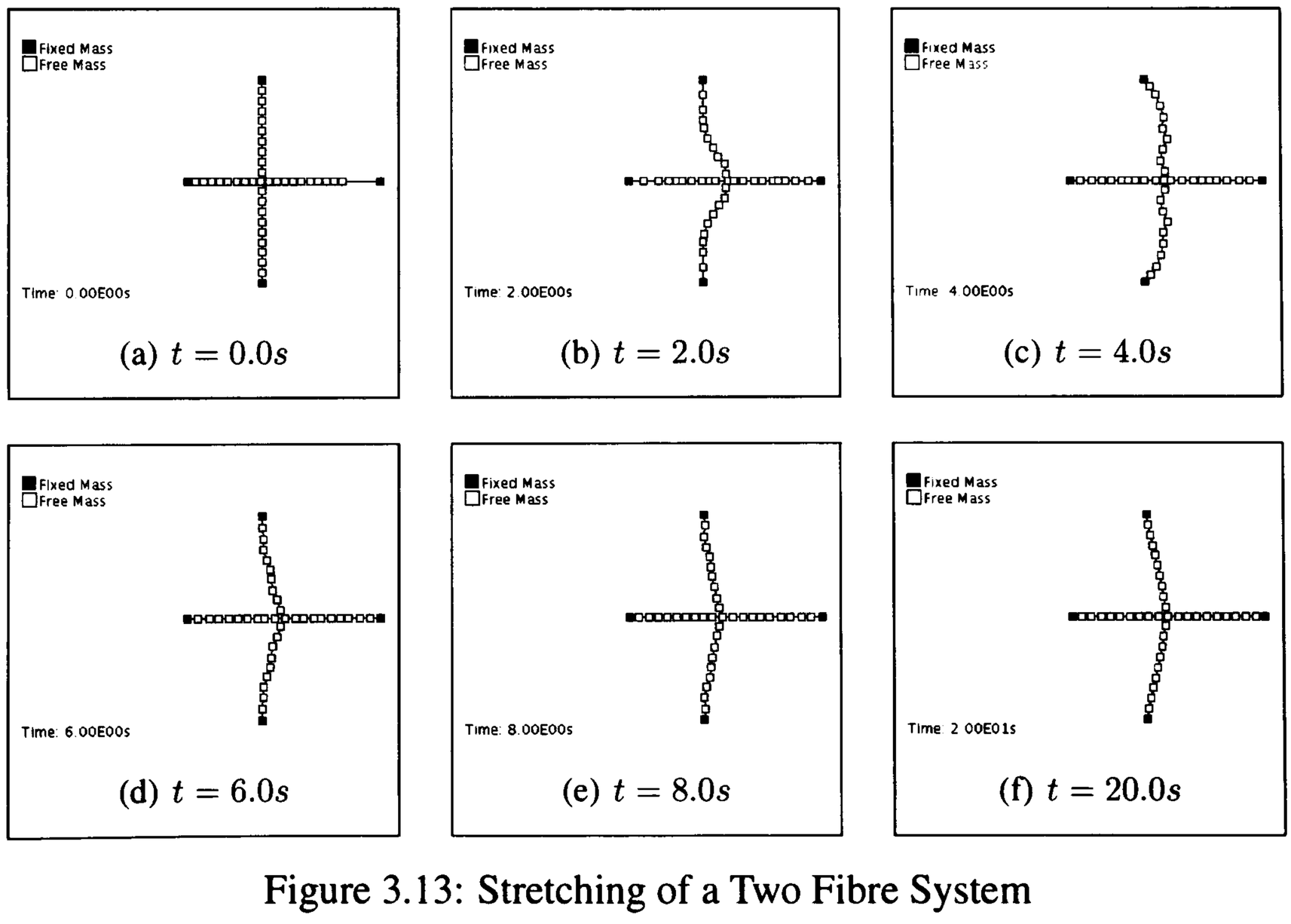

Figure 3.13: Stretching of a Two Fibre System

3.2.9 Damping Coefficient

The results from Section 3.2.7 have shown that the implicit Euler method provides a more accurate solution to the mass/spring model than the explicit methods. Inherent to any implicit scheme is the artificial damping of the solution. This section will present a detailed discussion of the nature of this artificial damping and propose a suitable time step and frictional damping coefficient b for the mass/spring simulations of the paper fibre structure. In contrast, only a cursory study of the damping coefficient is applied to the experimental data from a rubber band in Section 3.5.2.

It is presumed that the amplitude of the numerical and experimental AEs decay exponentially as shown by Equation 3.2.31.

$$y = y_0 e^{-\gamma t} \tag{3.2.31}$$

where:

y Amplitude of AE at time t

y_0 Maximum Amplitude of AE

γ Logarithmic Decrement

Figure 3.14 shows the relationship between the logarithmic decrement γ and the time step used in simulating a plucked paper fibre when no physical damping is present, i.e. $b = 0$. The results shows a linear increase in the logarithmic decrement as the time step increases. The typical logarithmic decrement from a set of experimental AEs generated from a notched paper sample is approximately 50000 Hz. Figure 3.14 suggests that the implicit Euler method with a time step of approximately 4.5E-08s would apply the required amount of numerical damping to the system to reproduce the logarithmic decrement seen in the experimental data. Therefore the frictional damping coefficient b is not required when using this time step.

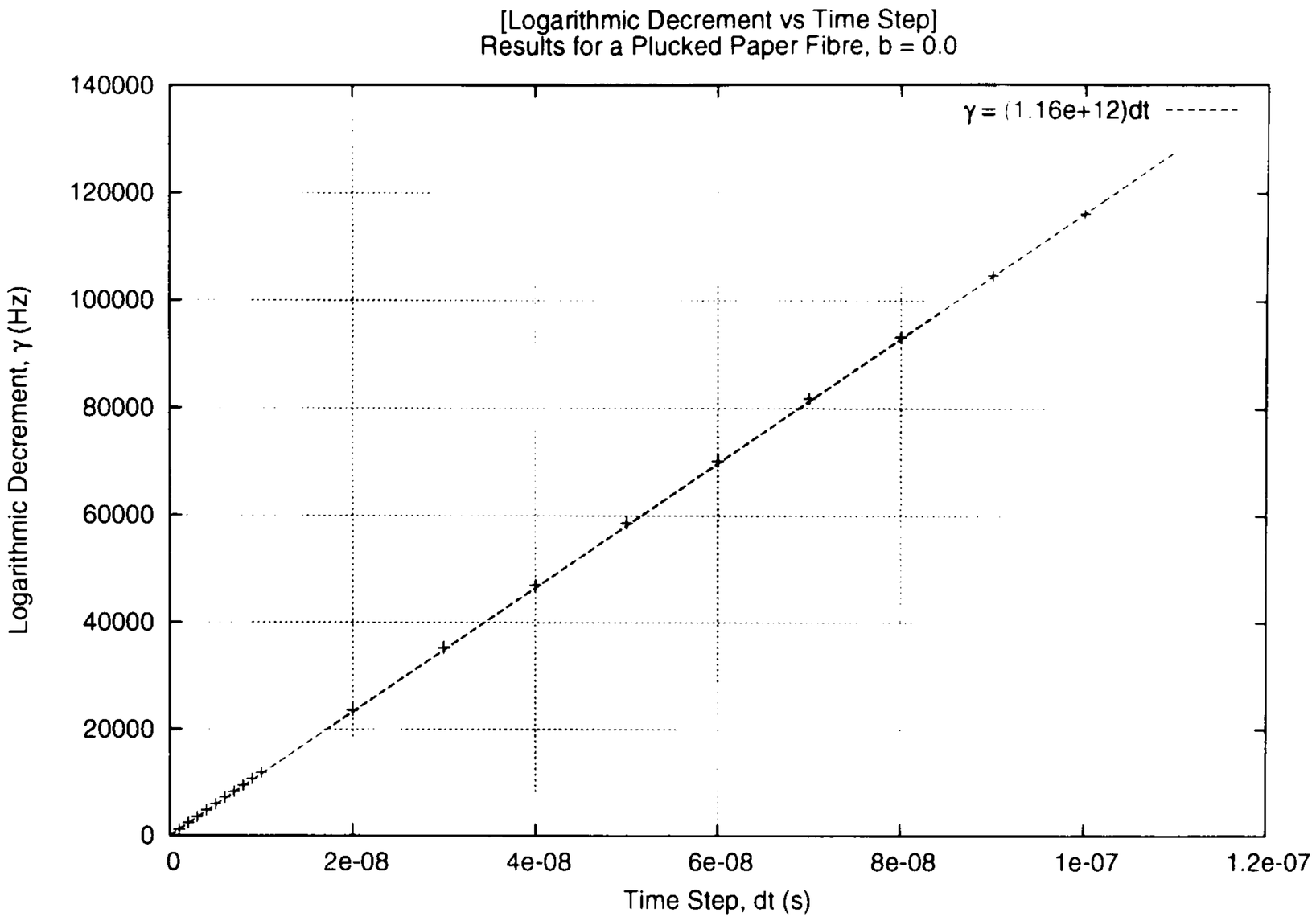

Figure 3.14: Logarithmic Decrement γ vs Time Step for a Plucked Paper Fibre

Figure 3.15 shows the effect the numerical damping has on the frequency response of the paper fibre for different time steps. As the time step increases, the number of harmonics that the fibre is able to produce decreases. For a time step of 5.0E-08s only the fundamental frequency and the first two harmonics are successfully represented. However, a time step of 1.0E-08 is able to capture all the harmonics of the paper fibre in the frequency range of 0 - 2500 kHz.

Figure 3.16 shows the computational run time required for simulating a plucked paper fibre using different time steps. The time required to complete one simulation increases exponentially as the time step decreases. The time step which provides the best frequency response of the paper fibre with the optimum computational efficiency is at around 1.0E-08s and as such will be used in all the simulations of the paper fibre structure.

Figure 3.14 suggests that a time step of 4.5E-08s is required for the numerical damping to be equivalent to the physical damping seen in the experimental data. However, a time step of 1.0E-08s is to be used as it best represents the frequency response of the plucked

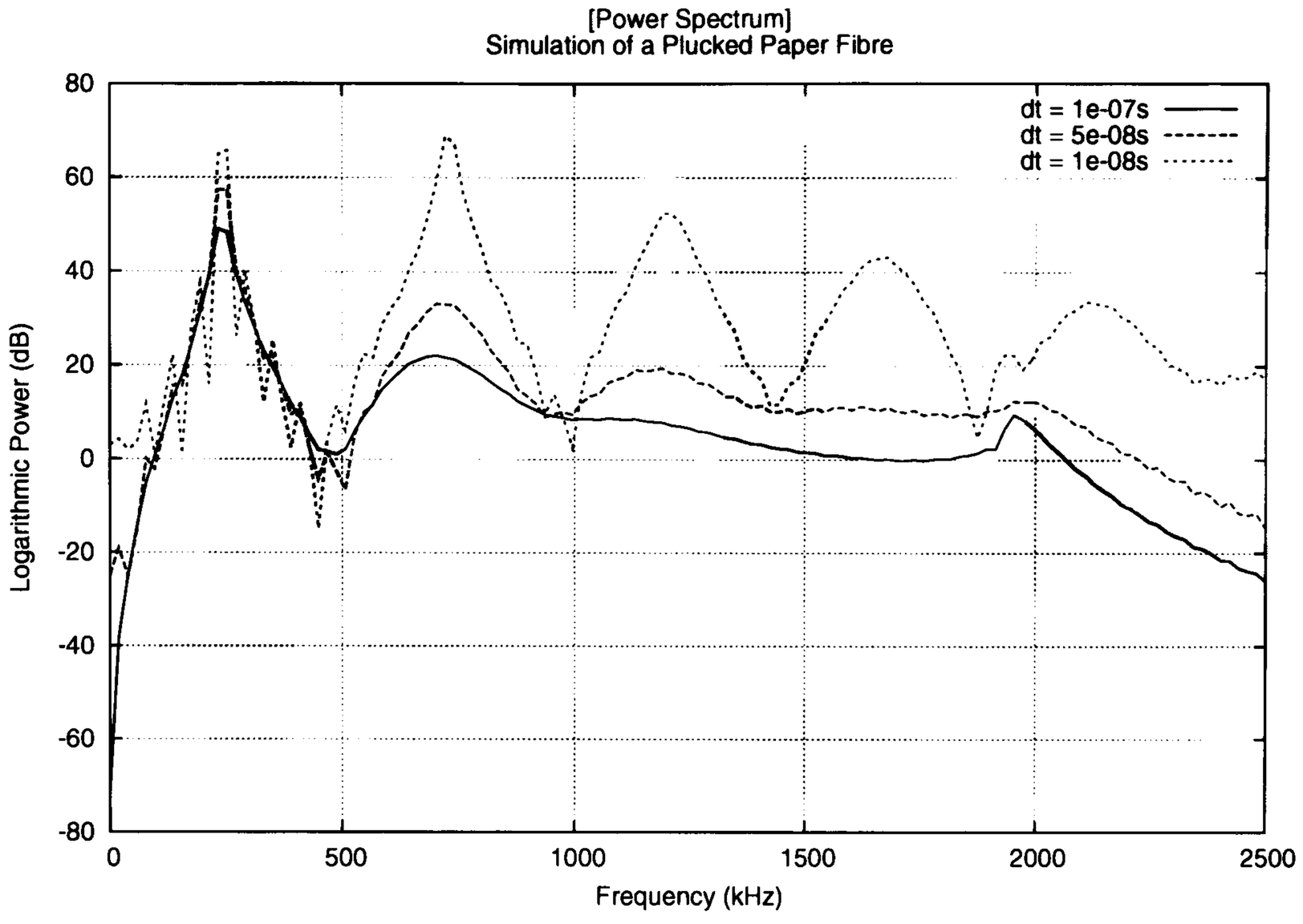

Figure 3.15: Frequency Response of a Plucked Paper Fibre using Different Time Steps

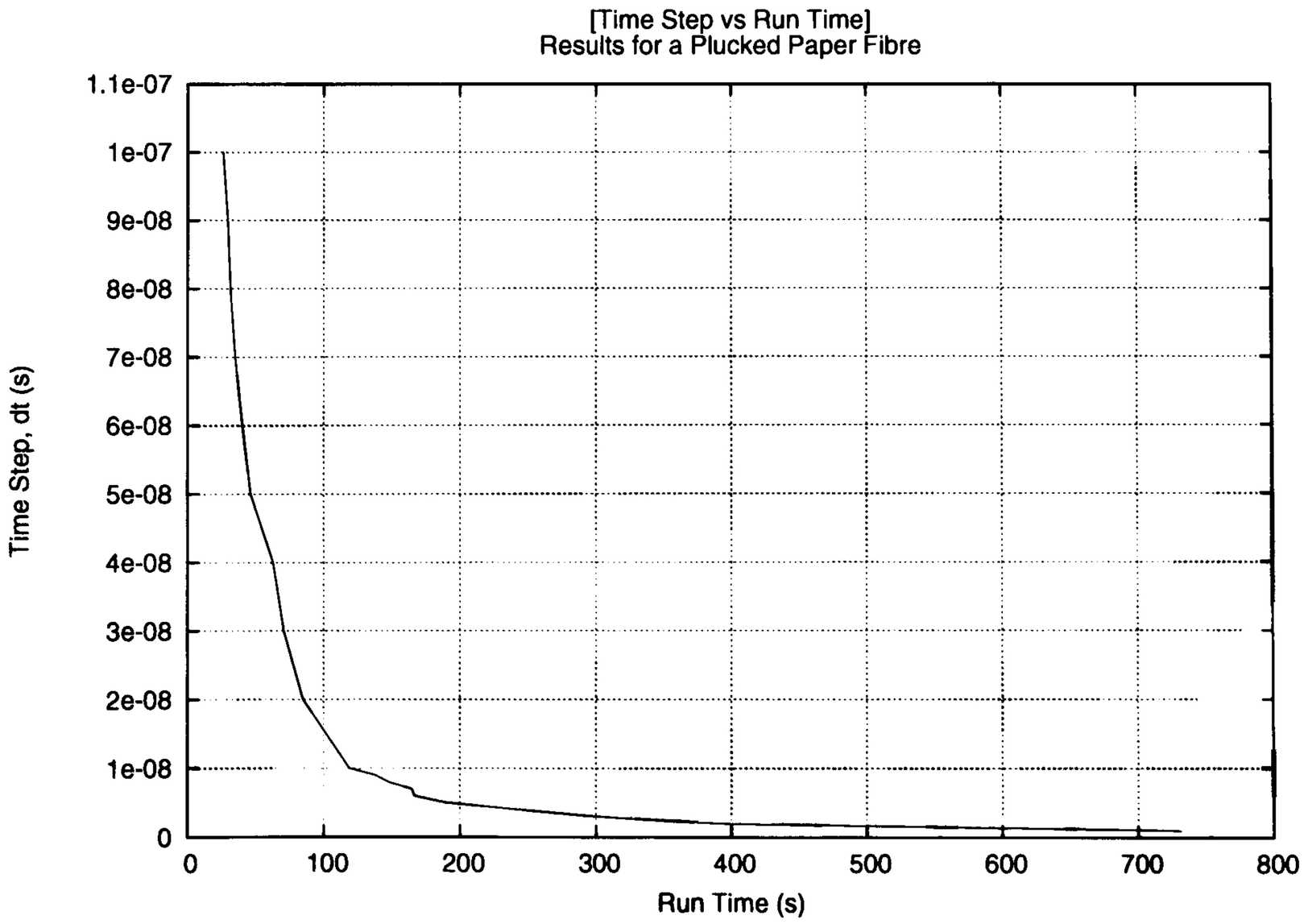

Figure 3.16: Time Step vs Run Time for a Plucked Paper Fibre

fibre with minimal computational expense. The numerical damping present in the implicit Euler method for the chosen time step is less than the physical damping seen in the experimental data, therefore a frictional damping coefficient b must be selected to represent the physical damping of the fibre structure.

Through a process of trial and error, a frictional damping coefficient of b = 1.5E-06 was chosen to best represent the physical damping present in the experimental data. Figures 3.17 and 3.18 show the simulated AEs generated from a fibre/fibre bond failure and fibre failure respectively, together with the exponential fit of the numerical results with b = 1.5E-06 and b = 0.0 and the exponential fit of a typical experimental AE generated from the respective damage mechanism. Figure 3.17 shows that the selected value of b results in the AE from the simulated fibre/fibre bond failure to be slightly over damped compared to the experimental data, with the AE from the fibre failure showing a good agreement with the experimental data, as highlighted by Figure 3.18.

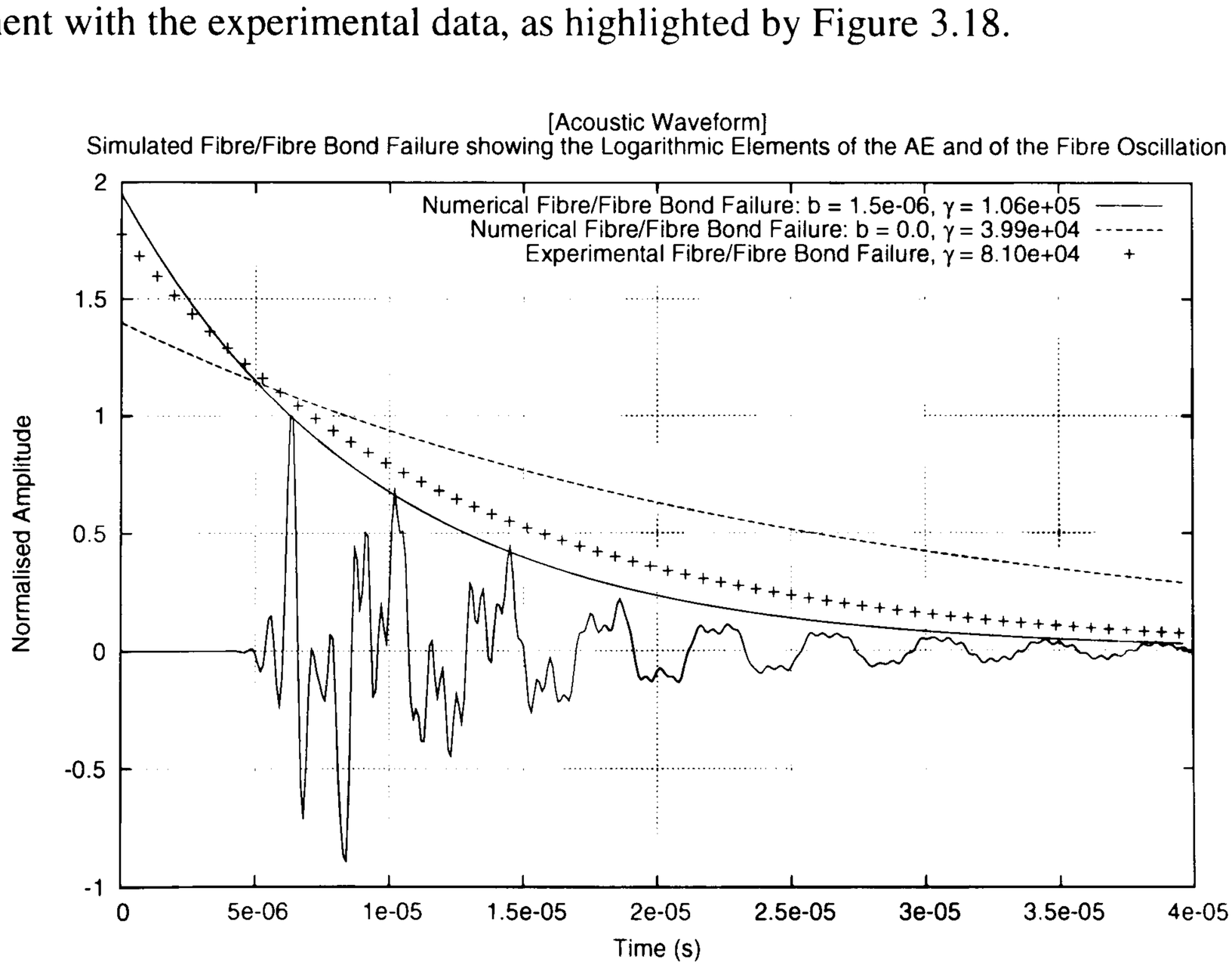

Figure 3.17: Attenuation Envelopes of the Numerical and Experimental Data from a Fibre/Fibre Bond Failure. (+) Attenuation of the Acoustic Signal, (—, ---) Attenuation of the Modelled Fibre Oscillations

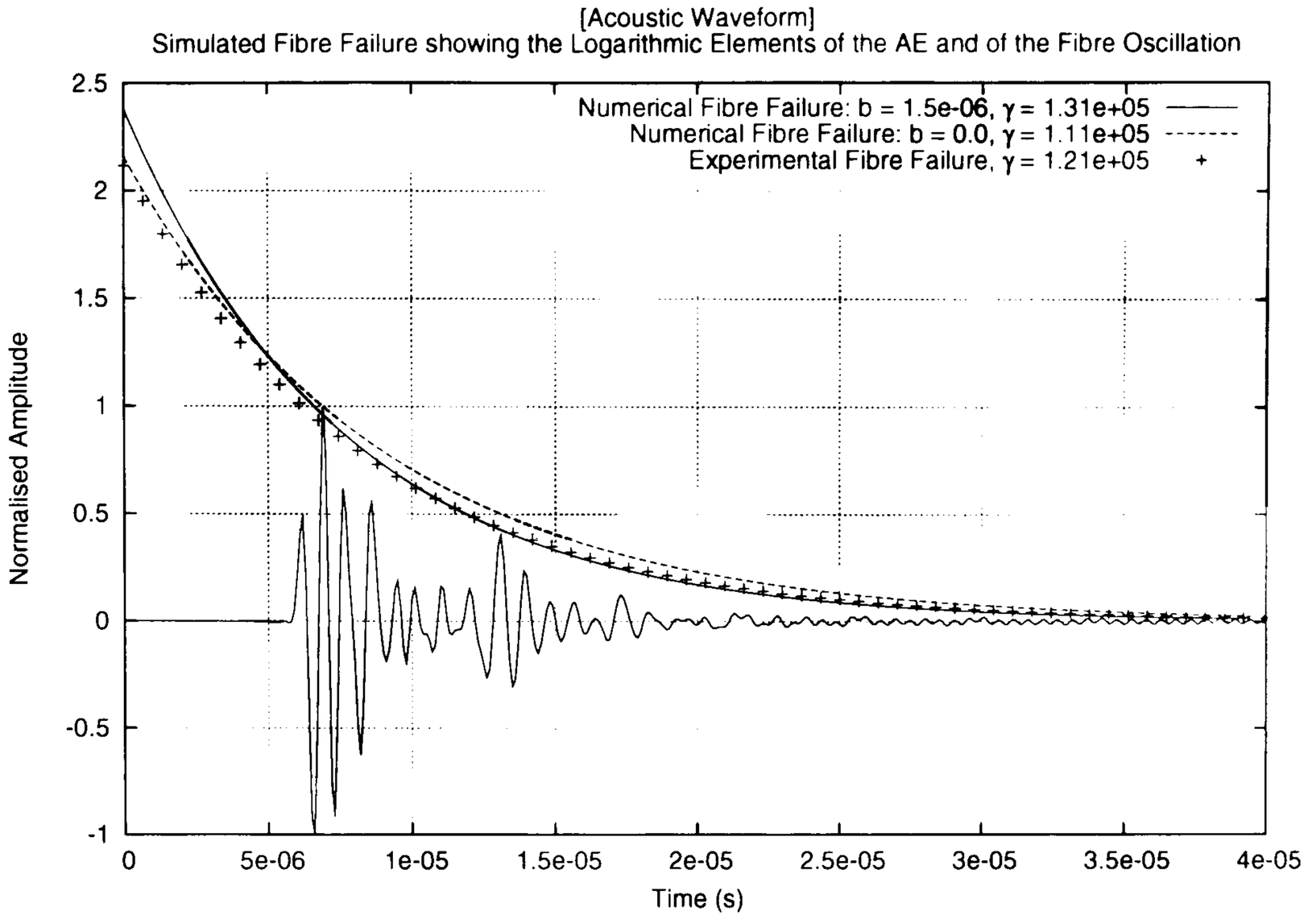

Figure 3.18: Attenuation Envelopes of the Numerical and Experimental Data from a Fibre Failure. (+) Attenuation of the Acoustic Signal, (—, ---) Attenuation of the Modelled Fibre Oscillations

3.3 Acoustic Wave Model

3.3.1 Derivation of the Acoustic Wave Model

The motion of an acoustic wave is governed by the weakly compressible form of the Continuity equation (Equation 3.3.1) and the Momentum equation (Equation 3.3.2), otherwise known as the Navier-Stokes equations.

$$\frac{\partial \rho}{\partial t} + \rho \nabla \cdot \mathbf{u} = 0 \tag{3.3.1}$$

$$\frac{\partial \mathbf{u}}{\partial t} = (\mathbf{u} \cdot \nabla)\mathbf{u} - \frac{1}{\rho}\nabla p + \frac{\mathcal{G}}{\rho} + \nu \nabla^2 \mathbf{u} \tag{3.3.2}$$

where:

ρ Fluid Density

$\mathbf{u}$ Fluid Velocity

p Pressure

$\mathcal{G}$ Gravitational Body Force

ν Fluid Viscosity

- The fluid has no gravitational body force, $\mathcal{G} = 0$
- The fluid flow is inviscid, $\nu = 0$

A fluid that has no gravitational body forces exhibits no change in its density in the direction of gravity. A fluid that is inviscid has no resistance to the flow of an acoustic wave through it. These two assumptions have no effect on the propagation of small amplitude AEs over short distances and are valid for the purpose of this work.

Applying these assumptions to Equation 3.3.2 gives the weakly compressible form of the Euler momentum equation for inviscid flow.

$$\frac{\partial \mathbf{u}}{\partial t} = (\mathbf{u} \cdot \nabla)\mathbf{u} - \frac{1}{\rho}\nabla p \tag{3.3.3}$$

Using Equations 3.3.1 and 3.3.3 it is now possible to derive the acoustic wave equation assuming that:

- The acoustic perturbations in the fluid are small
- The fluid is an ideal gas
- The fluid remains at a constant temperature

The first assumption allows the intrinsic properties of the fluid to be expressed as an average value plus a small change. Therefore, the density, velocity and pressure of the

acoustic mean-field can be expressed as:

$$\rho = \bar{\rho} + \delta\rho$$

$$\mathbf{u} = \delta\mathbf{u} \quad \text{where:} \quad \bar{\mathbf{u}} = 0 \tag{3.3.4}$$

$$p = \bar{p} + \delta p$$

As the perturbations in the fluid are small, then the product of two perturbations is infinitesimally small.

$$\delta\xi\delta\zeta \longrightarrow 0 \quad \text{where:} \quad \xi, \zeta = \rho, \mathbf{u}, p \tag{3.3.5}$$

Substituting Equations 3.3.4 in to Equations 3.3.1 and 3.3.3 and assigning variable names so that $\delta\xi \rightarrow \xi$ where: $\xi = \rho, \mathbf{u}, p$ to get:

$$\frac{\partial\rho}{\partial t} + \bar{\rho}\nabla \cdot \mathbf{u} = 0 \tag{3.3.6a}$$

$$\frac{\partial\mathbf{u}}{\partial t} + \frac{1}{\bar{\rho}}\nabla p = 0 \tag{3.3.6b}$$

As the medium the acoustic wave is travelling through is assumed to be an ideal gas, the speed of sound can be defined as:

$$c^2 = \frac{\partial p}{\partial \rho} \tag{3.3.7}$$

As the fluid is assumed to remain at a constant temperature, $c^2 = f(T)$ is constant. Therefore, Equation 3.3.6a becomes:

$$\frac{\partial p}{\partial t} + \bar{\rho}c^2\nabla \cdot \mathbf{u} = 0 \tag{3.3.8}$$

It is now possible to combine Equations 3.3.8 and 3.3.6b to either eliminate $\mathbf{u}$ or p. Eliminating $\mathbf{u}$ gives the acoustic pressure wave equation as discussed in Section 3.3.2. whilst eliminating p gives the particle velocity wave equation as discussed in Section 3.3.3.

3.3.2 Acoustic Pressure Wave Model

Combining Equation 3.3.8 and Equation 3.3.6b, it is possible to eliminate $\mathbf{u}$. First operate on Equation 3.3.8 with $\frac{\partial}{\partial t}$ to get:

$$\frac{\partial^2 p}{\partial t^2} + \bar{\rho} c^2 \nabla \cdot \left(\frac{\partial \mathbf{u}}{\partial t} \right) = 0$$

Substitute in Equation 3.3.6b to get:

$$\frac{\partial^2 p}{\partial t^2} + \bar{\rho} c^2 \nabla \cdot \left(-\frac{1}{\bar{\rho}} \nabla p \right) = 0$$

Re-arrange to get the wave equation in terms of the acoustic pressure.

$$\frac{\partial^2 p}{\partial t^2} - c^2 \nabla^2 p = 0 \tag{3.3.9}$$

where:

p Acoustic Pressure

c Speed of Sound in Medium

The acoustic pressure wave equation in two-dimensional Cartesian coordinates (x, y) is given as:

$$\frac{\partial^2 p}{\partial t^2} - c^2 \left\{ \frac{\partial}{\partial x} \left(\frac{\partial p}{\partial x} \right) + \frac{\partial}{\partial y} \left(\frac{\partial p}{\partial y} \right) \right\} = 0 \tag{3.3.10}$$

Second Order Accurate Approximation of the Acoustic Pressure Wave Equation

Equation 3.3.10 can be discretised using second order central differences for the temporal and spatial derivatives as shown below:

$$\frac{\partial^2 p}{\partial t^2} = \frac{p_{i,j}^{k+1} - 2p_{i,j}^{k} + p_{i,j}^{k-1}}{\Delta t^2} + \mathcal{O}(\Delta t^2)$$
$$\frac{\partial^2 p}{\partial x^2} = \frac{p_{i+1,j}^{k} - 2p_{i,j}^{k} + p_{i-1,j}^{k}}{\Delta x^2} + \mathcal{O}(\Delta h^2)$$

Substituting in for $\frac{\partial^2 p}{\partial t^2}$, $\frac{\partial^2 p}{\partial x^2}$ and similarly for $\frac{\partial^2 p}{\partial y^2}$, the finite difference approximation of the acoustic pressure wave equation can be shown to be:

$$p_{i,j}^{k+1} = 2(1 - 2\alpha^2)p_{i,j}^{k} - p_{i,j}^{k-1} + \alpha^2\left(p_{i+1,j}^{k} + p_{i-1,j}^{k} + p_{i,j+1}^{k} + p_{i,j-1}^{k}\right) \qquad (3.3.11)$$

where:

α	$\frac{c\Delta t}{\Delta h}$
Δt	Time Step
Δh	Cell Width/Height, $\Delta h = \Delta x = \Delta y$
i, j	Position in Space, $(x, y) = (i\Delta h, j\Delta h)$
k	Position in Time, $t = k\Delta t$

To prevent the reflection of outgoing acoustic waves at the computational boundaries, non-reflecting boundary conditions are applied to the pressure domain using the method discussed in Section 3.3.4. Finally, the stability condition for the finite difference scheme shown in Equation 3.3.11 according to Zakaria [94] is given in Equation 3.3.12.

$$\alpha < \frac{1}{\sqrt{2}} \qquad (3.3.12)$$

Fourth Order Accurate Approximation of the Acoustic Pressure Wave Equation

Equation 3.3.10 can be discretised using a second order accurate central difference for the temporal derivative and a fourth order accurate central difference for the spatial derivatives as shown below:

$$\frac{\partial^2 p}{\partial t^2} = \frac{p_{i,j}^{k+1} - 2p_{i,j}^{k} + p_{i,j}^{k-1}}{\Delta t^2} + \mathcal{O}(\Delta t^2)$$
$$\frac{\partial^2 p}{\partial x^2} = \frac{-p_{i+2,j}^{k} + 16p_{i+1,j}^{k} - 30p_{i,j}^{k} + 16p_{i-1,j}^{k} - p_{i-2,j}^{k}}{12\Delta h^2} + \mathcal{O}(\Delta h^4)$$

Substituting the central differences in to Equation 3.3.10 gives the following approximation as stated by Zakaria [94]:

$$\begin{aligned} p_{i,j}^{k+1} = (2 - 5\alpha^2)p_{i,j}^{k} - p_{i,j}^{k-1} + \frac{4}{3}\alpha^2\left(p_{i+1,j}^{k} + p_{i-1,j}^{k} + p_{i,j+1}^{k} + p_{i,j-1}^{k}\right) \\ -\frac{1}{12}\alpha^2\left(p_{i+2,j}^{k} + p_{i-2,j}^{k} + p_{i,j+2}^{k} + p_{i,j-2}^{k}\right) \end{aligned} \tag{3.3.13}$$

The stability condition for the fourth order accurate acoustic pressure wave as presented by Alford [112] is:

$$\alpha < \sqrt{\frac{3}{8}} \tag{3.3.14}$$

3.3.3 Particle Velocity Wave Model

Combining Equation 3.3.8 and Equation 3.3.6b it is possible to eliminate p. First operate on Equation 3.3.8 by $\frac{\partial}{\partial t}$ to get:

$$\frac{\partial^2 \mathbf{u}}{\partial t^2} + \frac{1}{\bar{\rho}}\nabla\left(\frac{\partial p}{\partial t}\right) = 0$$

Substitute in Equation 3.3.6b to get:

$$\frac{\partial^2 \mathbf{u}}{\partial t^2} + \frac{1}{\bar{\rho}} \nabla \left(-c^2 \bar{\rho} \nabla \cdot \mathbf{u} \right) = 0$$

Re-arrange to get the wave equation in terms of the particle velocity.

$$\frac{\partial^2 \mathbf{u}}{\partial t^2} - c^2 \nabla (\nabla \cdot \mathbf{u}) = 0 \tag{3.3.15}$$

Applying the triple product rule $a \times b \times c = a(b \cdot c) - (a \cdot b)c$,

$$\nabla (\nabla \cdot \mathbf{u}) = \nabla \times (\nabla \times \mathbf{u}) + \nabla^2 \mathbf{u} \tag{3.3.16}$$

The flow is assumed to be irrotational such that $\nabla \times \mathbf{u} = 0$. Therefore the particle velocity wave equation for irrotational flows can be expressed as:

$$\frac{\partial^2 \mathbf{u}}{\partial t^2} - c^2 \nabla^2 \mathbf{u} = 0 \tag{3.3.17}$$

where:

$\mathbf{u}$ Particle Velocity

c Speed of Sound in Medium

The particle velocity wave equation in two-dimensional Cartesian coordinates (x, y) is:

$$\frac{\partial^2 \mathbf{u}}{\partial t^2} - c^2 \left\{ \frac{\partial}{\partial x} \left(\frac{\partial \mathbf{u}}{\partial x} \right) + \frac{\partial}{\partial y} \left(\frac{\partial \mathbf{u}}{\partial y} \right) \right\} = 0 \tag{3.3.18}$$

Second Order Accurate Approximation of the Particle Velocity Wave Equation

Equation 3.3.18 can be discretised using second order central differences for the temporal and spatial derivatives as shown in Section 3.3.2 to give two second order accurate finite difference approximations of the particle velocity wave equation as shown below:

$$u_{i,j}^{k+1} = 2(1-2\alpha^2)u_{i,j}^{k} - u_{i,j}^{k-1} + \alpha^2\left(u_{i+1,j}^{k} + u_{i-1,j}^{k} + u_{i,j+1}^{k} + u_{i,j-1}^{k}\right) \quad (3.3.19a)$$

$$v_{i,j}^{k+1} = 2(1-2\alpha^2)v_{i,j}^{k} - v_{i,j}^{k-1} + \alpha^2\left(v_{i+1,j}^{k} + v_{i-1,j}^{k} + v_{i,j+1}^{k} + v_{i,j-1}^{k}\right) \quad (3.3.19b)$$

where:

u	Particle Velocity in x Direction
v	Particle Velocity in y Direction
α	$\frac{c\Delta t}{\Delta h}$
Δt	Time Step
Δh	Cell Width/Height, $\Delta h = \Delta x = \Delta y$
i, j	Position in Space, $(x, y) = (i\Delta h, j\Delta h)$
k	Position in Time, $t = k\Delta t$

The stability of the particle velocity wave equation is also subject to the condition stated in Equation 3.3.12.

Fourth Order Accurate Approximation of the Particle Velocity Wave Equation

Equation 3.3.18 can be discretised using a second order central difference for the temporal derivative and a fourth order central difference for the spatial derivatives as shown in Section 3.3.2 to give two spatially fourth order accurate finite difference approximations of the particle velocity wave equation:

$$\begin{aligned} u_{i,j}^{k+1} = (2-5\alpha^2)u_{i,j}^{k} - u_{i,j}^{k-1} &+ \frac{4}{3}\alpha^2\left(u_{i+1,j}^{k} + u_{i-1,j}^{k} + u_{i,j+1}^{k} + u_{i,j-1}^{k}\right) \\ &- \frac{1}{12}\alpha^2\left(u_{i+2,j}^{k} + u_{i-2,j}^{k} + u_{i,j+2}^{k} + u_{i,j-2}^{k}\right) \end{aligned} \quad (3.3.20a)$$

$$v_{i,j}^{k+1} = (2 - 5\alpha^2)v_{i,j}^{k} - v_{i,j}^{k-1} + \frac{4}{3}\alpha^2\left(v_{i+1,j}^{k} + v_{i-1,j}^{k} + v_{i,j+1}^{k} + v_{i,j-1}^{k}\right) - \frac{1}{12}\alpha^2\left(v_{i+2,j}^{k} + v_{i-2,j}^{k} + v_{i,j+2}^{k} + v_{i,j-2}^{k}\right) \quad (3.3.20b)$$

3.3.4 Non-Reflecting Boundary Conditions

One of the major obstacles in modelling acoustic wave propagation is that the domain in which the wave travels through must have a finite size. If the boundaries of the domain remain untreated, they will reflect the acoustic wave back into the domain causing the simulation to produce incorrect results. There are two proposed solutions to this problem; first, simply create a domain large enough so that the time taken for the acoustic wave to reflect off the boundary is greater than the time needed for the simulation. The second solution is to simulate free-field acoustic radiation at the computational domain boundaries by applying an appropriate numerical technique to the boundary grid cells.

The first solution although the most accurate is not economically viable, as even the shortest simulation would require an excessive amount of time to solve. This fact alone drives towards the use of non-reflecting boundary conditions.

The non-reflecting boundary conditions used in this model are due to Reynold [99], with Zakaria [94] presenting them in discretised form as shown in Equation 3.3.21. Equations 3.3.21a, 3.3.21b, 3.3.21c and 3.3.21d describe the conditions for the North, South, East and West boundaries respectively.

$$p_{i,0}^{k+1} = p_{i,0}^{k} + p_{i,1}^{k} - p_{i,1}^{k-1} + \alpha\left(p_{i,1}^{k} - p_{i,0}^{k} - (p_{i,2}^{k-1} - p_{i,1}^{k-1})\right) \quad (3.3.21a)$$

$$p_{i,N_y-1}^{k+1} = p_{i,N_y-1}^{k} + p_{i,N_y-2}^{k} - p_{i,N_y-2}^{k-1} + \alpha\left(p_{i,N_y-2}^{k} - p_{i,Ny-1}^{k} - (p_{i,N_y-3}^{k-1} - p_{i,N_y-2}^{k-1})\right) \quad (3.3.21b)$$

$$p_{0,j}^{k+1} = p_{0,j}^{k} + p_{1,j}^{k} - p_{1,j}^{k-1} + \alpha\left(p_{1,j}^{k} - p_{0,j}^{k} - (p_{2,j}^{k-1} - p_{1,j}^{k-1})\right) \quad (3.3.21c)$$

$$p^{k+1}_{N_x-1,j} = p^{k}_{N_x-1,j} + p^{k}_{N_x-2,j} - p^{k-1}_{N_x-2,j} + \alpha\left(p^{k}_{N_x-2,j} - p^{k}_{Nx-1,j} - (p^{k-1}_{N_x-3,j} - p^{k-1}_{N_x-2,j})\right) \tag{3.3.21d}$$

Figure 3.19 shows the implementation of the boundary conditions for a second and fourth order accurate Cartesian grid. The equations given in Equation 3.3.21 will simulate a non-reflecting boundary for the second order accurate grid. To simulate a non-reflecting boundary for the fourth order accurate grid, the boundary conditions given in Equation 3.3.21 must be first applied to the inner boundary grid cells, followed by the outer boundary grid cells for each iteration of the simulation.

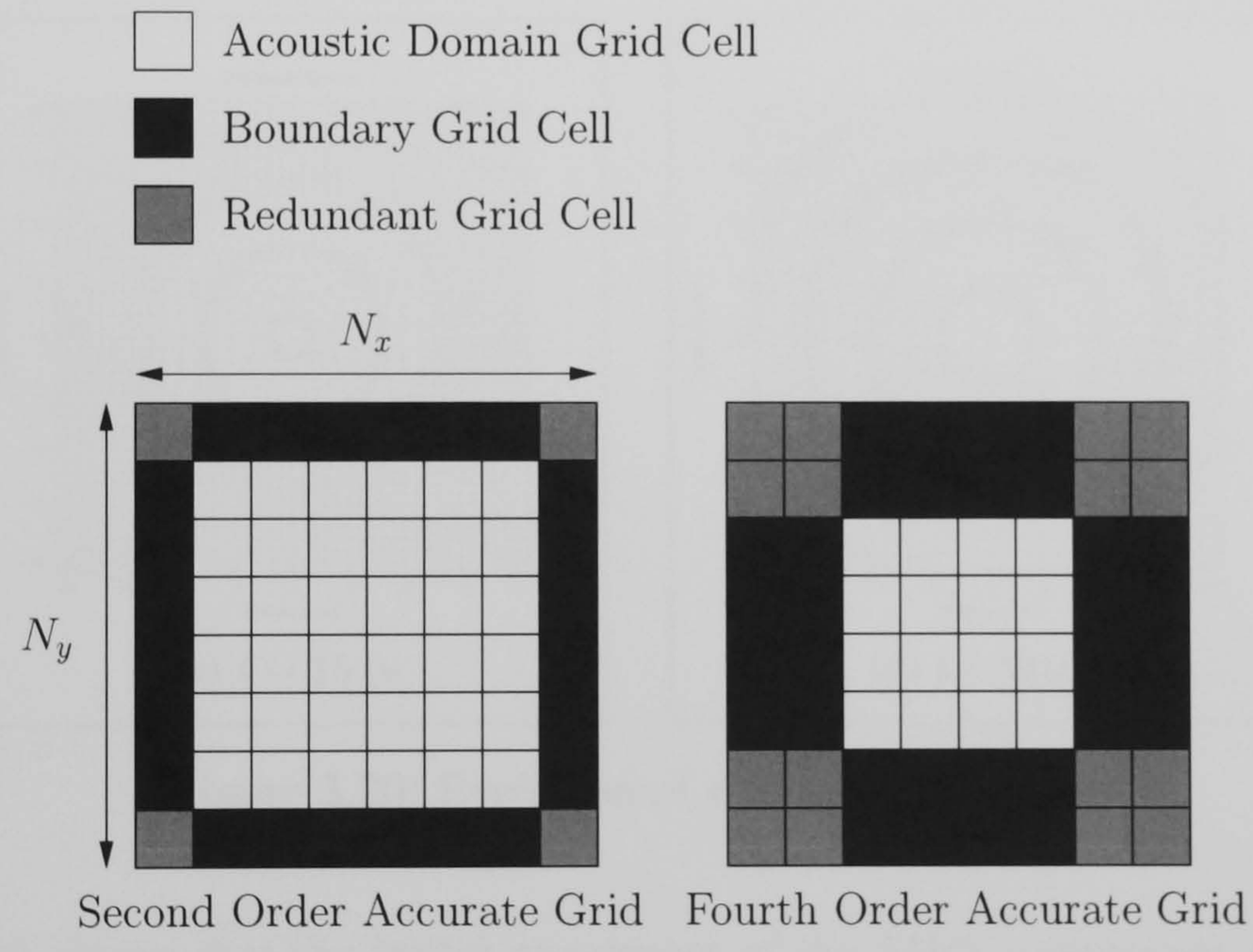

Figure 3.19: Boundary Grid Cells for the Second and Fourth Order Accurate Grids

3.3.5 Acoustic Sources

A monopole source is described as a point source, which is the limit of a pulsating sphere as its radius tends to zero [104]. Figure 3.20 shows the evolution of the acoustic near-field from a monopole source with time. This does not accurately describe the generation of sound from a vibrating structure, but rather a structure that is undergoing periodic com-

pression and expansion. To understand how sound is generated, consider the motion of the simple harmonic oscillator as shown in Figure 3.21.

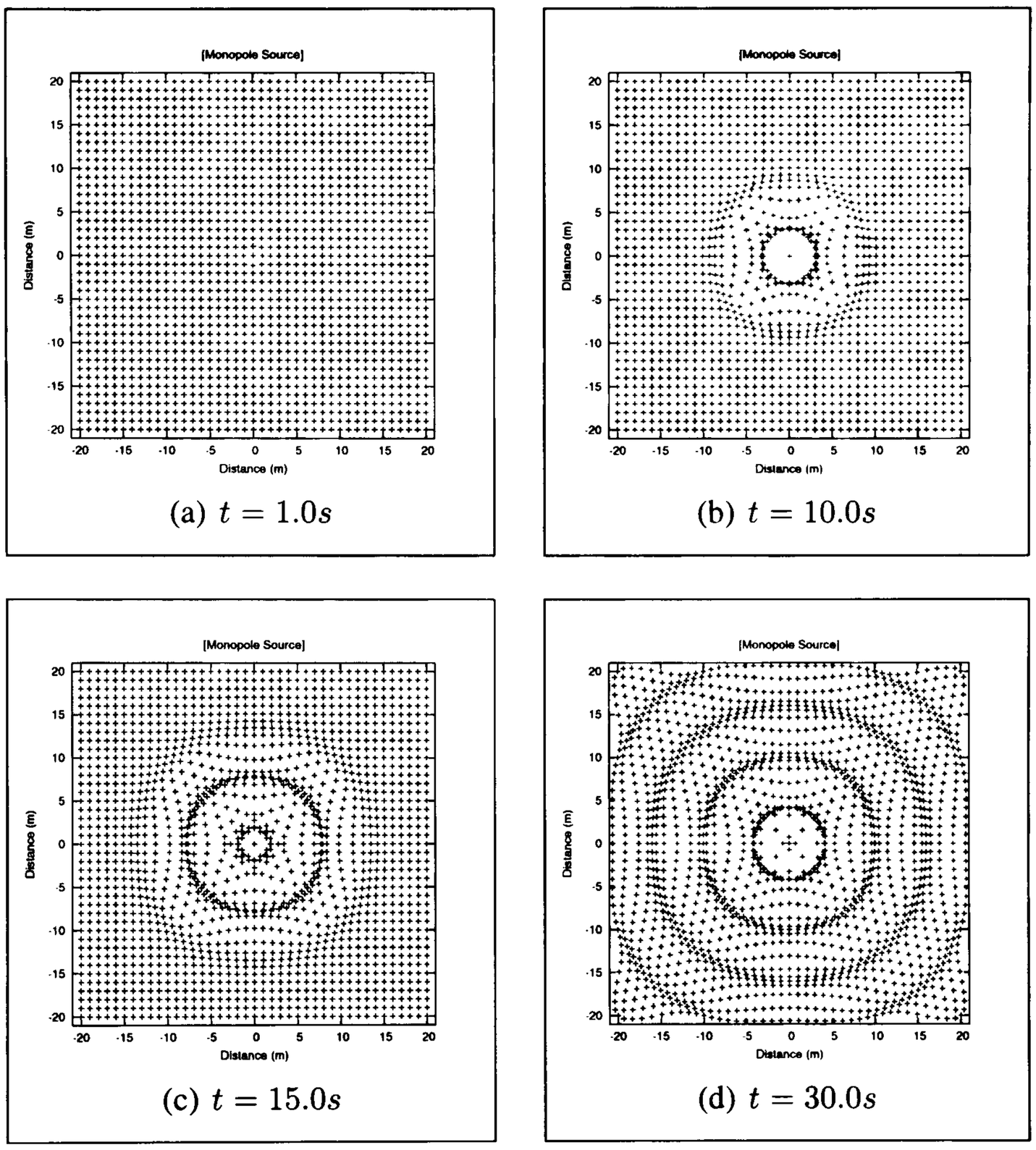

Figure 3.20: Evolution of a Monopole Source

Figure 3.21 shows that the initial movement of the SHO compresses the air directly in front of the mass causing an increase in pressure. At the same time rarefaction is occurring to the air directly behind the moving mass causing a decrease in the pressure. From viewing the pressure field at a distance such that the SHO becomes a point source, over time the pressure field generated will look similar to that shown in Figure 3.21. This is known as a dipole source which is equivalent to two monopole sources of equal strength but with opposite phase being placed close to one another. Figure 3.22 shows the evolution of the dipole source with time.

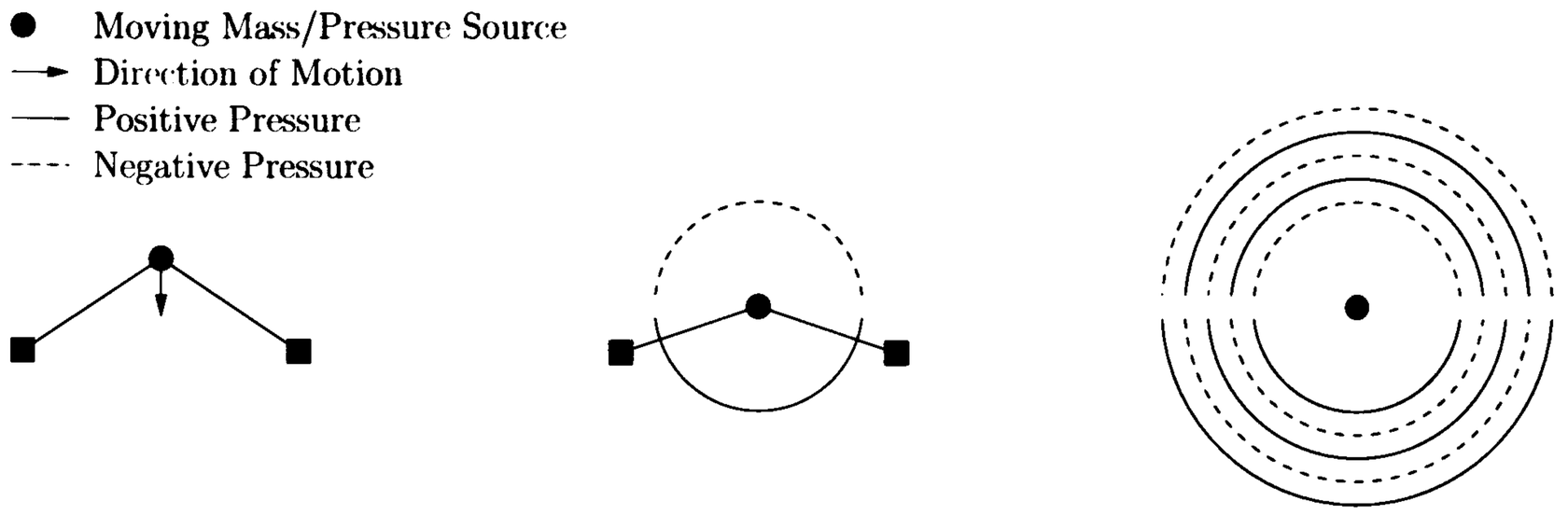

Figure 3.21: Representing the Simple Harmonic Oscillator as a Dipole Source

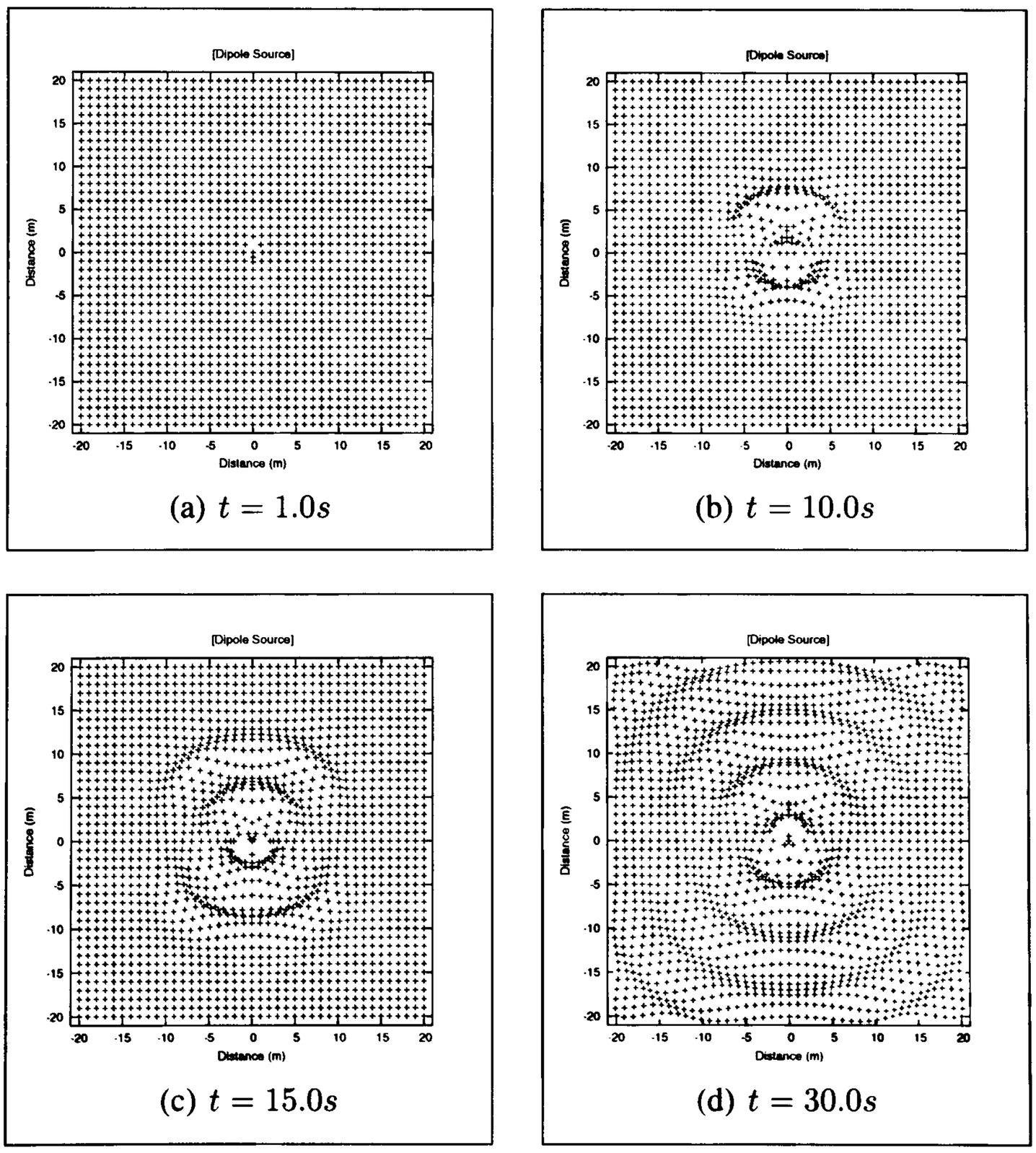

Figure 3.22: Evolution of a Dipole Source

For completeness, Figure 3.23 shows a quadrupole source which is equivalent to two dipole sources of equal strength but with opposite phase.

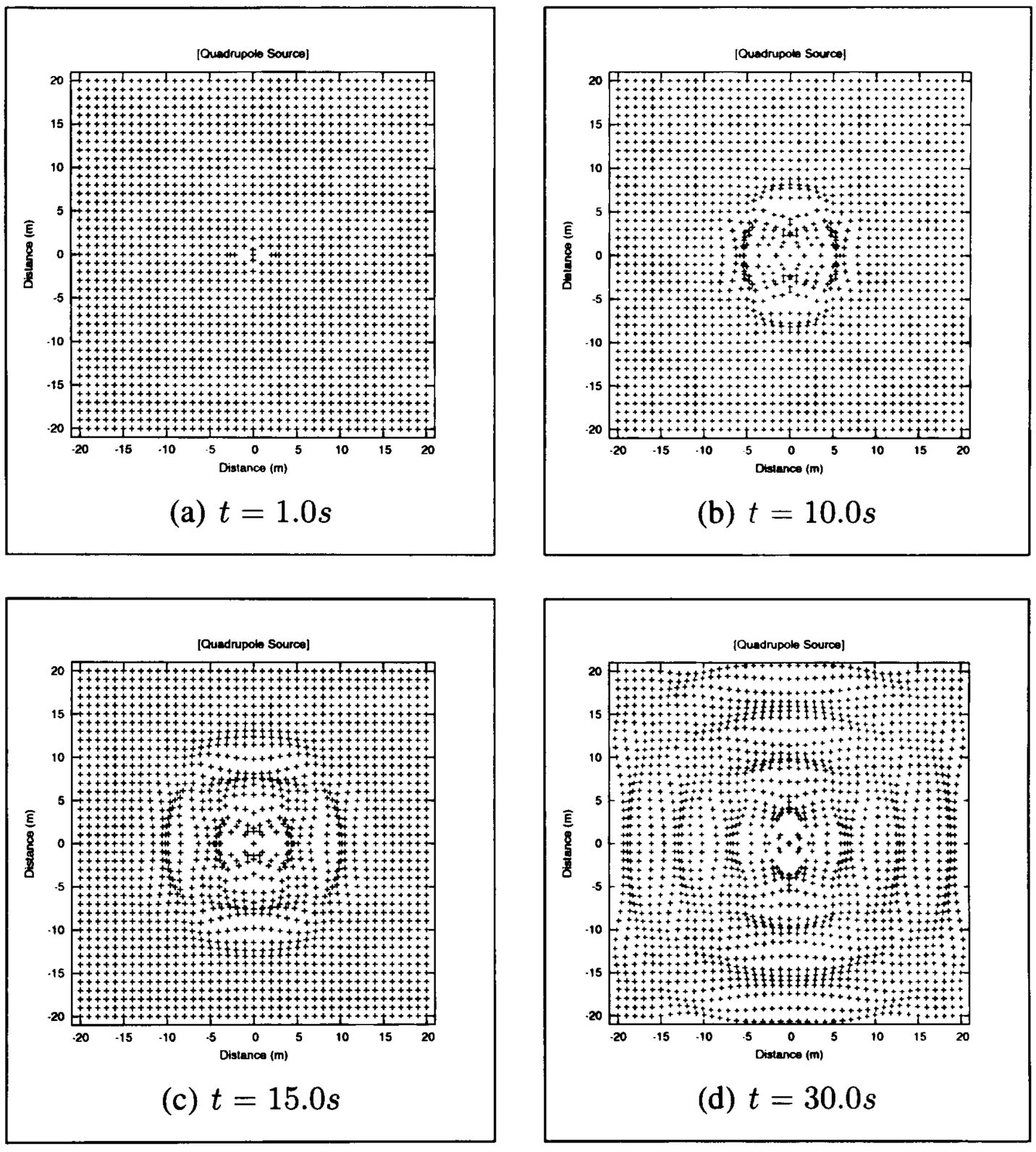

(a) $t = 1.0s$ (b) $t = 10.0s$

(c) $t = 15.0s$ (d) $t = 30.0s$

Figure 3.23: Evolution of a Quadrupole Source

3.3.6 Acoustic Wave Test Cases

This section will test the accuracy of both formulations of the acoustic wave model. Each algorithm will be subject to two different sources, the monopole source and the dipole source, with the source function being a single sine pulse. For each example the grid size is -10 m $\leq x \leq$ 10 m, -10 m $\leq y \leq$ 10 m with $\Delta h = 0.2$ m, $\Delta t = 0.1$ s, $c = 1$ m/s and $\rho = 1$ kg/m^3. Although the monopole source is physically incorrect for the purpose of this work, it will still be used to ascertain the accuracy of the acoustic wave models.

Acoustic Pressure Wave Model

Figures 3.24(a) and 3.24(b) show the acoustic pressure generated by a monopole source (see Figure 3.20), measured at the centre of the grid (0 m, 0 m) and at the corner of the grid (-9.8 m, -9.8 m)[1] respectively. Figure 3.24(c) showing the acoustic pressure at $t = 10.0s$. The black 'dots' on Figure 3.24(c) indicate the positions of the monitoring points 1 through 7.

Figure 3.24 shows that the acoustic pressure wave model is producing sensible results. The acoustic pressure wave model correctly reproduces the amplitude and speed of the acoustic wave, with only a slight discrepancy in the frequency of the acoustic wave. However Figure 3.24(d) shows evidence of a high frequency component due to small numerical inaccuracies caused in part by the truncation error of the discretised acoustic pressure equation and the numerical influence of the non-reflecting boundary conditions [102].

Figures 3.25(a) and 3.25(b) show the acoustic pressure generated by a dipole source (see Figure 3.21), measured at the centre of the grid (0 m, 0 m) and at the corner of the grid (-9.8 m, -9.8 m). The acoustic pressure wave model reproduces the correct amplitude and speed of the acoustic wave from the dipole source and provides a more accurate approximation of the frequency than for the monopole source. Figure 3.25(c) shows the acoustic pressure at $t = 10.0s$. The numerical errors can be seen in Figure 3.25(d) which is of the same order as the monopole source shown in Figure 3.24(d).

The fourth order accurate approximation of the acoustic pressure wave equation given by Equation 3.3.13 is also tested using a dipole source at the centre of the grid. Figures 3.26(b) and 3.26(d) clearly show the benefit of using the fourth order accurate discretisation of the acoustic pressure wave equation. Specifically, the spurious numerical errors in Figure 3.26(b) are about half the amplitude and twice the frequency of those in Figure 3.25(b), hence increasing the order of the spatial integration has attenuated but not

[1]The y axis appears to be inverted in the contour plots due to the JAVA 2D Graphics API using the top left of the image as the origin.

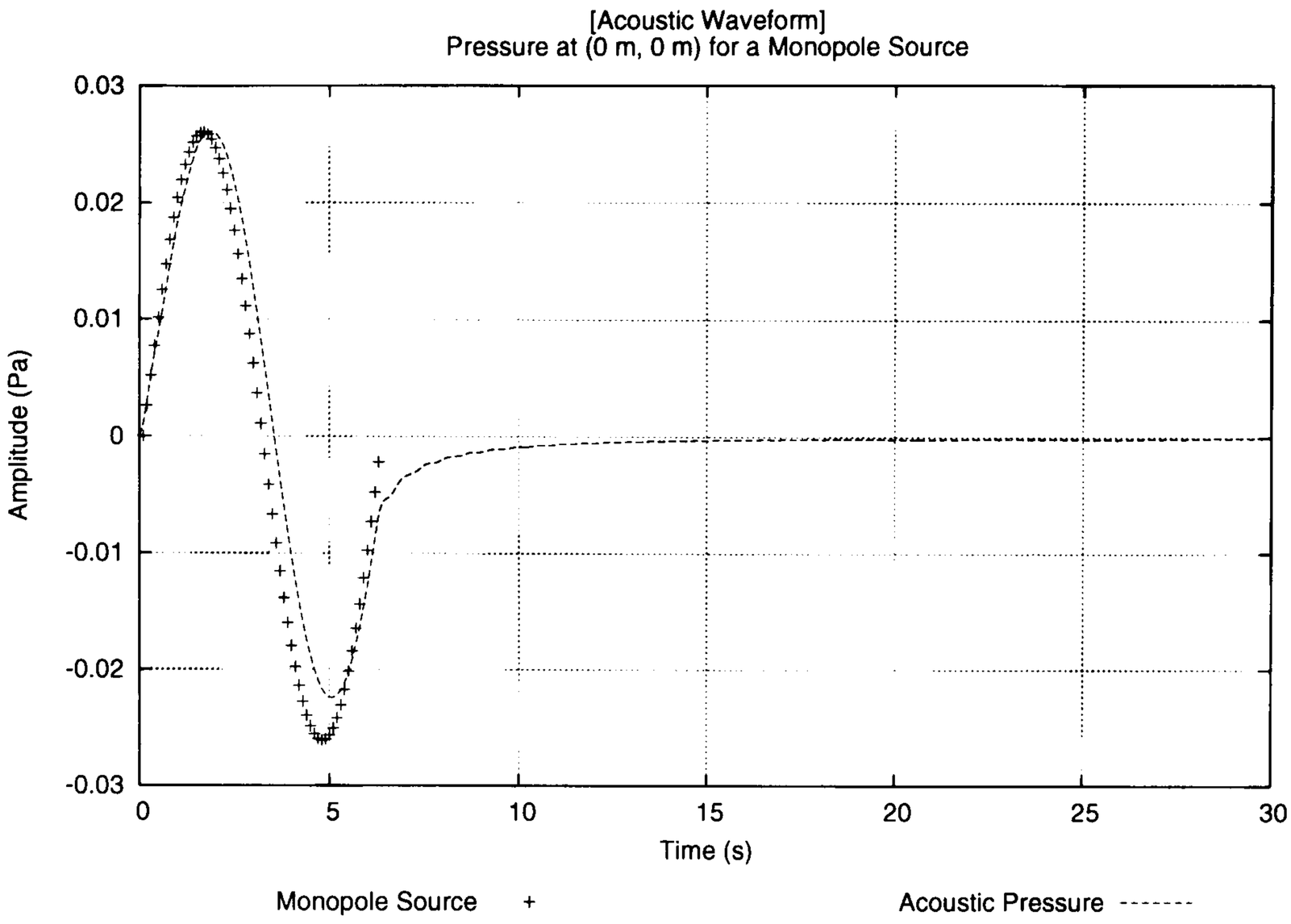

(a) Acoustic Pressure at (0 m, 0 m) from a Monopole Source

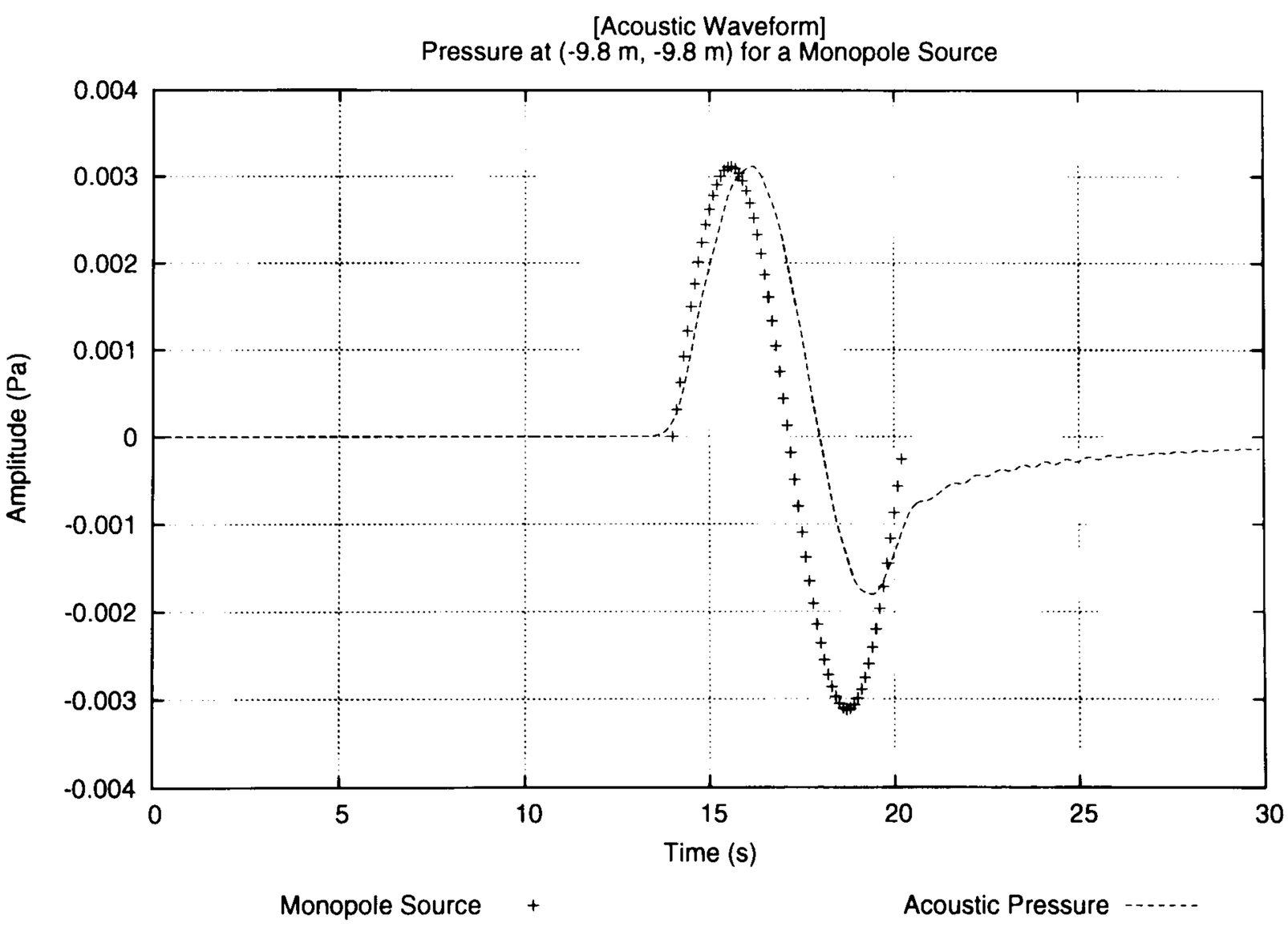

(b) Acoustic Pressure at (-9.8 m, -9.8 m) from a Monopole Source

Figure 3.24: Results for the Monopole Source using a Second Order Accurate Numerical Method

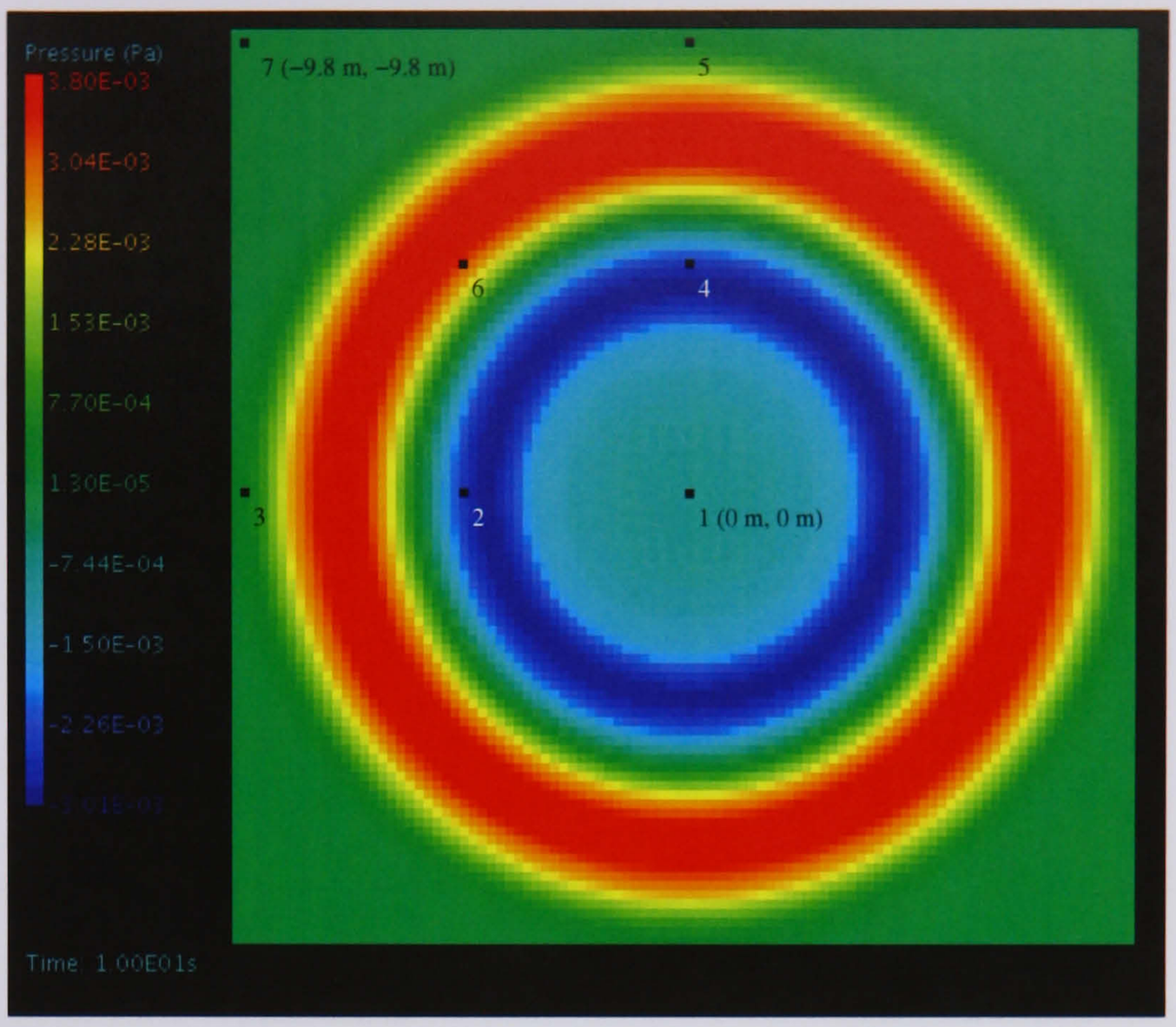

(c) Second Order Accurate Acoustic Pressure Prediction at $t = 10.0s$ (Monopole)

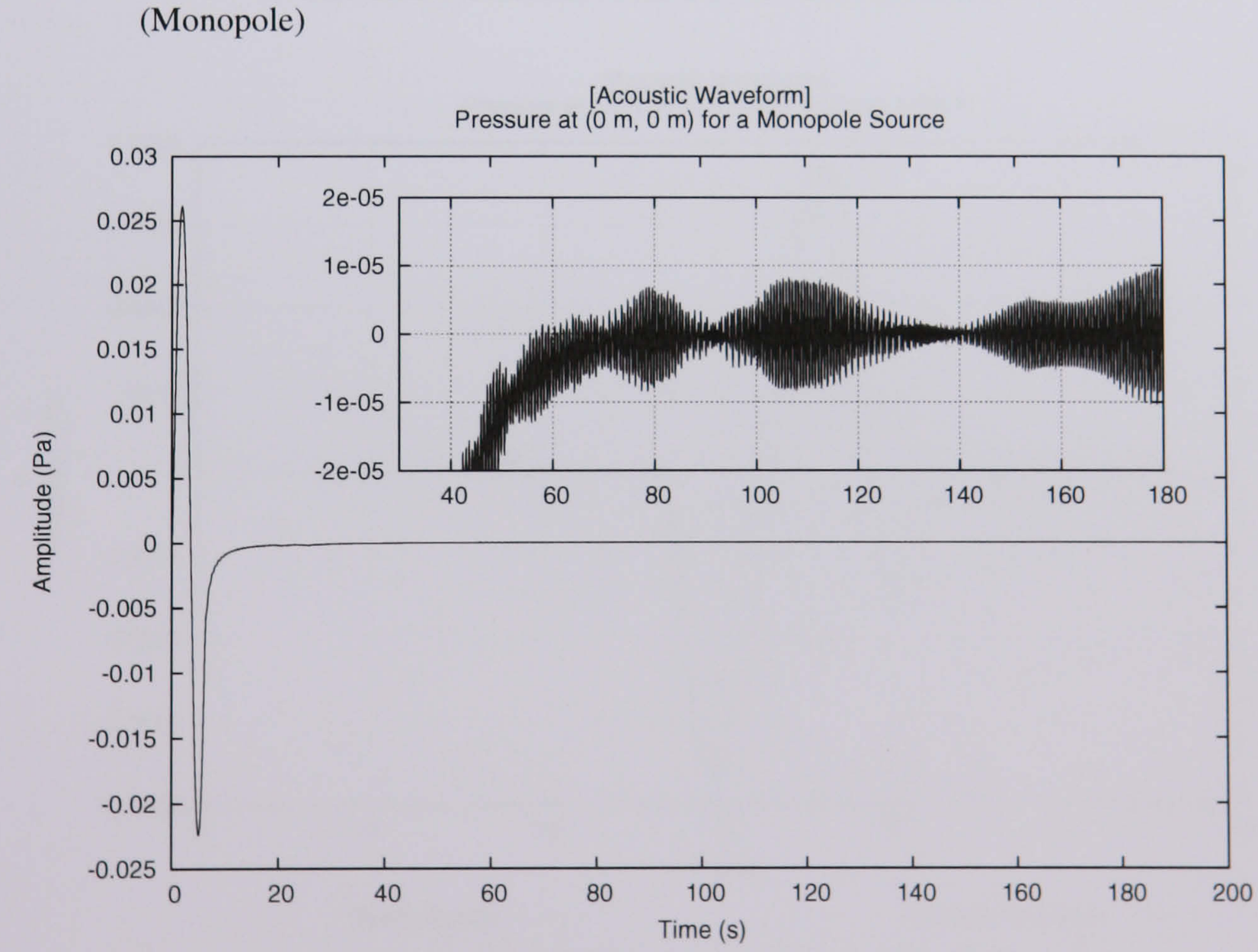

(d) Numerical Error in the Acoustic Pressure at (0 m, 0 m) from a Monopole Source

Figure 3.24: Results for the Monopole Source using a Second Order Accurate Numerical Method

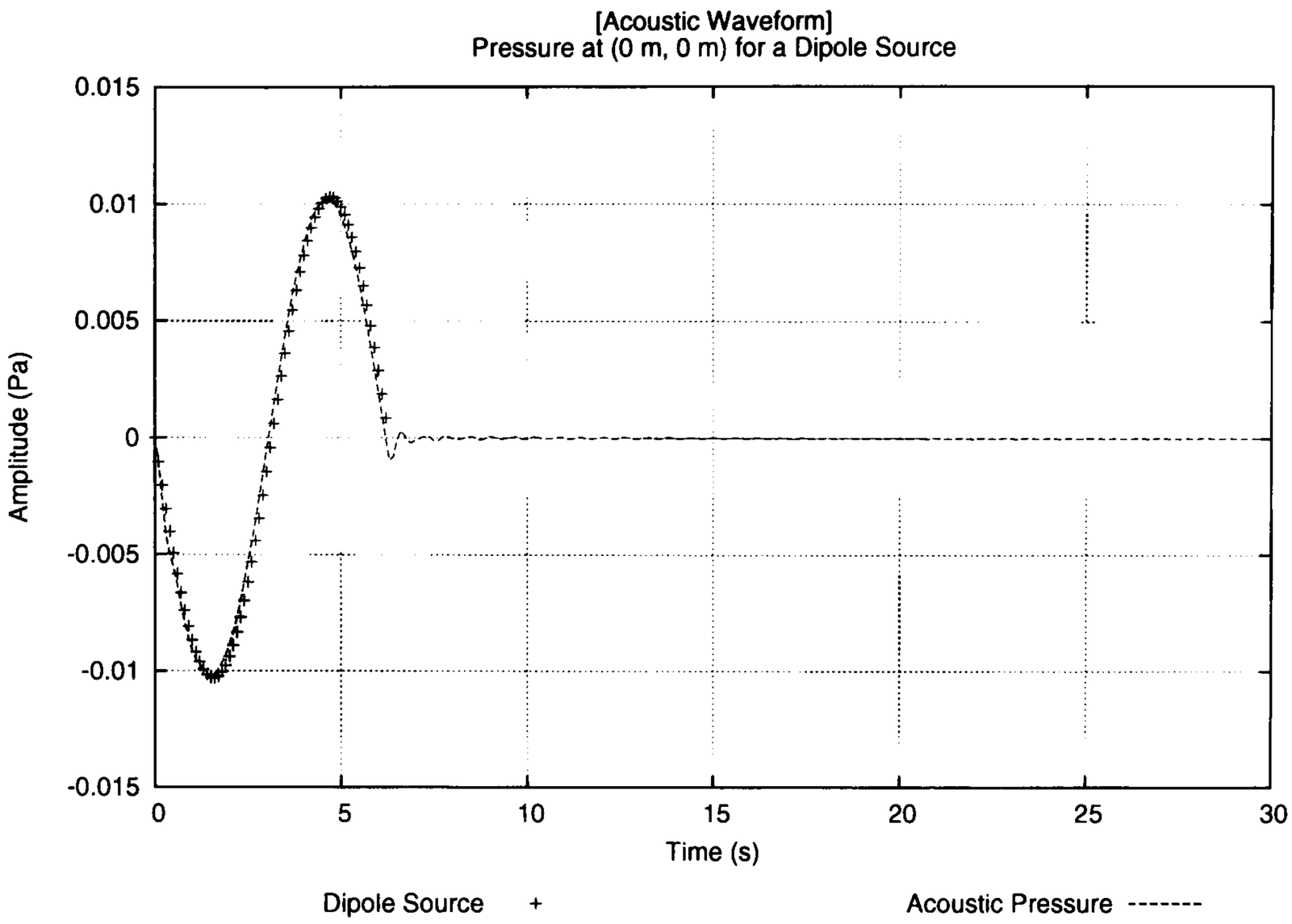

(a) Acoustic Pressure at (0 m, 0 m) from a Dipole Source

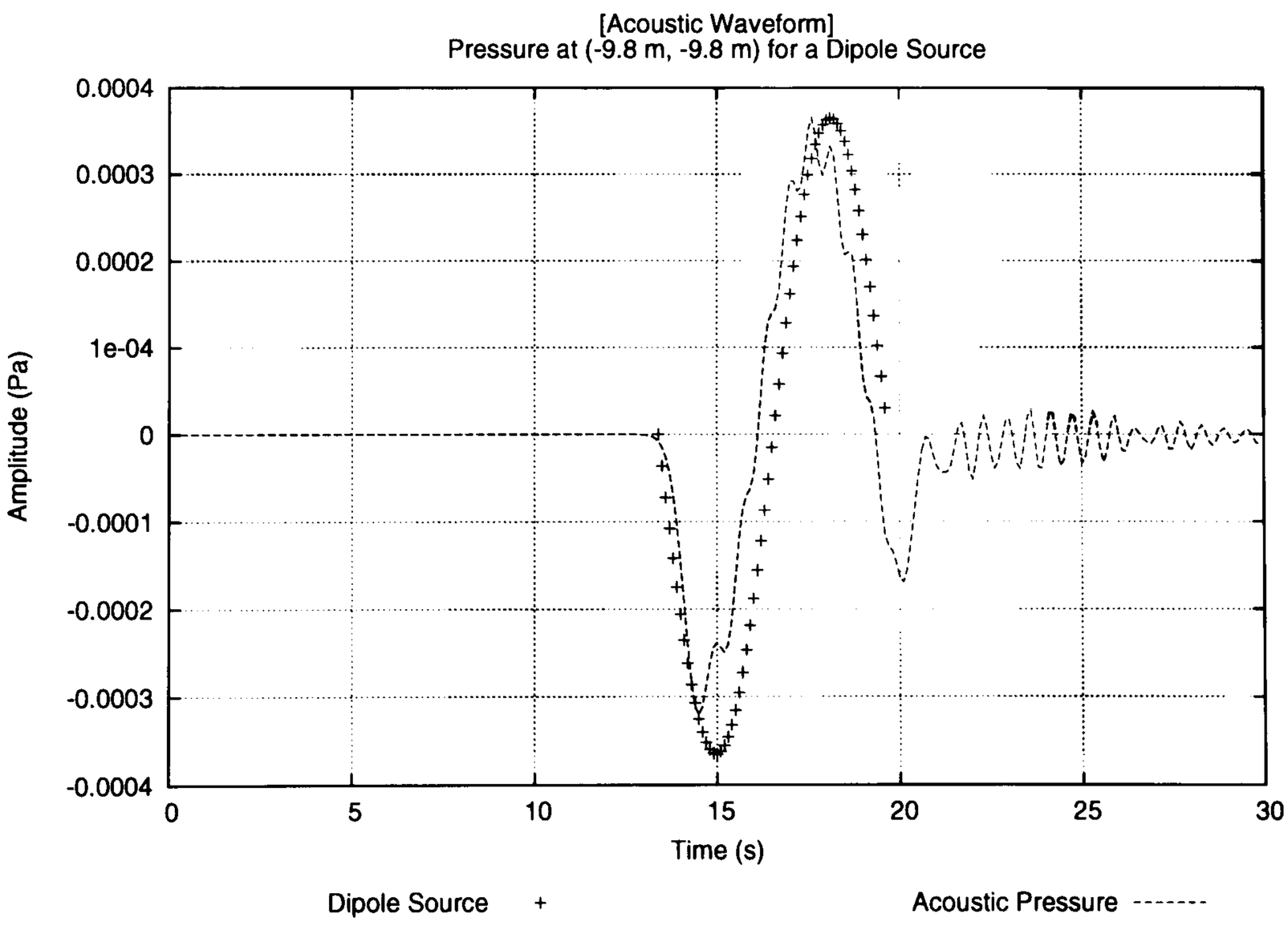

(b) Acoustic Pressure at (-9.8 m, -9.8 m) from a Dipole Source

Figure 3.25: Results for the Dipole Source using a Second Order Accurate Numerical Method

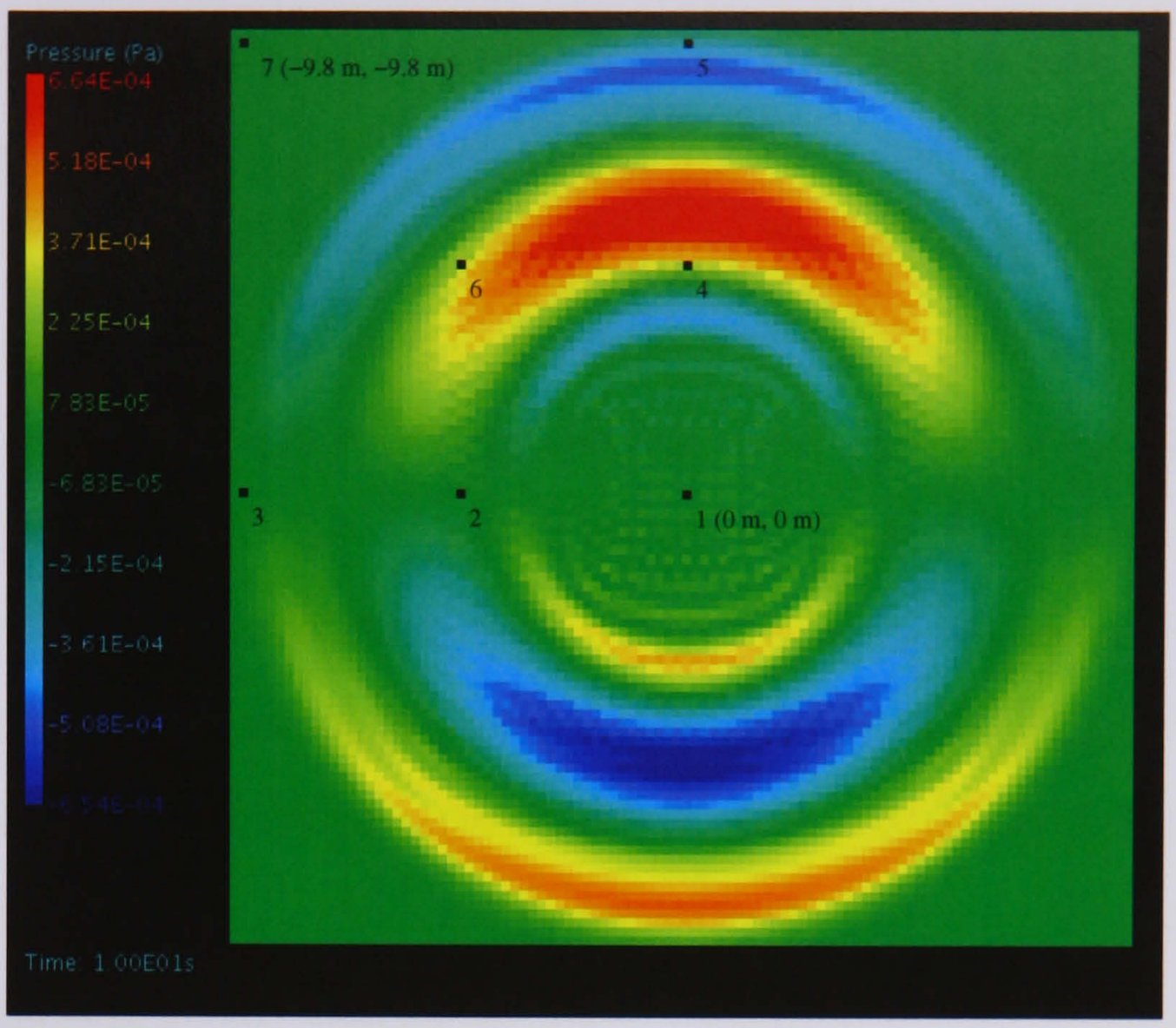

(c) Second Order Accurate Acoustic Pressure Prediction at $t = 10.0s$ (Dipole)

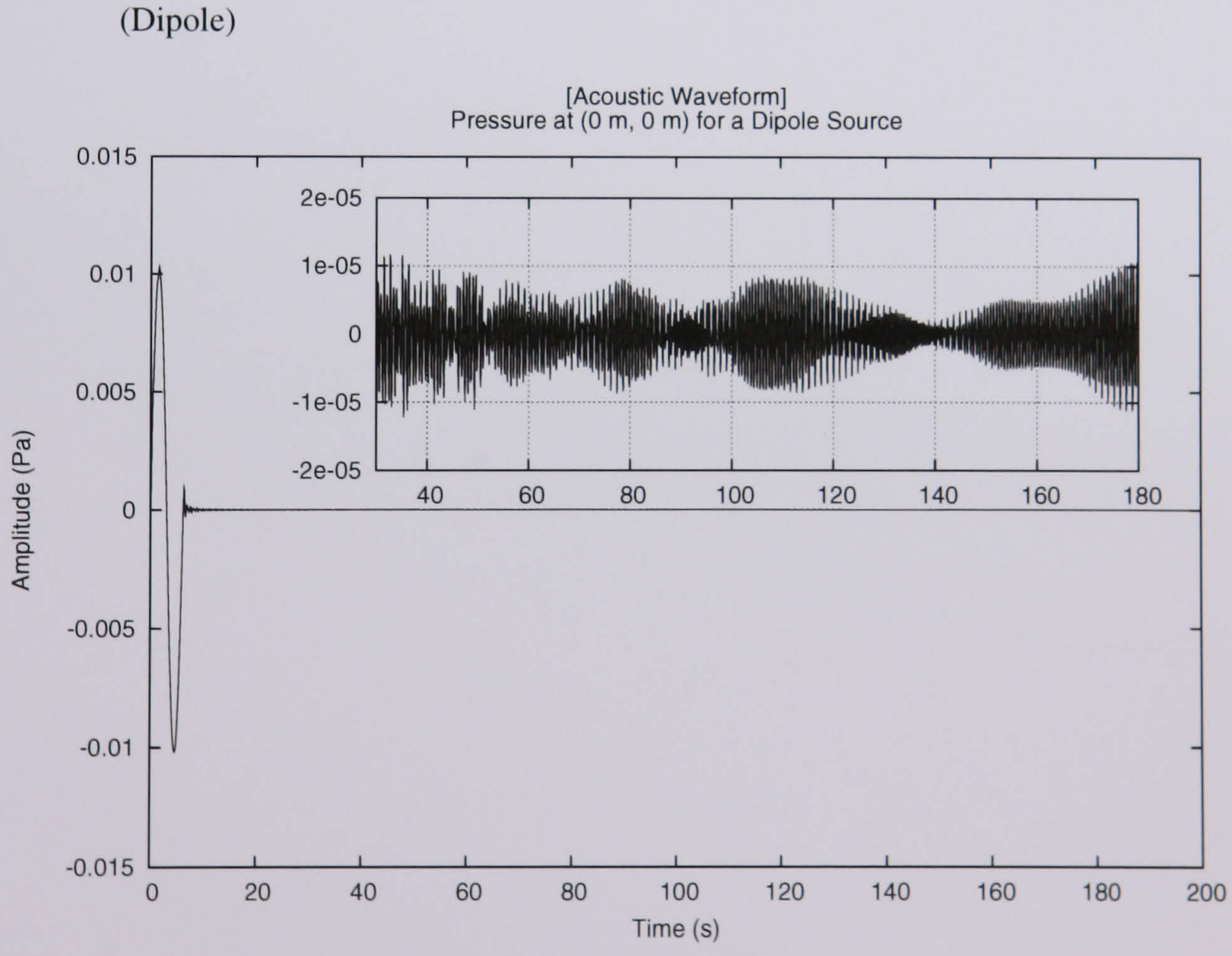

(d) Numerical Error in the Acoustic Pressure at (0 m, 0 m) from a Dipole Source

Figure 3.25: Results for the Dipole Source using a Second Order Accurate Numerical Method

eliminated the numerical noise from the domain boundary.

The previous test cases have shown the evolution of the numerical error for a single sine pulse is acceptable, but not ideal if a highly accurate solution is required. The following example uses a continuous dipole as a source term. This will show how the numerical errors evolve when an external force is always present. Figures 3.27(a) and 3.27(b) show an initial transient in the amplitude of the acoustic wave. The response of the medium in which the wave propagates requires several periods before the wave settles and oscillates about the equilibrium pressure. Figure 3.27(d) shows two periods of the predicted acoustic pressure oscillation from the dipole source. The waveform appears sinusoidal without any significant high frequency component. This suggests that this numerical scheme will produce accurate results as long as there are source terms which ensure that the amplitude of the wave is always greater than the numerical error.

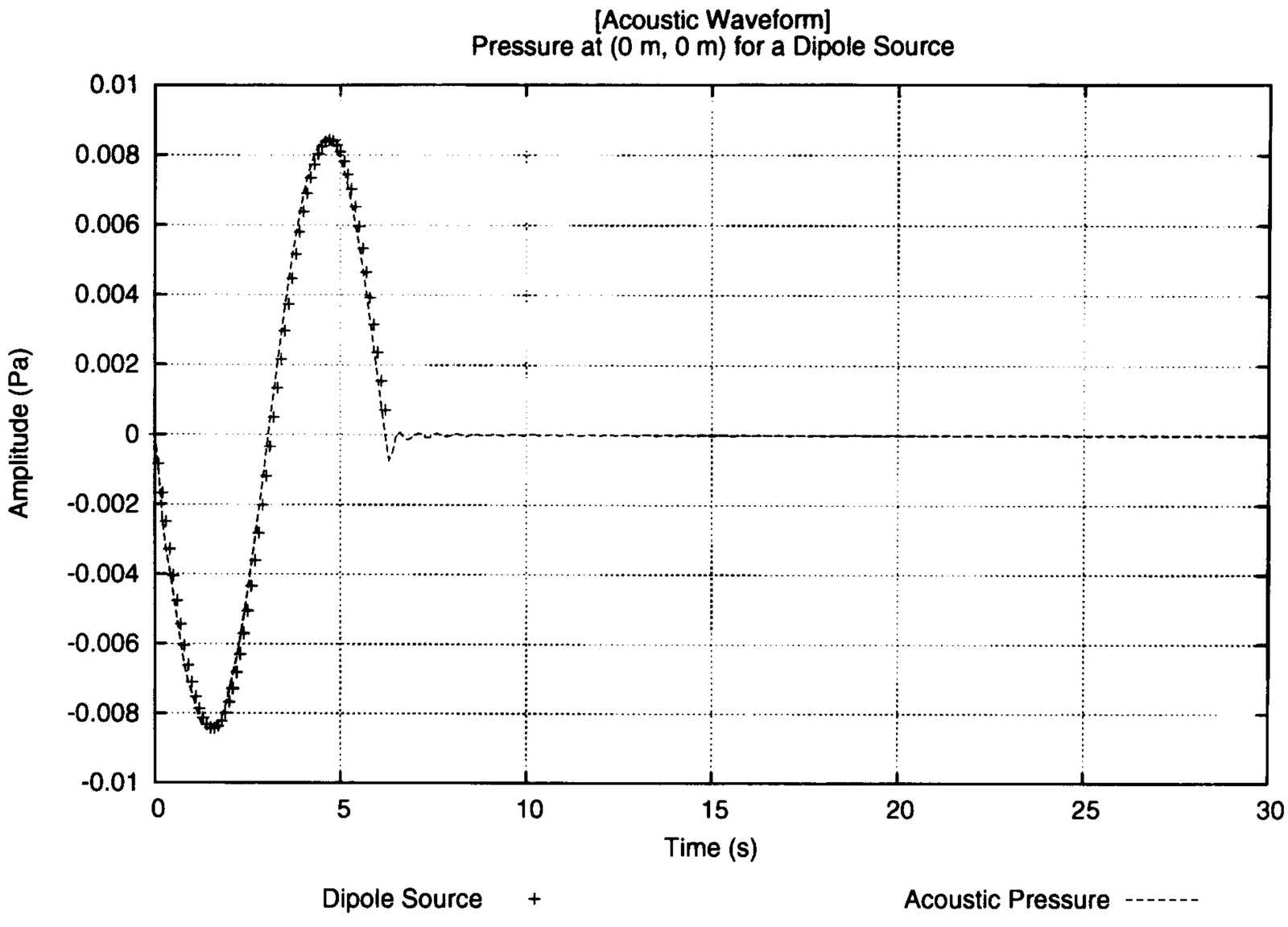

(a) Fourth Order Accurate Acoustic Pressure at (0 m, 0 m) from a Dipole Source

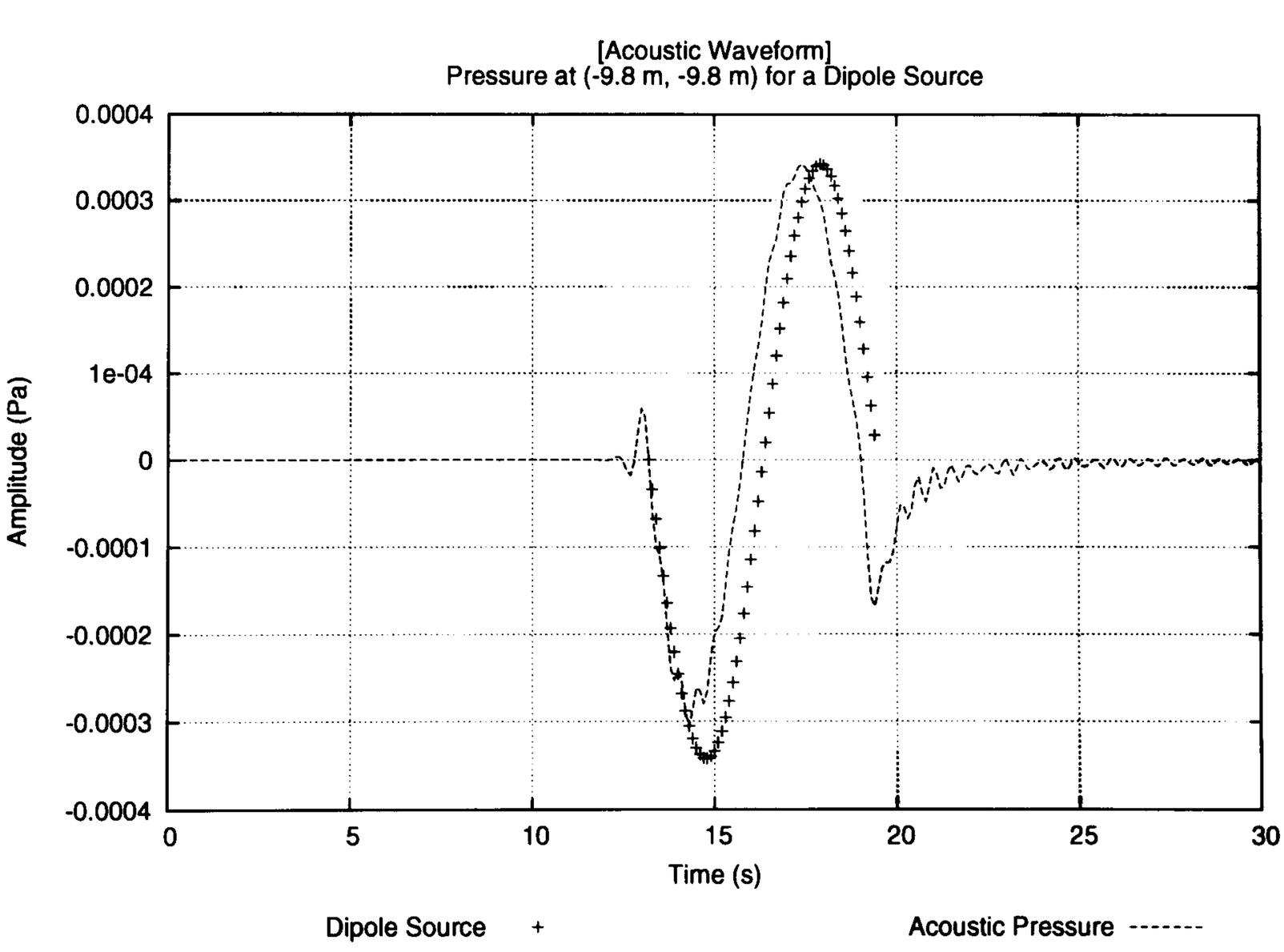

(b) Fourth Order Accurate Acoustic Pressure at (-9.8 m, -9.8 m) from a Dipole Source

Figure 3.26: Results for the Dipole Source using a Fourth Order Accurate Numerical Method

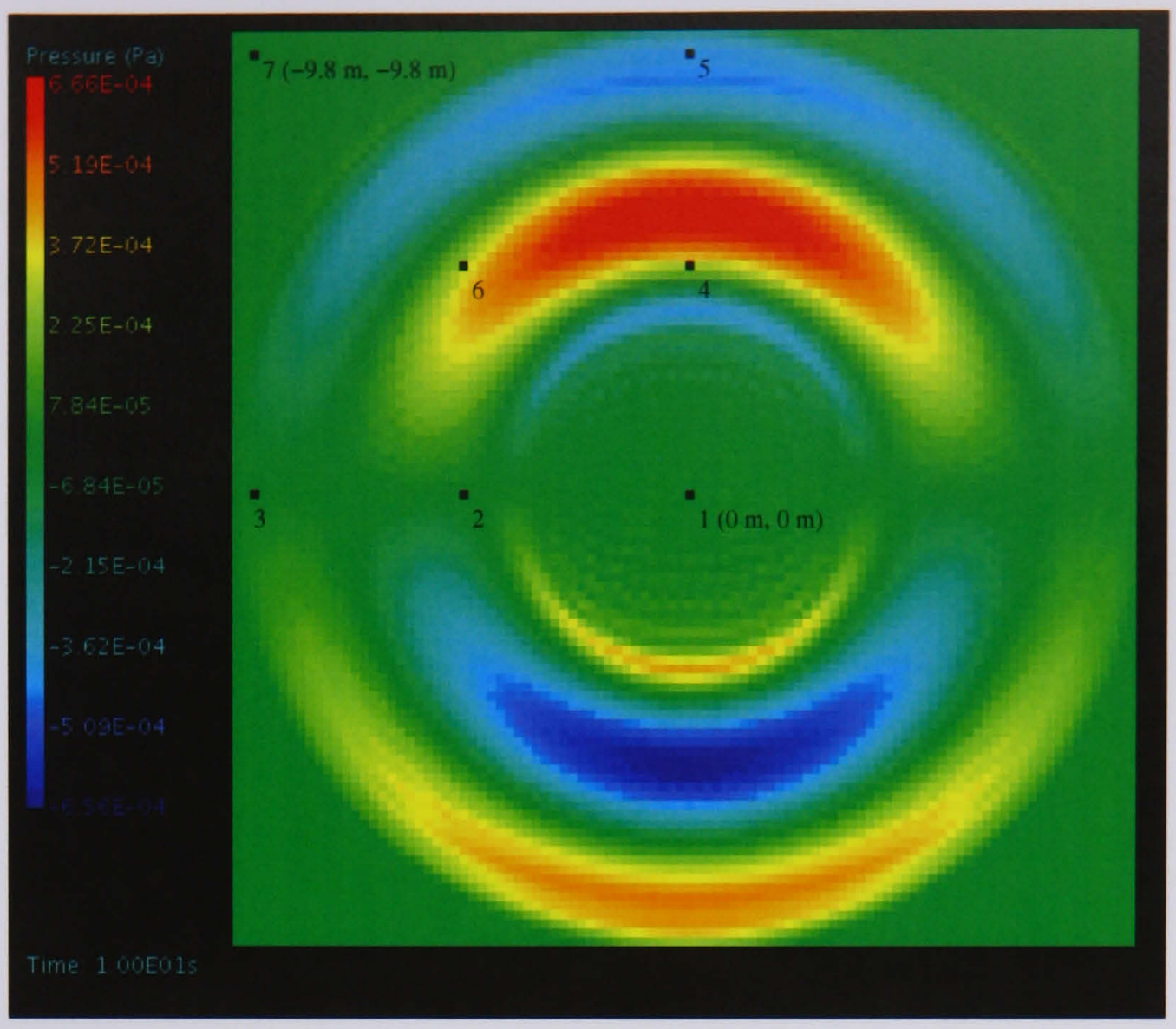

(c) Fourth Order Accurate Acoustic Pressure Prediction at $t = 10.0s$ (Dipole)

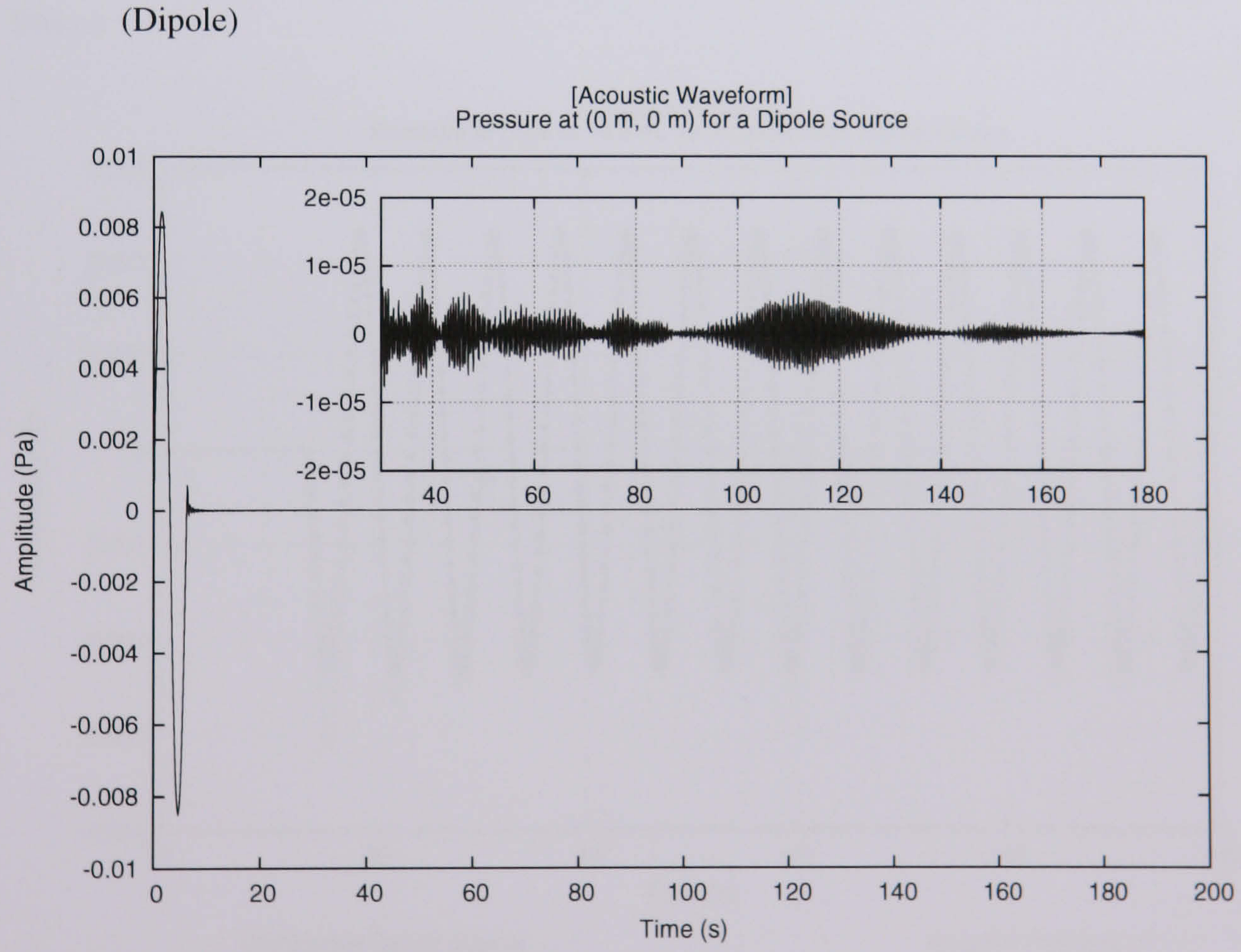

(d) Numerical Error in the Fourth Order Accurate Acoustic Pressure at (0 m, 0 m) from a Dipole Source

Figure 3.26: Results for the Dipole Source using a Fourth Order Accurate Numerical Method

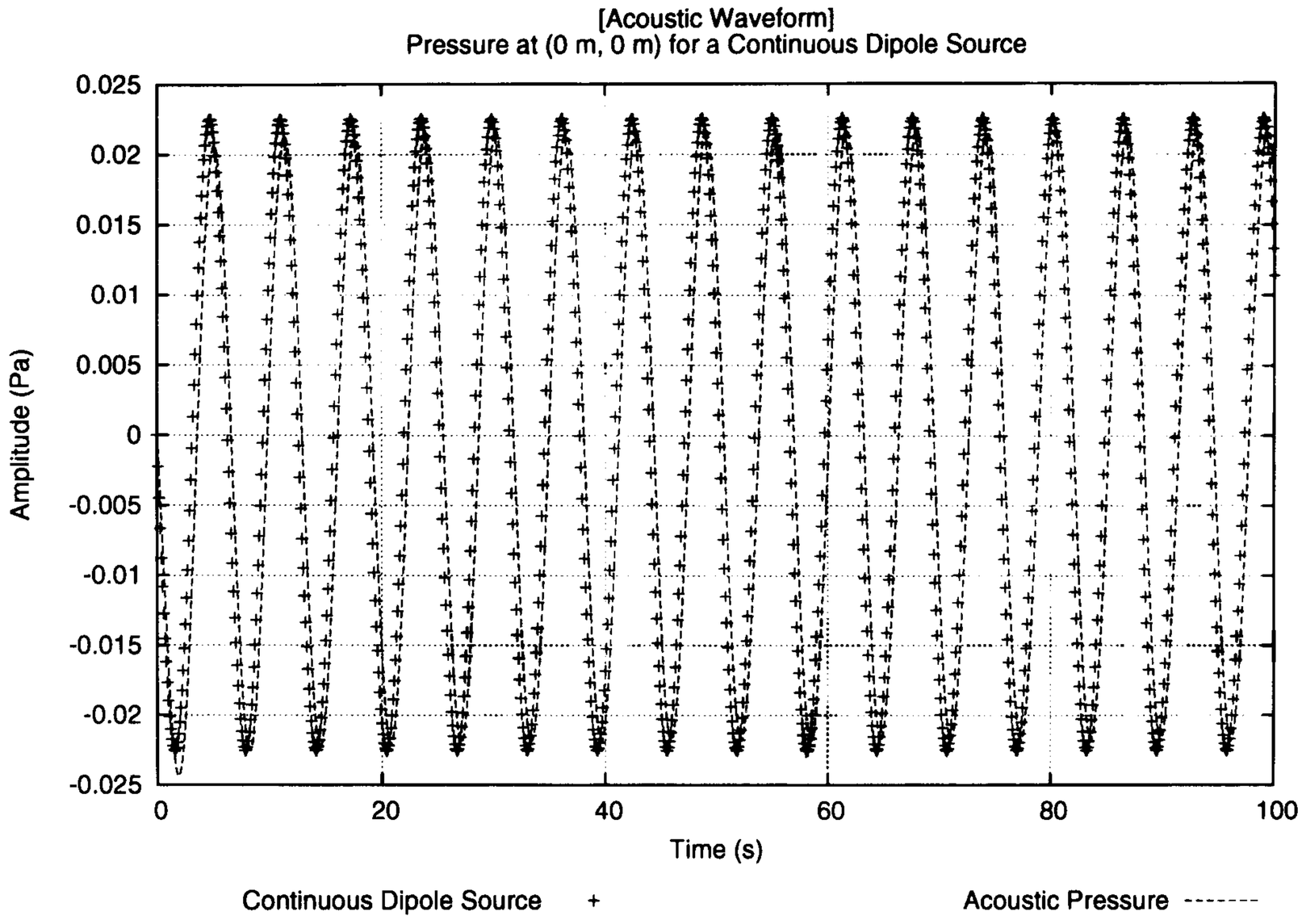

(a) Fourth Order Accurate Acoustic Pressure at (0 m, 0 m) from a Continuous Dipole Source

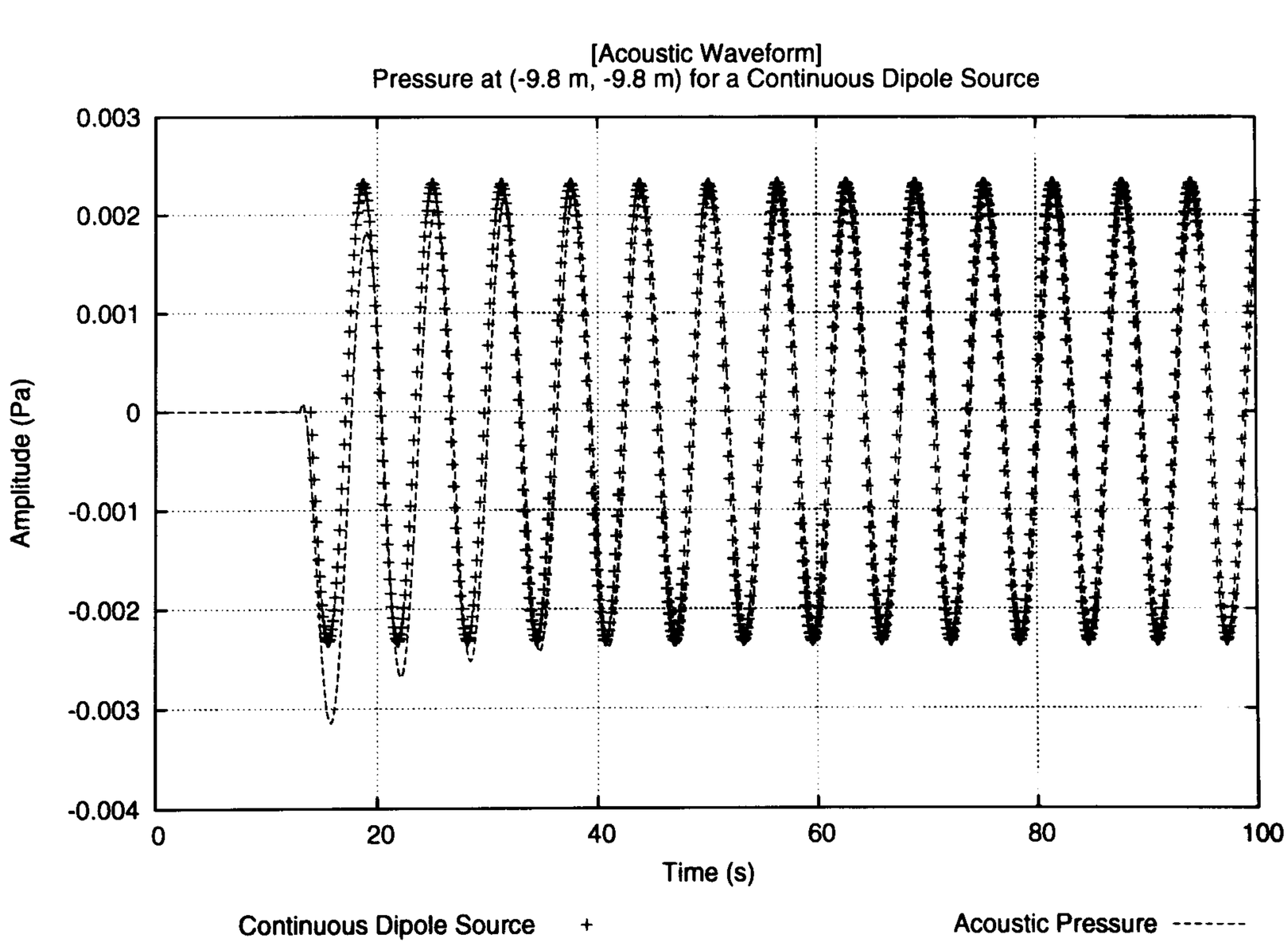

(b) Fourth Order Accurate Acoustic Pressure at (-9.8 m, -9.8 m) from a Continuous Dipole Source

Figure 3.27: Results for the Continuous Dipole Source using a Fourth Order Accurate Numerical Method

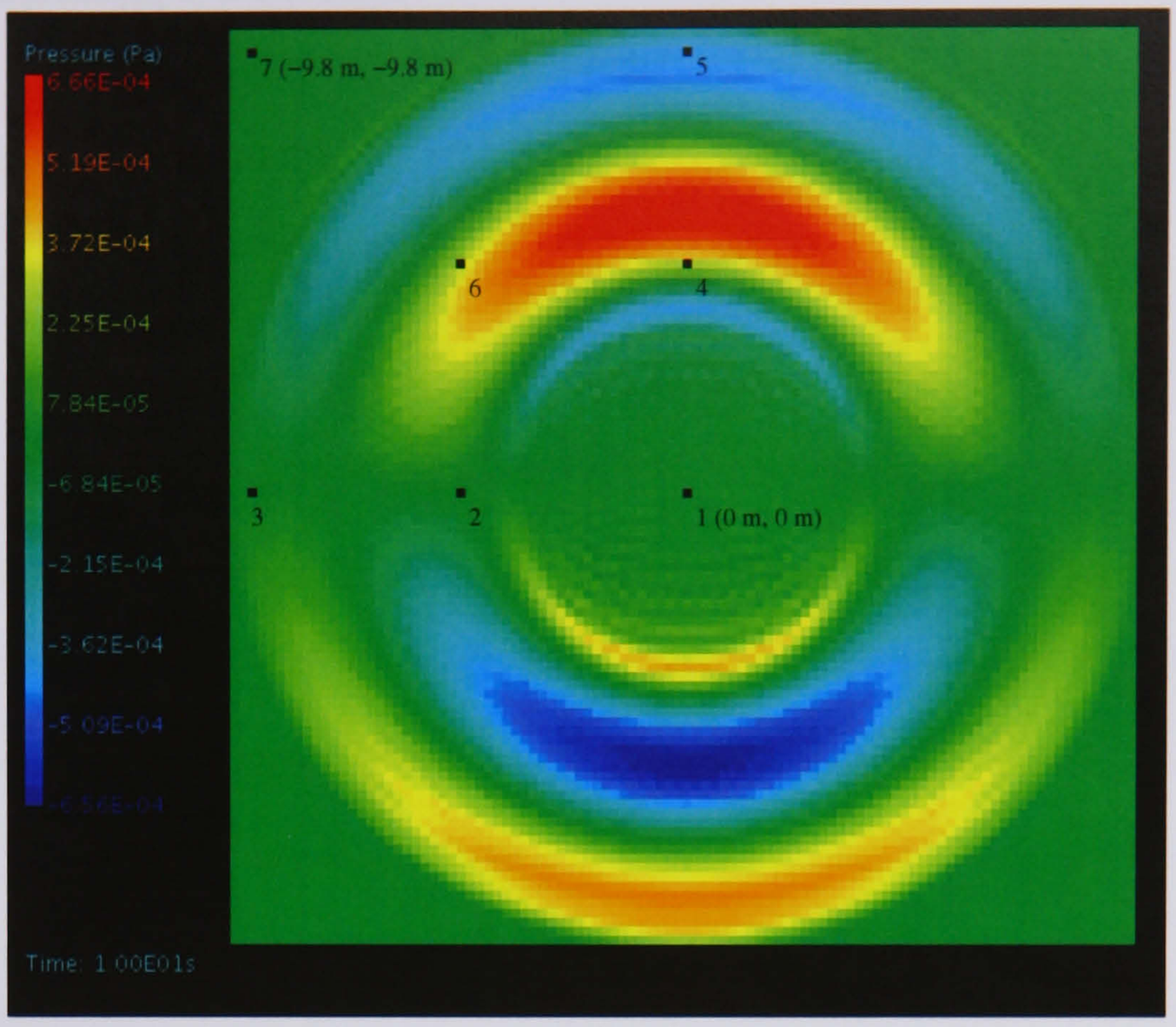

(c) Fourth Order Accurate Acoustic Pressure Prediction at $t = 10.0s$ (Dipole)

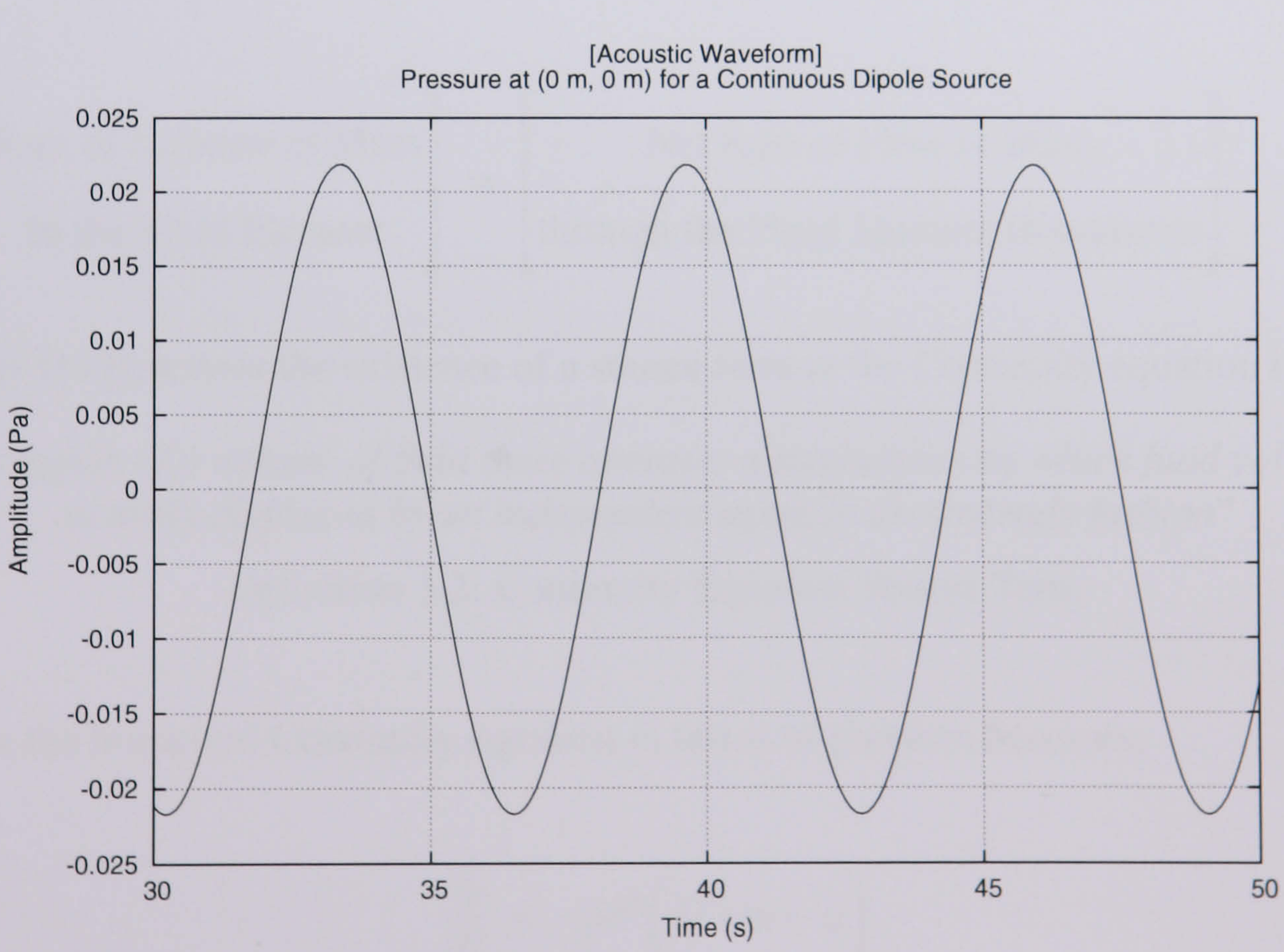

(d) Detail of the Fourth Order Accurate Acoustic Pressure Fluctuation at (0 m, 0 m) from a Continuous Dipole Source

Figure 3.27: Results for the Continuous Dipole Source using a Fourth Order Accurate Numerical Method

3.4 Coupling Method

3.4.1 Coupling Theory

When considering a method for coupling the movement of the mass/spring model to the acoustic wave propagation model, it is important to first understand which variables are available for coupling from the mass/spring model and secondly the definition of the source terms for the acoustic wave propagation model. The mass/spring model, regardless of the solver, will provide displacements and velocities for each of the masses. The acoustic pressure/particle velocity wave equation is formed by combining the Continuity equation and Momentum equation, therefore it is essential that the source terms for the Continuity and Momentum equations are analysed.

Consider the following definition of the Continuity equation for a control volume [93].

$$\left[\begin{array}{c}\text{Rate of Increase of Mass} \\ \text{in the Fluid Element}\end{array}\right] = \left[\begin{array}{c}\text{Net Rate of Flow of Mass} \\ \text{through the Fluid Element Boundaries}\end{array}\right] \tag{3.4.1}$$

Fahy [113] defines the existence of a source term in the Continuity equation if:

"*In a region of a volume of fluid there operates a mechanism by which fluid volume is actively displaced by an independent agent in an unsteady fashion*"

Definition 3.2: Continuity Equation Source Term

then the linearised Continuity equation in terms of pressure becomes:

$$\frac{\partial p}{\partial t} = -\bar{\rho}c^2\left(\nabla \cdot \mathbf{u} - q\right) \tag{3.4.2}$$

where $\bar{\rho}q$ is the rate of mass introduction in to the control volume. Consider the following definition of the Momentum equation for a control volume [93]:

$$\begin{bmatrix}\text{Rate of Increase}\\ \text{of Momentum inside}\\ \text{the Fluid Element}\end{bmatrix} = \begin{bmatrix}\text{Net Flux of Momentum}\\ \text{through the Fluid}\\ \text{Element Boundaries}\end{bmatrix} + \begin{bmatrix}\text{Sum of Forces}\\ \text{Acting on the}\\ \text{Fluid Element}\end{bmatrix} \quad (3.4.3)$$

Fahy [113] defines the existence of a source term in the Momentum equation if:

"*In a region of fluid there operates a mechanism by which an external force acts on the fluid*"

Definition 3.3: Momentum Equation Source Term

If $\bar{\mathbf{u}} = 0$, then the linearised form of the Momentum equation becomes:

$$\frac{\partial \mathbf{u}}{\partial t} = -\frac{1}{\bar{\rho}}\nabla p + \frac{1}{\bar{\rho}}\mathbf{F} \quad (3.4.4)$$

where $\mathbf{F}$ is the external force acting on the control volume from the mass/spring system. The following sections will investigate the mathematical evolution of the two source terms as the acoustic pressure wave equation and the particle velocity wave equation are formulated. From this, it will be decided which wave equation is best suited for the purpose of this work. Finally, Section 3.4.4 will test the accuracy of the suitable coupling method.

3.4.2 Coupling the Mass/Spring Model to the Acoustic Pressure Wave Model

This section investigates combining Equations 3.4.4 and 3.4.2 to eliminate $\mathbf{u}$ to form the inhomogeneous acoustic pressure wave equation as shown in Equation 3.4.5. Differentiating Equation 3.4.2 with respect to time and substituting for $\frac{\partial u}{\partial t}$ from Equation 3.4.4 gives:

$$\frac{\partial^2 p}{\partial t^2} = c^2\left(\nabla^2 p - \nabla \cdot \mathbf{F} + \rho\frac{\partial q}{\partial t}\right) \tag{3.4.5}$$

The source term in the form of an external force is now represented by the divergence of that force, hence $\nabla \cdot \mathbf{F}$, with the mass source term represented by $\bar{\rho}\frac{\partial q}{\partial t}$. The movement of the mass/spring system displaces the surrounding fluid, which means $c^2\bar{\rho}\frac{\partial q}{\partial t} \neq 0$ at the model paper fibre.

$\bar{\rho}\frac{\partial q}{\partial t}$ is known as the volumetric acceleration. This volumetric acceleration must be caused by the movement of the masses, therefore it is possible to express the volumetric acceleration in terms of the mass/spring model as:

$$\frac{\partial q}{\partial t} = \frac{\partial \mathbf{u}_{ms}}{\partial t} \cdot \mathbf{n} \tag{3.4.6}$$

where $\mathbf{n}$ is the inwards unit normal vector to the acoustic domain boundary and $\mathbf{u}_{ms}$ is the mass/spring model velocity vector. A mass displacing into the acoustic domain, in the positive $\mathbf{n}$ direction, adds mass to the mass balance as expressed by Equation 3.4.2 and it is therefore a positive source. It is also important to note that any vibrating source will always produce a dipole as shown by the three examples in Figure 3.28. Using this method, it is possible to accurately couple the mass/spring model to the acoustic pressure wave equation.

3.4.3 Coupling the Mass/Spring Model to the Particle Velocity Wave Equation

This section investigates combining Equations 3.4.4 and 3.4.2 to eliminate p to form the inhomogeneous particle velocity wave equation as shown in Equation 3.4.7, assuming that the flow is irrotational.

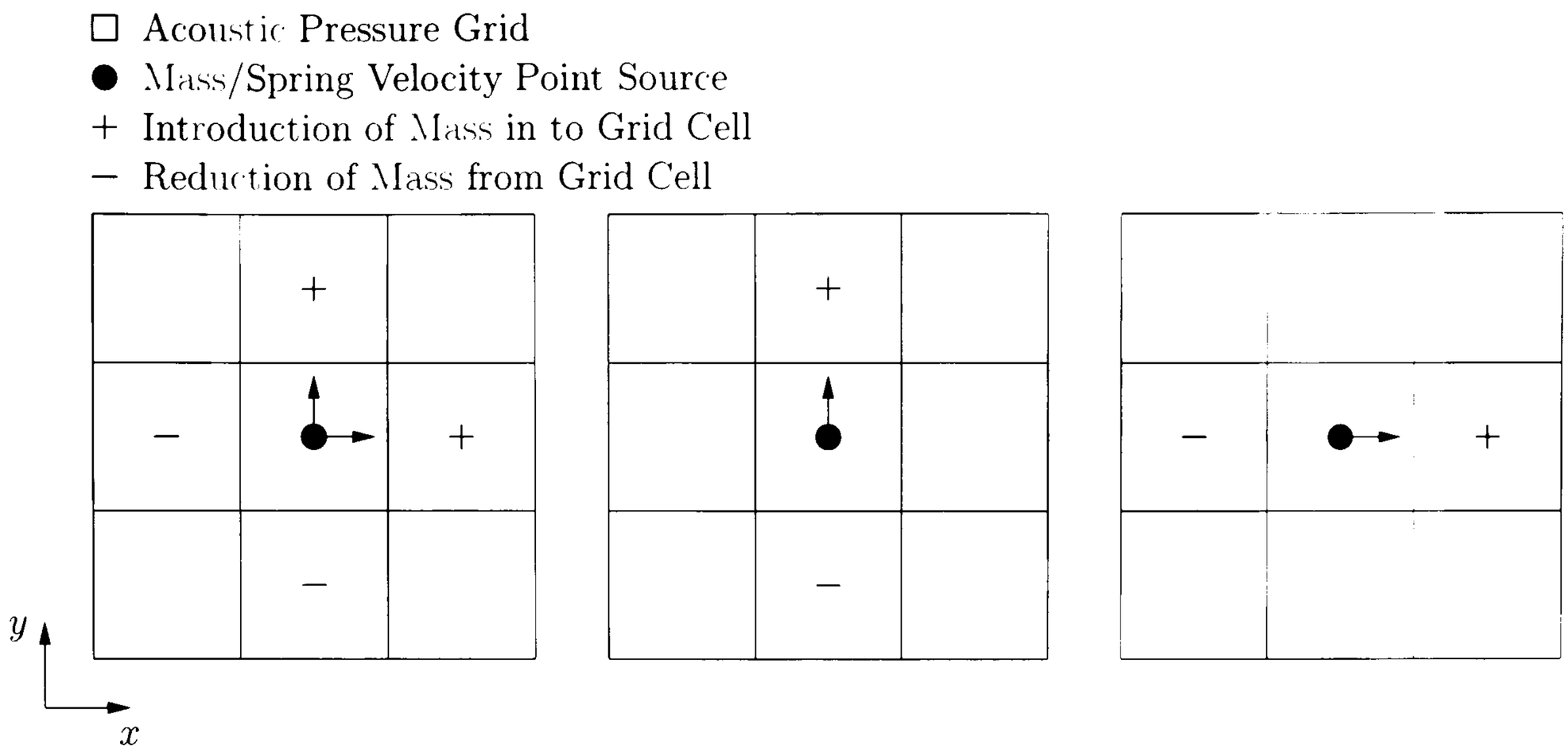

Figure 3.28: Coupling the Mass/Spring Model to the Acoustic Pressure Wave Equation

$$\frac{\partial^2 \mathbf{u}}{\partial t^2} = c^2 \left(\nabla^2 \mathbf{u} - \nabla q + \frac{1}{\bar{\rho}} \frac{\partial \mathbf{F}}{\partial t} \right) \tag{3.4.7}$$

In Equation 3.4.7, the non-zero source term is given by ∇q. The mass/spring model can only offer the displacement, velocity or acceleration of each mass at a particular point. The source term for the particle velocity wave equation requires the gradient of the rate of mass introduction in to the control volume, which means that a velocity field is required. As only velocity point sources are available, it is not possible to readily couple the mass/spring model to the particle velocity wave equation.

3.4.4 Simple Harmonic Oscillator

In this section, the coupling method between the mass/spring model and the acoustic pressure wave equation will be tested using the Simple Harmonic Oscillator (SHO) as shown in Figure 3.3. Table 3.1 states the model parameters and initial conditions of the simple harmonic oscillator. Figure 3.29 compares the normalised acceleration of the SHO to the normalised acoustic pressure wave generated at the acoustic domain, with the resulting

power spectra shown in Figure 3.30. The results show an almost exact coupling between the mass/spring model and the acoustic pressure wave equation.

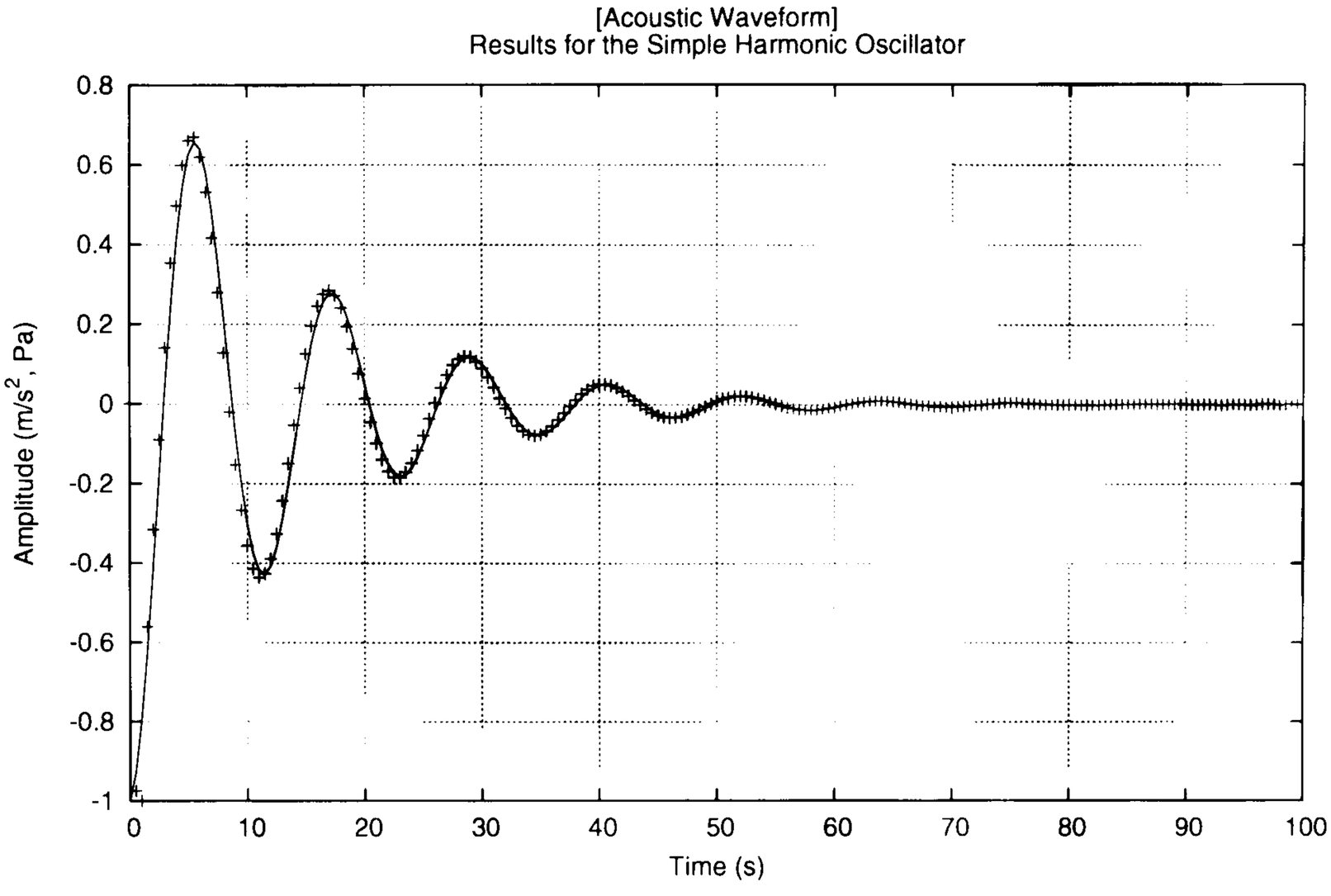

Figure 3.29: Normalised Acceleration/Pressure Results from the Simple Harmonic Oscillator

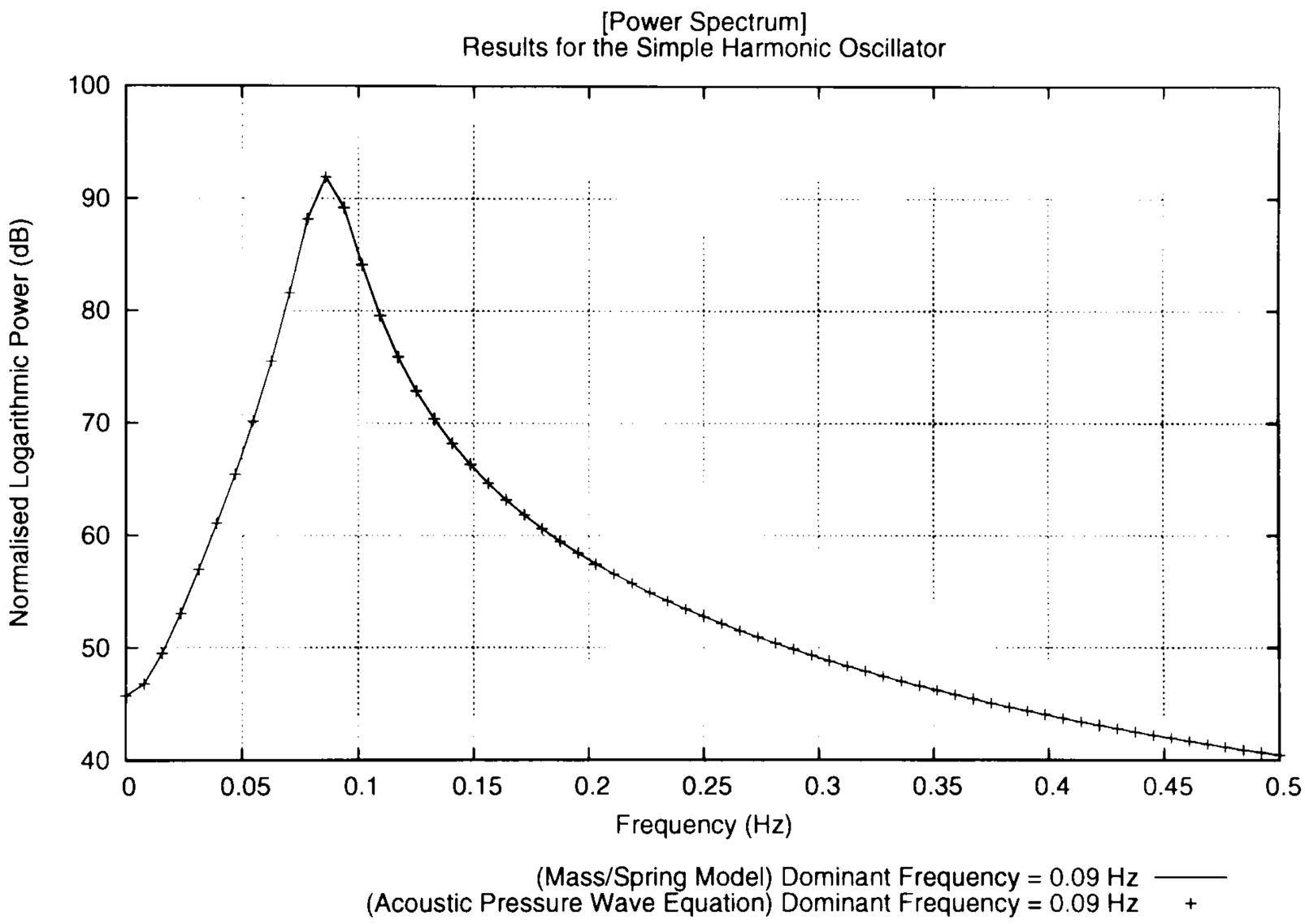

Figure 3.30: Power Spectra of the Simple Harmonic Oscillator

3.5 Results - Validating the Model

3.5.1 Overview

This section will assess the accuracy of the hybrid model by comparing the measured data of two experimental set-ups involving two different materials to the results of their numerical counterparts. The two experimental set-ups involve a tensile force being applied along the length of the rubber band and paper specimen.

3.5.2 Plucked Rubber Band

This section describes a simple experiment that is conducted to validate the accuracy of the model. A rubber band is stretched between two points and then plucked. The resulting AE is recorded using a standard microphone connected to a computer. The microphone is placed directly over the centre of the rubber band as close as possible without interfering with its motion. Table 3.7 states the model parameters and initial conditions of the plucked rubber band.

Model Parameters	
Δt	2.00E-05 s
b	7.00E-04 kg/s
m	1.96E-05 kg
E	8.63E05 Pa
t	1.00E-03 m
w	6.00E-03 m
L	3.40E-03 m
ν	0.144

Initial Conditions			
Mass	$\mathbf{r}^0$ (m)	$\Delta\mathbf{r}^0$ (m)	$\mathbf{u}^0$ (m/s)
(0)[2], 10	[(-)0.0760, 0.00]	[0.00, 0.000]	[0.00, 0.00]
(1), 9	[(-)0.0608, 0.00]	[0.00, 0.002]	[0.00, 0.00]
(2), 8	[(-)0.0456, 0.00]	[0.00, 0.004]	[0.00, 0.00]
(3), 7	[(-)0.0304, 0.00]	[0.00, 0.006]	[0.00, 0.00]
(4), 6	[(-)0.0152, 0.00]	[0.00, 0.008]	[0.00, 0.00]
5	[0.00, 0.00]	[0.00, 0.010]	[0.00, 0.00]

Table 3.7: Model Parameters and Initial Conditions for a Plucked Rubber Band

Figure 3.31 shows the experimental and simulated AE waveforms of the plucked rubber band. Using the experimental data from Figure 3.31(a), an exponential fit is applied to the data of the following form:

[2]The () indicates that Mass 0 is placed at [-0.0760, 0.00] and Mass 10 is placed at [0.0760, 0.00]

$$y = y_0 e^{-\gamma t} \tag{3.5.1}$$

where:

y Amplitude of AE at time t

y_0 Maximum Amplitude of AE

γ Logarithmic Decrement

The data fit gives γ =22.135 Hz. It is assumed that the logarithmic decrement γ is linearly related to the frictional damping coefficient b of Equation 3.2.4 such that:

$$\gamma = \alpha b \tag{3.5.2}$$

where α is the mechano-acoustic attenuation ratio. To calculate α, the rubber band numerical model was run with an estimated value of b = 5.5E-04 kgHz, with the resulting AE having a logarithmic decrement of γ = 17.329 Hz. The damping ratio for the rubber band model can was calculated from Equation 3.5.1 as α = 3.15E04 kg^{-1}. Therefore, the correct frictional damping coefficient for the numerical model that matches the experimental γ = 27.135 Hz is b = 7.0E-04 kgHz, with the resulting AE shown in Figure 3.31(b).

The logarithmic power spectrum for both signals can be seen in Figure 3.32. Figure 3.32 shows a fundamental tone of the experimental AE at 196.29 Hz, with the simulated AE producing a fundamental frequency of 189.21 Hz. With only a 4% difference in the experimental and numerical fundamental frequencies, this suggests that the numerical model is producing sensible results. Rossing [104] states that the n^{th} harmonic of a plucked string has a frequency of $(2n + 1)F$ where F is the fundamental frequency of vibration. Therefore, the first harmonic of the experimental data occurs at 588.87 Hz, and similarly with the numerical data at 567.63 Hz. The experimental data clearly show the first and second harmonics, but the numerical data only shows the first harmonic. This is due to the

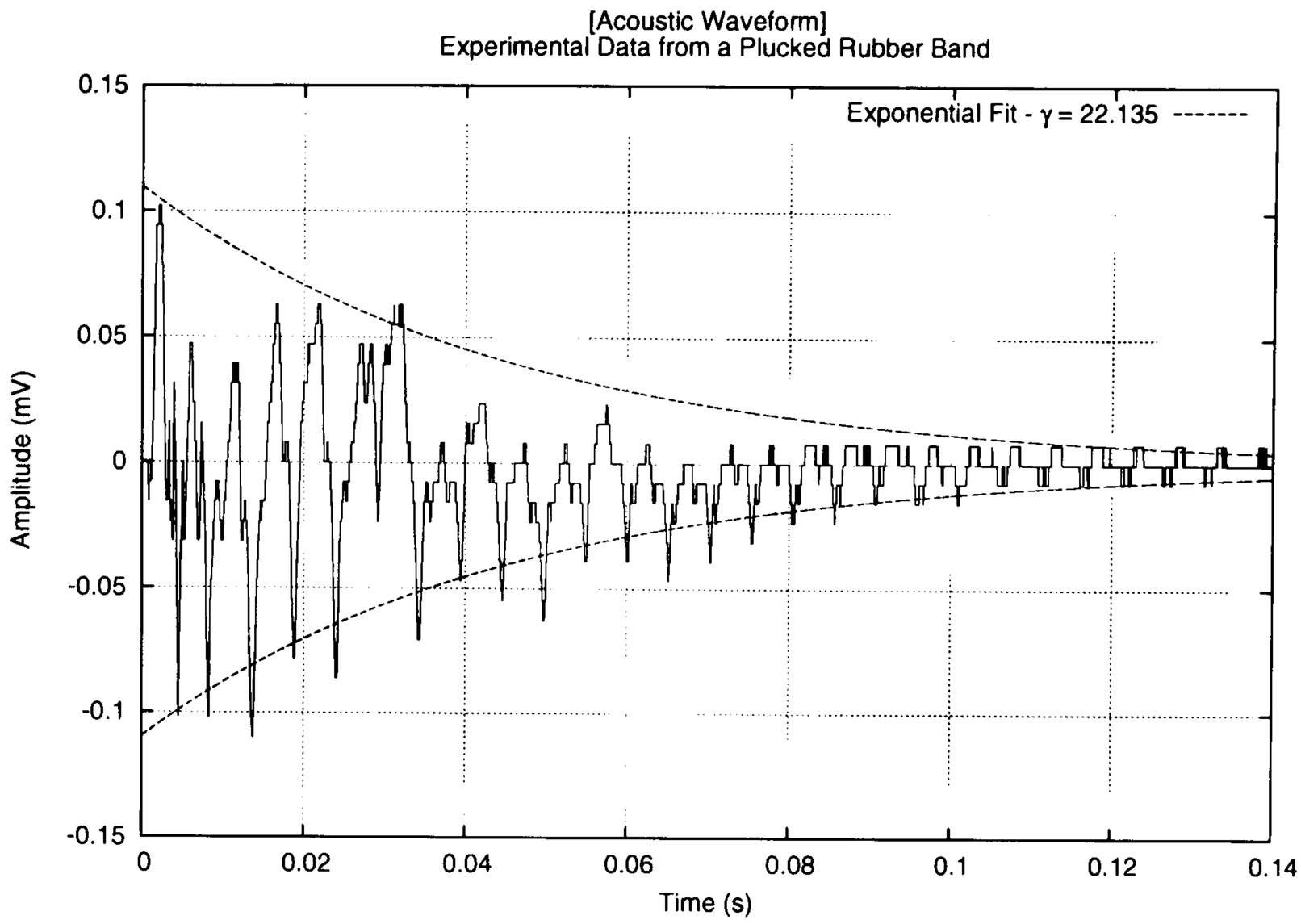

(a) Experimental Acoustic Emission

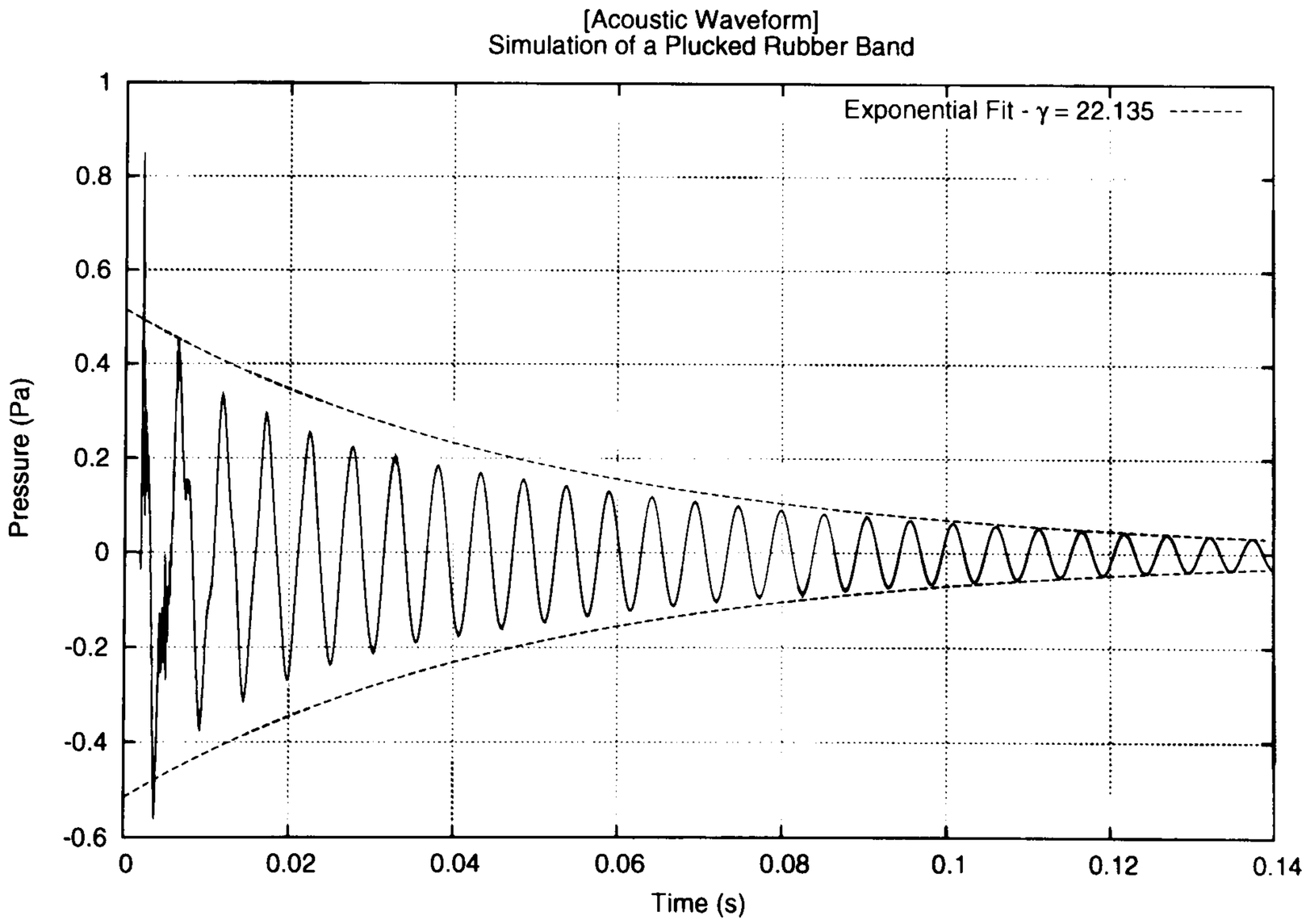

(b) Numerical Acoustic Emission

Figure 3.31: Acoustic Emissions

artificial damping intrinsic to the implicit method affecting the frequency response of the mass/spring system. A detailed analysis of the artificial damping factor can be found in Section 3.2.9.

3.5.3 Notched Paper Sample

The experimental set-up for the notched paper sample involves stretching a 10mm x 100mm paper sample until fracture occurs. The acoustic sensor is located in the centre of the paper sample directly between the two notches. This process releases hundreds of AEs and due to the complexity of the paper, as seen in Figure 3.33, most of the AEs will be complex waveforms. However, a small fraction of the AEs exhibit a sinusoidal waveform and it is thought these AEs are produced from a microscopic region where sufficient de-bonding of the paper fibres has occurred so that the characteristic length of the paper fibre is allowed to freely vibrate.

The simulated AE is produced from a similar same mass/spring set-up as the rubber band with the material properties corrected for paper. Table 3.8 states the model parameters and initial conditions for the plucked paper fibre.

Model Parameters	
Δt	1.00E-08 s
b	1.50E-06 kg/s
m	1.01E-11 kg
E	3.50E10 Pa
t	2.80E-06 m
w	3.50E-05 m
L	7.14E-05 m
ν	0.28

Initial Conditions			
Mass	$\mathbf{r}^0$ (m)	$\Delta\mathbf{r}^0$ (m)	$\mathbf{u}^0$ (m/s)
(0), 14	[(-)5.00E-04, 0.00]	[0.00, 0.000]	[0.00, 0.00]
(1), 13	[(-)4.29E-04, 0.00]	[0.00, 7.14E-07]	[0.00, 0.00]
(2), 12	[(-)3.57E-04, 0.00]	[0.00, 1.43E-06]	[0.00, 0.00]
(3), 11	[(-)2.86E-04, 0.00]	[0.00, 2.14E-06]	[0.00, 0.00]
(4), 10	[(-)2.14E-04, 0.00]	[0.00, 2.86E-06]	[0.00, 0.00]
(5), 9	[(-)1.43E-04, 0.00]	[0.00, 3.57E-06]	[0.00, 0.00]
(6), 8	[(-)7.14E-05, 0.00]	[0.00, 4.29E-06]	[0.00, 0.00]
7	[0.00, 0.00]	[0.00, 5.00E-06]	[0.00, 0.00]

Table 3.8: Model Parameters and Initial Conditions for a Plucked Paper Fibre

Figure 3.34 shows the selected experimental and simulated AE waveforms from the paper sample. Figure 3.35 shows the power spectra for the experimental and numerical

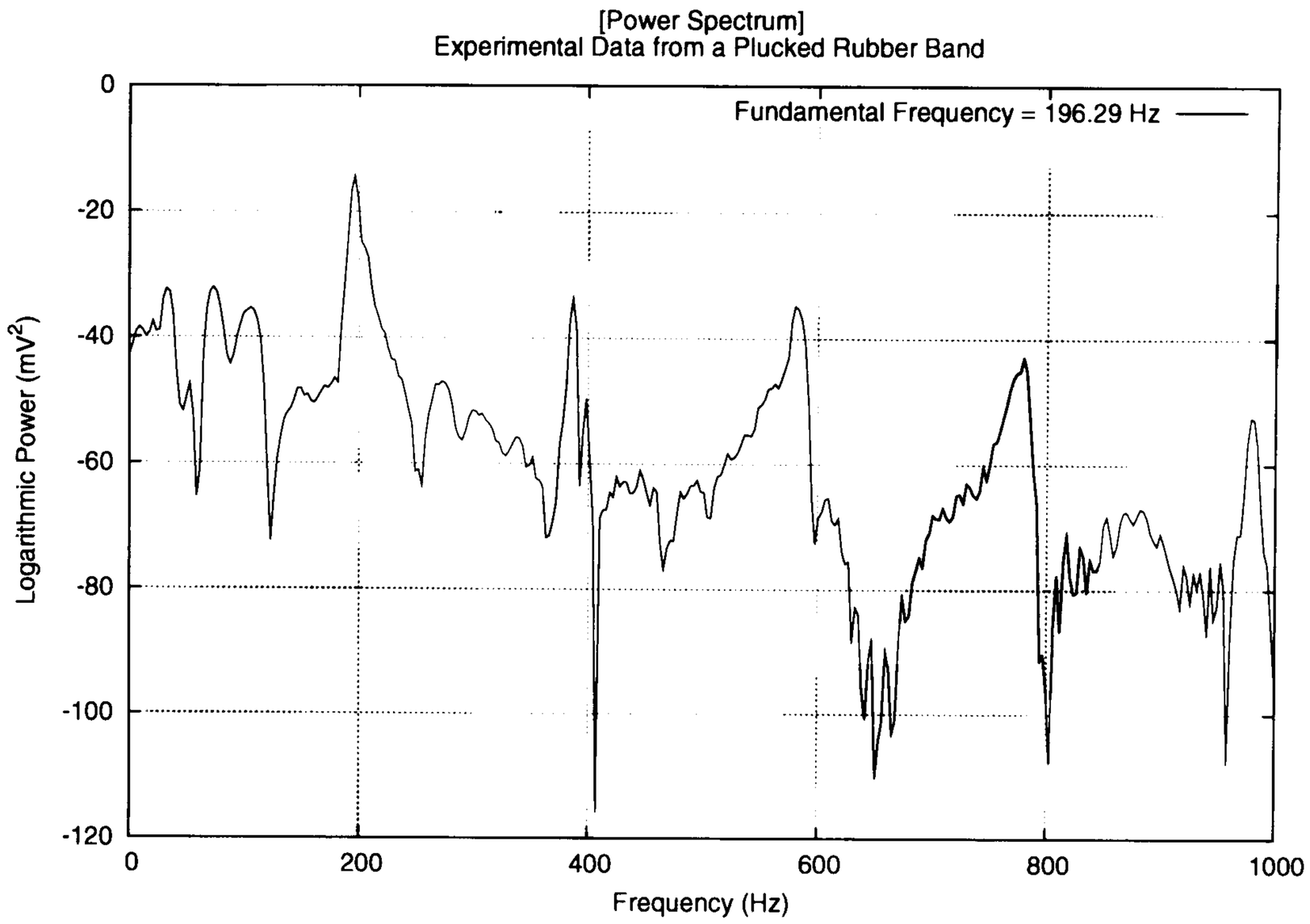

(a) Experimental Acoustic Emission Power Spectrum

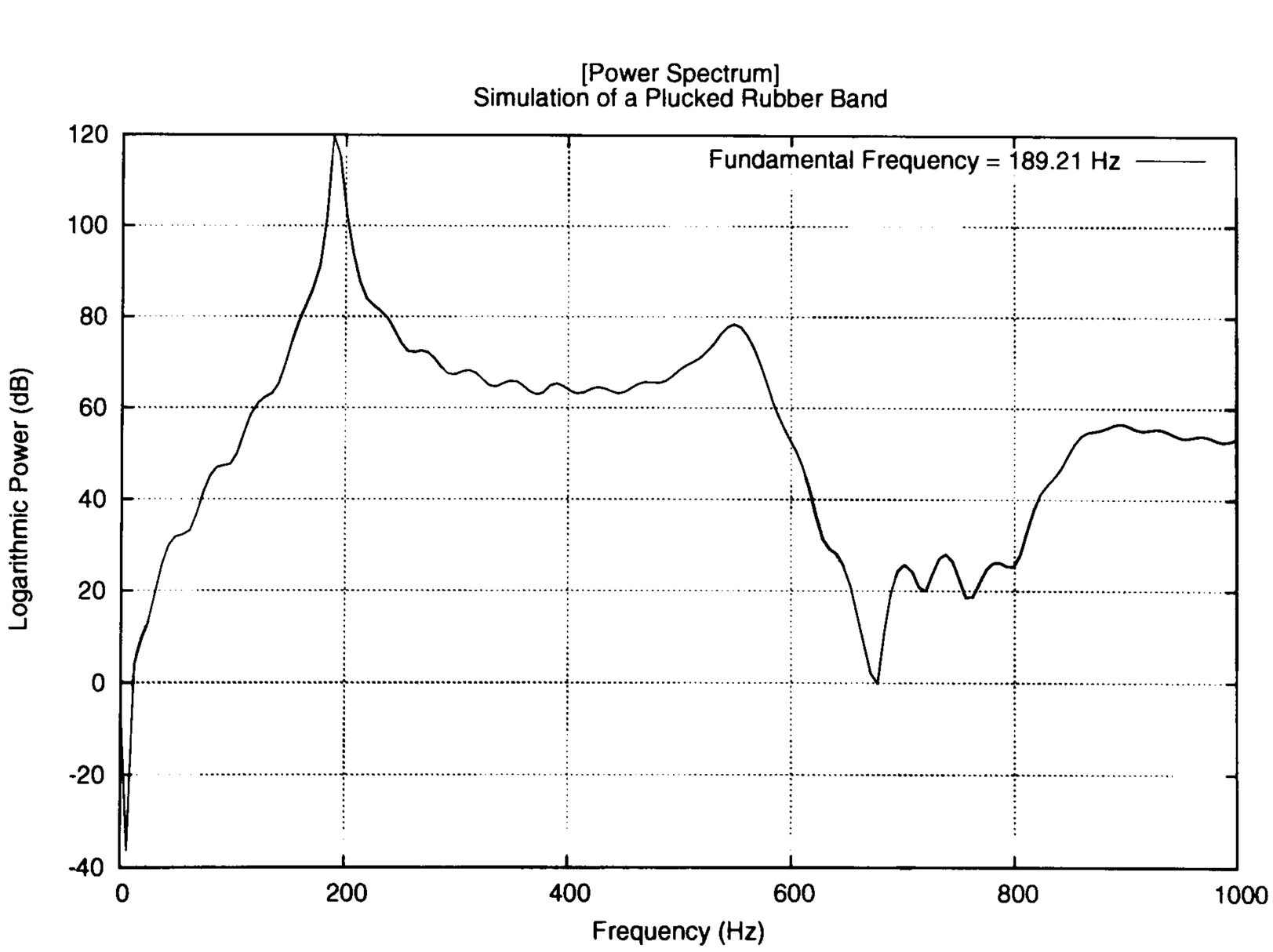

(b) Numerical Acoustic Emission Power Spectrum

Figure 3.32: Power Spectra

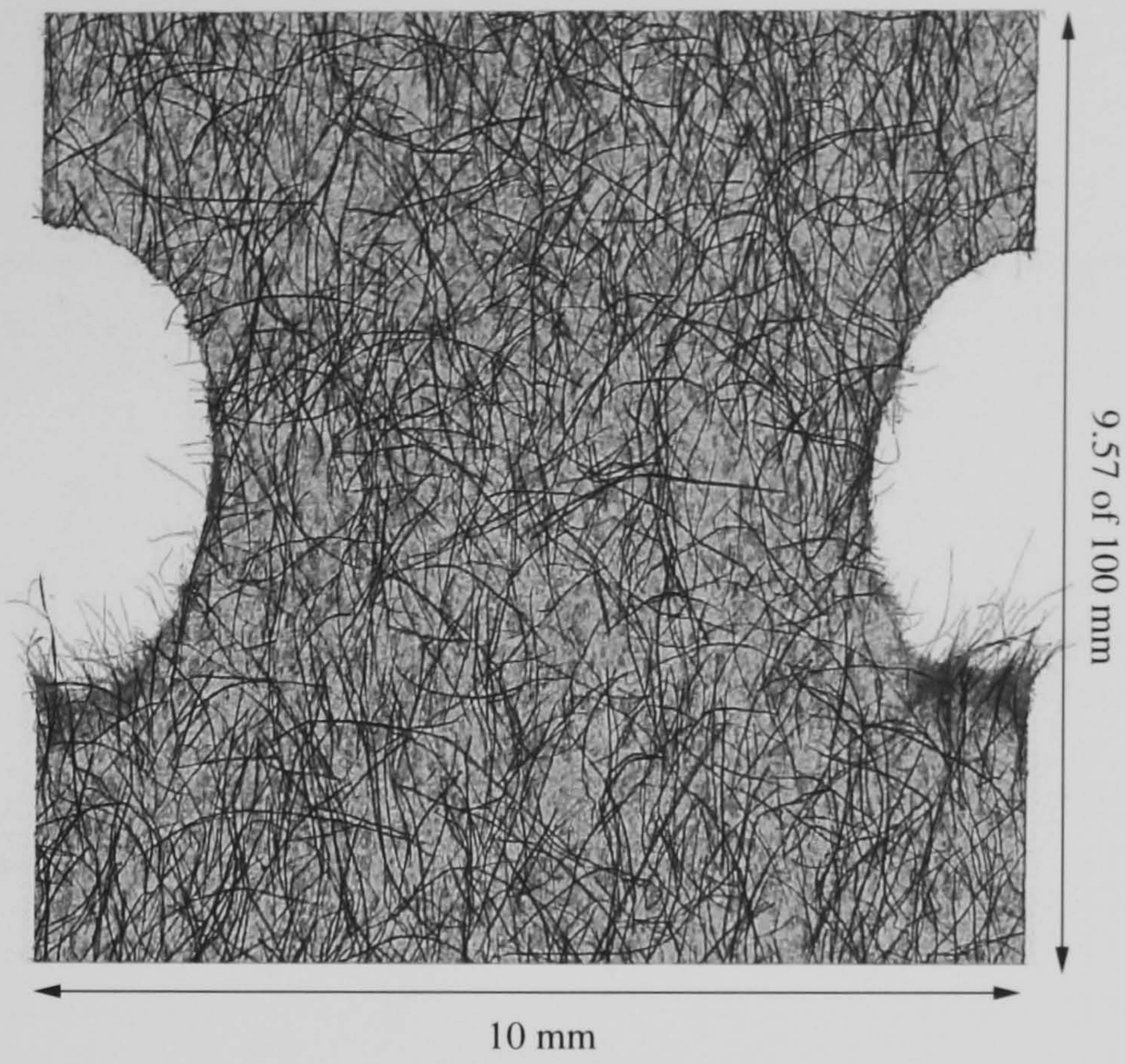

Figure 3.33: Notched Paper Sample

AEs. The fundamental frequency of the experimental AE is shown as 253.91 kHz with the simulated AE also having a fundamental frequency of 253.91 kHz. The results show that the model is correctly predicting the first resonant frequency of the paper fibre.

3.6 Summary

The work presented in this chapter has shown that the mass/spring model and acoustic wave equation are good candidates for use in the simulation of AEs generated from vibrating fibre structures. To achieve the best results, the implicit Euler method must be implemented for solving the equation of motion of the mass/spring system as it overcomes the problems associated with 'stiff' systems. The implicit Euler method also has the advantage of being unconditionally stable irrespective of the time step, giving the best performance among the ODE solvers tested.

The implicit Euler method does have one shortcoming; if the time step chosen for the

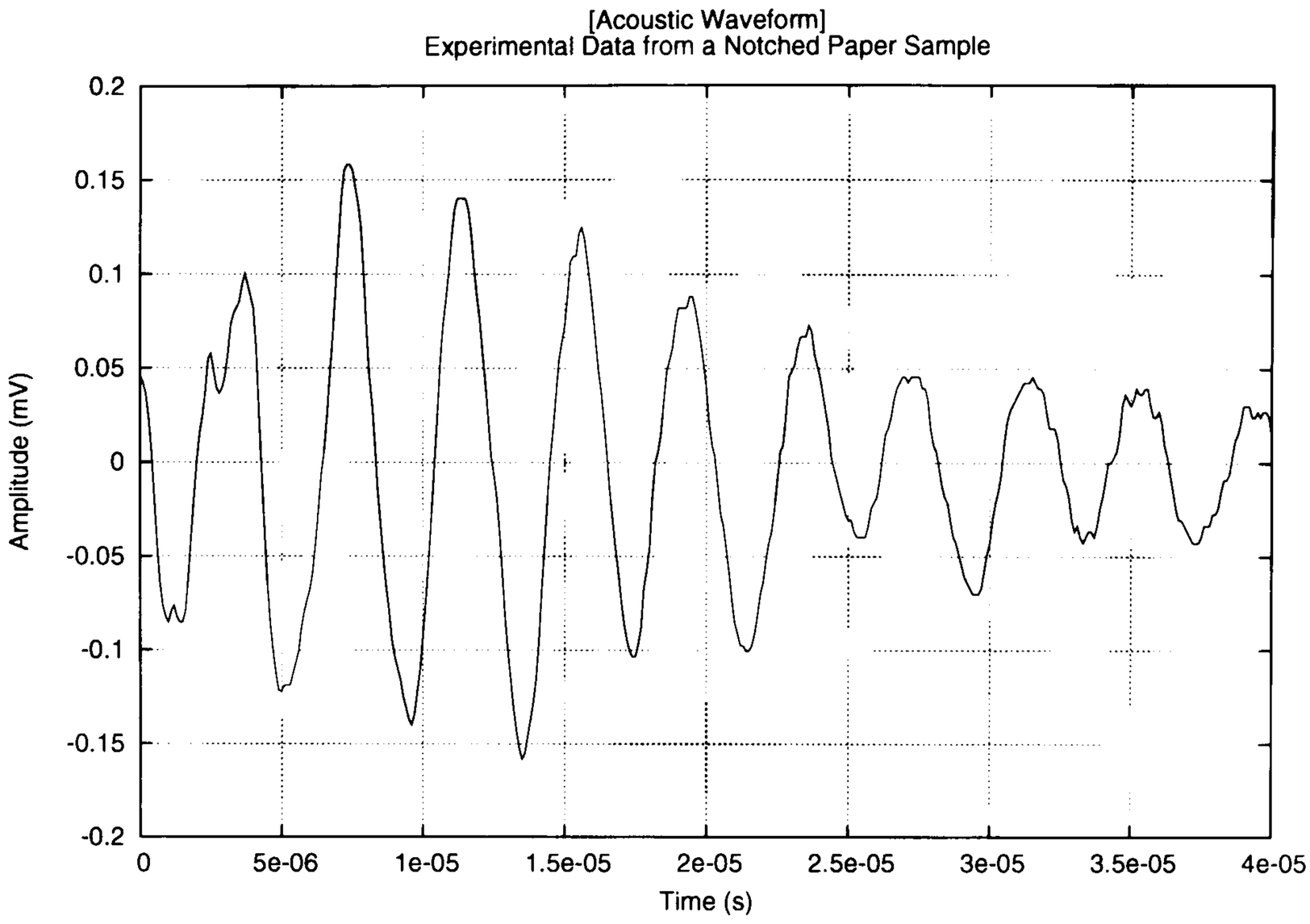

(a) Experimental Data

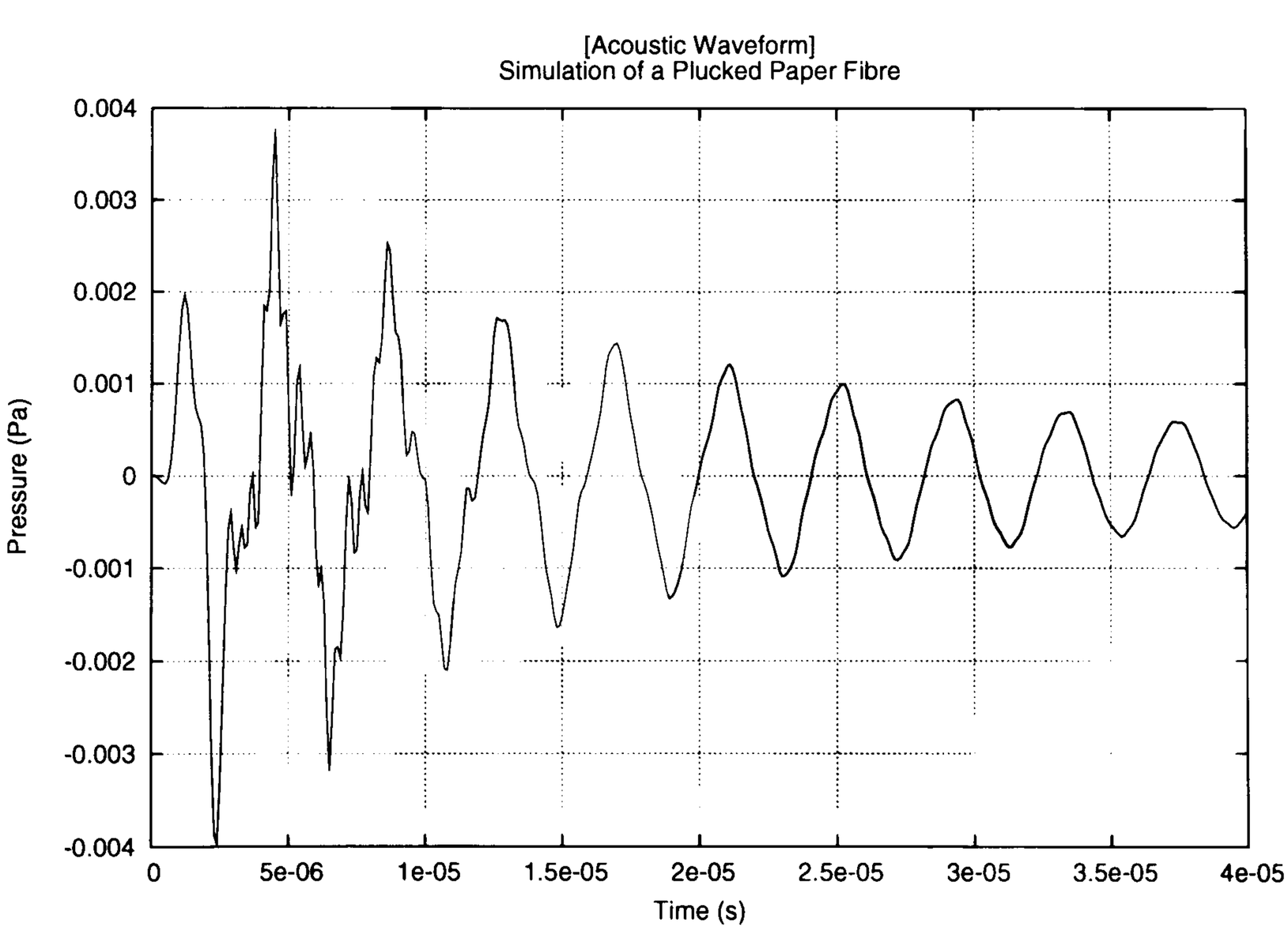

(b) Numerical Data

Figure 3.34: Acoustic Emissions

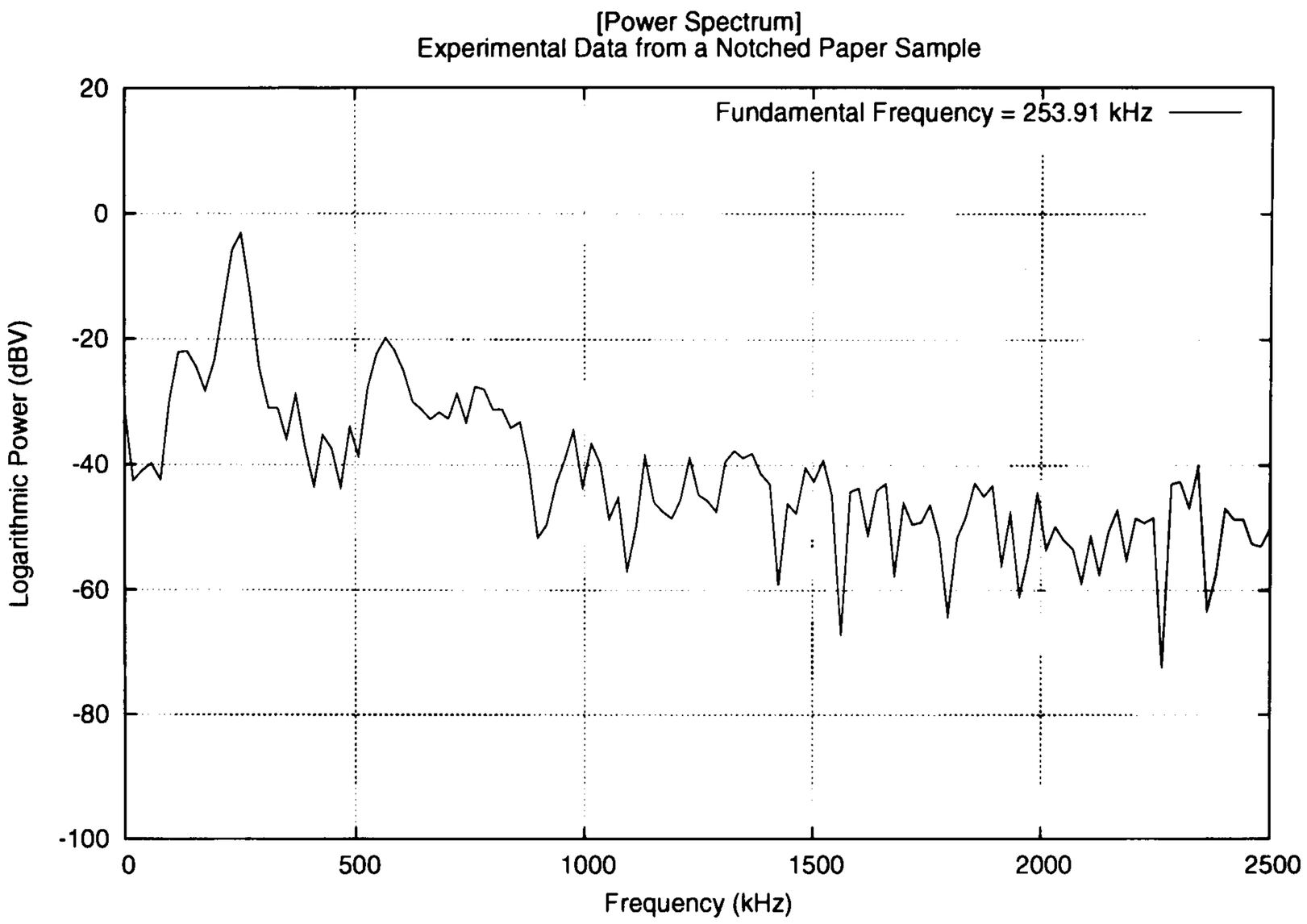

(a) Experimental

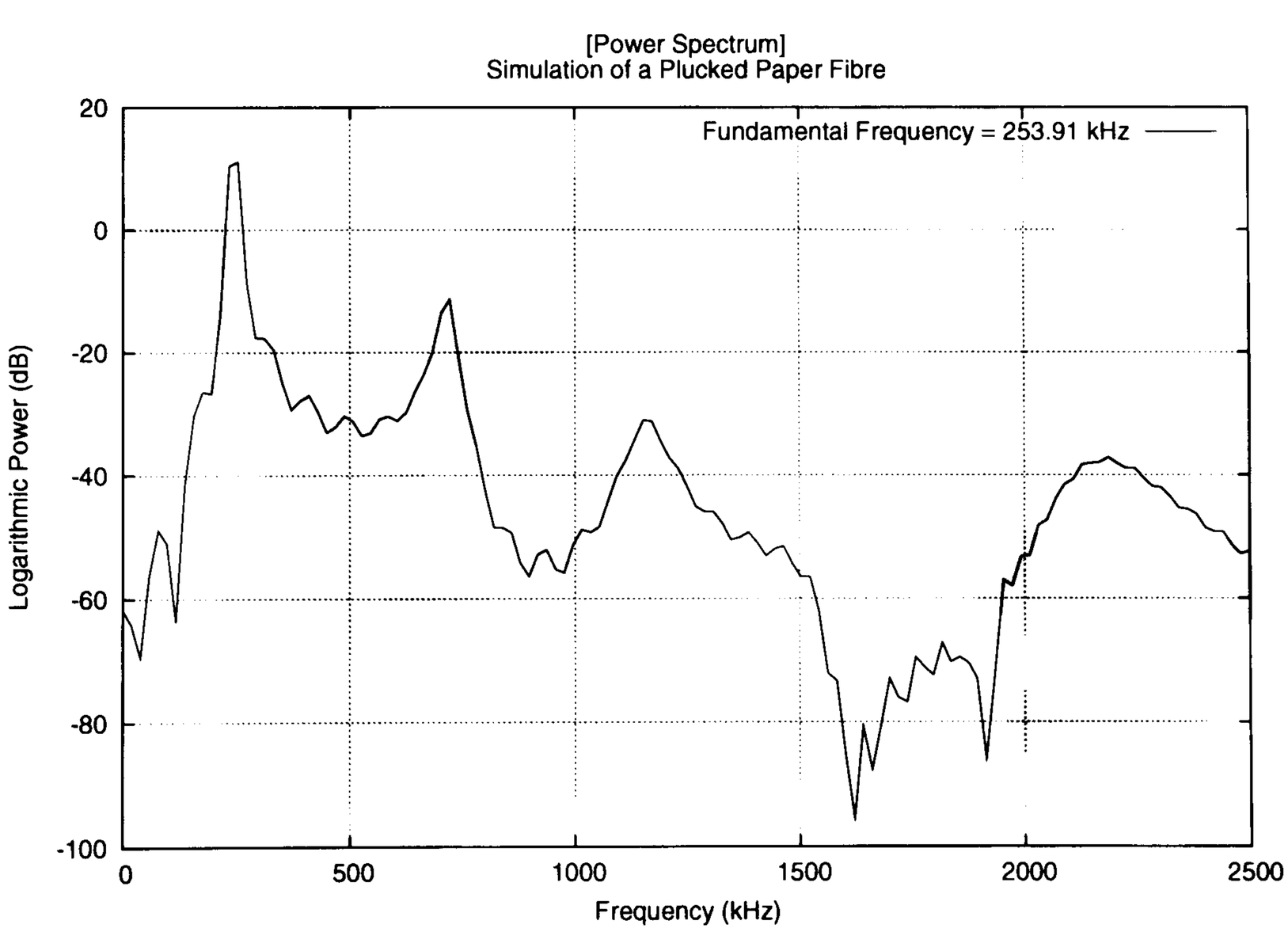

(b) Numerical

Figure 3.35: Power Spectra of the Acoustic Emissions

simulation is too large, the frequency response of the mass/spring model is compromised and will not produce the harmonics of the motion. Using too small a time step will increase the simulation time exponentially, therefore a balance between the frequency response of the mass/spring model and the simulation time must be reached.

The tests for the acoustic wave equation clearly show the advantages of using a fourth order accurate approximation to minimise the errors associated with the discretisation process and the effects of the non-reflecting boundary conditions. It is also important to consider the frequency response of the acoustic wave equation. The time step used in the acoustic wave equation is analogous to the inverse of the sampling rate of a sensor and, as such, the maximum frequency (Nyquist frequency) of the recorded signal is governed by the Nyquist's Sampling Theorem:

$$f_N = \frac{1}{2} f_s \quad \text{where:} \quad f_s = \frac{1}{\Delta t} \tag{3.6.1}$$

where:

f_N Nyquist Frequency

f_s Sampling Rate

Δt Time Step of the Simulation

The sampling rate of the sensors used in recording the experimental data is 10 MHz [114], which means the theoretical maximum frequency that is captured is 5 MHz, therefore the time step used for the acoustic wave equation must be Δt = 1E-07s. In practise, the sensors provide an optimal response within the frequency range of 500 - 800 kHz and are able to capture signals with a frequency range of 100 - 2500 kHz [115].

The results for the plucked rubber band and the paper fibre show that the fundamental frequency of the numerical data is within 3% of the fundamental frequency of the experimental data. This shows that the hybrid model is providing sensible results and is ready to be challenged with more complex fibre structures.

Chapter 4

Acoustic Evidence of the Damage Mechanisms

4.1 Overview

The following chapter will present the classical relationship describing the frequency of a plucked string to its material properties, as shown in Equation 4.2.2. Using this relationship, the assumptions connected with each material property are then presented. Having justified the assumptions used in generating a numerical representation of the microscopic structure of the paper, the numerical model is then used to simulate the vibration of a range of simple fibre structures when undergoing the two types of damage mechanisms.

The numerical results are then analysed to determine whether there is any detectable difference between the resulting AEs of the two damage processes. It is important to note that these results will only provide a very basic understanding of the micro-mechanics of the paper; partly due to the two dimensional approximation of the model and the simplified structures it is used to model. However, it will be shown that the results will still provide important information in the identification of the damage mechanisms.

4.2 Frequency Relationship

The frequency produced by a vibrating string is dependent on the tension within the string and the linear density of the string. In terms of the mass/spring model, it leads to:

$$F \propto \frac{T}{m} \tag{4.2.1}$$

Using $T = -kx$ given by Hooke's law and substituting k with Equation 3.2.5, the frequency relationship can be expressed by the paper fibre physical parameters and its strain.

$$F \propto \frac{Et_s w_s x}{Lm} \tag{4.2.2}$$

where:

E Young's Modulus of the Paper Fibre

t_s Thickness of the Paper Fibre

w_s Width of the Paper Fibre

x Displacement of the Paper Fibre from Equilibrium

L Free Vibrating Length of the Paper Fibre

m Mass of the Paper Fibre

Using Equation 4.2.2, it is possible to predict how the changes in the fibre properties due to the two damage mechanisms affect its frequency of vibration. The following sections will address the assumptions associated with each variable of Equation 4.2.2 and investigate the mechanics of a fibre/fibre bond failure and a fibre failure respectively.

4.3 Assumptions of the Fibre Structure

4.3.1 Overview

To successfully model the acoustic response of the damage mechanisms, several assumptions regarding the fibre structure and individual fibre properties must be properly described. There are four assumptions presented below, each dealing with different aspects of the relationship given in Equation 4.2.2.

4.3.2 Free Vibrating Length of a Paper Fibre

Figure 4.1(a) shows a typical undamaged paper sample with Figure 4.1(b) showing the same paper sample post failure. Figure 4.1(c) shows a second undamaged paper sample with Figure 4.1(d) showing the second paper sample at 98% of the load required for failure of the first paper sample. The paper samples have been created so that 5% of the fibres have been dyed. The images have been filtered to enhance the definition of the fibres.

Figure 4.1(d) clearly shows two opaque regions next to the middle of each notch on the paper sample. The opaque regions highlight where damage of the fibre structure has already occurred and shows that the length of the damage area is not greater than 1 mm. Therefore it is assumed that the fibre structure outside of the damage zone remains undamaged suggesting that no plastic deformation of the fibre structure has occurred here. If no deformation has occurred then the fibre structure outside of the damage zone can be thought of as having an infinite mass for dynamic modelling purposes. This leads to the first assumption that the maximum free vibrating length of a paper fibre in the damage zone is equal to 1 mm.

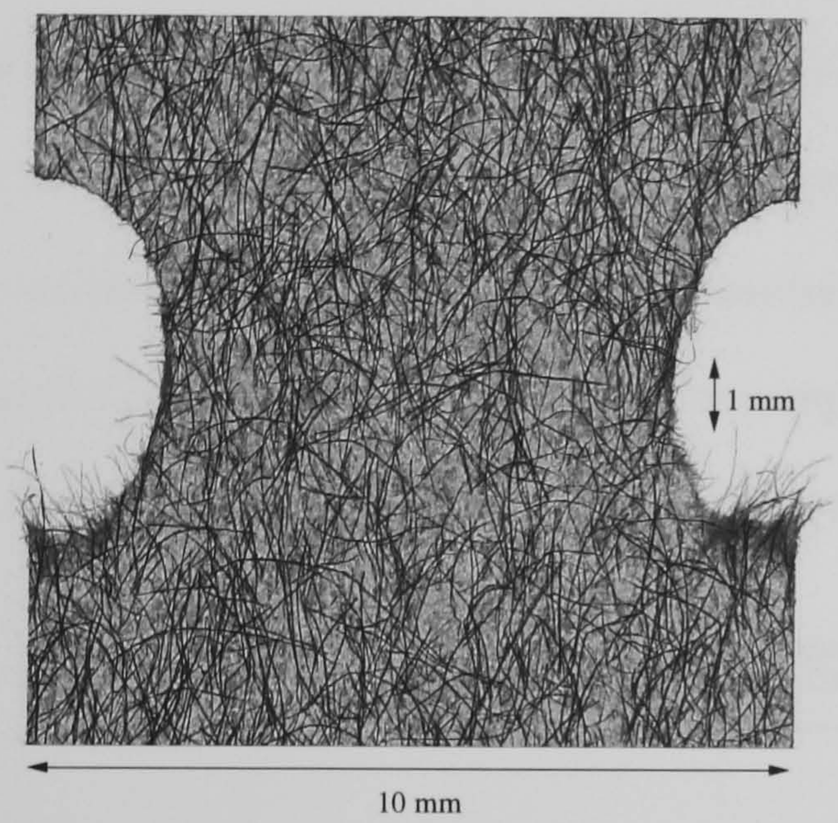

(a) Undamaged Paper Sample 1 at Zero Load

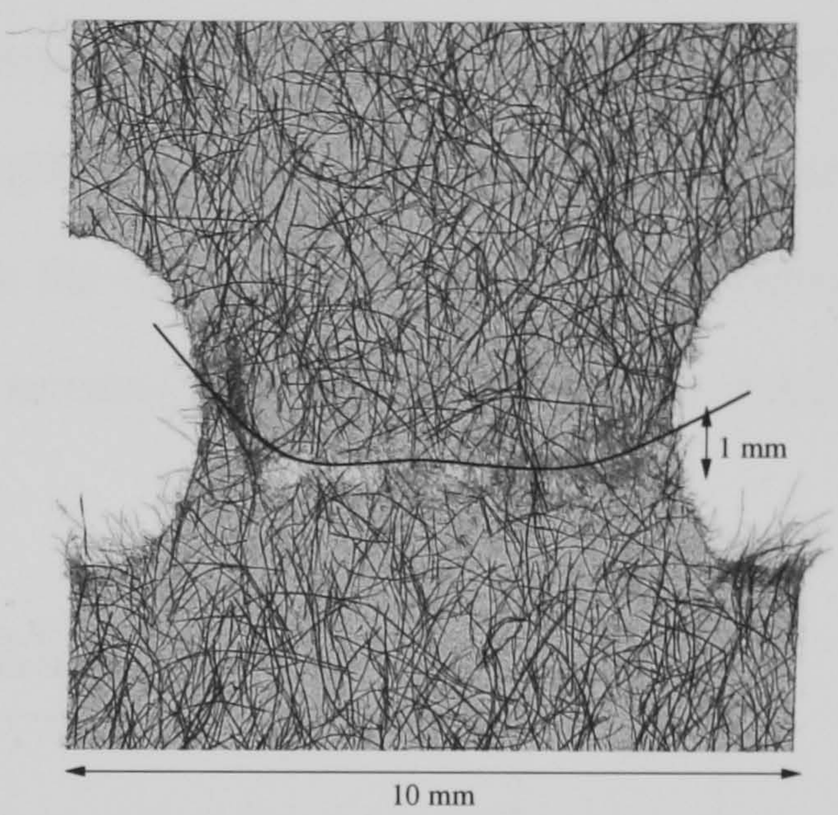

(b) Failure of Paper Sample 1

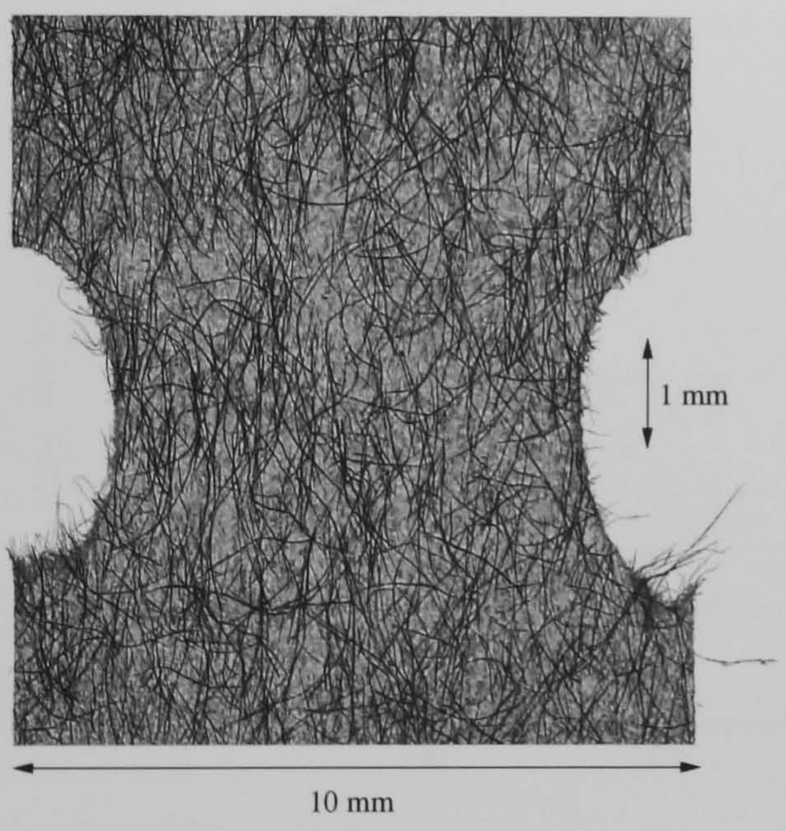

(c) Undamaged Paper Sample 2 at Zero Load

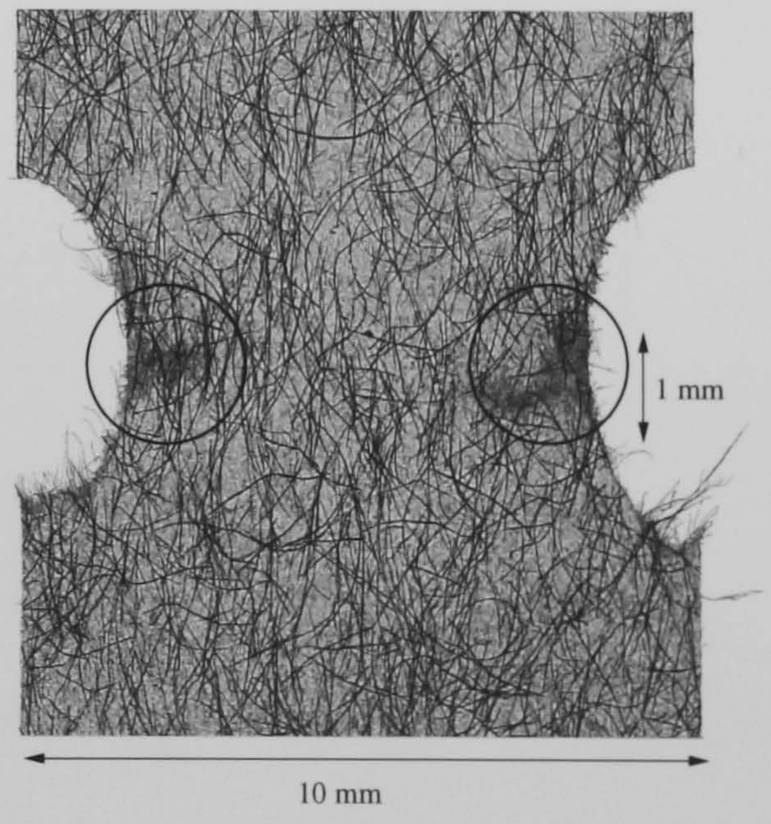

(d) Paper Sample 2 at 98% of Failure Load

Figure 4.1: Details of the 10 mm x 10 mm Central Section of the 10 mm x 100 mm of 2 Paper Samples under Varying Degrees of Load

4.3.3 Extension of the Paper Fibre

Figure 4.2 shows the extension of the paper specimen versus the AE number. The paper sample has a length of 100 mm which undergoes a maximum extension of approximately 0.85 mm. This equates to approximately 1% of the length of the paper sample. For simplicity, it is assumed that the paper is constructed from a Cartesian mesh of fibres so that an extension of 1% in the macroscopic length of the paper is equal to an extension of 1% in each fibre. Therefore, it is assumed that the damage zone will also experience an extension of 1% of its length. This assumption remains valid as long as the size of the side notches is small compared to the sample width.

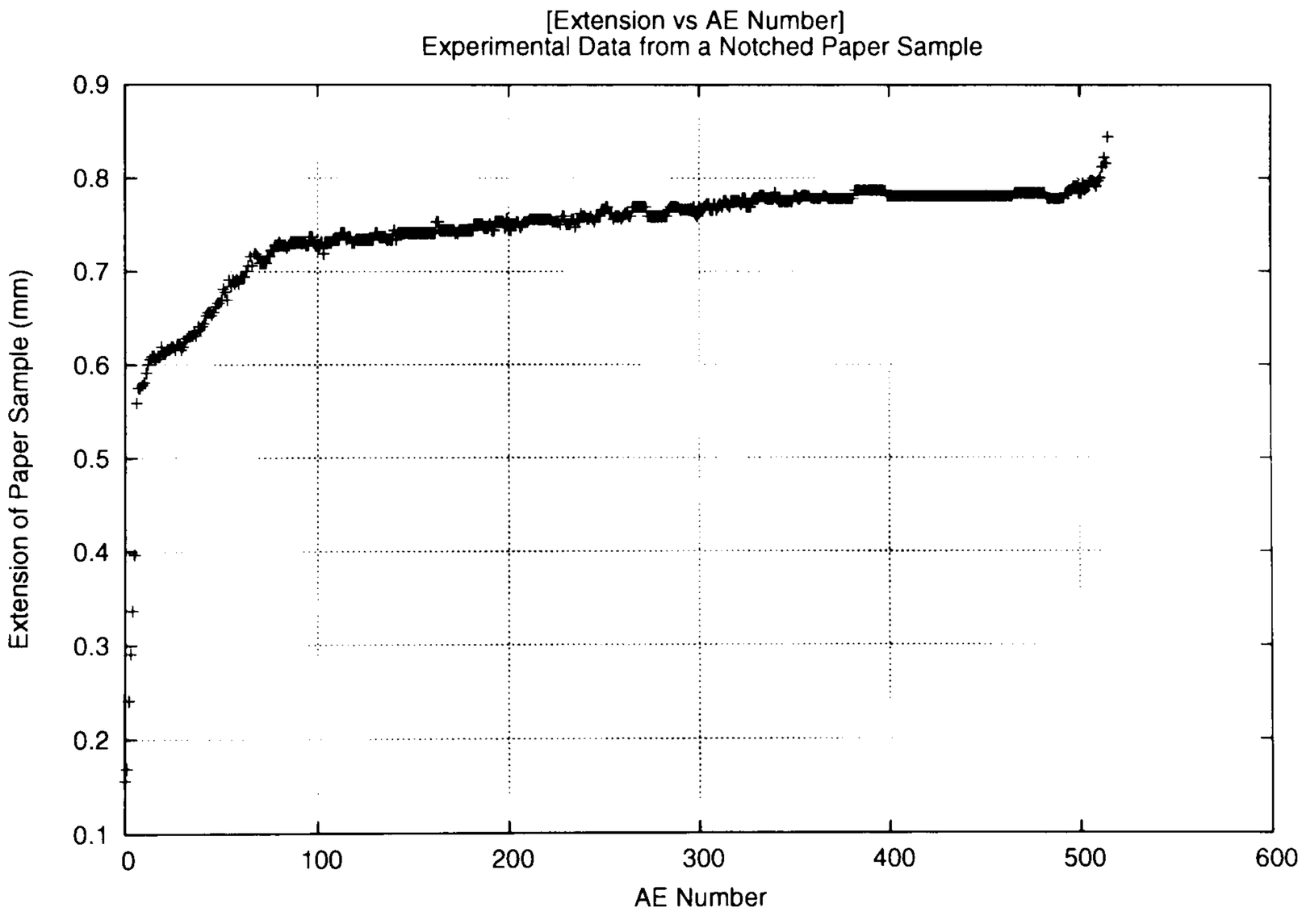

Figure 4.2: Extension of a Typical Paper Sample

4.3.4 Material Properties of the Paper Fibre

The previous two sections have dealt with the variables L and r from Equation 4.2.2 respectively. This section will define values for the remaining material properties specified

in Equation 4.2.2. Due to the collaborative nature of this EU project, the material properties of the paper fibre were obtained from the project partner with particular expertise in the paper physics field [116].

Material Property	**Value**	**Average Value**
Young's Modulus	30 - 80 GPa	35 GPa
Fibre Length (Chemical)	< 4 mm	3 mm
Fibre Thickness	2 - 6 μm	2.8 μm
Fibre Width	30 - 40 μm	35 μm
Fibre Density	1.5 g/cm^3	1.5 g/cm^3
Poisson Ratio	0.28 - 0.29	0.28

Table 4.1: Material Properties of a Fibre

For all simulations, unless otherwise stated, the average values of the material properties are used. The fibre length as stated in Table 4.1 is different to the free vibrating length as discussed in Section 4.3.2. The connectivity of the fibre structure ensures that the free vibrating length is always less than the average fibre length.

4.3.5 Degrees of Freedom of the Paper Fibre

This final section addresses the need for approximating the number of degrees of freedom a fibre has. This encompasses the ability of the vibrating paper fibre to accurately represent its harmonic frequencies as well as the freedom the fibre has when it is connected to a larger structure. Rossing [104] states that the frequency F_n of the n^{th} harmonic of a plucked fibre is given by:

$$F_n = (2n+1)F \quad n = 0, 1, 2, \ldots \tag{4.3.1}$$

where F is the fundamental frequency of vibration. Figure 4.3 shows the minimum number of free masses required to produce the fundamental frequency and first two harmonic frequencies of a plucked fibre.

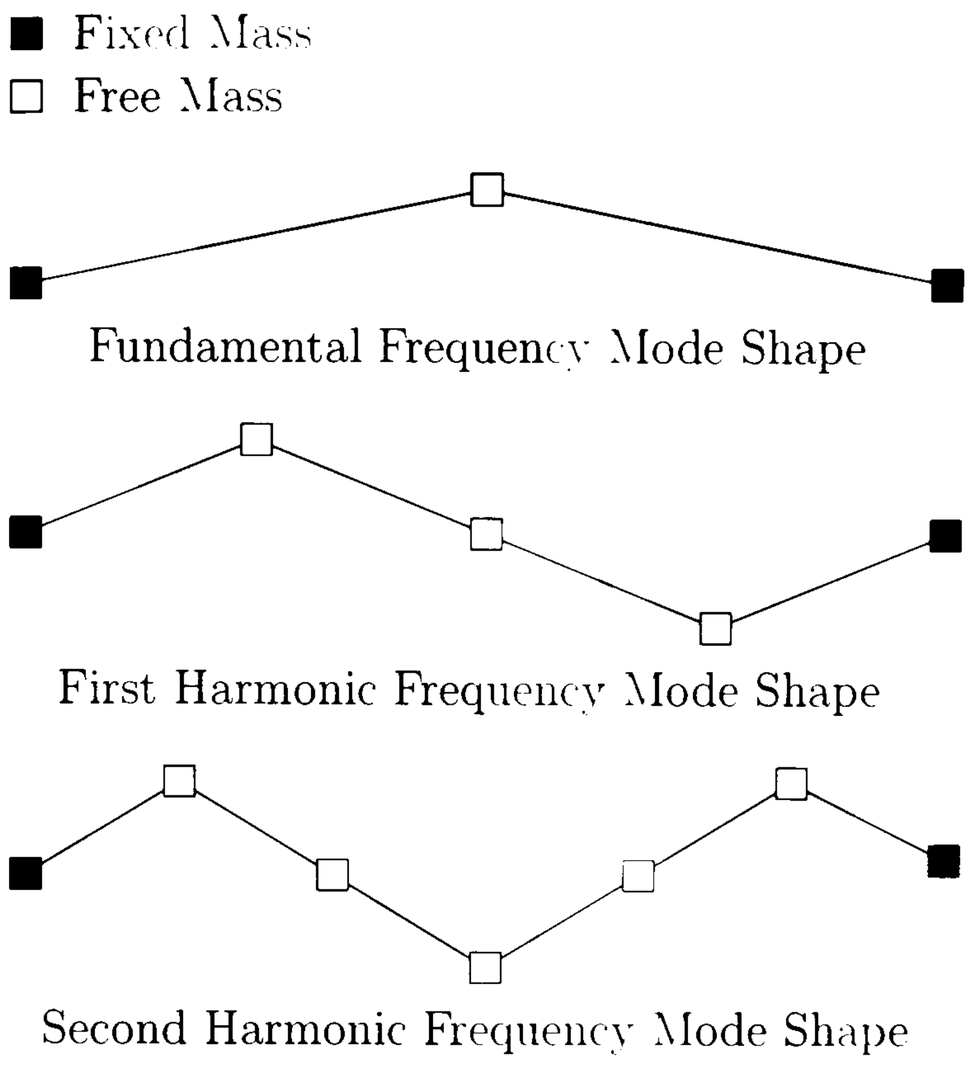

Figure 4.3: Mode Shapes for the Fundamental Frequency and First 2 Harmonic Frequencies

Figure 4.3 shows that the number of masses required to reproduce the n^{th} harmonic is:

$$m = (2n + 1) \quad n = 0, 1, 2, \ldots \tag{4.3.2}$$

where m is the number of masses. Figure 4.4 highlights the need for enough masses to allow for sufficient movement between two fibre/fibre bonds. Figure 4.4(a) shows a rigid system where there are no degrees of freedom between two fibre/fibre bonds, with Figure 4.4(b) showing a loose system where there is one degree of freedom between two fibre/fibre bonds.

It is also important to note that if there are too few masses, the error in the displacement of the mass along the length of the fibre becomes greater, resulting in an unrealistic vibration. Therefore, unless otherwise stated, each fibre will be approximated by 29 masses and 28 springs. This number of masses and springs allows for a good level of accuracy at an acceptable computational expense.

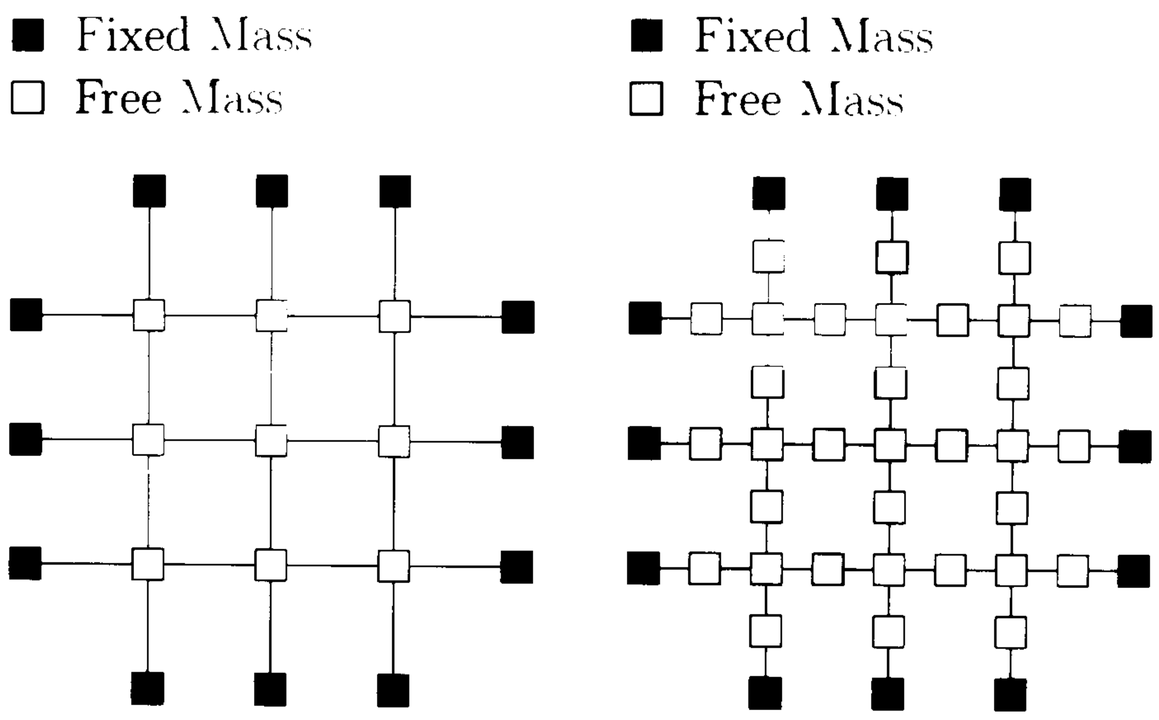

(a) Rigid 3x3 Cartesian Mesh (b) Loose 3x3 Cartesian Mesh

Figure 4.4: Degrees of Freedom in a 3x3 Cartesian Mesh

4.4 Acoustic Evidence of a Vibrating Fibre

This section will investigate the frequency generated from the vibration of the middle section of a single fibre within the damage zone. This will determine the fundamental frequency of the vibration of the free section of the fibres within the damage zone. Figure 4.5 shows the model used for the simulation of the vibrating free section of the fibre.

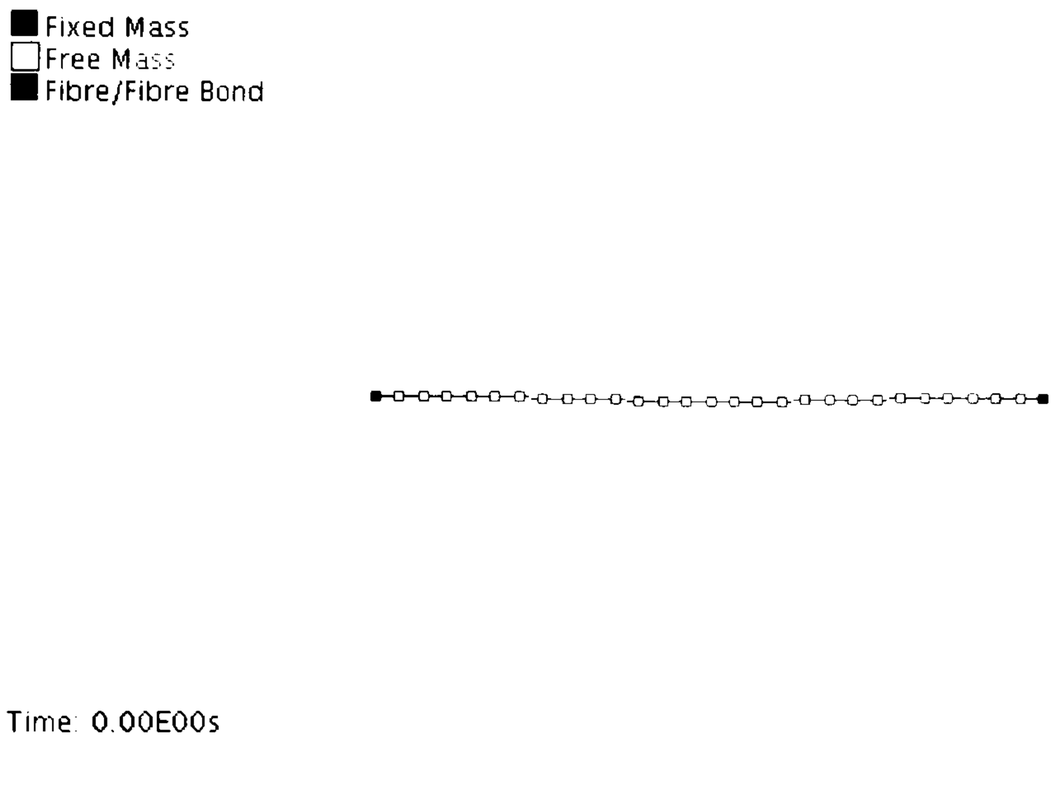

Figure 4.5: Vibrating Fibre Unit Cell

Figure 4.6(a) shows the AE generated from the simple harmonic motion of the single fibre. Figure 4.6(b) shows the Continuous Wavelet Transform (CWT) of the AE. The wavelet software is provided by Vallen Systeme [46] and is based on the work by Takemoto

[47] and Suzuki [48].

The fundamental frequency of vibration for the single fibre is given as 253.91 kHz as shown by the dark spot maximum in Figure 4.6(b). Using the frequency relationship given in Equation 4.2.2 it is possible to use the numerical model to calculate the fundamental frequency for a range of single fibres with varying material properties. The subsequent frequency relationship map can be seen in Figure 4.7.

Figure 4.7 only uses a range of $\pm$ 10% of the average value of the material properties given in Table 4.1. This suggests that there is a wide range of fibres with differing material properties that will produce any given frequency. However, if the range of $\pm$ 10% of the average value of the material property is accurate enough to encompass the majority of the fibres, the change in the frequency response is limited to less than $\pm$ 150 kHz. Therefore, if the changes in the fibre structure due to the damage mechanisms shift the structure's frequency response by more than 150 kHz, the damage mechanisms should be distinguishable. It will be shown in the forthcoming sections that there is little need for concern in using the average material properties of the paper fibre as the two types of damage mechanisms can be identified from different shapes and frequency ranges in the CWT.

4.5 Acoustic Evidence of a Fibre/Fibre Bond Failure

4.5.1 Predicting the Change in Frequency of Vibration of a Fibre Structure as a Fibre/Fibre Bond Failure Occurs

Consider the 3x3 Cartesian mesh shown in Figure 4.8. Where two fibres overlap, it assumed that they are bonded by a fibre/fibre bond. As the mass/spring model approximates the fibre's mass to particular points, the fibre/fibre bonds are restricted to forming where the masses from two fibres overlap. The mass of the fibre/fibre bond is the sum of the

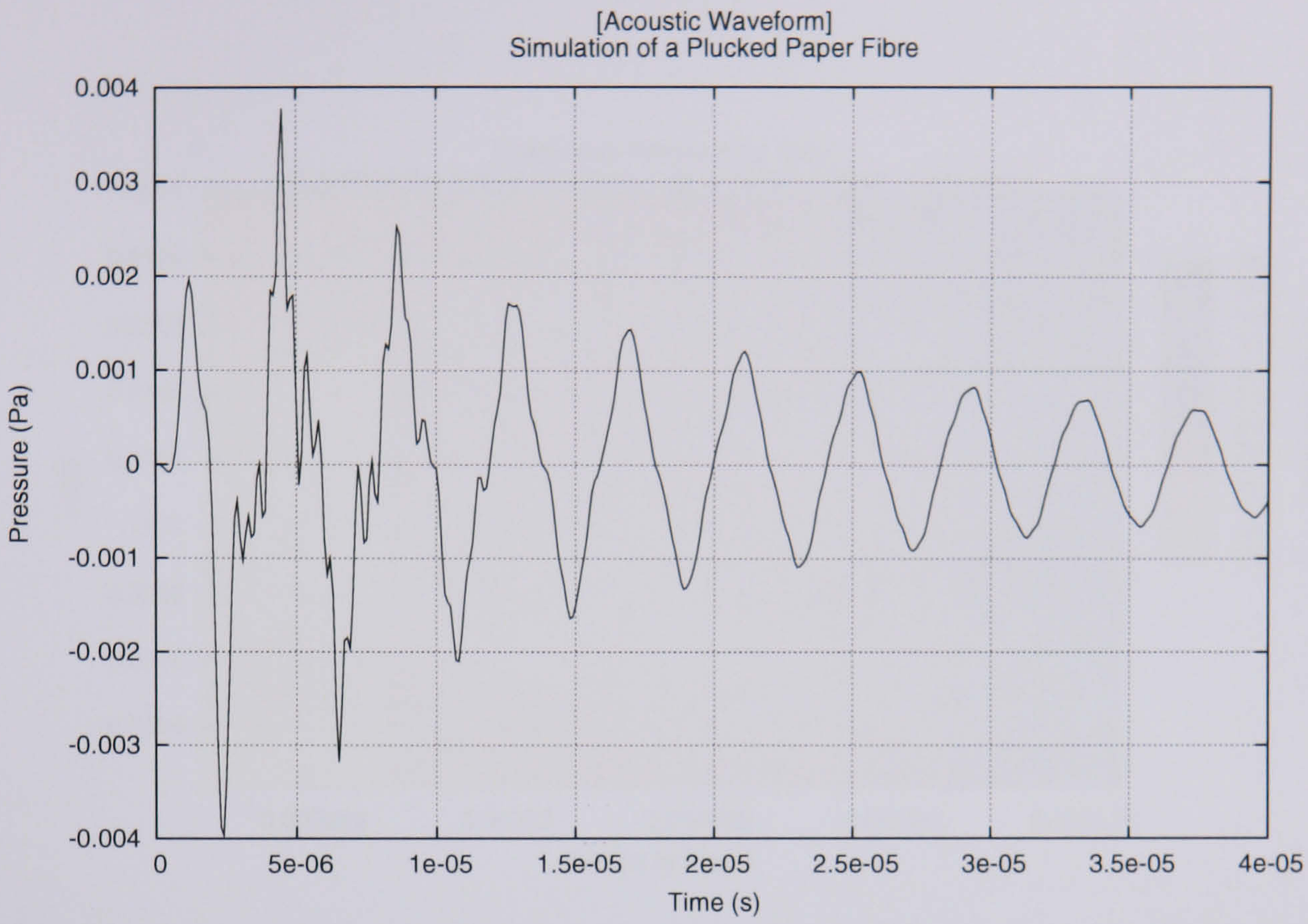

(a) Acoustic Waveform

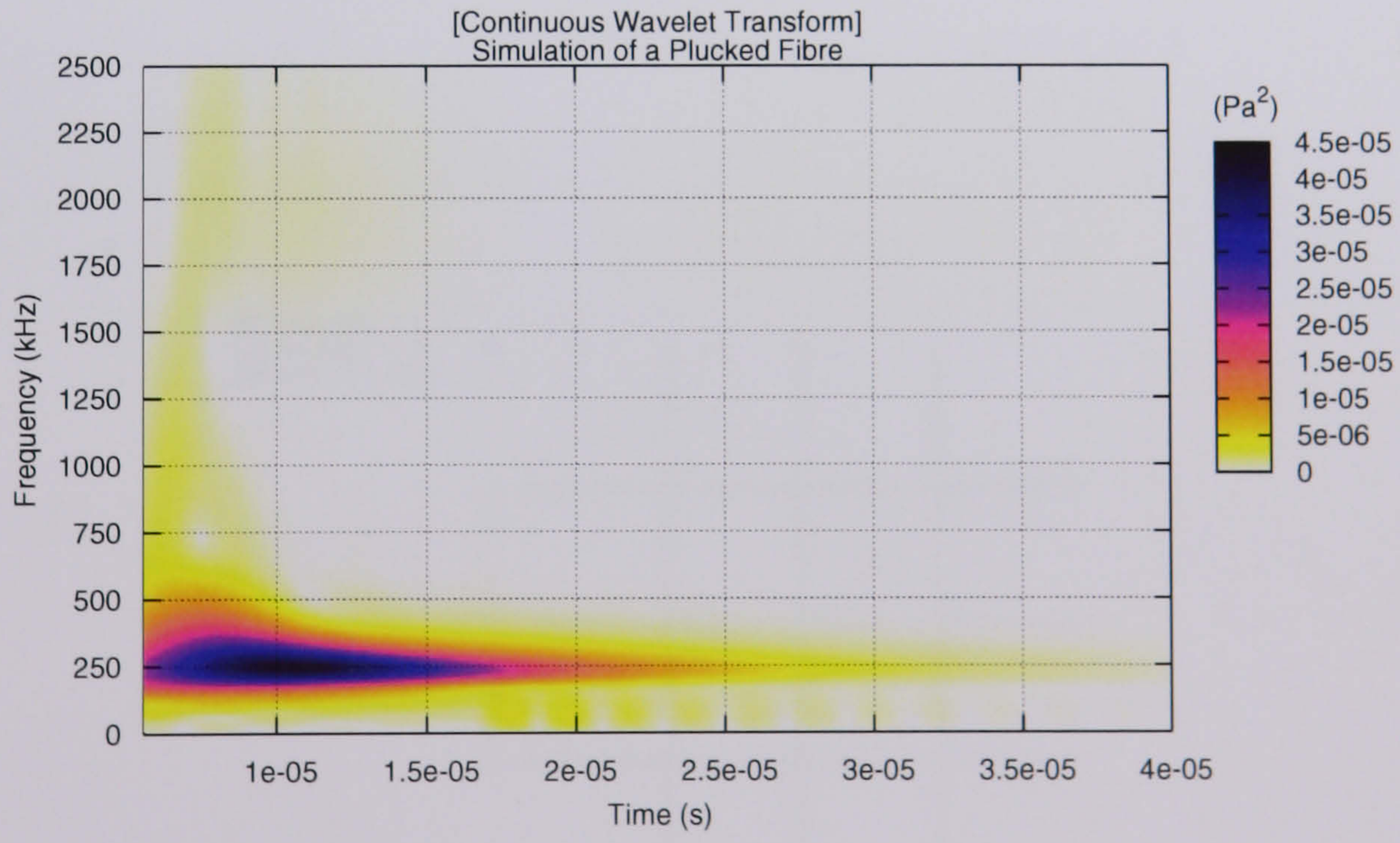

(b) Continuous Wavelet Transform

Figure 4.6: Results for a Vibrating Fibre

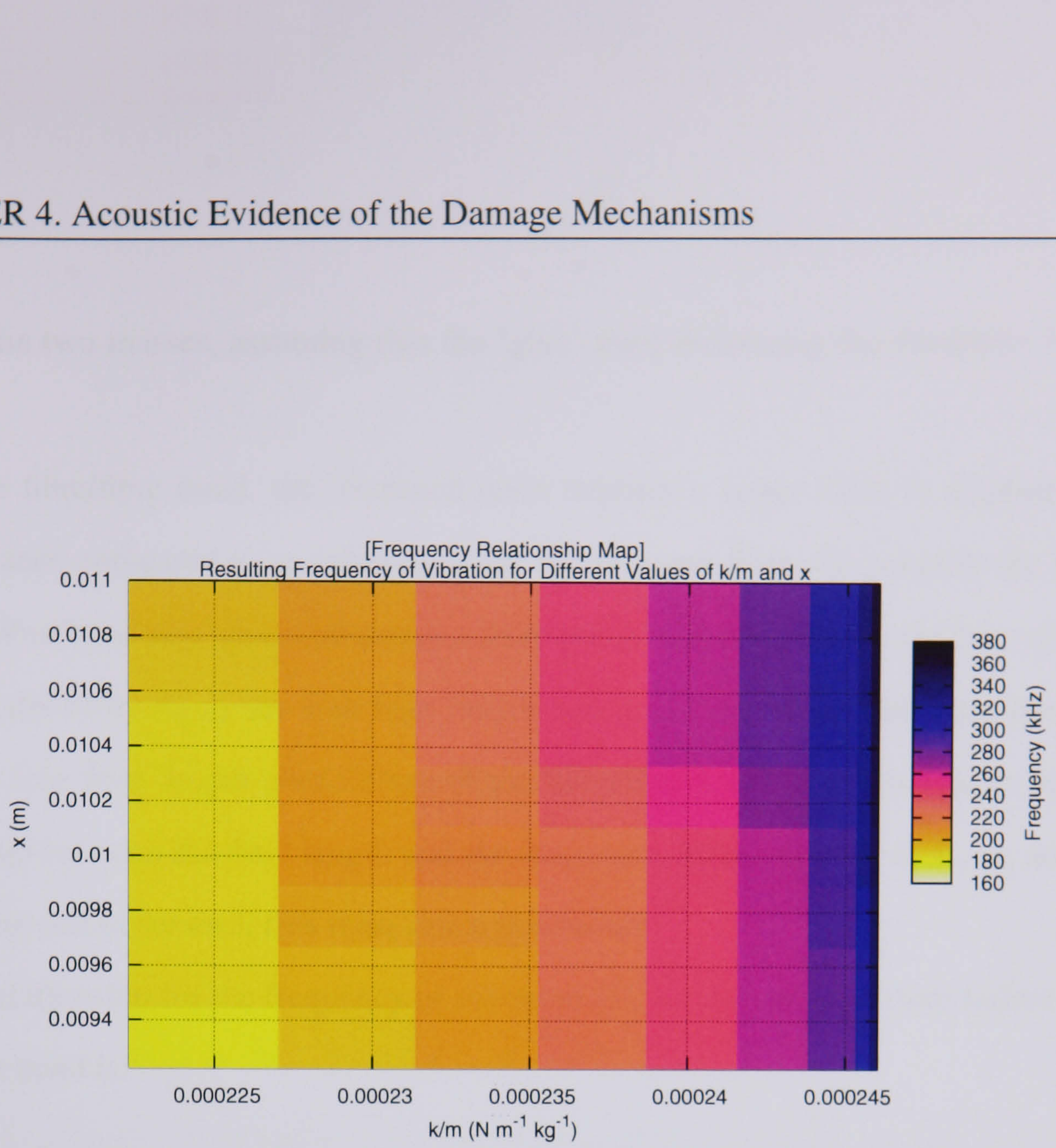

Figure 4.7: Frequency Relationship Map for a Single Vibrating Fibre

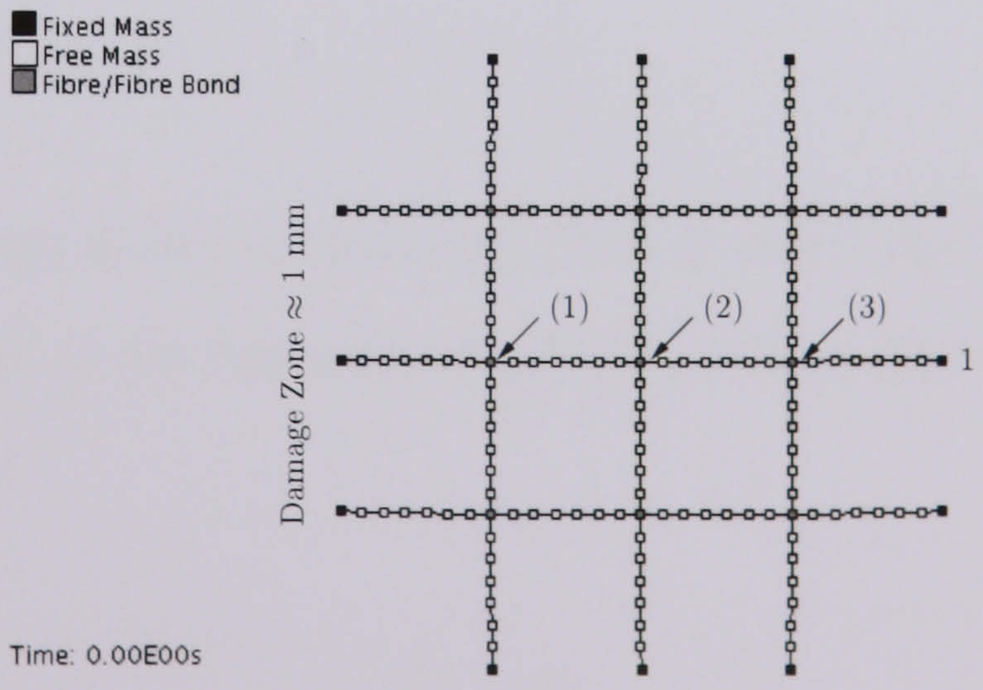

Figure 4.8: 3x3 Cartesian Mesh showing Potential Fibre/Fibre Bond Failures

mass of the two masses, assuming that the 'glue' used in forming the fibre/fibre bond is massless.

At the fibre/fibre bond, the increased mass requires a larger force to displace it the same distance compared to an arbitrary point on the paper fibre. To simplify the model, the fibre/fibre bond was approximated to a fixed point. If L is defined as the free vibrating length of the fibre, L_0 as the free fibre length before failure of the fibre/fibre bond and L_1 as the free fibre length after failure of the fibre/fibre bond, it is possible to derive a relationship between the fibre length and the frequency, assuming that E, t_s, w_s and x of each spring and m for each free mass remains constant.

The relationship for the frequency of vibration (F_0) of the system before failure of the fibre/fibre bond is:

$$F_0 \propto \frac{1}{L_0} \tag{4.5.1}$$

When the fibre/fibre bond fails, the free vibrating length of the two fibres that were bonded together increases, so that $L_1 > L_0$. The relationship for the frequency of vibration (F_1) of the system after failure of the fibre/fibre bond is:

$$F_1 \propto \frac{1}{L_1} \tag{4.5.2}$$

Therefore the change in the 3x3 Cartesian mesh produces the following general relationship for the change in the frequency of vibration of any fibre structure, following a fibre/fibre bond failure.

$$F_1 < F_0 \tag{4.5.3}$$

Using Equation 4.5.3 it is possible to find evidence of the fibre/fibre bond failure in the experimental data by searching for a drop in the frequency of the AEs. However, this

change can only be seen by analysing a group of AEs over an entire experiment rather on an individual AE basis, due to the random nature of the fibre structure. The experimental results showing this trend are presented in Section 4.5.5.

A second method is first investigated which will determine whether a fibre/fibre bond failure can be identified directly from the AE rather than requiring a group of AEs. This requires the simulation of the 3x3 Cartesian mesh consisting of 9 identical fibres each with a length of 2 mm. The Cartesian mesh was chosen as it represents an ordered, highly connected structure, with the middle part of the structure representing the damage zone. Although the microscopic structure of paper is not ordered in this way, the model does represent the damage zone, with a length of 1 mm, and the presence of the neighbouring structure, with a length of 0.5 mm either side of the damage zone. The results are also easier to understand if they have originated from a well defined structure. Figure 4.8 shows the 3x3 Cartesian mesh and also highlights two of the bonds in the damage zone labelled by (1) and (2) respectively.

Section 4.5.2 describes the numerical aspects of the implementation of the fibre/fibre bond failure damage mechanism, with Section 4.5.3 presenting the results generated from the model. Equivalent experimental results can be found in Section 4.5.4.

4.5.2 Numerical Implementation of the Fibre/Fibre Bond Failure Damage Mechanism

As discussed in Section 4.5.1, a fibre/fibre bond exists when two fibres overlap at that particular point. In terms of the mass/spring model, this is represented by two masses bonded together producing a larger mass. This larger mass has a mass which is equal to the sum of the two individual masses.

The presence of a fibre/fibre bond mass could change the material properties of the its surrounding springs, such as the spring thickness. For example, consider two fibres

perpendicular to one another. The width and length of the fibre/fibre bond is the same as the width of the fibre. It also possible to approximate the thickness of a fibre/fibre bond to twice that of the spring thickness. However, the mass/spring model dictates that the fibre/fibre bond be represented by a point in space and therefore, the thickness of the fibre/fibre bond is dependent on the length of the springs attached to the fibre/fibre bond. For a spring length L, and spring width w_s, where $L \approx w_s$, increasing the thickness of the springs connected to the fibre/fibre bond mass becomes more realistic, but, as $L >> w_s$, the approximation of the fibre/fibre bond as a point in space is more accurate, hence there is no need to modify the thickness of the connected springs. Therefore, it has been decided for simplicity that, irrespective of the spring length, the only difference between a fibre/fibre bond mass and a normal mass is the increased mass of the fibre/fibre bond mass.

The pseudocode for the failure of a fibre/fibre bond can be seen in Algorithm 8.

Algorithm 8 Simulating a Fibre/Fibre Bond Failure

```
if Fibre/Fibre Bond Failure = TRUE then
    i ← fibre/fibre bond mass
    m_i ← mass of the fibre/fibre bond
    Create new fibre mass j
    Find the 4 springs, a, b, c, d, connected to i
    Connect the 2 pairs of opposing springs to i and j respectively
    m_i, m_j ← m_i
end if
```

It is also interesting to understand how the dynamic addition of an extra mass in the mass/spring model changes the structure of $A = \left(I + \Delta t M^{-1} \frac{\partial \mathbf{f}^n}{\partial \mathbf{u}} + \Delta t^2 M^{-1} \frac{\partial \mathbf{f}^n}{\partial \mathbf{r}}\right)$ as given in Equation 3.2.29. The shape of A before and after the failure of the fibre/fibre bond in a 3x3 Cartesian mesh, where each fibre consists of 9 mass and 8 springs, can be seen in Figure 4.9.

The arrows in Figure 4.9(b) shows the addition of extra elements into matrix A caused by the creation of an extra mass in the fibre structure. The matrix A still remains asym-

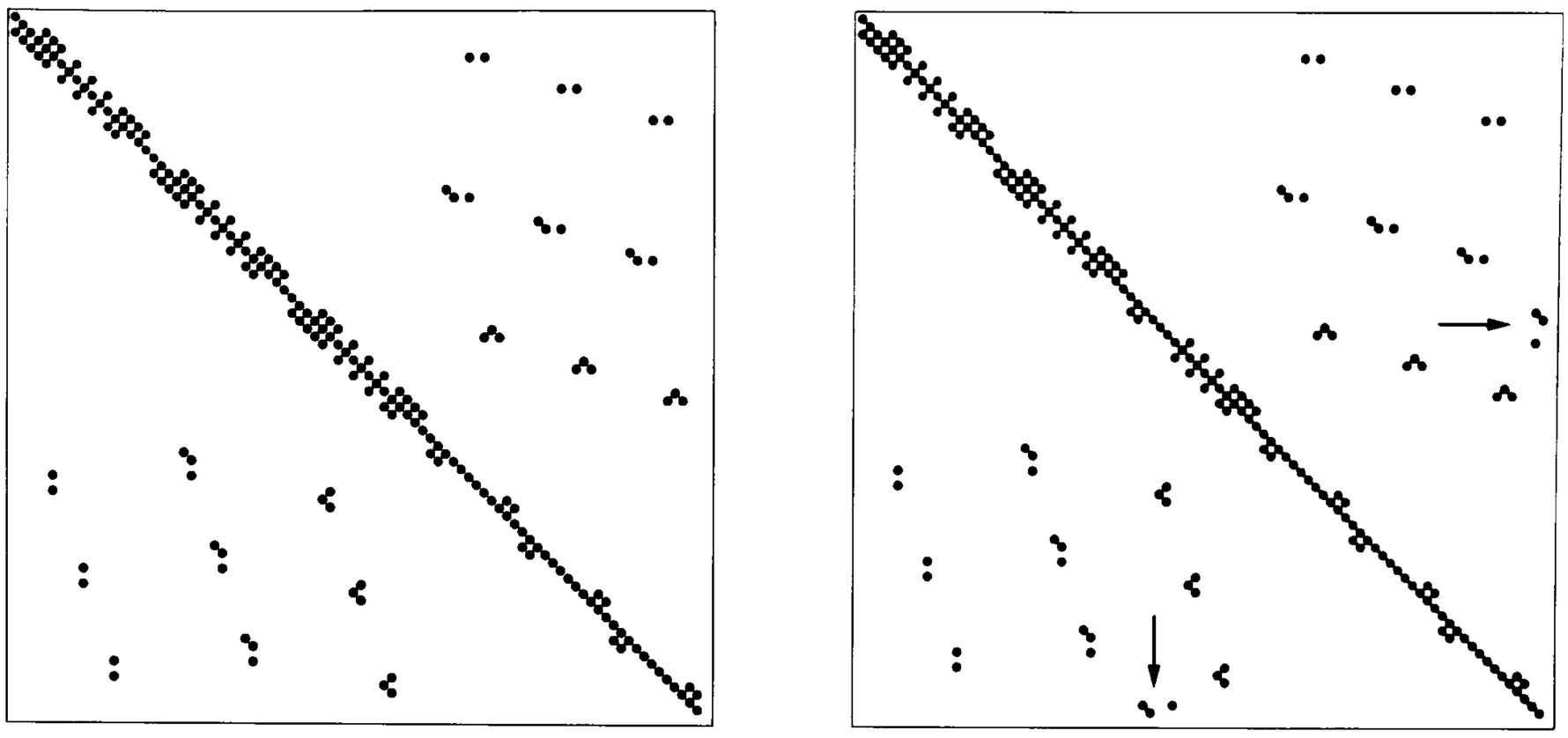

(a) Before Failure

(b) After Failure

Figure 4.9: Changes in the Matrix A due to the Failure of One Fibre/Fibre Bond

metric due to the fixed masses within the mass/spring system.

4.5.3 Theoretical Results of a Fibre/Fibre Bond Failure

This section presents two sets of results. The first set, Figure 4.10, shows the AE and CWT resulting from the failure of the fibre/fibre bond designated by (1). The second set, Figure 4.11, shows the AE and CWT resulting from the multiple failures of the fibre/fibre bonds designated by (1) and (2). In this simulation, fibre/fibre bond (1) is the first to fail and then, 40 ms later, fibre/fibre bond (2) fails.

4.5.4 Experimental Evidence of a Fibre/Fibre Bond Failure

The experimental results presented in this section have been acquired from a typical notched paper sample under load. The fibre/fibre bond failure is the predominant damage mechanism in the paper, generating a high proportion of the AEs in the dataset. Therefore, the *ensemble average of the measured AEs*, provides an insight into the *average AE of a fibre/fibre bond failure*. Figure 4.12 shows the CWT of the average AE of the experimental

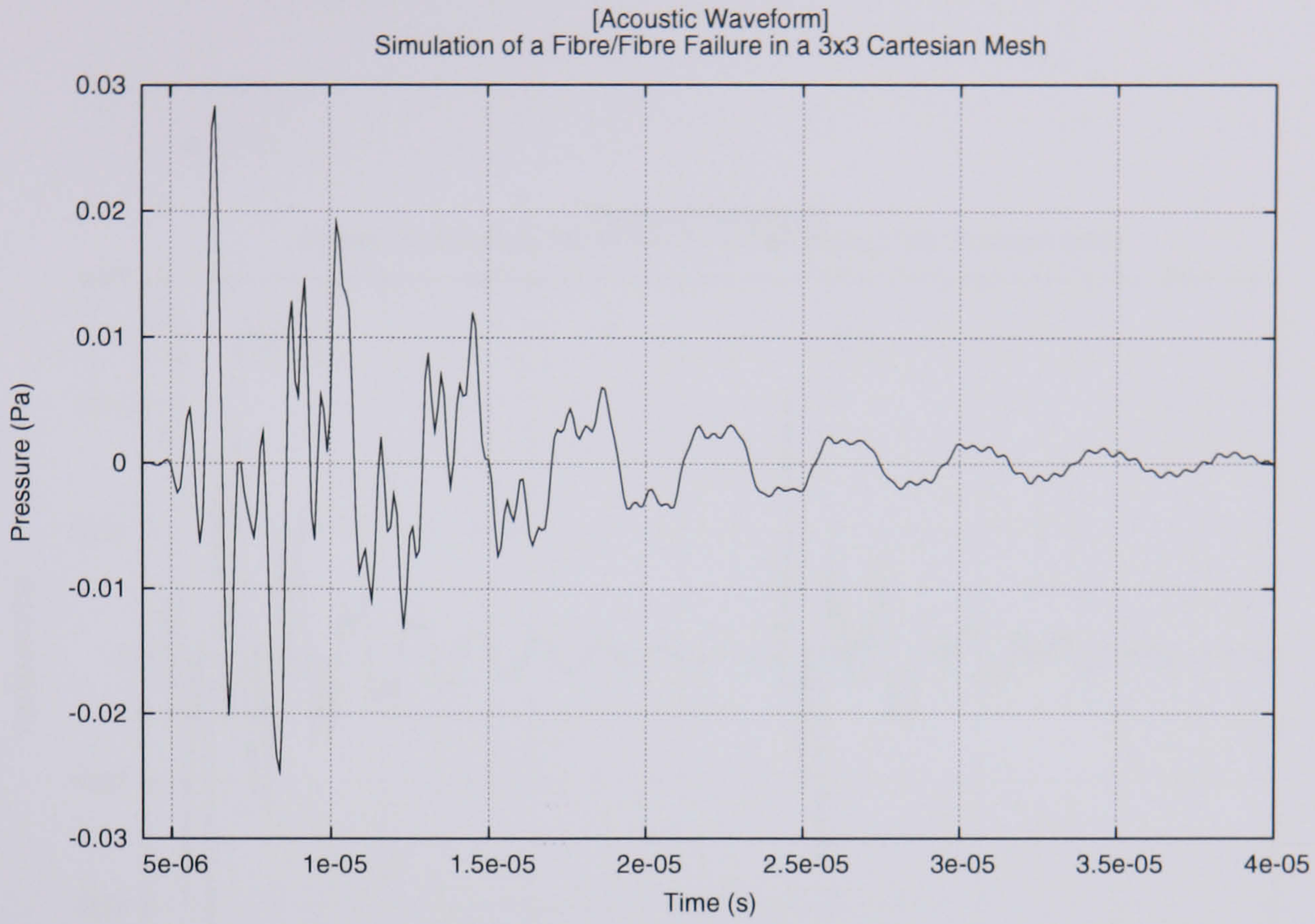

(a) Acoustic Waveform

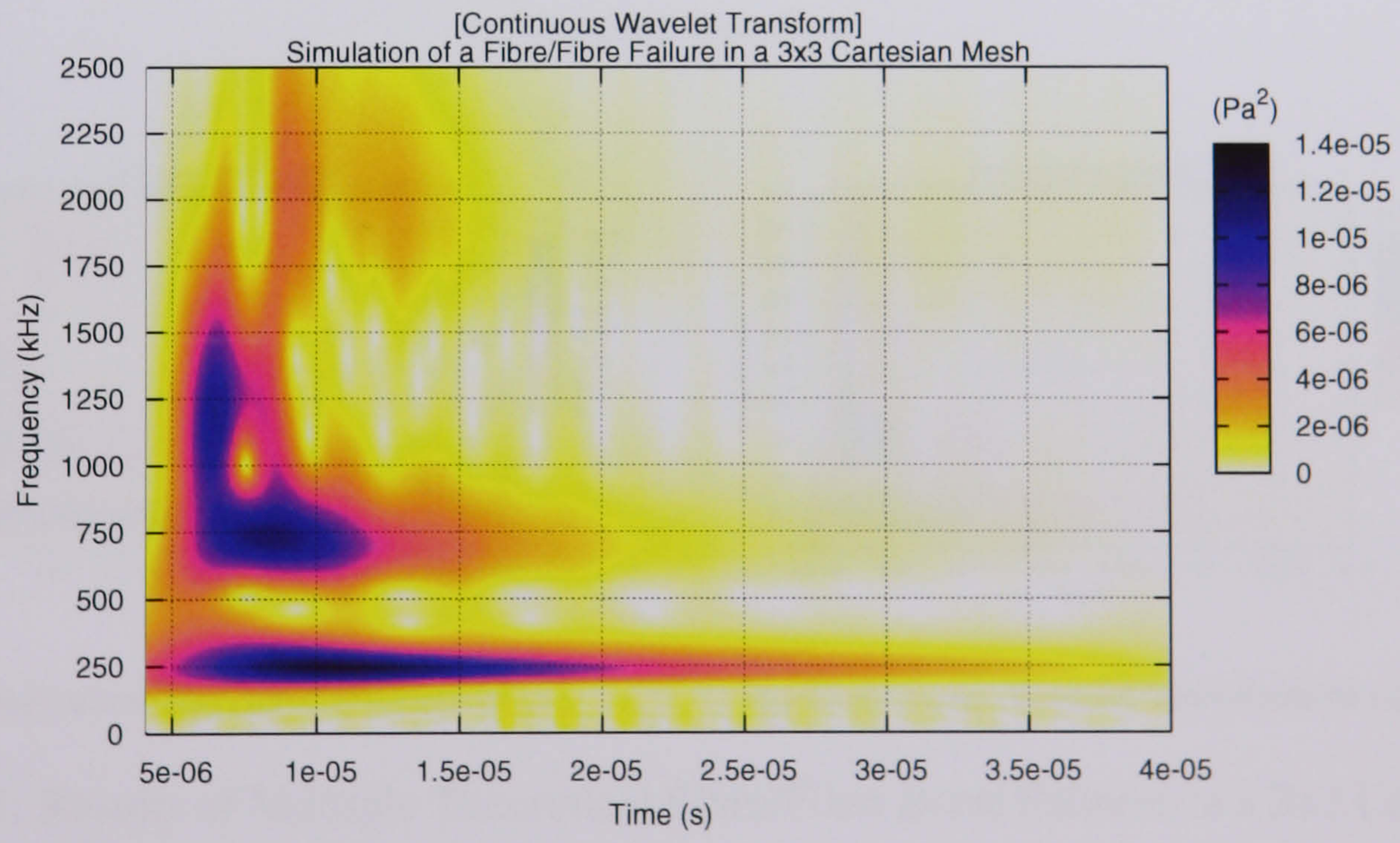

(b) Continuous Wavelet Transform

Figure 4.10: Results of a Theoretical Fibre/Fibre Bond Failure in a 3x3 Cartesian Mesh

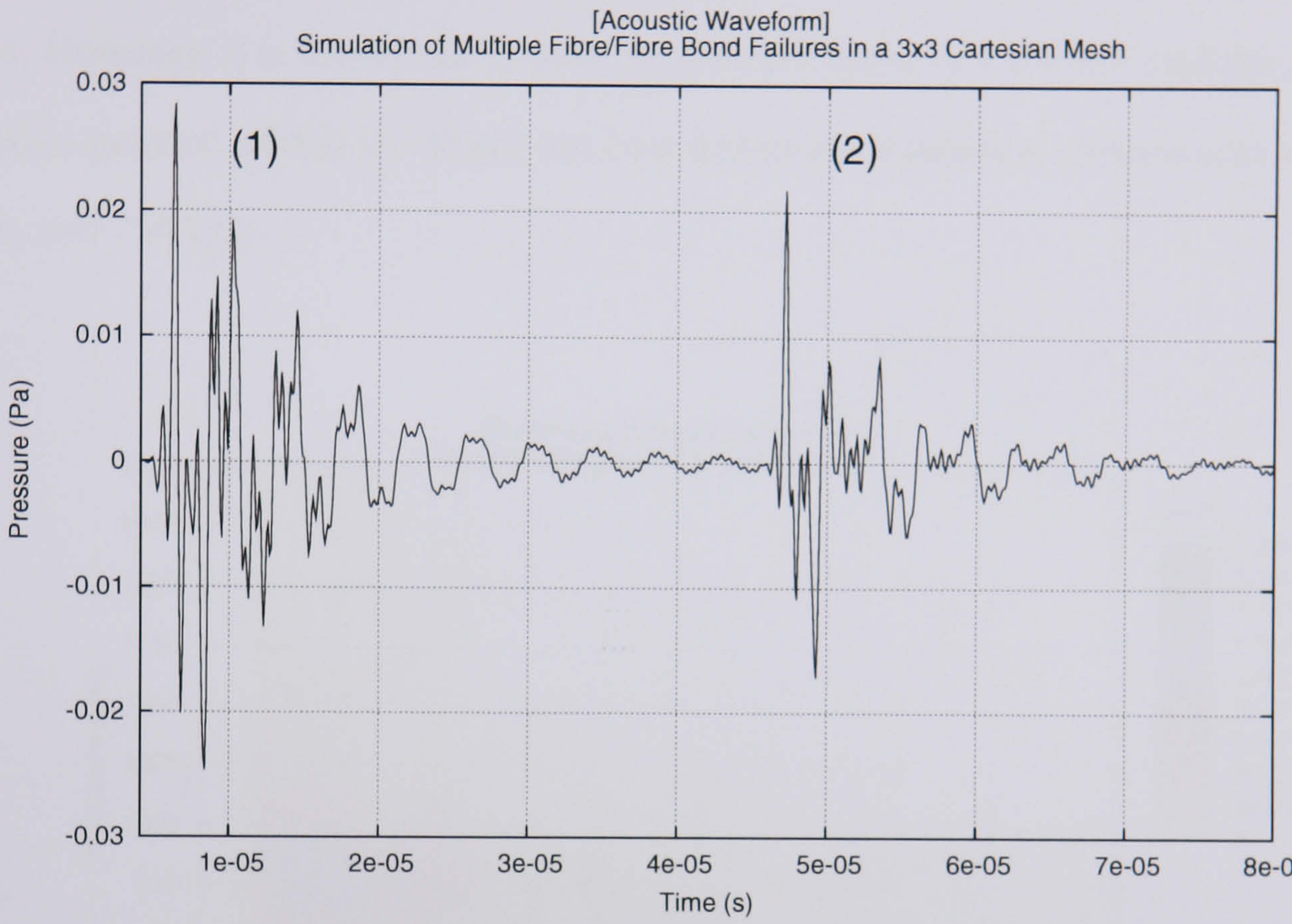

(a) Acoustic Waveform

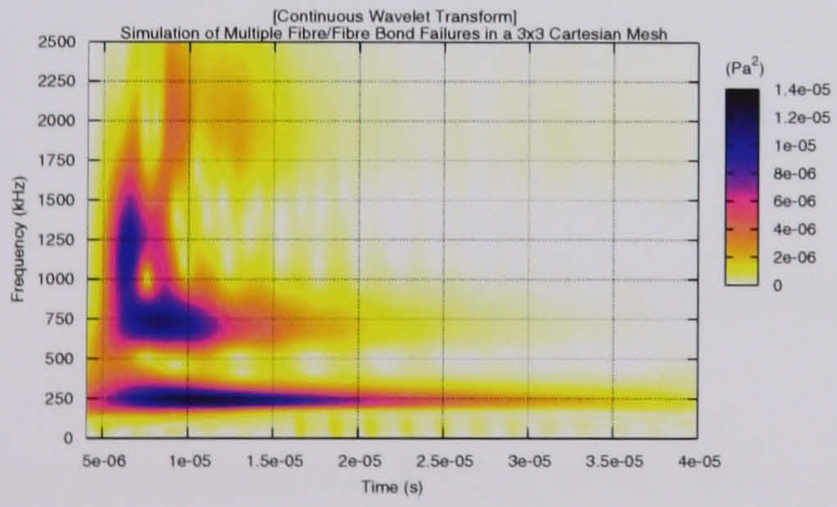

(b) Continuous Wavelet Transform of (1)

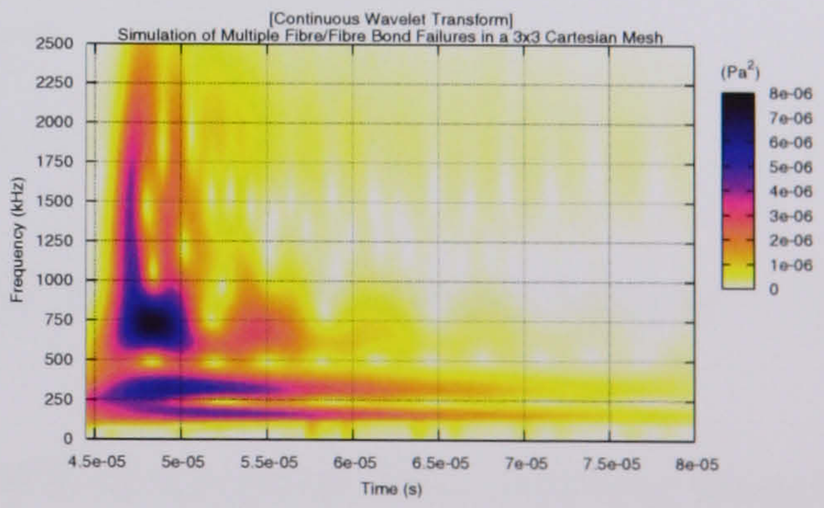

(c) Continuous Wavelet Transform of (2)

Figure 4.11: Results of Multiple Theoretical Fibre/Fibre Bond Failures in a 3x3 Cartesian Mesh

data.

The first point to note is that temporal representation of the average AE provides inaccurate information regarding the duration of each AE. This is caused by each experimental AE having different arrival times at the sensor, causing the average duration of the AE to increase. However, it is important to note the *general shape* of the CWT and the *dominant frequencies* present within it. There are two dominant frequency components at around 250 kHz and 750 kHz.

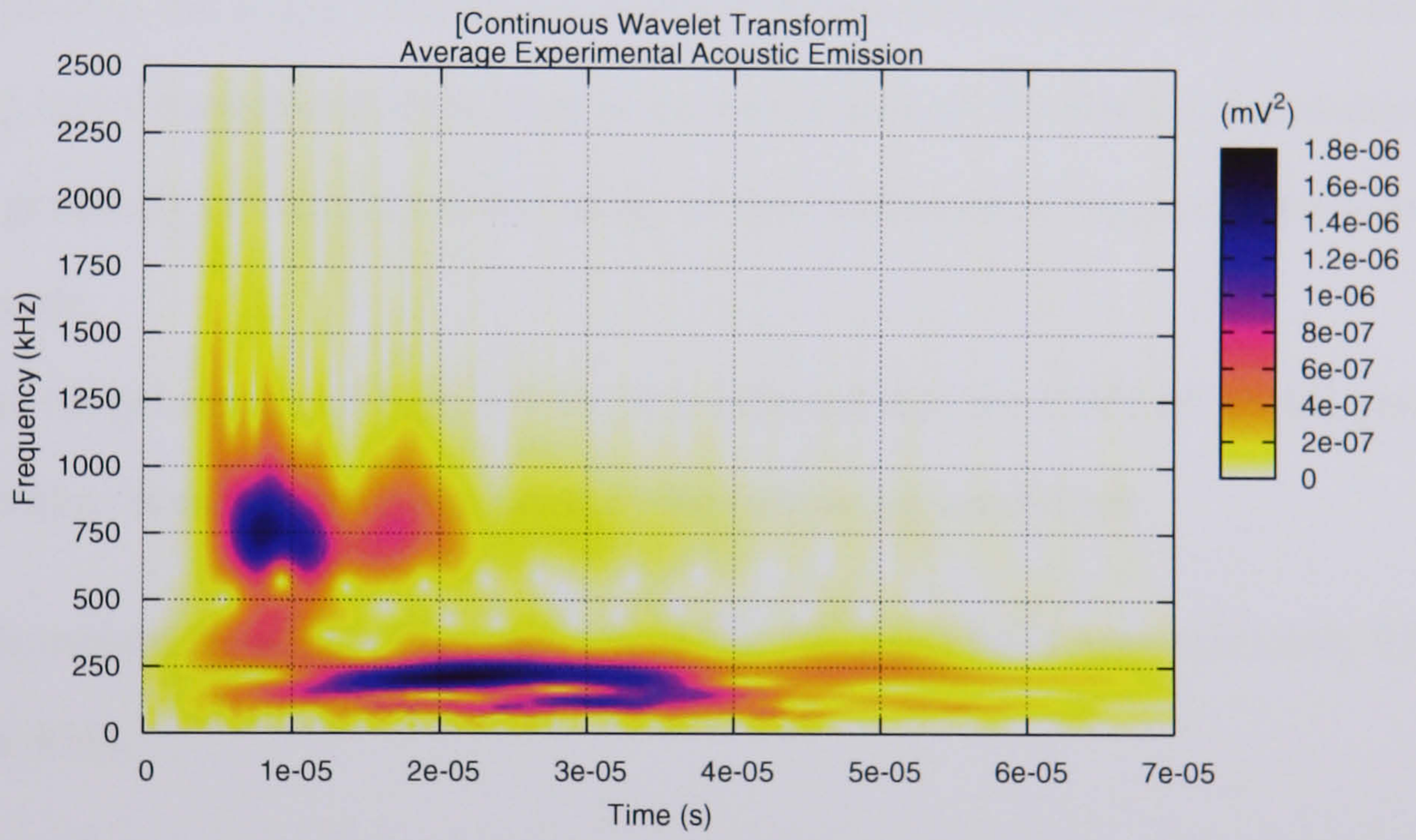

Figure 4.12: The CWT of an Average AE from a Notched Paper Sample

For completeness, Figure 4.14 shows the CWT of 6 typical AEs, resulting from suspected fibre/fibre bond failures, chosen from the experimental data. They all show a similar shape and frequency content, but it is the strength of the dominant frequency components that are of particular interest. The lowest dominant frequency is at approximately 250 kHz. This agrees with the prediction in Section 4.4 of the fundamental frequency of a single vibrating fibre that has a length equal to that of the damage zone in the paper. The other dominant frequency is at approximately 750 kHz, which, from Equation 4.3.1 is the

first harmonic of a single vibrating fibre.

The presence of the first harmonic can be explained by investigating the initial shape of the fibres in the fibre structure. Figure 4.13(a) shows the initial conditions of the single vibrating fibre of Figure 4.5. Figure 4.13(b) shows the initial conditions of fibre 1 in the 3x3 Cartesian mesh of Figure 4.8.

The initial conditions of the fibre shown in Figure 4.13(a) are identical to the mode shape of the fundamental frequency and result in the generation of a sinusoidal AE with a frequency of approximately 250 kHz. In contrast, the initial conditions of fibre 1 in Figure 4.13(b) is closer to the string's fourth eigenvector. When one of the fibre/fibre bonds fails, the resulting initial movement of the fibre is a combination of the first few harmonics, with the motion gradually converging to the mode of the fundamental frequency between each remaining node.

From the model results of Figure 4.11, it is inferred that the CWT of an AE generated from a fibre/fibre bond failure must satisfies the following conditions.

- The dominant frequency components of the AE must be at approximately 250 kHz or 750 kHz.
- The dominant tone may be at either approximately 250 kHz or 750 kHz.
- The duration of the AE frequency component at approximately 250 kHz is longer than that of the frequency component at approximately 750 kHz.

4.5.5 Experimental Evidence of Multiple Fibre/Fibre Bond Failures

The damage zone area of Figure 4.1(d) was digitally magnified and compared with the corresponding area of the undamaged paper sample of Figure 4.1(c). It was noted that most of the dyed fibres were displaced but not broken. This indicates that in this test the predominant damage mechanism is the failure of the fibre/fibre bonds. Therefore, when

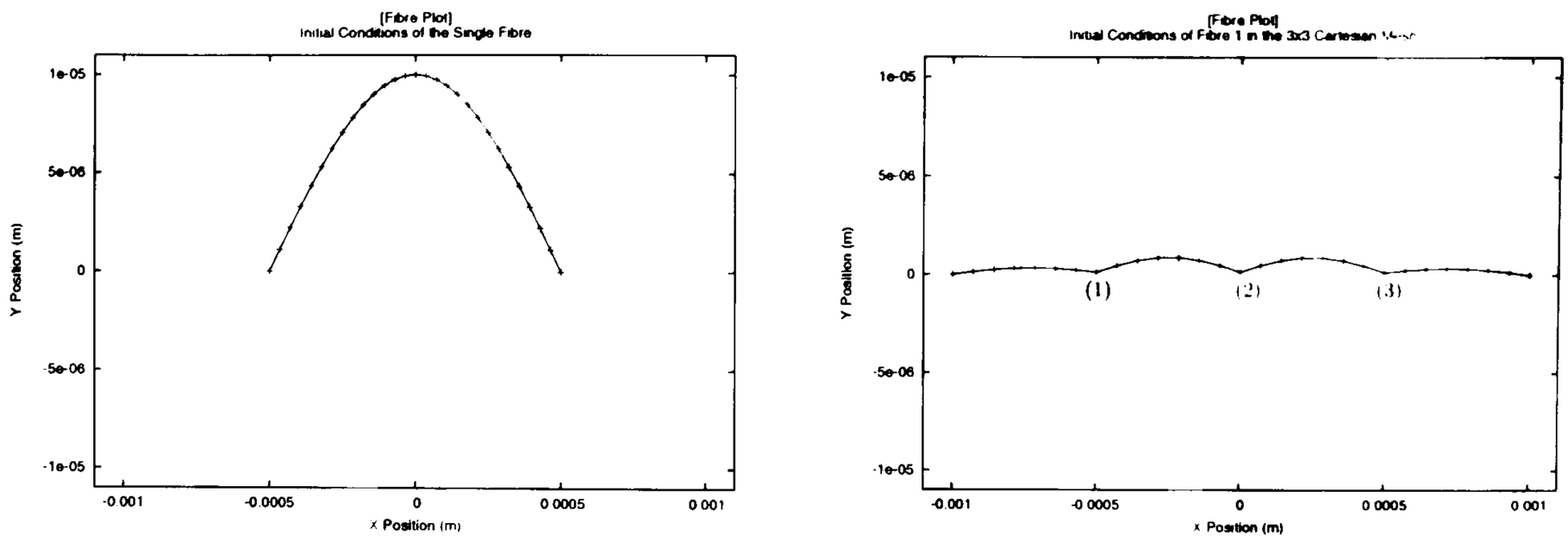

(a) Single Fibre

(b) Fibre 1 in the 3x3 Cartesian Mesh

Figure 4.13: Initial Conditions of the Single Fibre and Fibre 1 in the 3x3 Cartesian Mesh

analysing a set of data from one experiment, it can be assumed that AEs generated from fibre failures have little effect on the overall results. Therefore, the AEs from suspected fibre failures are not filtered out from the data set.

This section will use data from several 100 mm x 10 mm notched paper samples similar to the one shown in Figure 4.1 to prove that as the fibre/fibre bonds fail, the frequency of the generated AEs decreases as predicted by Equation 4.5.3. The paper samples are placed under a load which increases at a constant rate until fracture of the specimen occurs. Figure 4.15 shows the load applied to the paper sample over time.

Figure 4.15 shows the time trace of the axial load applied to the paper sample. Figure 4.15 shows that up until 32 seconds, the load in the paper sample is increasing or remaining constant. This suggests that the frequency of the AEs generated will increase, if the free vibrating length of the fibres remain constant, as shown by the relationship given in Equation 4.2.2. Conversely, if fibre/fibre bonds fail during the tensile test, the average free fibre vibrating length will increase, which will reduce the AE frequency, according to Equation 4.5.3.

Figure 4.15 shows that, after 32 seconds, the load that the paper sample is under will start to decrease. If the tension in the paper sample decreases, so does the frequency of the generated AEs, making it impossible to distinguish whether the decrease in the frequency

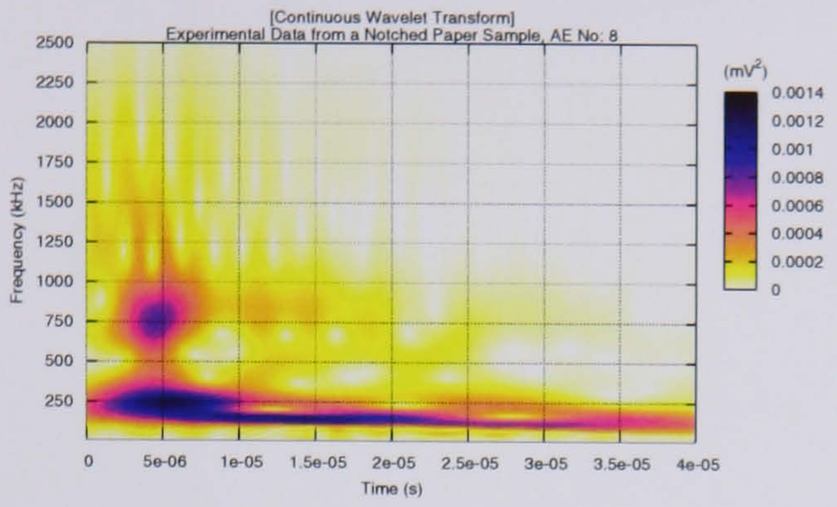

(a) AE No: 8

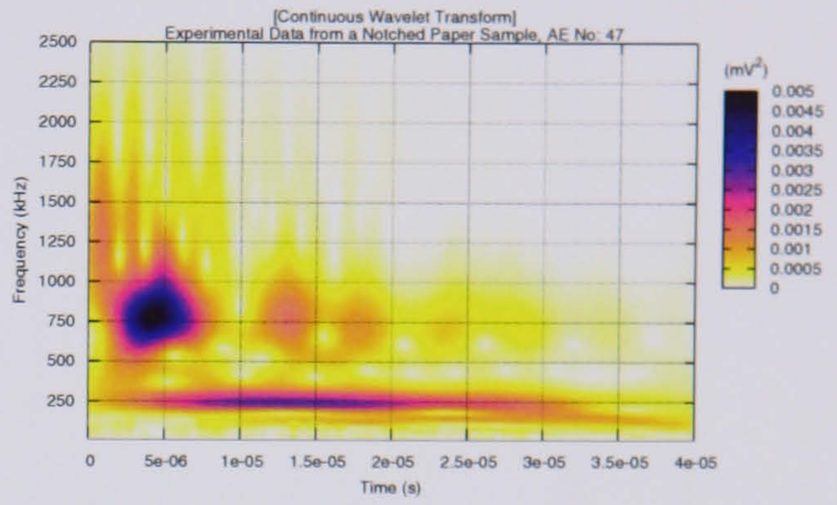

(b) AE No: 47

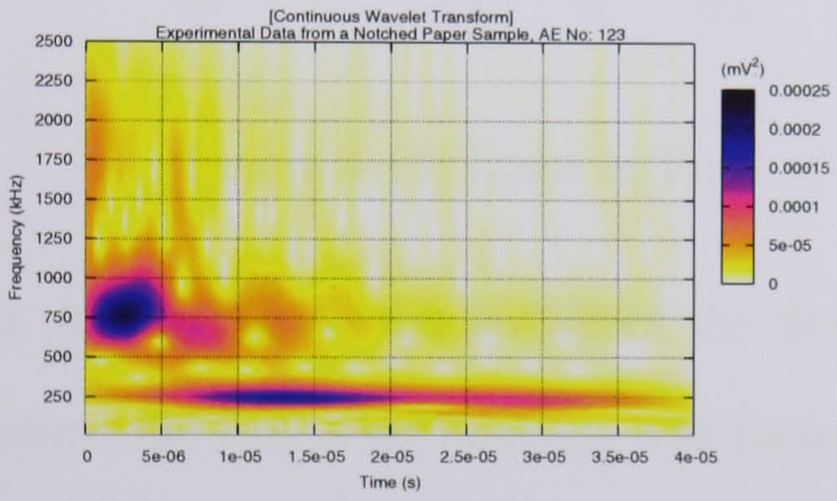

(c) AE No: 123

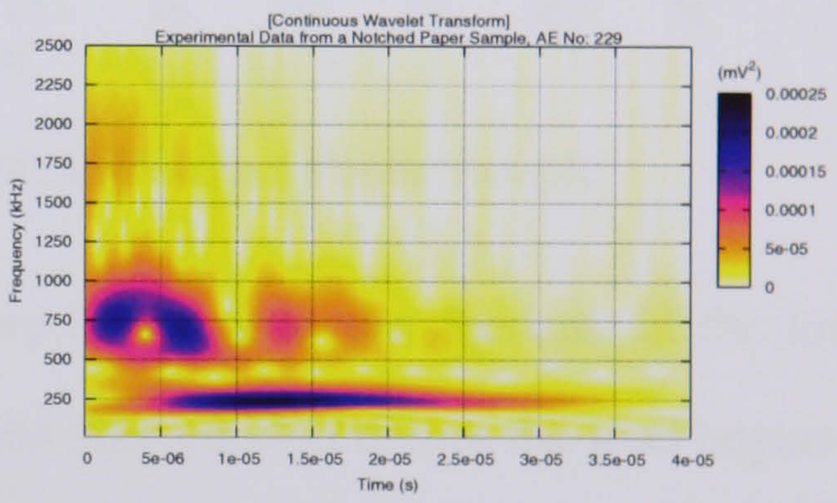

(d) AE No: 229

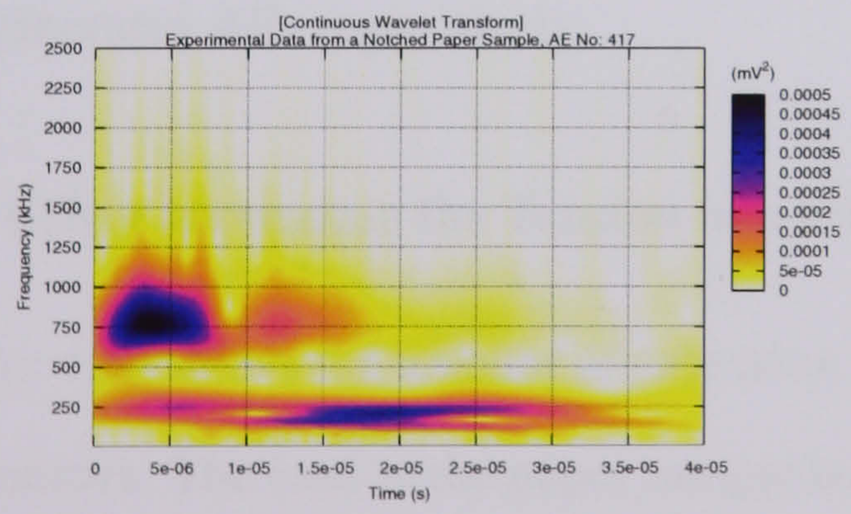

(e) AE No: 417

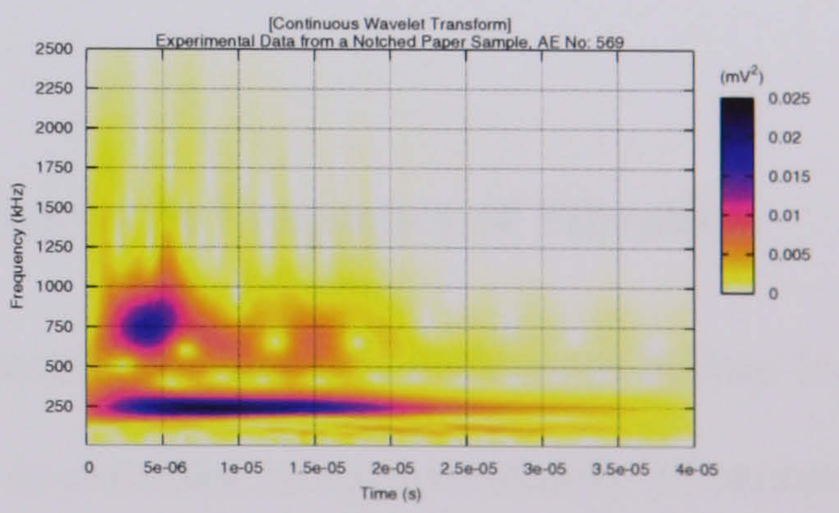

(f) AE No: 569

Figure 4.14: The CWTs of 6 AEs from Suspected Fibre/Fibre Bond Failures in a Notched Paper Sample

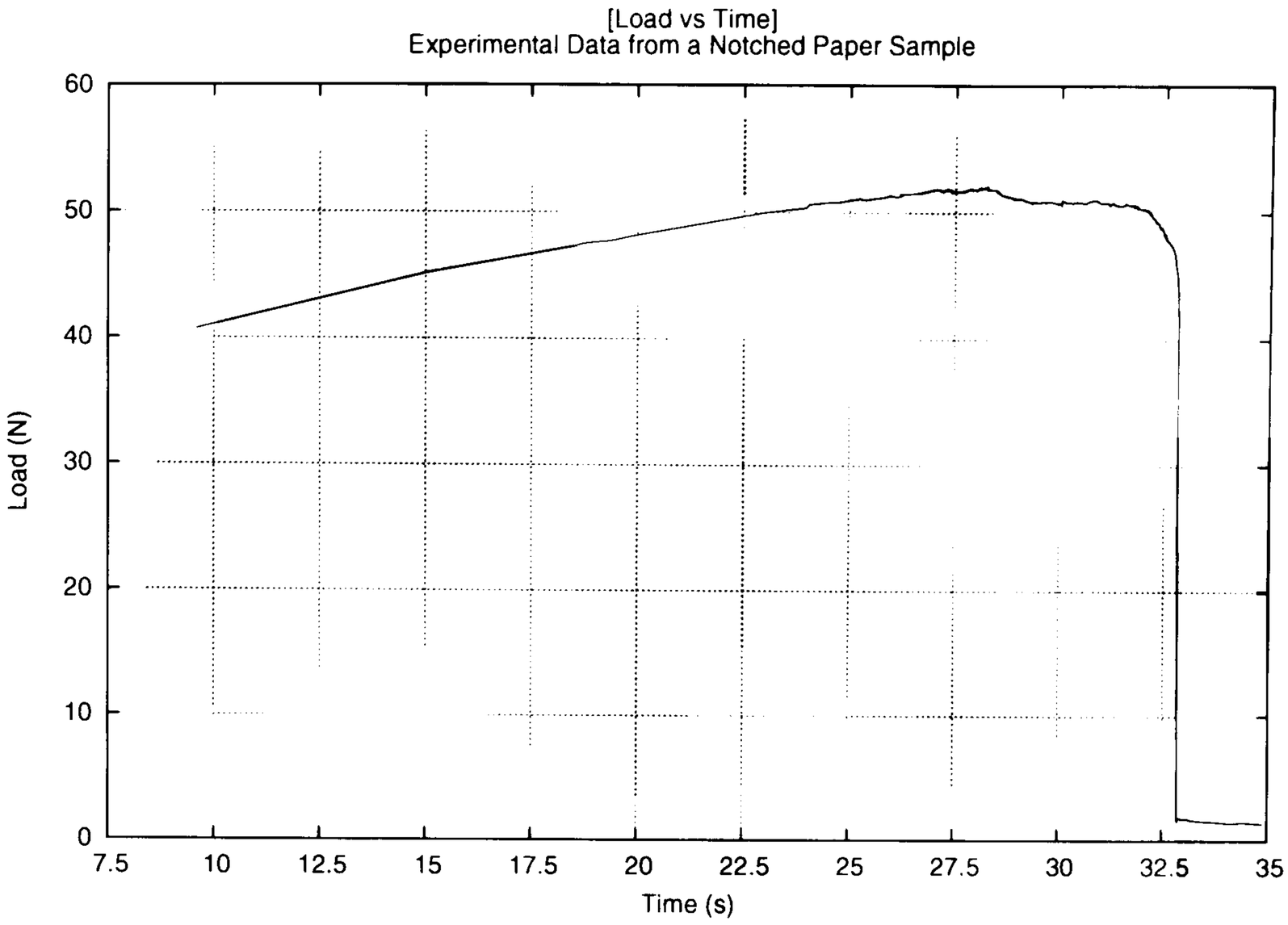

Figure 4.15: Load vs Time of a Typical Notched Paper Sample

of the AEs is due to the failure of the fibre/fibre bonds or to the decrease in the load. Therefore, the following analysis will focus on the AEs emitted before the load begins to decrease. The following two sections will ascertain from the numerical model the impact the increasing tension and the effect the fibre/fibre bond failures have on the frequency of the generated AEs respectively.

The Effect Increasing the Tension in a Fibre has on its Frequency of Vibration

Figure 4.16 shows the amount of extension a typical paper sample undergoes before fracture occurs. The load in the paper sample begins to decrease at approximately 32 seconds, when the extension of the paper sample is around 0.82 mm. Using this information, a single plucked fibre as shown in Figure 4.5 is simulated using the average material properties with an extension varying between 0.2% to 1.0% of its length. The resulting frequencies can be seen in Figure 4.17.

The equation of the line of best fit in Figure 4.16 is $F = 1.27\text{E}07x + 115.21$, where F is

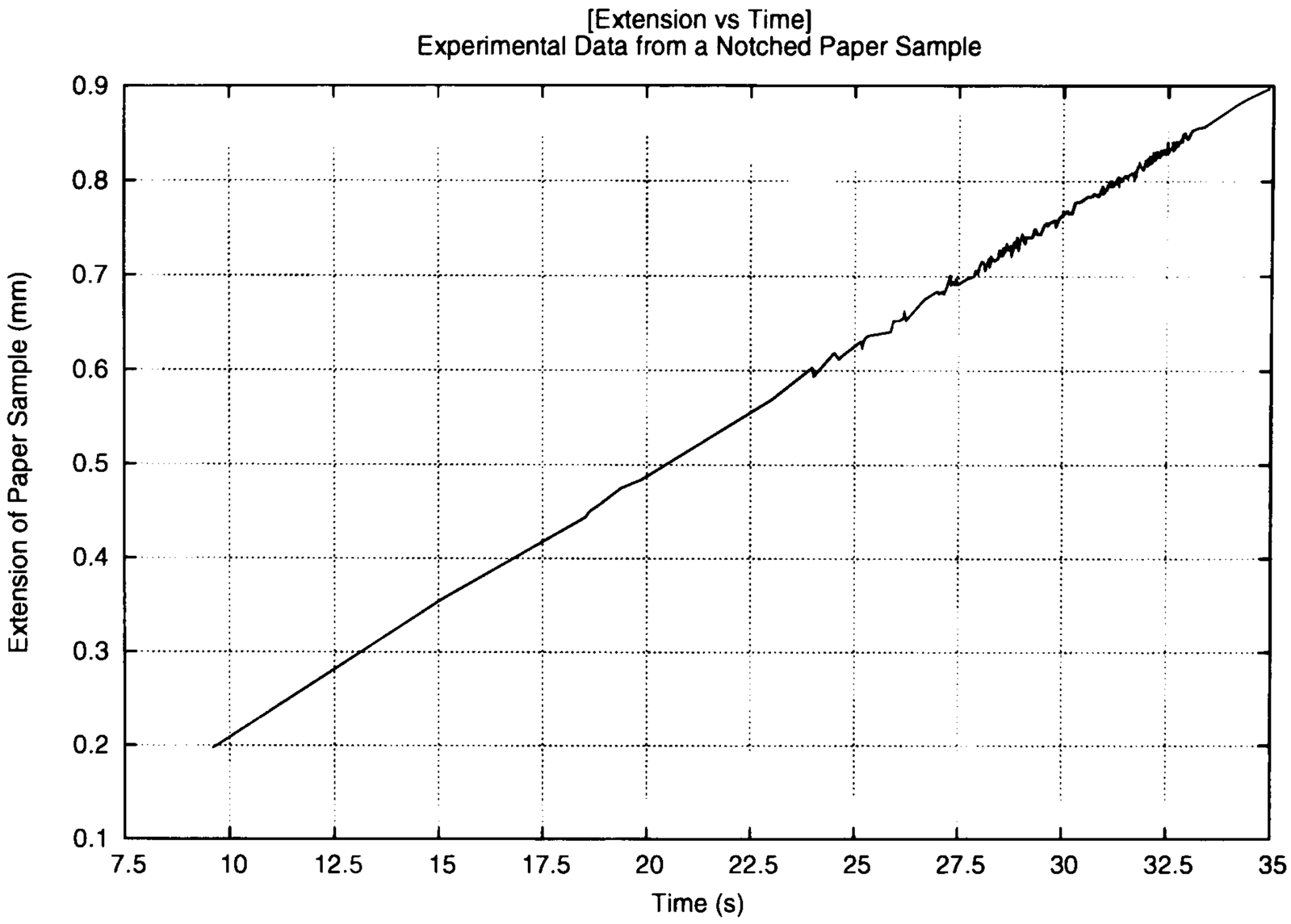

Figure 4.16: Extension vs Time of a Typical Notched Paper Sample

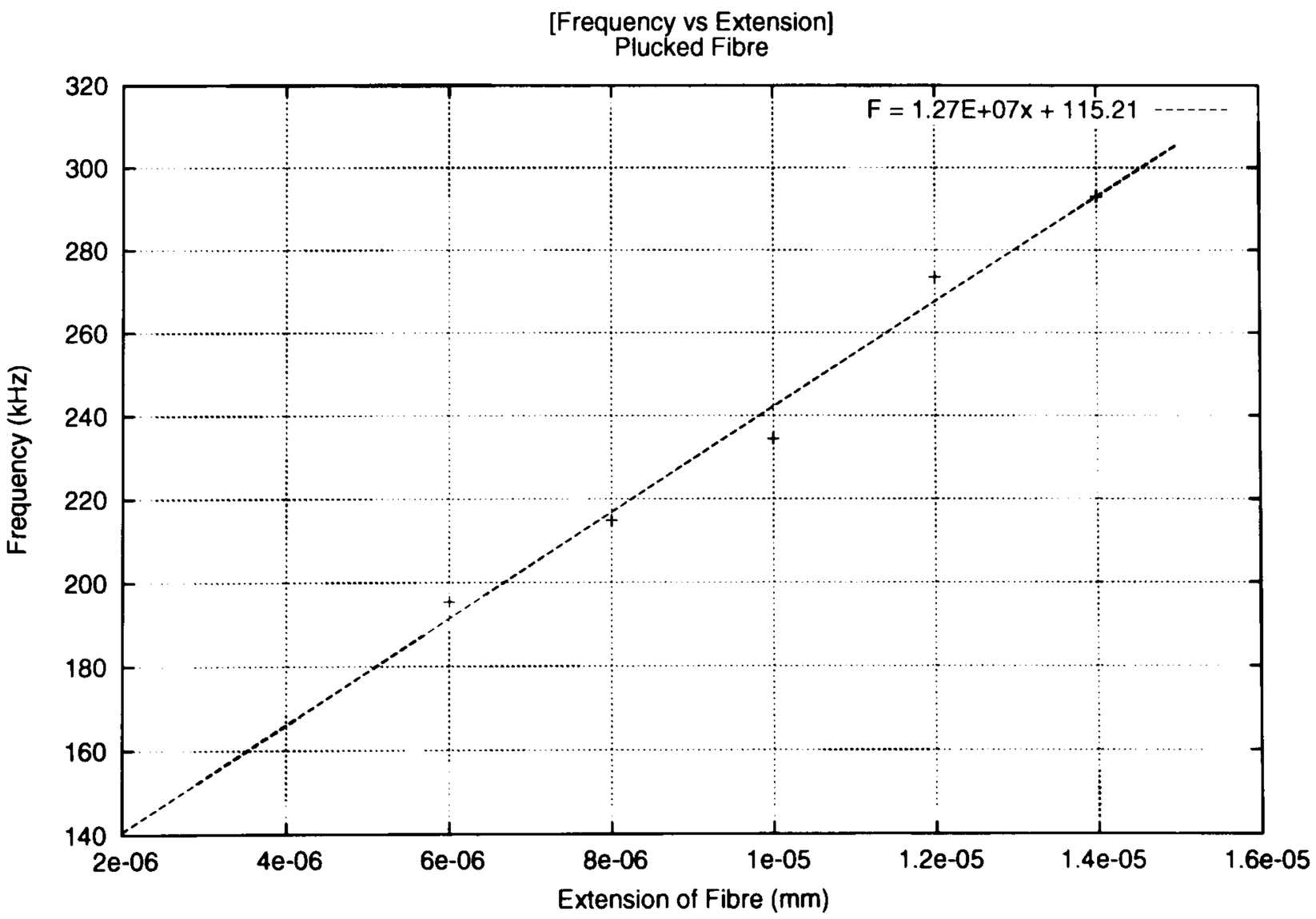

Figure 4.17: Frequency vs Extension of a Plucked Fibre

the frequency in kHz and x is the extension of the paper fibre in mm. Using this equation, the change in the frequency of vibration of a fibre which has been extended by 0.6% will only increase by approximately 10%. This increase in frequency is much smaller than the decrease in frequency of approximately 67% caused by the failure of a fibre/fibre bond. Therefore, it is expected that the effect of increasing the tension in the paper sample has a negligible effect on the frequency of the AEs.

The Effect a Fibre/Fibre Bond Failure has on the Frequency of Vibration of a Fibre

The theoretical and experimental results have shown that the failure of a fibre/fibre bond generates an AE which contains strong frequency components at around 250 kHz and 750 kHz as seen in Figures 4.10 and 4.14 respectively. Section 4.4 has shown that the movement of a single fibre produces an AE with a fundamental frequency equal to approximately 250 kHz. Section 4.5.3 has shown that when a fibre is part of a larger structure, the AEs generated contain a higher dominant frequency at approximately 750 kHz. Therefore, it is proposed that as damage occurs within the paper sample, there will be a decrease in the number of fibre/fibre bonds in the damage zone, causing the fibre structure in the damage zone to disintegrate into individual fibres. In doing so, there will be a noticeable shift in power from the higher frequency to the lower frequency.

The failure of a fibre/fibre bond is a localised event and will only affect the neighbouring fibre structure. This suggests that the transfer of power from the high frequencies to the low frequencies will rarely be seen in two consecutive AEs; instead it must be measured over a complete set of AEs from the same experiment. Using the numerical results as guidelines, it was decided to split the frequency components of each experimental AE into equal windows of bandwidth $\Delta f = 100$ kHz for the range 0 - 2500 kHz. The power ratio for the i^{th} window is:

$$W_i = \frac{\frac{1}{\Delta f}\int_{(i-1)\Delta f}^{i\Delta f} PSD^{(f)}df}{\frac{1}{2500}\int_{0}^{2500} PSD^{(f)}df} \approx \frac{\sum_{j=(i-1)m+1}^{im} SPLj}{\sum_{j=1}^{N} SPLj} \quad \text{where:} \quad i = 1, 2, \ldots, 25 \qquad (4.5.4)$$

where:

W_i	Power Ratio of Window i
PSD	Power Spectral Density
SPL	Sound Power Level generated by DFT of the AE
N	Number of Frequency Bands in the DFT
j	$j^{(th)} DFT$ Frequency Band
m	Window Size $= 100$ khz

For each experimental AE, a Pearson's product moment correlation (Pearson's correlation) is performed on the power ratios of each frequency window. The formula for the Pearson's correlation as given by Allan [117] is shown in Equation 4.5.5.

$$r = \frac{\sum_{i=1}^{n} x_i y_i - \left(\sum_{i=1}^{n} x_i \sum_{i=1}^{n} y_i\right)}{\sqrt{\left(\sum_{i=1}^{n} x_i^2 - \frac{(\sum_{i=1}^{n} x_i)^2}{n}\right)\left(\sum_{i=1}^{n} y_i^2 - \frac{(\sum_{i=1}^{n} y_i)^2)}{n}\right)}} \qquad (4.5.5)$$

where:

r	Pearson's Correlation Coefficient $(-1 \leq r \leq 1)$
	$r = 1$ - Strong Positive Correlation, $r = -1$ - Strong Negative Correlation
x	AE Number
y	Power Ratio
n	Number of AEs Recorded Consecutively in Sample

Table 4.2 shows the results of the Pearson's correlation coefficient r for each of the *significant* frequency windows from the experimental data of a typical paper sample.

Frequency Window	r	p
200 - 300 kHz	0.19	6.08E-03
300 - 400 kHz	0.29	3.96E-05
500 - 600 kHz	-0.28	7.69E-05
700 - 800 kHz	-0.29	4.45E-05
1300 - 1400 kHz	0.34	9.05E-07
1400 - 1500 kHz	0.20	4.86E-03
1500 - 1600 kHz	0.22	1.63E-03
1900 - 2000 kHz	0.22	2.07E-03

Table 4.2: Pearson's Correlation Coefficients and p Values for the Experimental Data for Frequency Windows with Significant Correlation

Table 4.2 also shows the observed significance level p, which is the smallest fixed level at which the null hypothesis can be rejected [118]. The results for the 200 - 300 kHz frequency window show a weak positive correlation, $r = 0.19$, with an observed significance level $p = 6.08\text{E-}03$, which means there is 0.6% chance that the observed correlation is a fluke. Table 4.2 only lists the correlation coefficient of the frequency windows where the significance level is less than 1%. Whereas correlation does not imply causation, the results from Table 4.2 suggest that a trend does exist. This will be explored using a linear regression.

Figure 4.18 shows the linear regression ($y = mx + c$) of the power ratio, y vs the AE number, x for the same data used in Table 4.2.

The details of the linear regression are summarised in Table 4.3 where m is the gradient of the linear regression and c is the value of the y when $x = 0$.

Frequency Window	m	c	r	p
200 - 300 kHz	7.68E-04	0.19	0.19	6.08E-03
300 - 400 kHz	7.31E-05	0.01	0.29	3.96E-05
500 - 600 kHz	-2.96E-04	0.10	-0.28	7.69E-05
700 - 800 kHz	-8.30E-04	0.34	-0.29	4.45E-05
1300 - 1400 kHz	1.27E-04	0.01	0.34	9.05E-07
1400 - 1500 kHz	1.00E-04	0.02	0.20	4.86E-03
1500 - 1600 kHz	1.15E-04	0.01	0.22	1.63E-03
1900 - 2000 kHz	1.54E-05	0.00	0.22	2.07E-03

Table 4.3: Summary of the Linear Regression

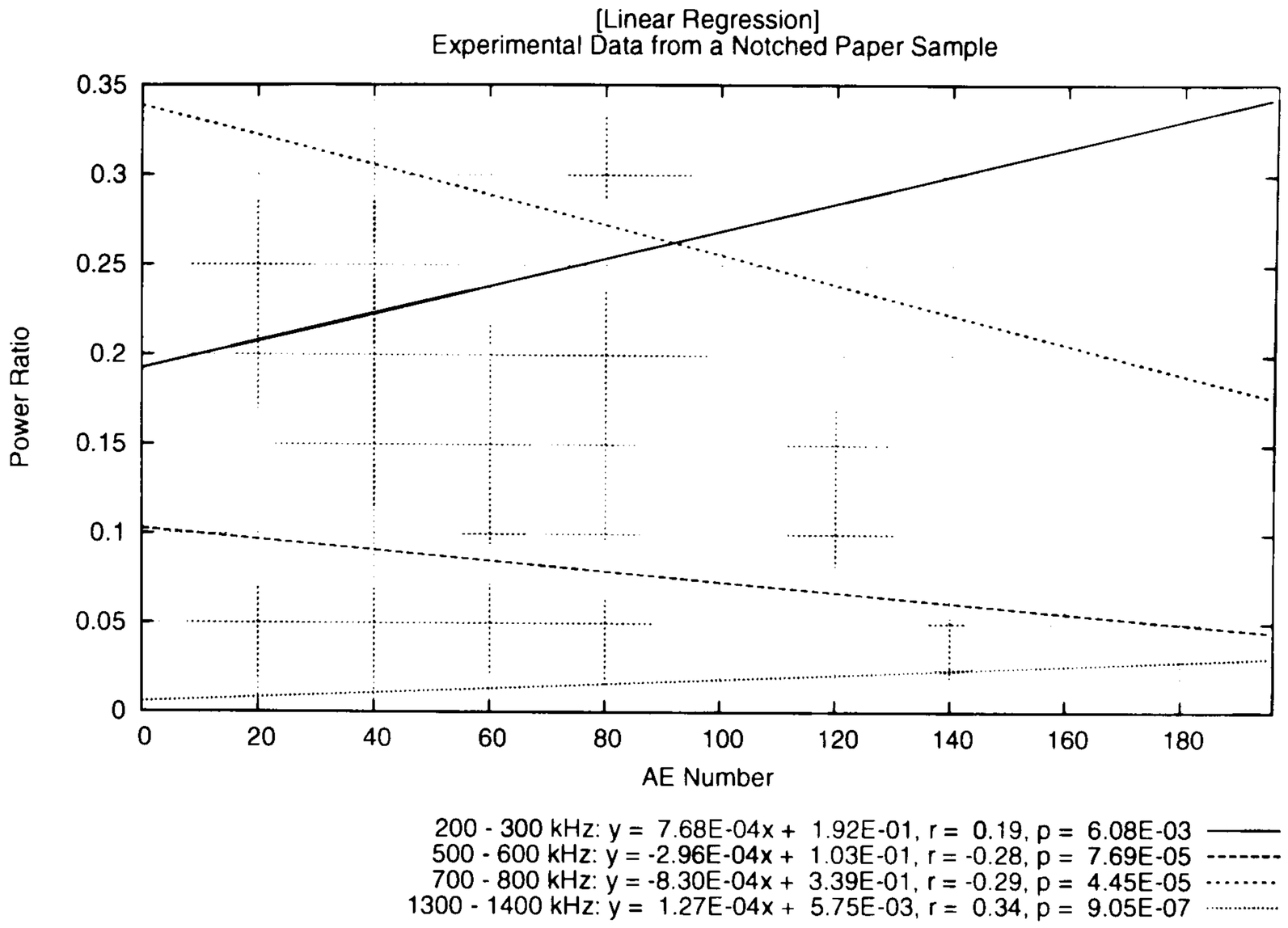

Figure 4.18: Results from the Linear Regression

Using the Pearson's correlation coefficient it was shown in Table 4.2 that 8 of the frequency windows showed significant correlations. Figure 4.18 shows the 4 frequency windows that exhibit the strongest relationship (linear regressions with the steepest gradient) between the power ratio and the AE number, of which the 200 - 300 kHz and 700 - 800 kHz windows are the strongest. The CWTs of the numerical and experimental AEs have shown that the most powerful frequency components can be found around 250 and 750 kHz. The symmetry of these two lines of best fit about the $y = 0.26$ line show that there is a linear transfer of power from the frequency components in the range of 700 - 800 kHz to the frequency components in the range 200 - 300 kHz.

As the power ratio is a measure of the strength of the frequency components within the specified bandwidth, it must also represent the dominating frequency of the AE. The generation of each AE within the specified range is caused by the failure of a fibre/fibre bond, therefore the AE number is proportional to the amount of damage present within the fibre structure. Figure 4.18 shows that the statistical frequency of the 700 - 800 kHz

signals is inversely proportional to the amount of damage within the paper sample and the statistical frequency of recording the 200 - 300 kHz signals is proportional to the amount of damage within the paper sample. From the relationship presented in Equation 4.2.2 and the analysis of the variability of E, t_s, w_s, x, L, and m in Section 4.4, the only parameter that undergoes a significant change due to the failure of the fibre/fibre bond is the free vibrating length of the fibre L, which increases as the damage increases. Therefore it is inferred that the probability $P(\hat{f})$ of the dominant SPL frequency $\hat{f}$ of the AE being high or low is:

$$P(700\text{ kHz} \leq \hat{f} \leq 800\text{ kHz}) \propto \frac{1}{L} \propto \frac{1}{\text{damage}} \tag{4.5.6a}$$

$$P(200\text{ kHz} \leq \hat{f} \leq 300\text{ kHz}) \propto L \propto \text{damage} \tag{4.5.6b}$$

4.6 Acoustic Evidence of a Fibre Failure

4.6.1 Predicting the Change in Frequency of Vibration of a Fibre Structure as a Fibre Failure Occurs

Consider the 2x1 fibre structure shown in Figure 4.19. The fibre structure uses identical fibres to those of the 3x3 Cartesian mesh used for the fibre/fibre bond failure simulations. Certain fibres were omitted from this structure to represent the absence of fibre/fibre bonds in the damage zone, consistent with the assumption that the fibre/fibre bonds in the local structure will have failed first [119].

Before failure occurs in the fibre, the fibre behaves like a string, with the frequency of its vibration defined by Equation 4.2.2. When the fibre fails, it no longer has both ends fixed, but consists of two smaller fibres with one fixed end and one free end. The dominant movement of the fibre as failure occurs is a sharp compression along the length of the fibre,

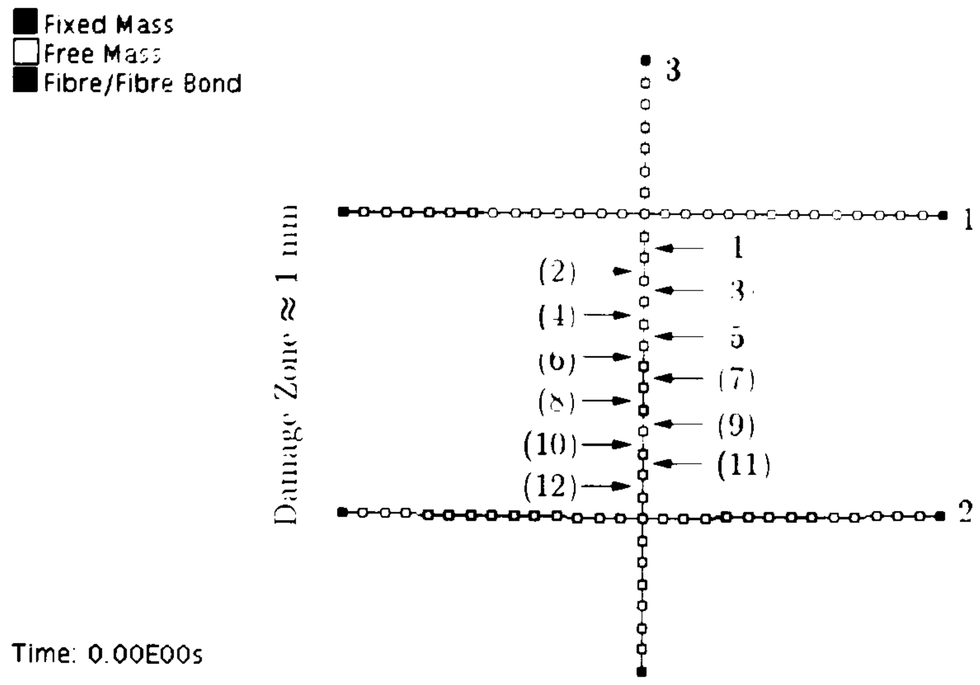

Figure 4.19: 2x1 Fibre Structure with Potential Fibre Failures

in contrast to that of an undamaged fibre, where the dominant movement is perpendicular to that of the fibre.

Physically, as failure occurs, the fibre no longer behaves like a string, instead it behaves like a spring. Equation 4.6.1 presents the well known relationship of the natural frequency of a mass connected to a spring as shown in Figure 3.1.

$$F_n = \frac{1}{2\pi}\sqrt{\frac{k}{m}} = \frac{1}{2\pi}\sqrt{\frac{Et_s w_s}{Lm}} \tag{4.6.1}$$

where:

F_n Natural Frequency of Oscillation

E Young's Modulus of the Paper Fibre

t_s Thickness of the Paper Fibre

w_s Width of the Paper Fibre

L Free Vibrating Length of the Paper Fibre

m Mass of the Paper Fibre

Using Equation 4.6.1, it is possible to predict an approximate frequency of the AEs generated from the fibre failure damage mechanism. Figure 4.20 presents the predicted frequency of oscillation of a simple mass/spring system using the average material properties of paper with varying spring length.

It is important to stress that the predicted frequencies shown in Figure 4.20 are approximate as the mass/spring system shown in Figure 3.1 is connected to a fixed point, whereas the failing fibre in Figure 4.19 is connected to a flexible fibre structure.

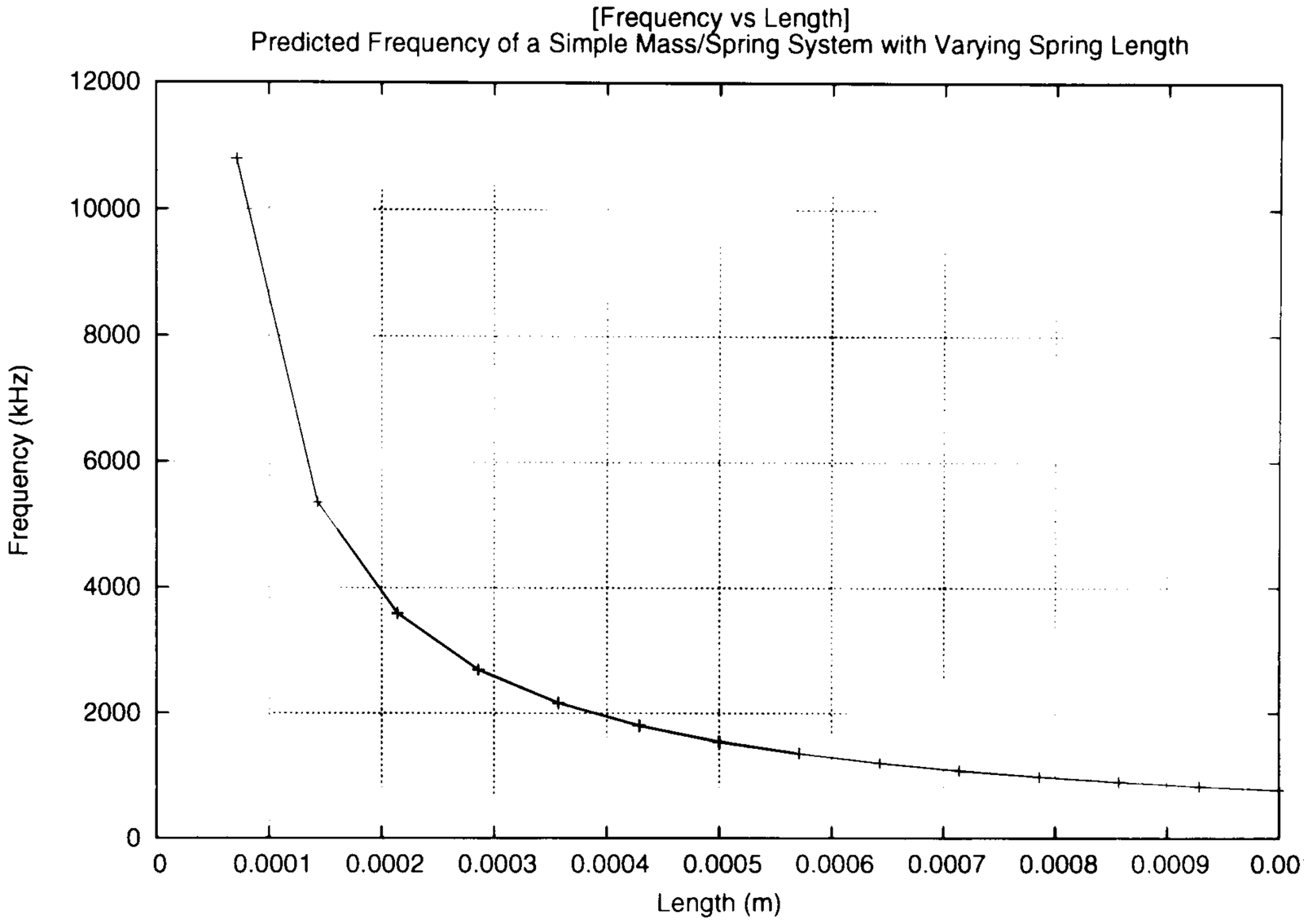

Figure 4.20: Predicted Frequencies of Oscillation of the Simple Mass/Spring System with Varying Spring Length

Figure 4.19 shows 12 points, denoted by (1) to (12), at which failure of the fibre can occur. For example, failure of the fibre at point (1) leaves two smaller fibres with one end fixed and one end free. Figure 4.23 shows the fundamental frequency of the AE resulting from when failure occurs at each point. Each occurrence of the damage mechanism will produce a pair of fibres where the sum of the individual lengths is equal to the original length of the fibre. The two smaller fibres, according to Figure 4.23 will produce two distinct frequencies, unless they have exactly the same length. It is also important to note that the failure of a fibre produces a monopole source at the point of failure, in contrast to the failure of a fibre/fibre bond which produces a dipole source along the length of the vibrating fibres. Figure 4.21 shows that the method for coupling the mass/spring model

to the acoustic wave equation described in Section 3.4.1 reproduces the monopole source when a fibre fails. The change in mass of the grid cells where there is an introduction of mass and a reduction of mass is effectively zero, which leaves an initial net reduction of mass located around the point of failure.

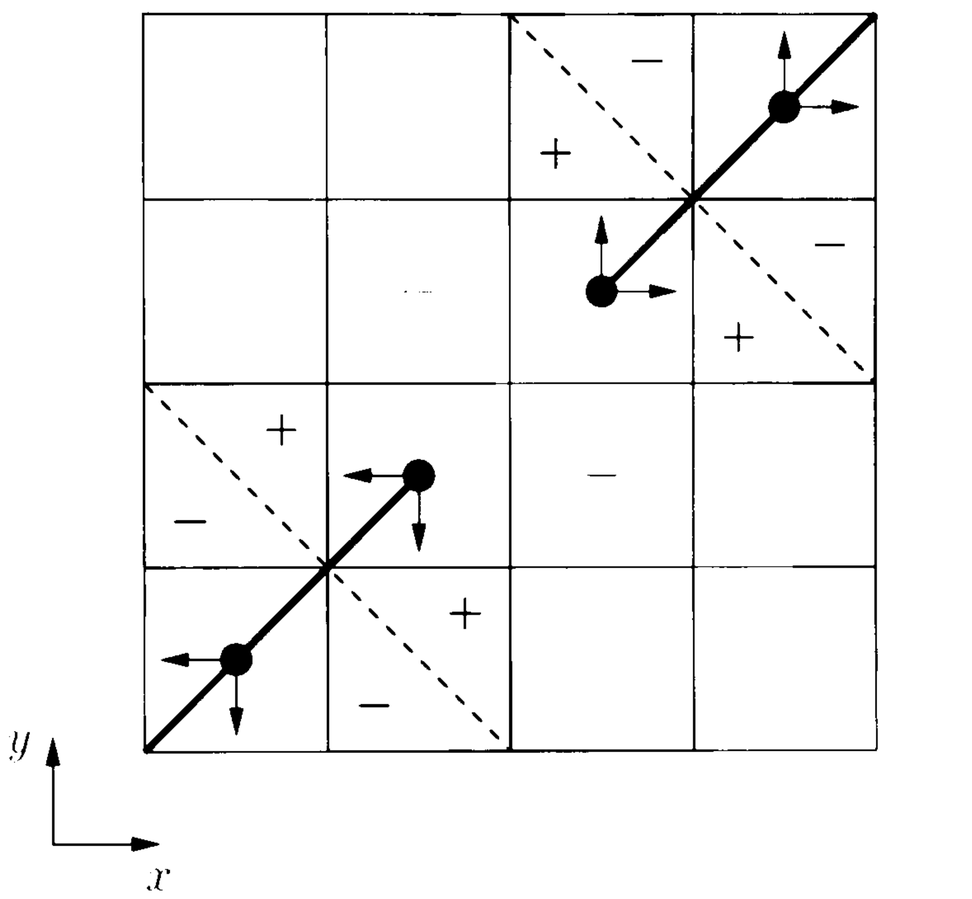

Figure 4.21: Resulting Monopole Source from a Fibre Failure

Simulations of the damage mechanism have suggested that only one frequency produced by the fibre failure is dominant. This can be explained by the tension in the local fibre structure. Consider the fibre structure in Figure 4.19 where the fibre in question, denoted by 3, is connected to two other fibres at each end, denoted by 1 and 2. The system is stretched along the length of fibre 3, so that fibre 2 is under a higher tension than fibre 1 as shown in Figure 4.22. As fibre 3 fails, the lower tension in fibre 1 causes it to absorb more of the resulting movement of its connected half of fibre 3. In contrast, as fibre 2 is under a higher tension, it is unable to absorb the movement of the other half of fibre 3. This results in an AE with a fundamental frequency which is proportional to the length of the half of

fibre 3 which is connected to fibre 2.

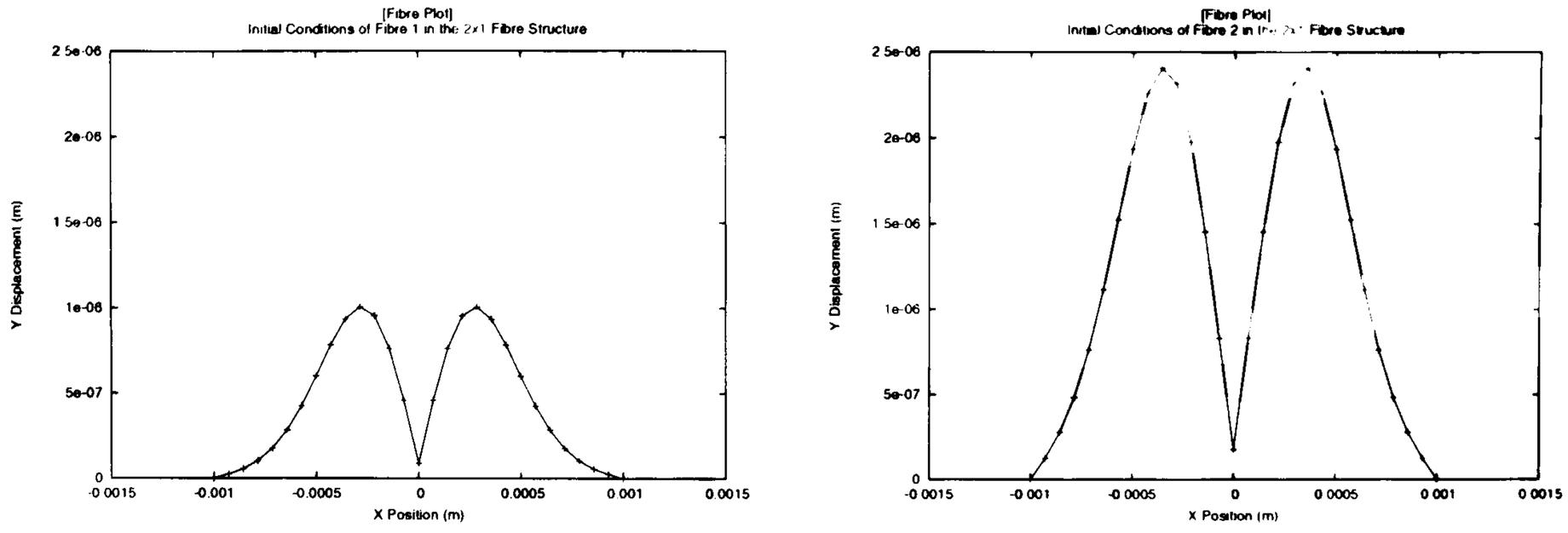

(a) Fibre 1 in the 2x1 Fibre Structure

(b) Fibre 2 in the 2x1 Fibre Structure

Figure 4.22: Initial Conditions of Fibres 1 and 2 in the 2x1 Fibre Structure

Figure 4.23 shows a linear relationship between the frequency and the length of the fibre after failure has occurred. Although the relationship in Figure 4.23 differs from that in Figure 4.20, it is possible to propose a more general correlation between the frequency and length of the fibre as shown in Equation 4.6.2.

$$F \propto \frac{1}{L} \tag{4.6.2}$$

It is also important to investigate whether the extension of fibre 3 is a factor on the resulting AE of the fibre failure. Figure 4.24 shows the power spectrum of 6 fibre failures as the extension in the fibre is increased from 1.0% to 2.0%. It shows that the fundamental frequency of the AE remains constant at around 1175 kHz, with the SPL at this frequency increasing as the extension increases. Therefore, a higher tension in a failing fibre causes a stronger AE to be generated, but has no effect on its dominant frequency. This behaviour is unlike that of an undamaged fibre, where an increase in the tension causes an increase in the frequency of the AE. It is important to note from Figure 4.24 that the frequency content of the AE does slightly increase, most likely due to the increased tension in the surrounding fibre structure.

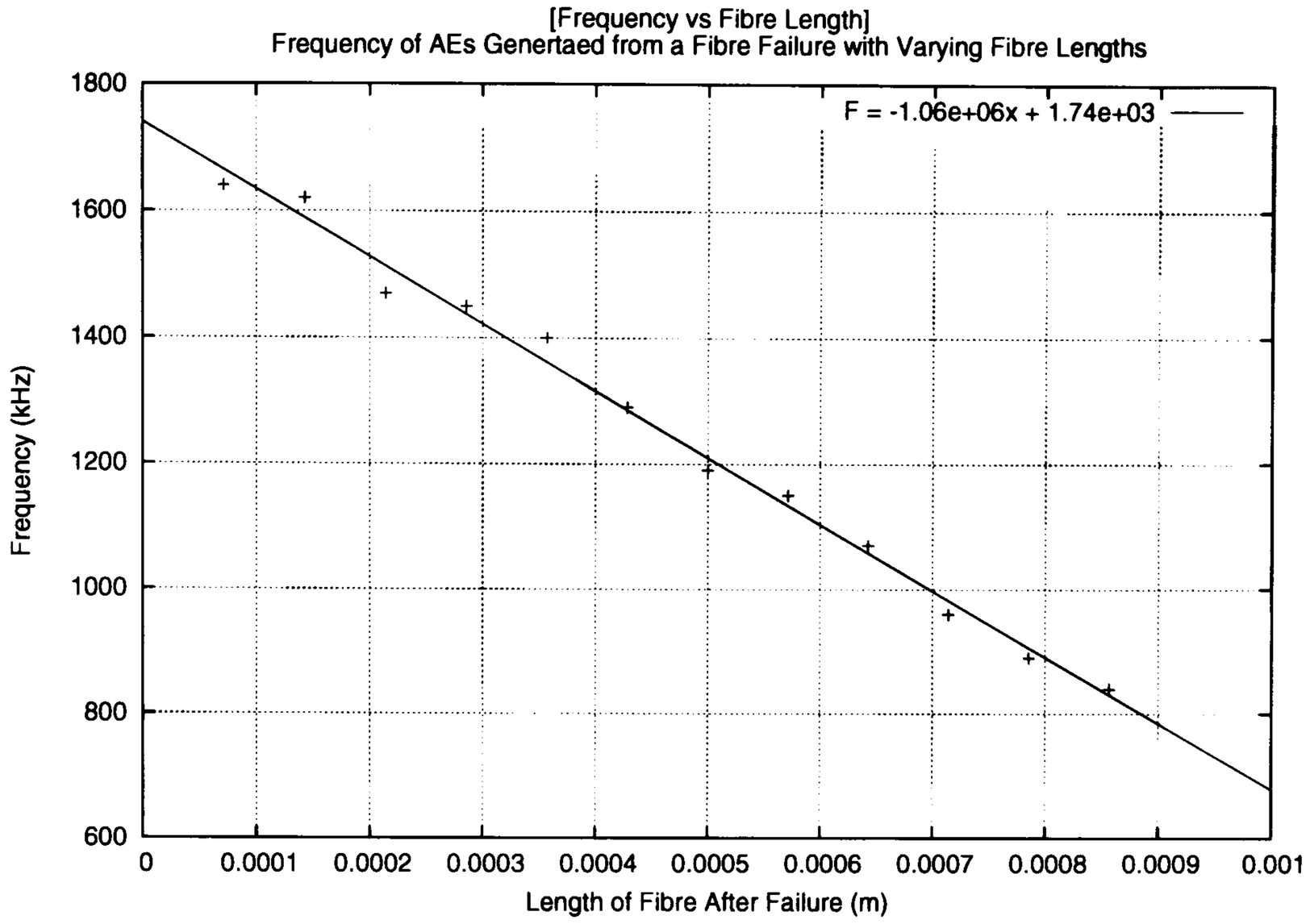

Figure 4.23: Frequency of the AE resulting from a Fibre Failure at Different Points along the Fibre

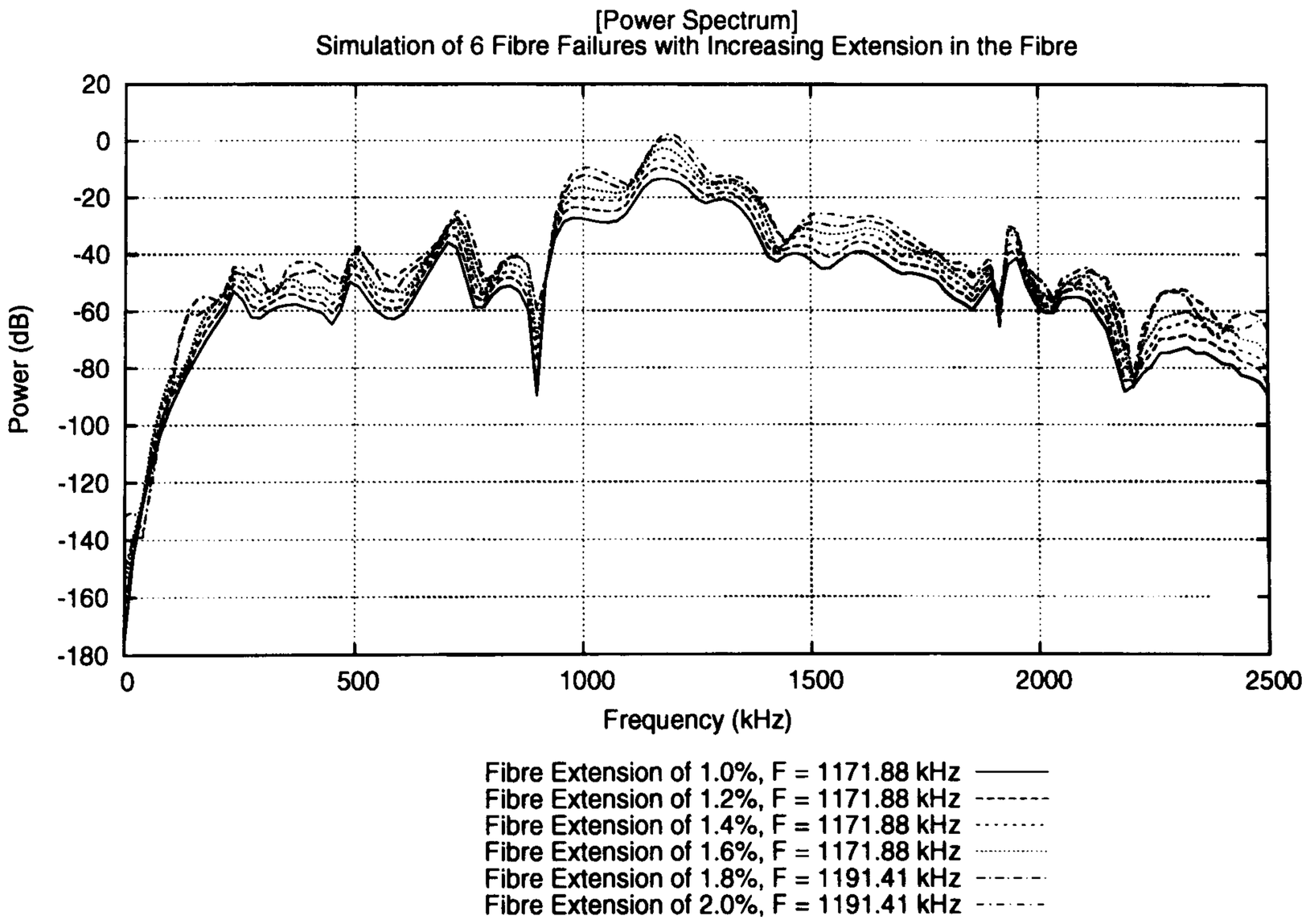

Figure 4.24: Power Spectrum of 6 Fibre Failures with Increasing Extension in the Fibre

To summarise, the expected frequency range of an AE resulting from the failure of a fibre with average material properties is between 800 kHz and 1700 kHz as shown in Figure 4.23. Section 4.6.2 describes the numerical aspects of the implementation of the fibre failure damage mechanism, with Section 4.6.3 presenting the results generated from the 2x1 fibre structure. Equivalent experimental results can be found in Section 4.6.4.

4.6.2 Numerical Implementation of the Fibre Failure Damage Mechanism

The failure of a fibre is conceptually simpler with regard to the numerical implementation than the failure of a fibre/fibre bond. There are no additional assumptions to the fibre structure as there are with the fibre/fibre bond failure. However, a single manipulation of the mass/spring model is required. The failure of a fibre can be represented by simply removing the spring that connects two masses together. In terms of the material properties of that spring, the stiffness is simply set to zero.

The accuracy of this method is dependent on the spring length; a larger spring length results in a larger section of the fibre being removed. The sum of the length of the resulting two fibres is always less than the length of the original fibre. As the frequency is inversely proportional to the length of the split fibre, a larger discrepancy in the sum of the fibre lengths produces a larger error in the frequency. The fundamental frequency of the resulting AE will always be slightly higher than that of the experimental data, due to the removal of a section of fibre.

The pseudocode of for the failure of a fibre can be seen in Algorithm 9.

Algorithm 9 Simulating a Fibre Failure

```
1: if Fibre Failure = TRUE then
2:     i ← damaged spring
3:     k_i ← 0
4: end if
```

Also of interest is how the dynamic subtraction of a spring in the mass/spring model changes the structure of $A\left(I + \Delta t M^{-1}\frac{\partial \mathbf{f}^n}{\partial \mathbf{u}} + \Delta t^2 M^{-1}\frac{\partial \mathbf{f}^n}{\partial \mathbf{r}}\right)$ as given in Equation 3.2.29. The shape of A before and after the failure of the fibre in a 2x1 fibre structure where each fibre consists of 9 masses and 8 springs can be seen in Figure 4.25.

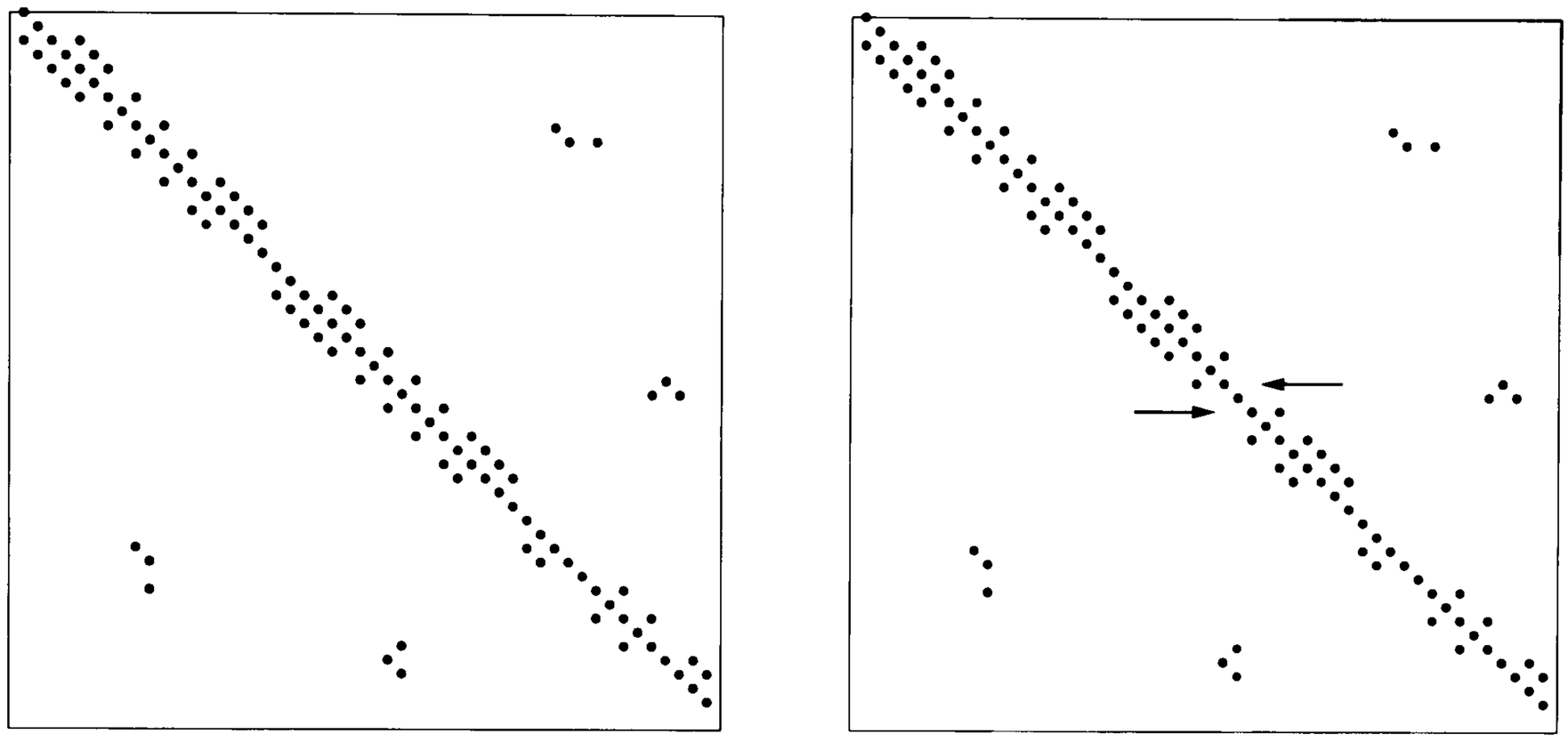

(a) Before Failure (b) After Failure

Figure 4.25: Changes in Matrix A due to the Failure of a Fibre

The arrows in Figure 4.25(b) show the absence of certain elements in matrix A caused by the removal of a spring in the fibre structure. The matrix A remains asymmetric due to the fixed masses within the mass/spring system.

4.6.3 Theoretical Results of a Fibre Failure

This section will present three sets of results, each showing the AE and CWT resulting from the failure of a fibre at different points in the 2x1 fibre structure. Figures 4.26 and 4.27 show the removal of springs (1) and (12) shown in Figure 4.19, each producing an unequal pair of fibre segments. The short segment near fibre 1 after the removal of spring (1) has the same length as the short segment near fibre 2 after the removal of spring (12). The corresponding long segments also match in length. However, the CWTs in Figures

4.26 and 4.27 show two different dominant frequencies. Namely, 800 kHz in the case of Figure 4.26 and 1750 kHz in the case of Figure 4.27. This is the result of the difference in tension of fibres 1 and 2 as explained in the previous section. For completeness, Figure 4.28 shows the AE and CWT of the failure of spring (7) in the 2x1 fibre structure. The removal of spring (7) creates fibre segments of lengths different to those in Figures 4.26 and 4.27. This results in the different dominant frequency of 1250 kHz.

4.6.4 Experimental Evidence of a Fibre Failure

The experimental results presented in this section have been acquired from a typical notched paper sample under load. The failure of a fibre is rare event in paper, generating only a handful of AEs in the experimental data. Opinion is very much divided in the paper physics community as to whether fibre failures actually occur [119], or if the fibre/fibre bonds fail and the damage zone just slides apart.

Figure 4.29(a) shows a typical undamaged paper sample, with Figure 4.29(b) showing the same paper sample at 98% of the average fracture load. The damage zone is marked by the circles. Figures 4.29(c) and 4.29(d) show a close up of a region in the damage zone before and after damage has occured, respectively. Figure 4.29(d) shows that the fibre in the white circle has failed. Therefore, fibre failure occurs in paper samples subjected to axial loads.

The theoretical results have shown that the CWT of an AE resulting from a fibre failure has a distinct form. *The fibre failure causes an acoustic pulse, rather than the acoustic wave, produced from a fibre/fibre bond failure.* In terms of the CWT, this produces a strong high frequency component above 800 kHz, with a *duration of less than 5.00E-06 seconds.* Figure 4.30 shows the CWT of 6 typical AEs of suspected fibre failures chosen from the experimental data.

The experimental results in Figure 4.30 show that the high frequency short duration

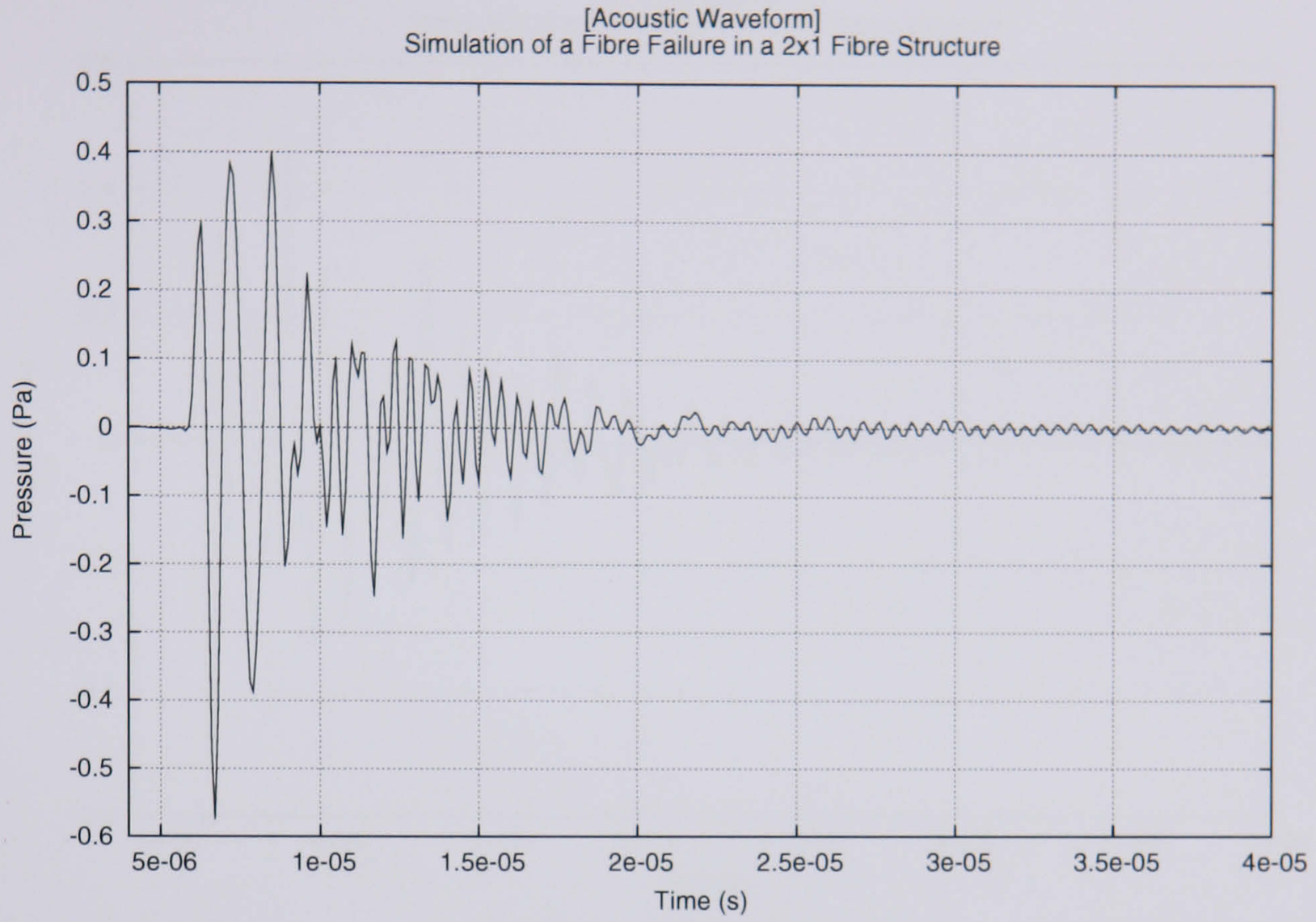

(a) Acoustic Waveform

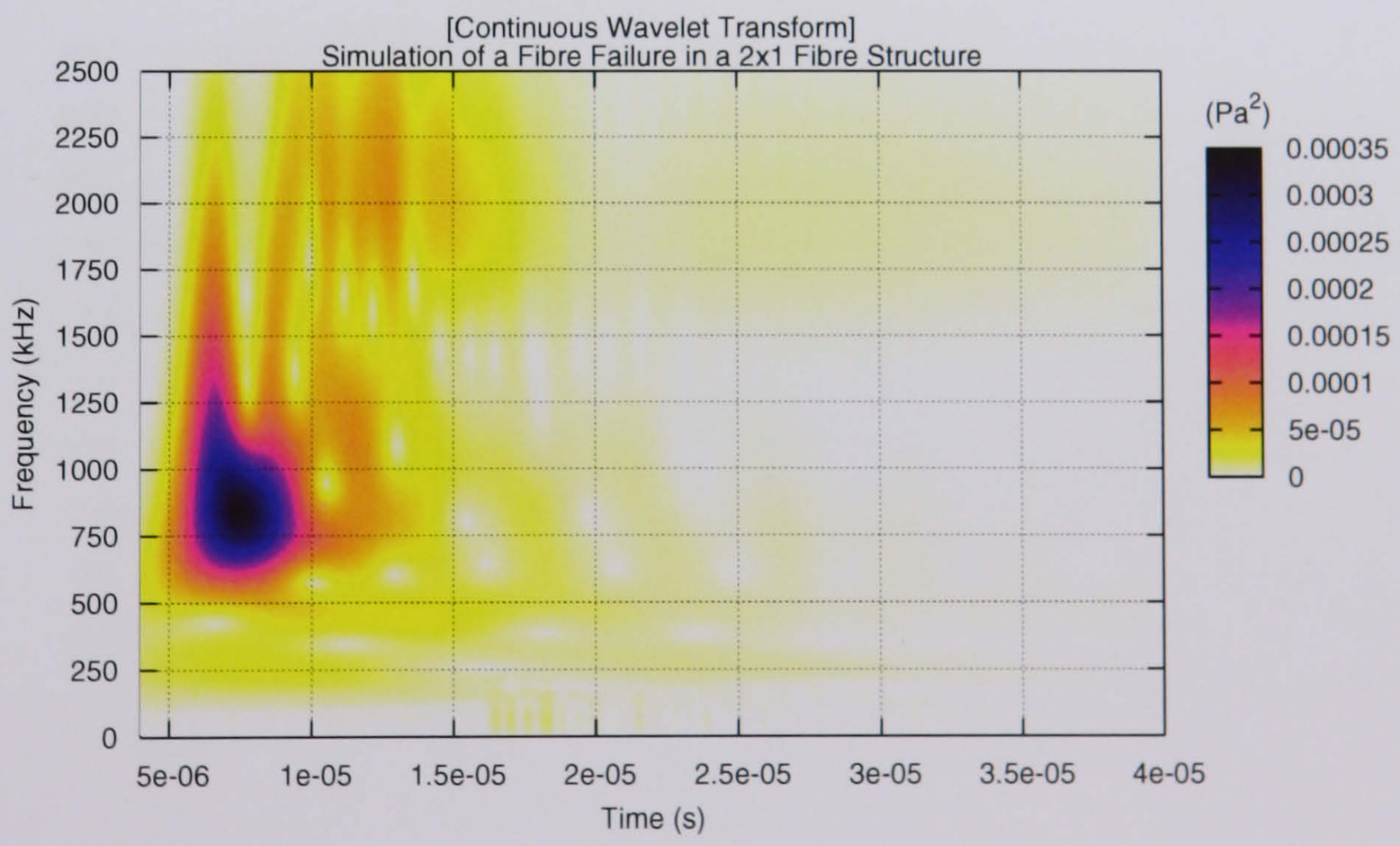

(b) Continuous Wavelet Transform

Figure 4.26: Results of a Theoretical Fibre Failure Denoted by (1) in a 2x1 Fibre Structure

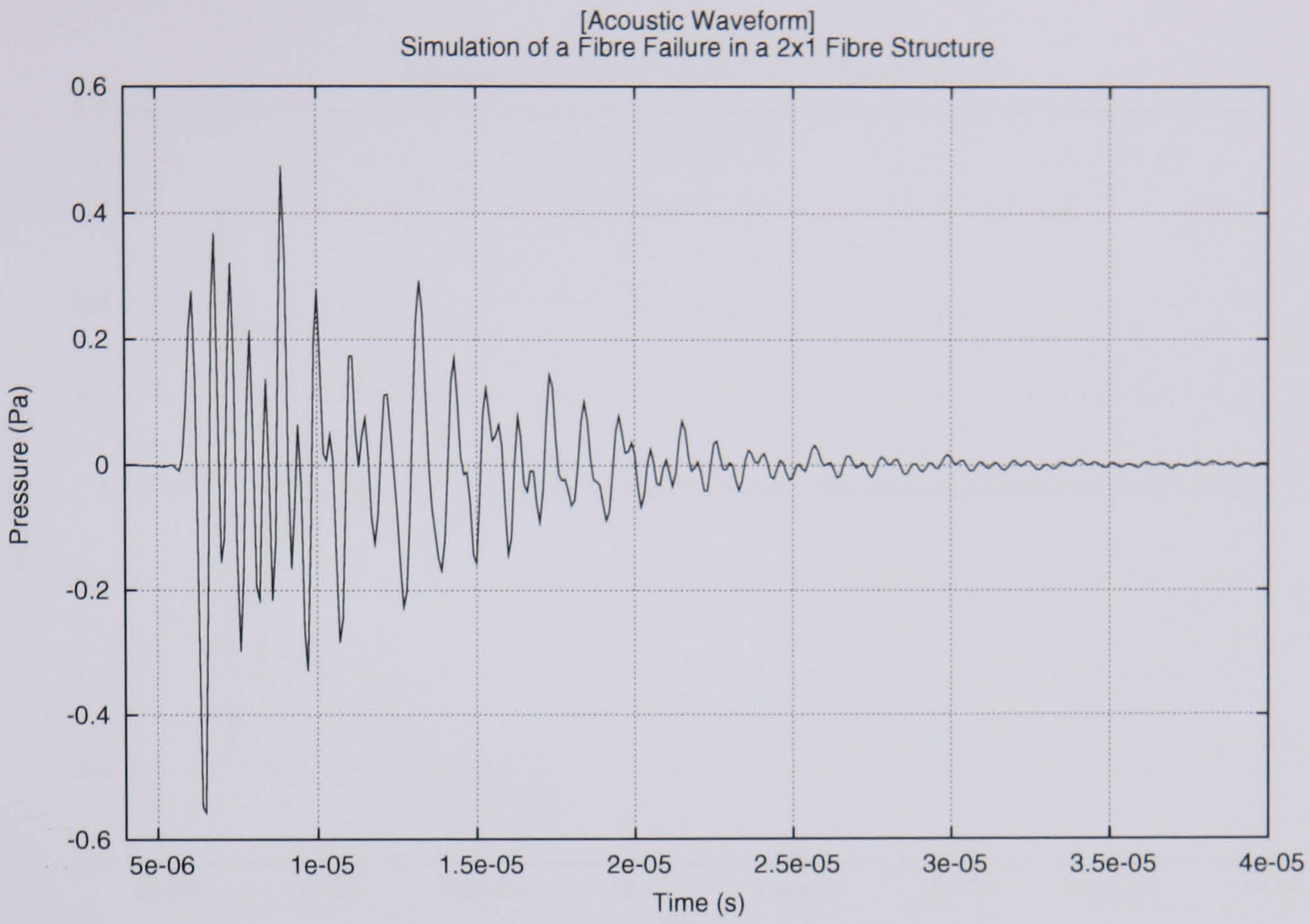

(a) Acoustic Waveform

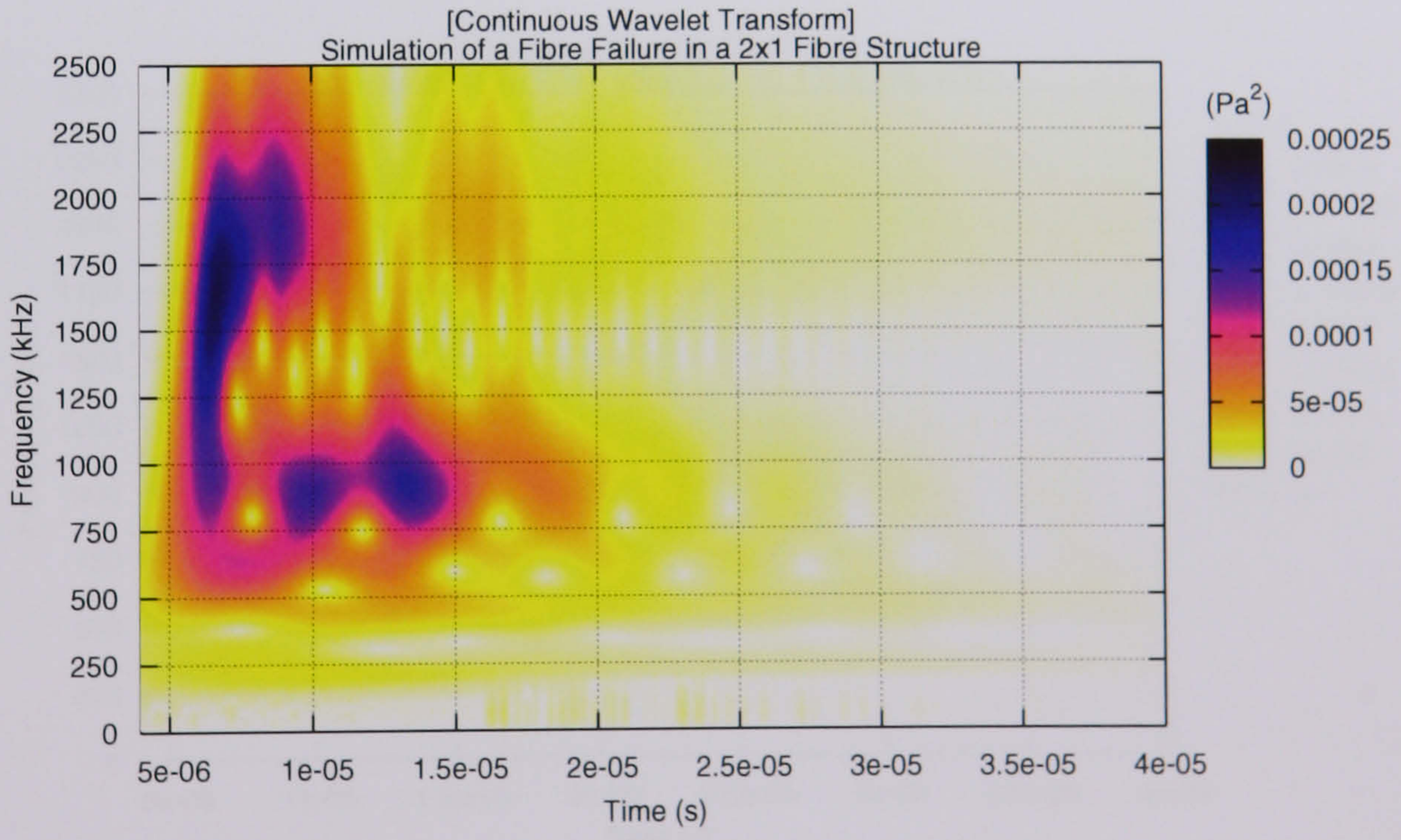

(b) Continuous Wavelet Transform

Figure 4.27: Results of a Theoretical Fibre Failure Denoted by (12) in a 2x1 Fibre Structure

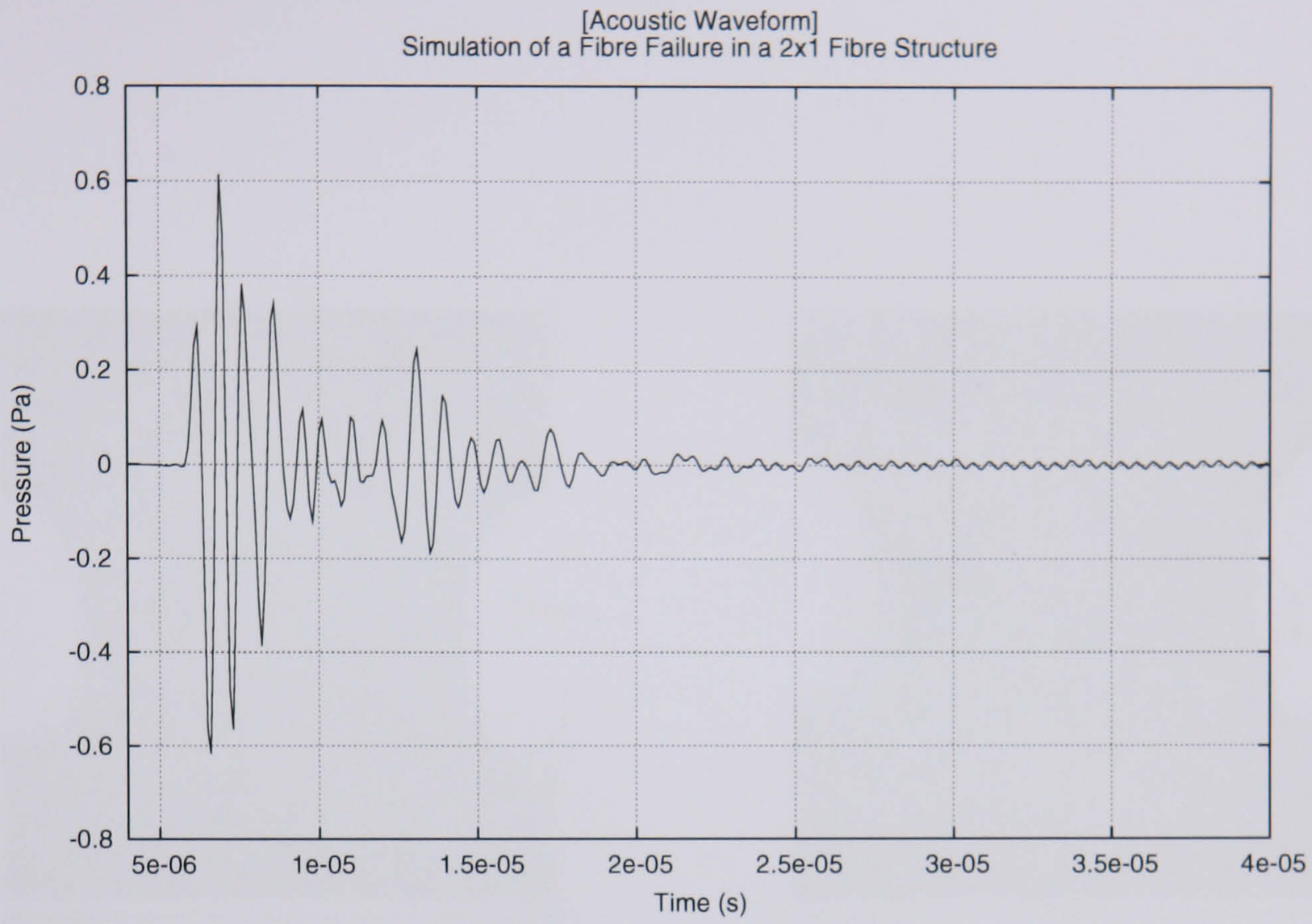

(a) Acoustic Waveform

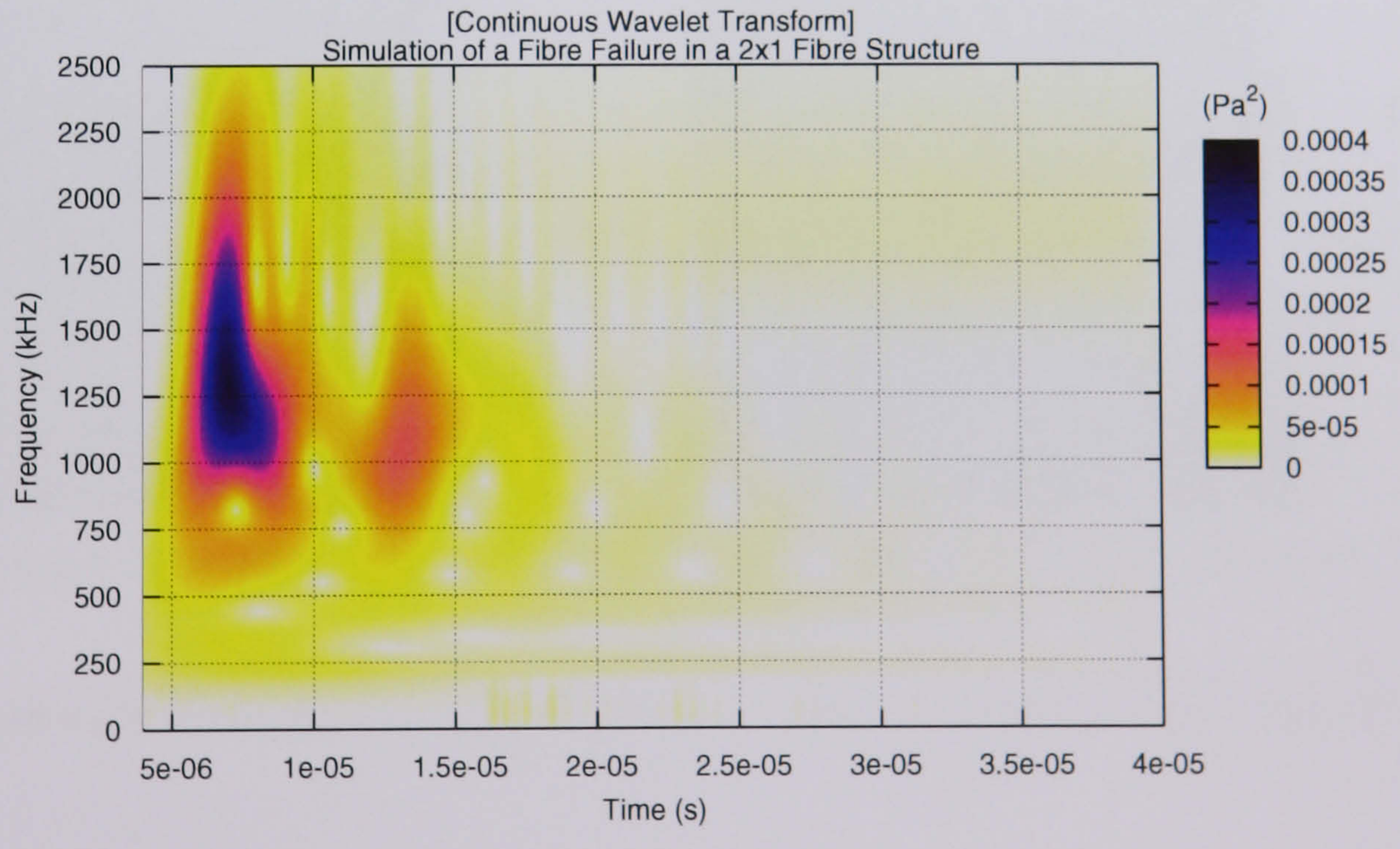

(b) Continuous Wavelet Transform

Figure 4.28: Results of a Theoretical Fibre Failure Denoted by (7) in a 2x1 Fibre Structure

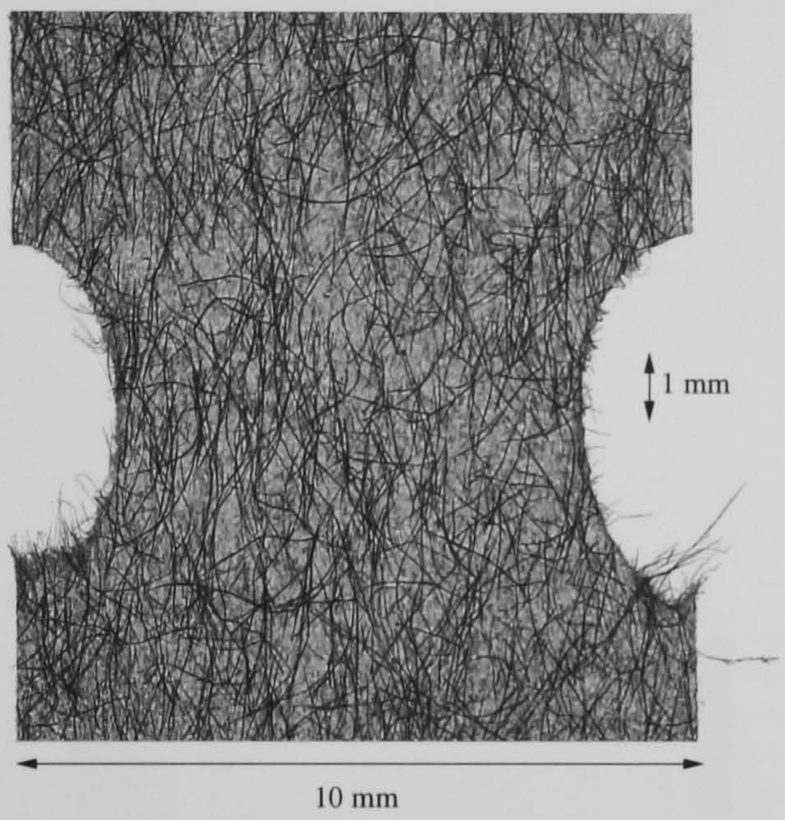

(a) Undamaged Paper Sample

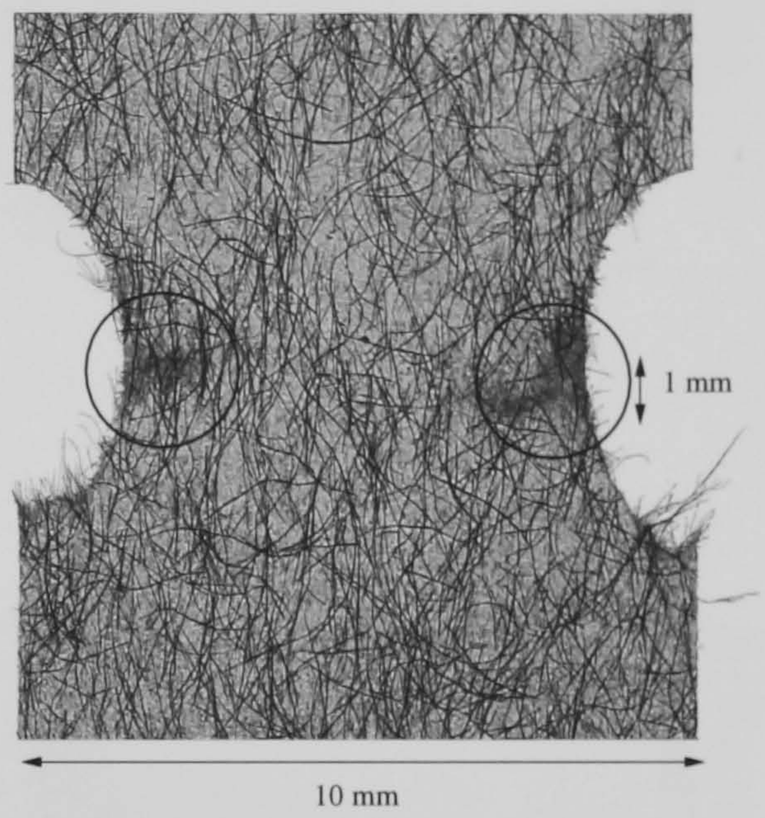

(b) Paper Sample at 98% of Failure Load

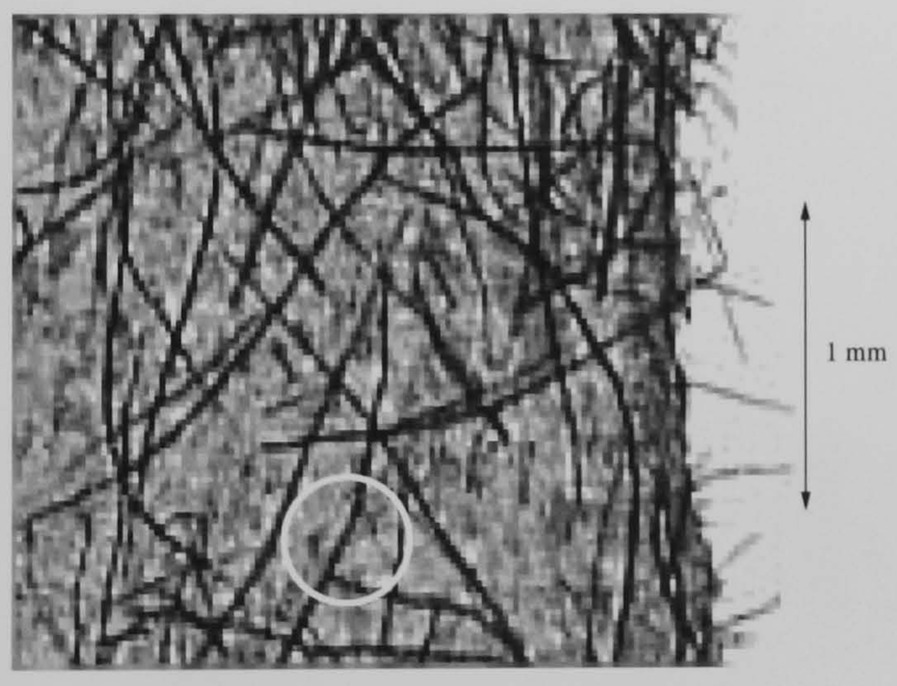

(c) Undamaged Paper Sample - Notched Area

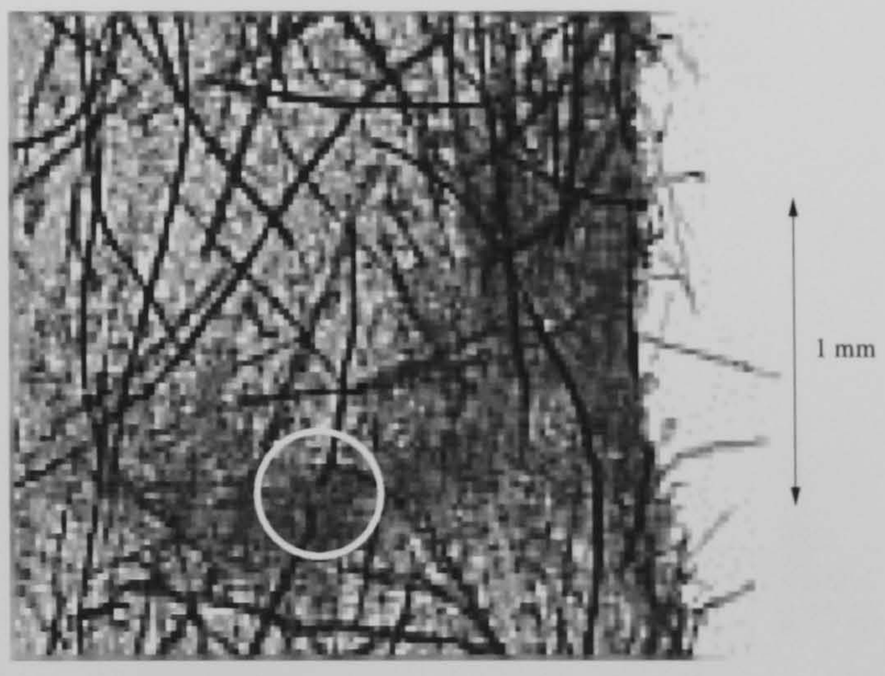

(d) Paper Sample at 98% of Failure Load - Damage in Notched Area

Figure 4.29: Example of a Fibre Failure in a Typical Notched Paper Sample

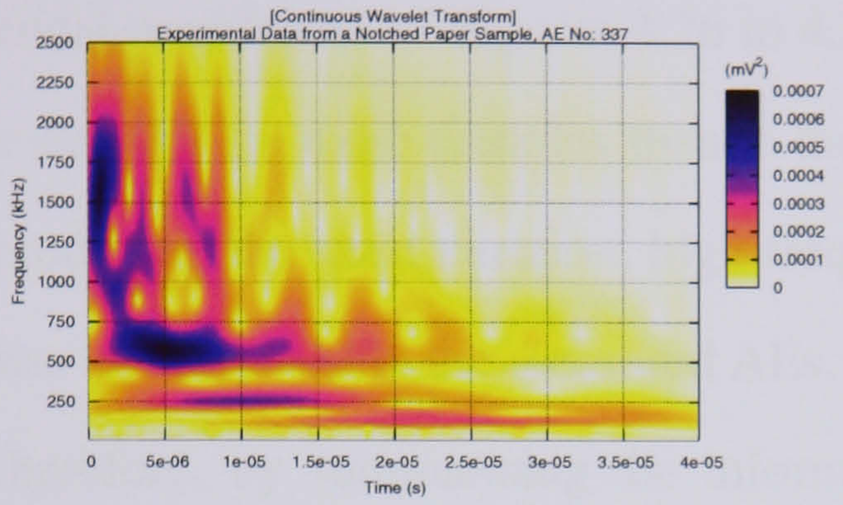

(a) AE No: 337

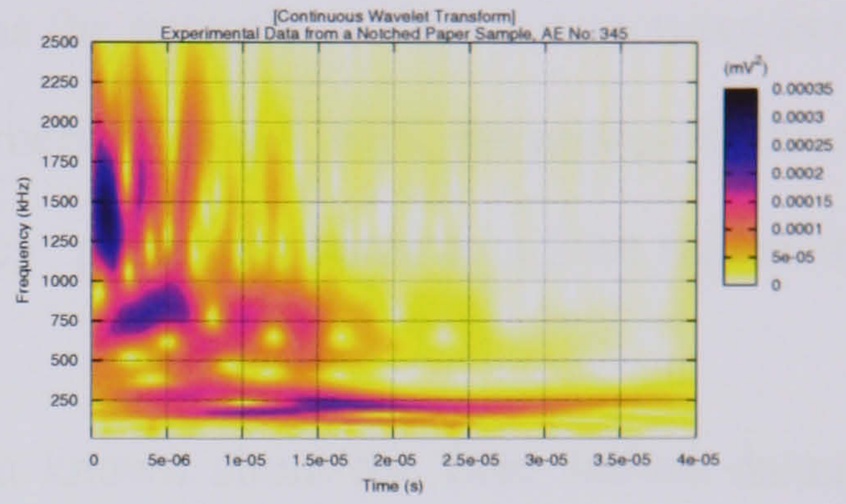

(b) AE No: 345

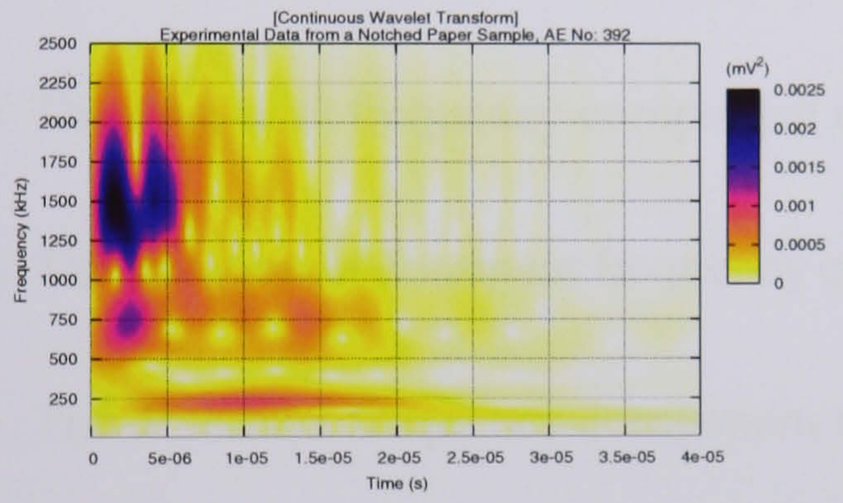

(c) AE No: 392

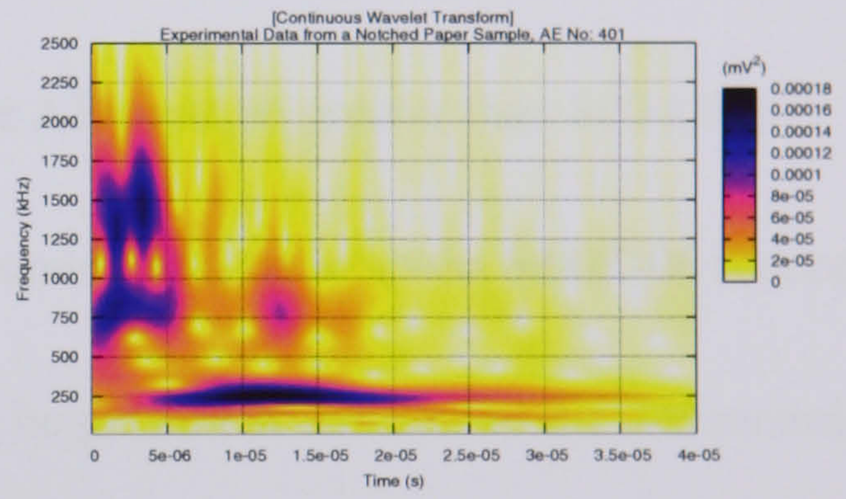

(d) AE No: 401

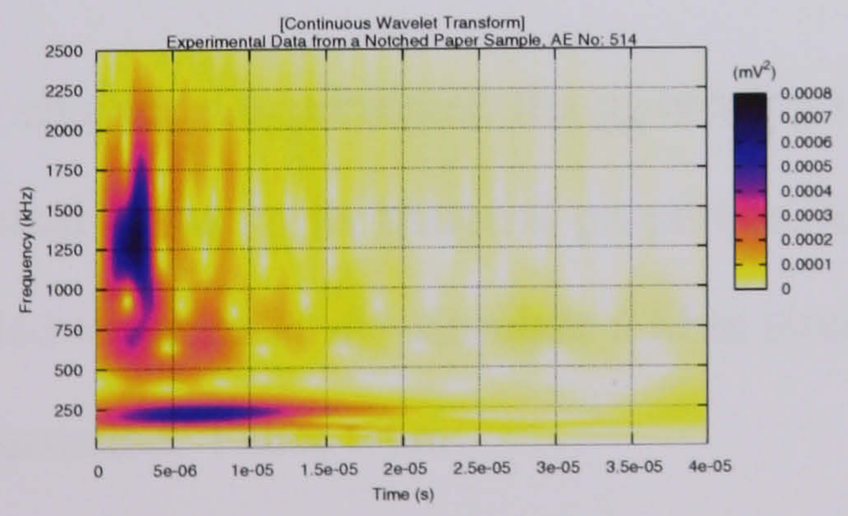

(e) AE No: 514

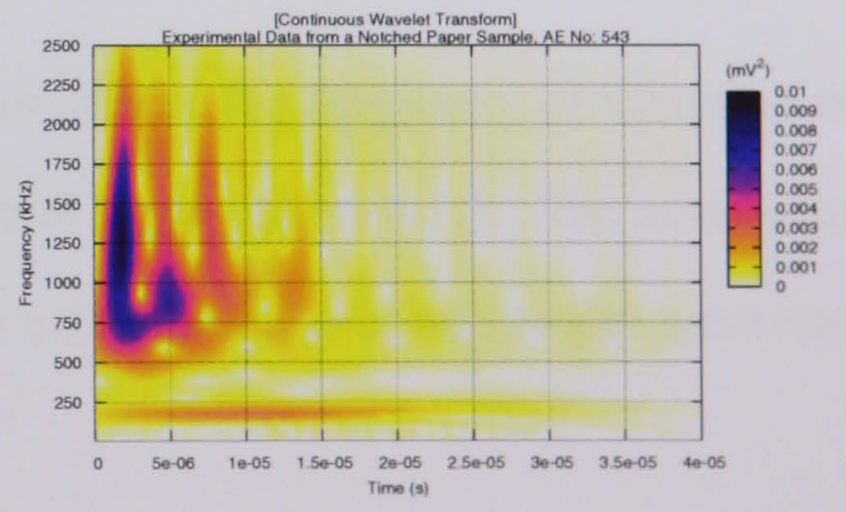

(f) AE No: 543

Figure 4.30: The CWTs of 6 AEs from Suspected Fibre Failures in a Notched Paper Sample

'pulses' due to the failing fibres in the selected AEs are accompanied by lower frequency oscillations of lower amplitude, attributable to the vibration of the surrounding structure that is excited by the fibre failure event. This lattice feature was less prominent in the numerical predictions of Figures 4.26 to 4.28, as the network of fibre connections in the paper samples are more complex than in the numerical model. Still, the numerical model is reproducing the short duration, high frequency 'pulse' attributed to a fibre failure that can also be identified in the measured AEs.

Therefore, by summarising the information known about the fibre failure damage mechanism, it is proposed that the CWT of an AE generated from a fibre failure must satisfy the following conditions:

- The dominant frequency component of the AE must be greater than 800 kHz.
- The duration of dominant frequency component must be less than 5.00E-06 seconds.
- The dominant frequency component must be present at the start of the AE record.

4.7 Summary

This chapter has presented the governing relationship of the frequency of vibration of a classical string to its material properties, as shown by Equation 4.2.2. The assumptions needed to successfully simulate a fibre structure using the mass/spring model were stated and justified. These were:

- The free vibrating length of a paper fibre is equal to 1 mm.
- The extension in the length of the paper fibre is equal to 1%.
- The average material properties of a paper fibre are as stated in Table 4.1.

- The paper fibre mass is evenly distributed along its length, resulting in a lumped mass model with 29 masses.

The first system to be simulated was that of a single vibrating fibre to ascertain its fundamental frequency. The frequency produced was approximately 250 kHz. This provides the starting point for the analysis of the AEs produced from the fibre/fibre bond failures and fibre failures. Having modelled the movement of the most basic fibre structure, a 3x3 Cartesian mesh was used to simulate the failure of a fibre/fibre bond. Simulations showed that dominant frequency components existed at 250 kHz and 750 kHz. It was also shown that failure of fibre/fibre bonds gradually decreases the frequency of the recorded AEs when analysed over an entire set of experimental data. Finally, the fibre failure damage mechanism was simulated using a 2x1 fibre structure showing the existence of dominant frequency components above 800 kHz, which are dependent on the point along the fibre at which failure occurs.

Therefore, using the results presented in this chapter, it is possible to state the defining characteristics of the two selected damage mechanisms by looking at the CWT of the resulting AEs. The criteria for identifying a fibre/fibre bond failure are:

- The dominant frequency components of the AE is at approximately 250 kHz or 750 kHz.
- The strongest frequency component maybe at either approximately 250 kHz or 750 kHz.
- The duration of the frequency component at approximately 250 kHz is longer than that of the frequency component at approximately 750 kHz.

The criteria for a identifying a fibre failure are:

- The dominant frequency component of the AE is greater than 800 kHz.

- The duration of dominant frequency component is less than 5.00E-06 seconds.
- The dominant frequency component is present at the start of the AE record.

Chapter 5 describes the use of the above criteria to train an intelligent classifier to dynamically identify AEs from the two damage mechanisms.

Chapter 5

Classification of the Damage Mechanisms

5.1 Overview

This chapter documents the training of an intelligent classifier to dynamically identify the AEs from the two selected damage mechanisms. To achieve this, a Self-Organising Map (SOM) is used, due to its ability to visualise the inter dependencies of high-dimensional data into simple geometric relationships on a two-dimensional grid. A complete description of the SOM from first principles is presented by Kohonen [59]. The software used in this work is known as SOM_PAK and is provided free of charge by Kohonen [120]. Alhoniemi [121] and Honkela [122] provide examples of past research where SOM_PAK has been used.

5.2 Feature Extraction

This section will propose a method for extracting features from the CWT to best represent the criteria set in Sections 4.5.4 and 4.6.4 for the fibre/fibre bond failure and the fibre

failure respectively. The basis of the criteria for distinguishing between the two damage mechanisms is on the frequency and duration of the dominant frequency component in the CWT of the AE. It is clear that the feature extraction method must preserve the general shape of the AE with minimal information loss.

Figure 5.1 shows typical examples of AEs generated from a fibre/fibre bond failure and from a fibre failure respectively. These two AEs will be used as examples in the feature extraction processes.

The feature extraction method involves splitting the normalised CWT of each AE into windows that are 5.00E-06s in duration and cover a frequency range of 100 kHz. This results in 200 windows for which the power ratio W_i is calculated as in Equation 4.5.4 and used as a feature in the SOM. Figure 5.2 shows the location of each of the 200 windows.

This method effectively resamples the CWT with a frequency bandwidth and time interval that are just enough to preserve the relevant time-frequency information in the AEs. Figure 5.3 shows examples of the simplified representation of the CWT for a fibre/fibre bond failure and a fibre failure.

5.3 The Self-Organising Map

This section presents a brief theory of the Self-Organising Map invented by Teuvo Kohonen. For a full discussion of the SOM refer to Kohonen [59]. The software used to produce the SOMs is also supplied by Kohonen [120]. The SOMs used in this work consist of a two dimensional network of nodes in a rectangular lattice. An example of a 4x4 SOM can be seen in Figure 5.4. Each node has a specific topological position in the SOM and consists of a n dimensional weight vector w, where n is the number of features in the input data. For the purpose of this work, $n = 200$.

Before the SOM can be used as a classification tool, it must be trained by a sample of the input data. The training of the SOM consists of three algorithms, the competitive

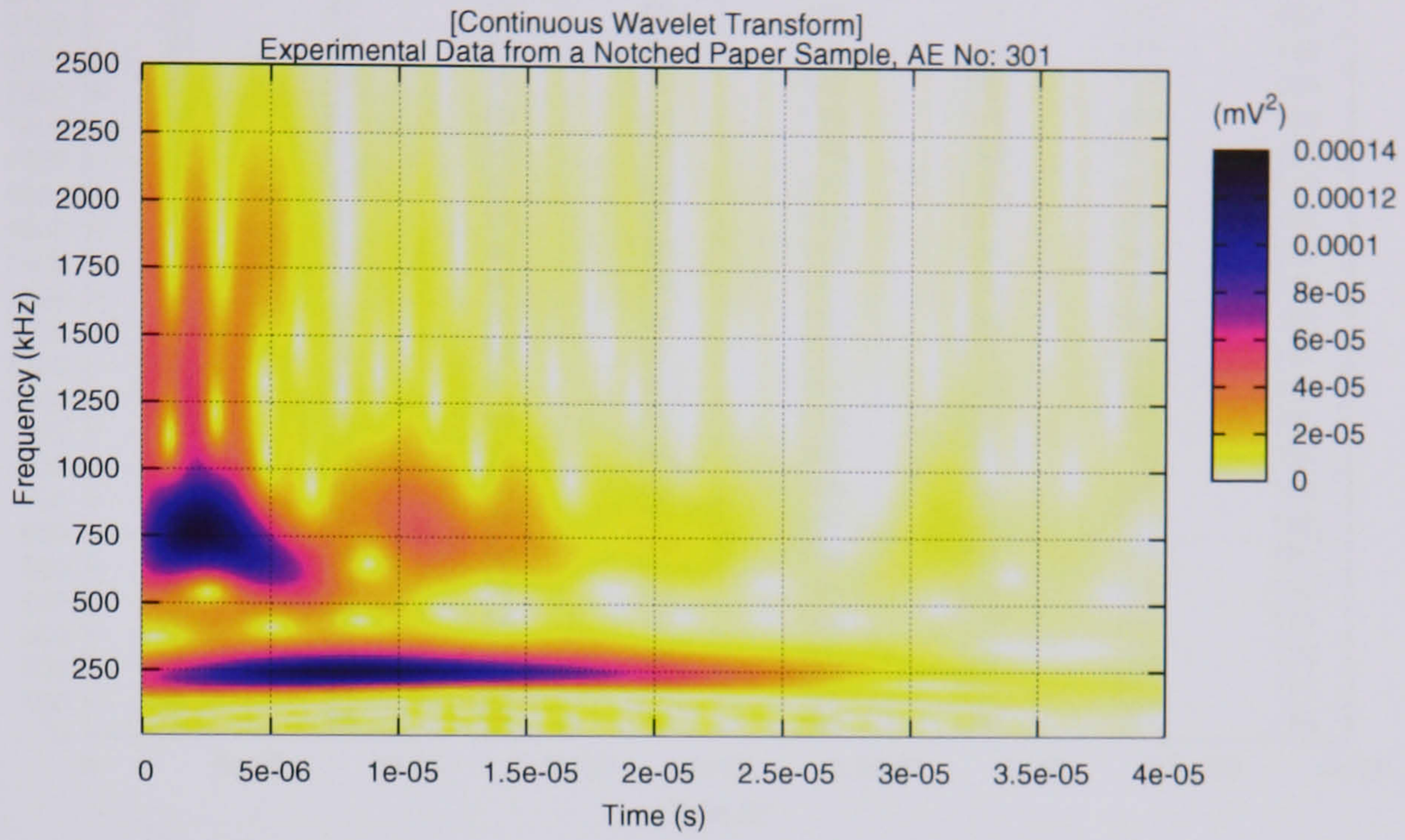

(a) CWT of a Typical Fibre/Fibre Bond Failure

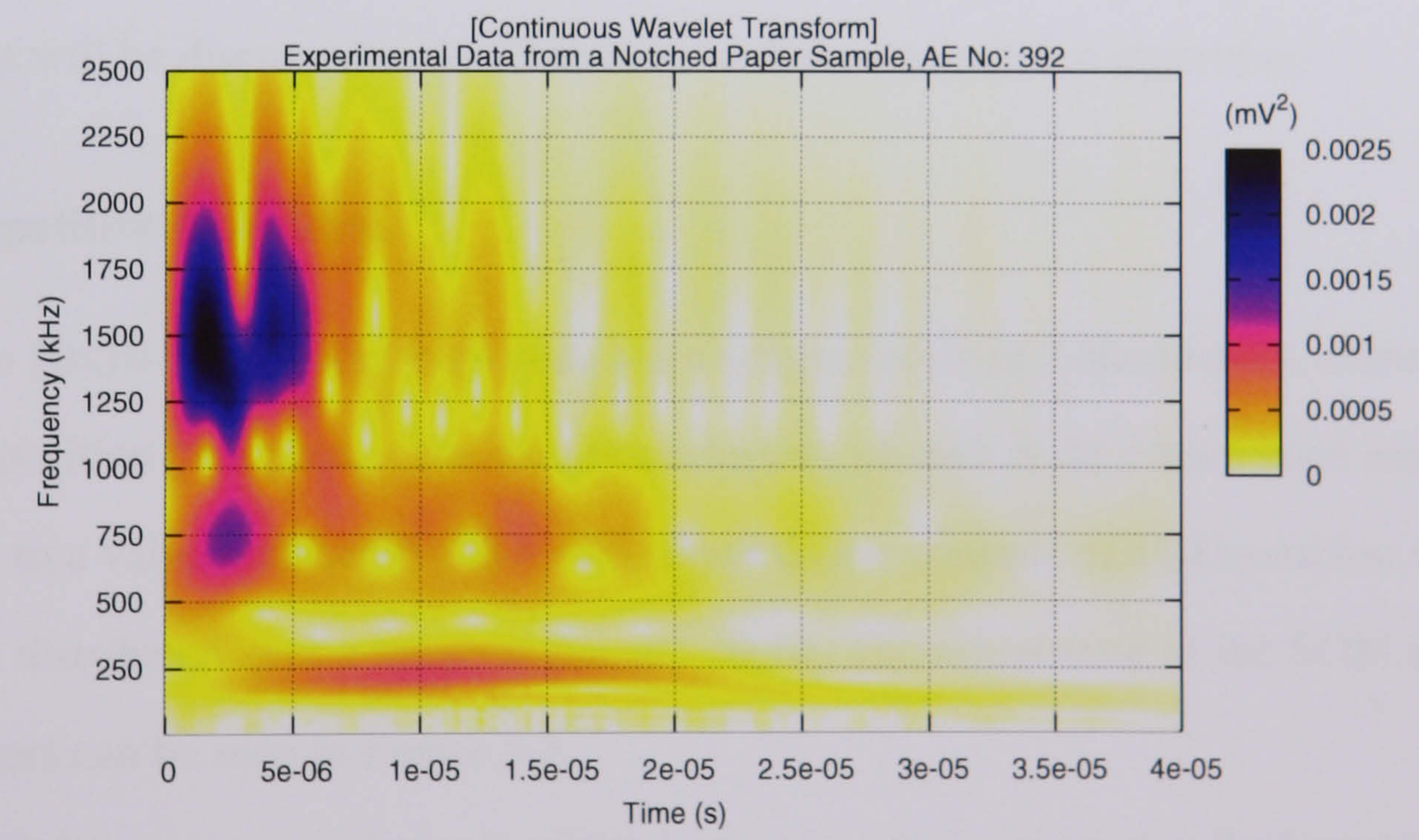

(b) CWT of a Typical Fibre Failure

Figure 5.1: Examples of AEs Generated from a Fibre/Fibre Bond Failure and a Fibre Failure

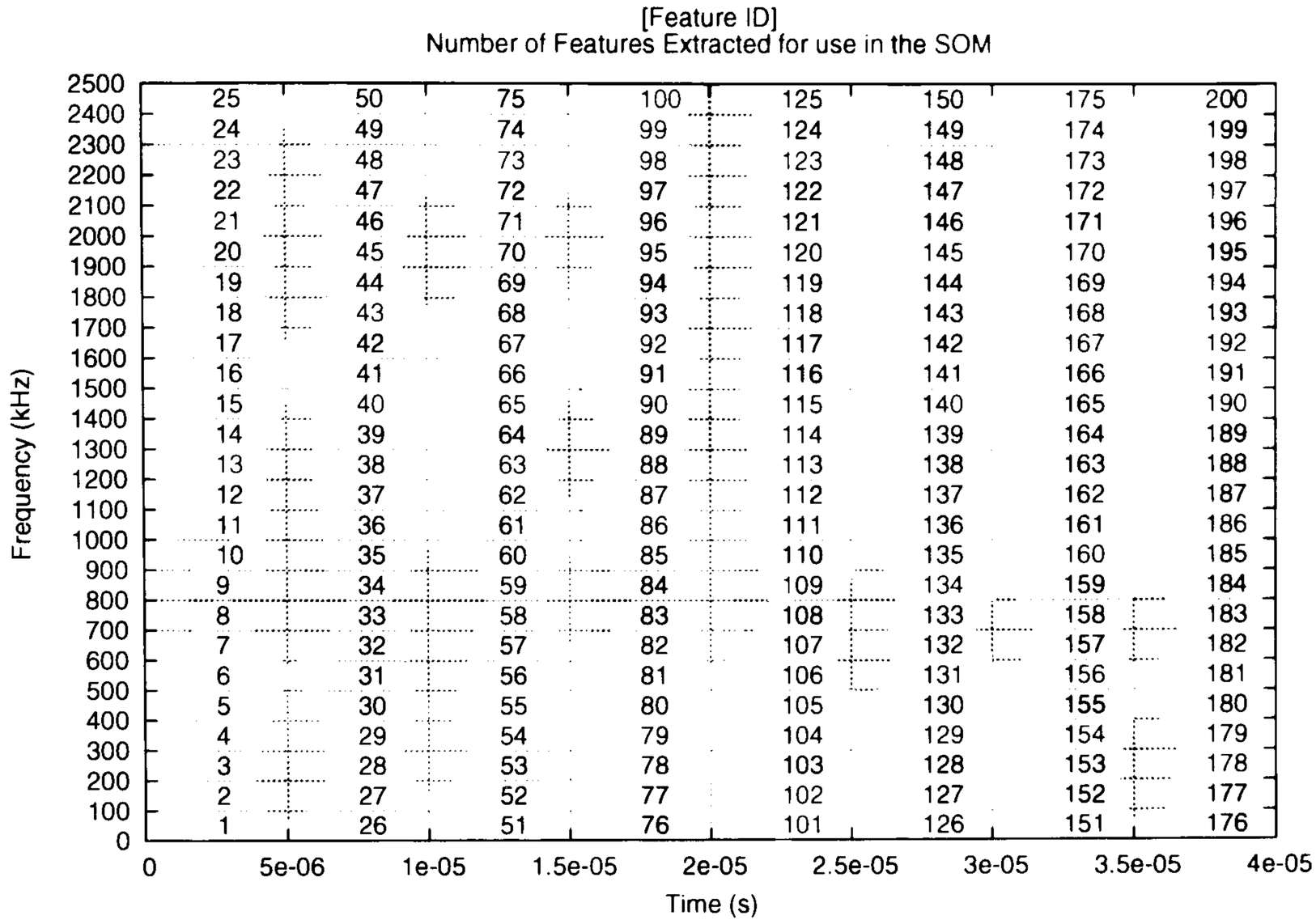

Figure 5.2: Location and Bin Number of the Resampled CWT where Δt = 5E-06 s and Δf = 100 kHz

algorithm, the cooperative algorithm and the synaptic adaptation algorithm. Each of these algorithms will be discussed in detail starting with the competitive algorithm.

The Competitive Algorithm

Consider a 10x10 SOM where each node has a weight vector of 2 dimensions, corresponding to its position on a plane. The weight vectors w_j of each node j have been randomly initialised to a value between 0 and 1. The input data x consists of 1000 position vectors uniformly distributed over a range of 0,0 and 10,10. The initial state of the SOM and the input vectors can be seen in Figure 5.5.

For each input vector x, the node which is most similar is selected as the best matching unit. To do this, the Euclidean distance is calculated between the input vector and each node, as shown in Equation 5.3.1, with the best matching unit being the node with the smallest distance to the input vector.

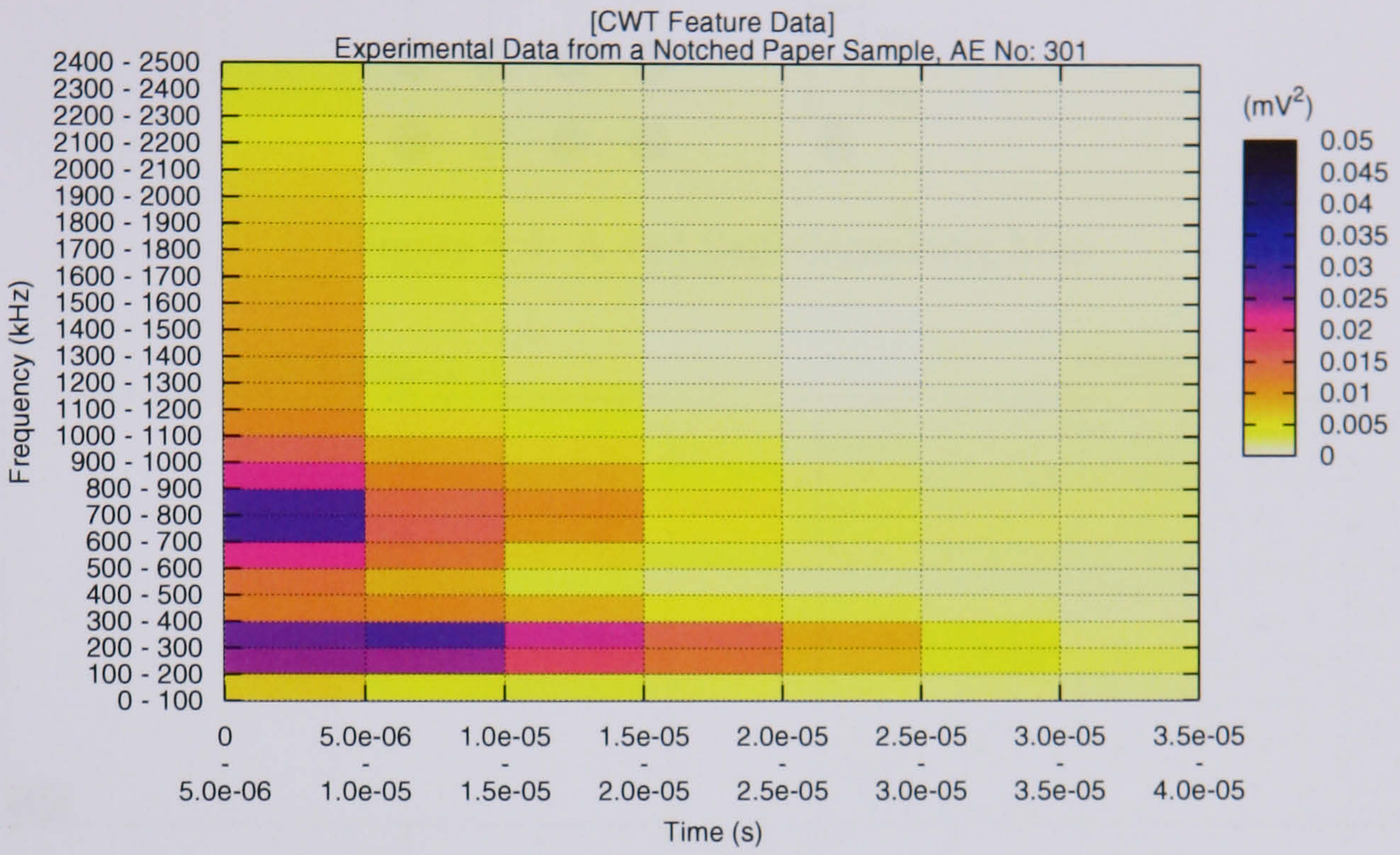

(a) Feature Data of a Typical Fibre/Fibre Bond Failure

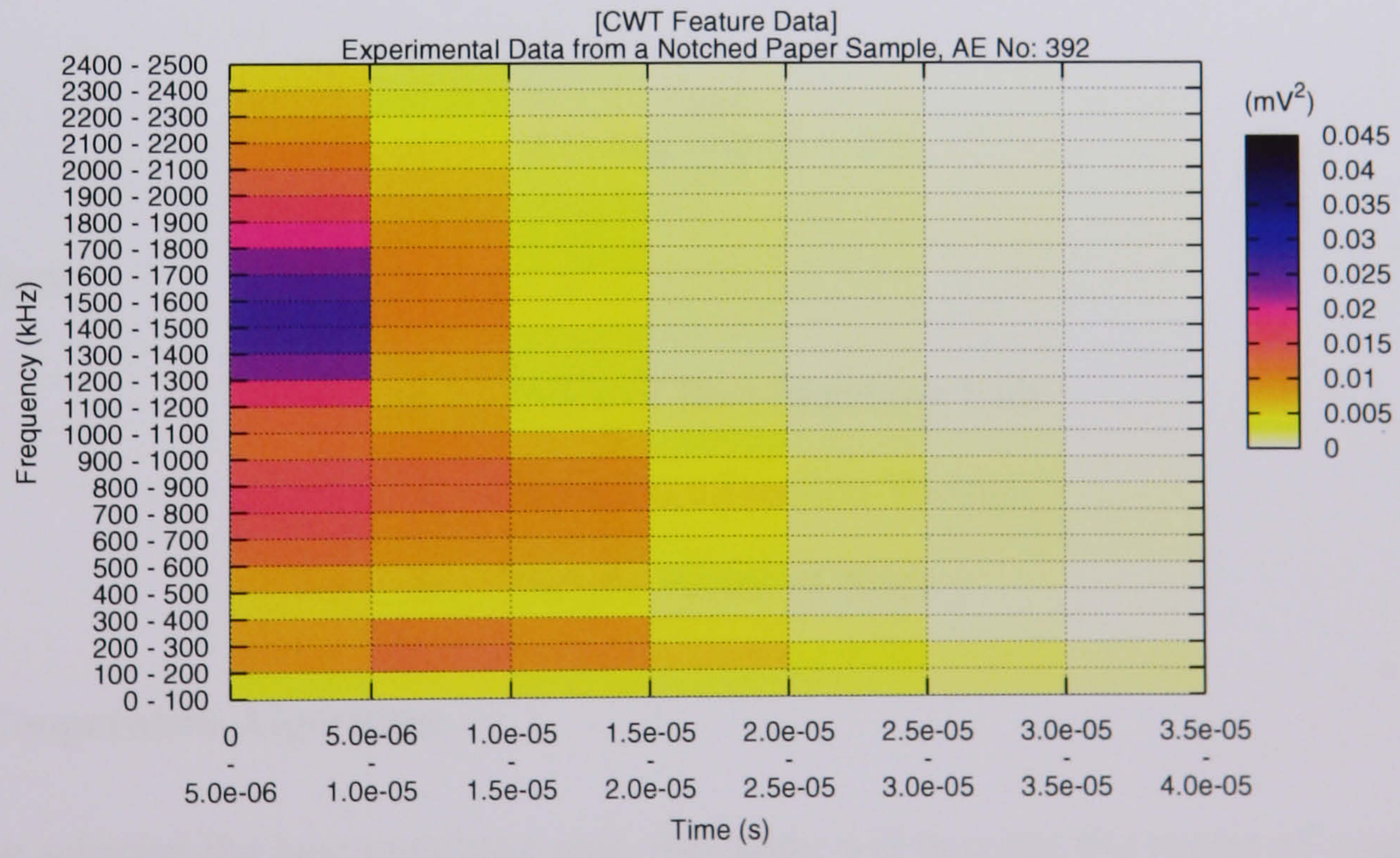

(b) Feature Data of a Typical Fibre Failure

Figure 5.3: Examples of Feature Data for a Typical Fibre/Fibre Bond Failure and a Fibre Failure

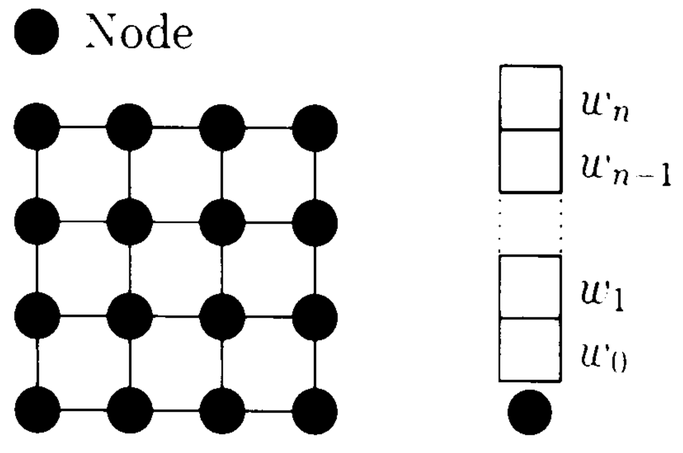

Figure 5.4: A 4x4 Self-Organising Map

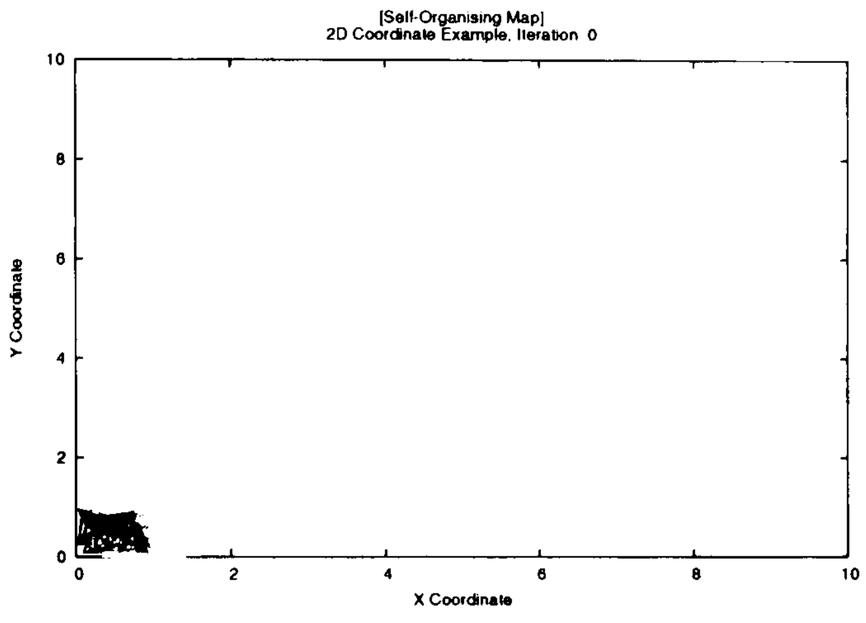

(a) Initial Position of the Nodes

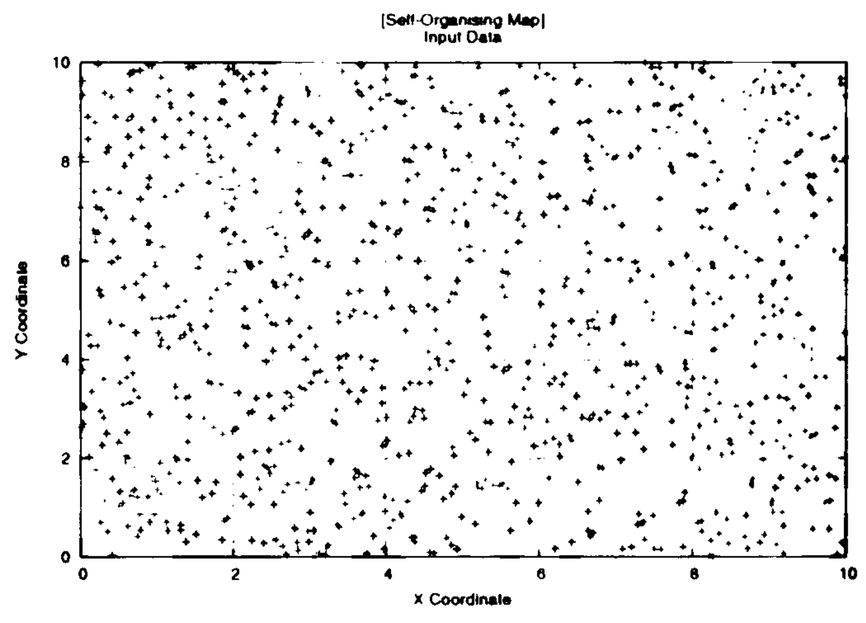

(b) Input Data

Figure 5.5: Initialising the SOM

$$i = \arg \min_{j=1}^{1000} |x - w_j| \tag{5.3.1}$$

where:

i	Index of Best Matching Unit
x	Input Data Position Vector
w_j	Weight Vector of Node j

The Cooperative Algorithm

Having selected the best matching unit, this node will become the centre of a neighbourhood, where all nodes within the neighbourhood will learn from the input data. By learning, it is intended that the weight vector $w_j(t)$ will change over time. The neighbourhood function used for the SOMs in this work is the Gaussian function.

$$h_{ij} = \alpha(t) \exp\left(-\frac{||r_{ij}||^2}{2\sigma^2(t)}\right) \tag{5.3.2}$$

where:

h_{ij} Neighbourhood Function between Nodes i and j

r_{ij} Distance Between Nodes i and j

$\alpha(t)$ Learning Rate, which decreases linearly over time

$\alpha(t) = \alpha_0 \rightarrow 0$, as $t \rightarrow \infty$

$\sigma(t)$ Neighbourhood Size, which decreases linearly over time

$\sigma(t) = \sigma_0 \rightarrow 1$, as $t \rightarrow \infty$

Figure 5.6 shows the shape of the Gaussian neighbourhood function at different points in time. It is important to note that the learning rate and neighbourhood size decrease with time.

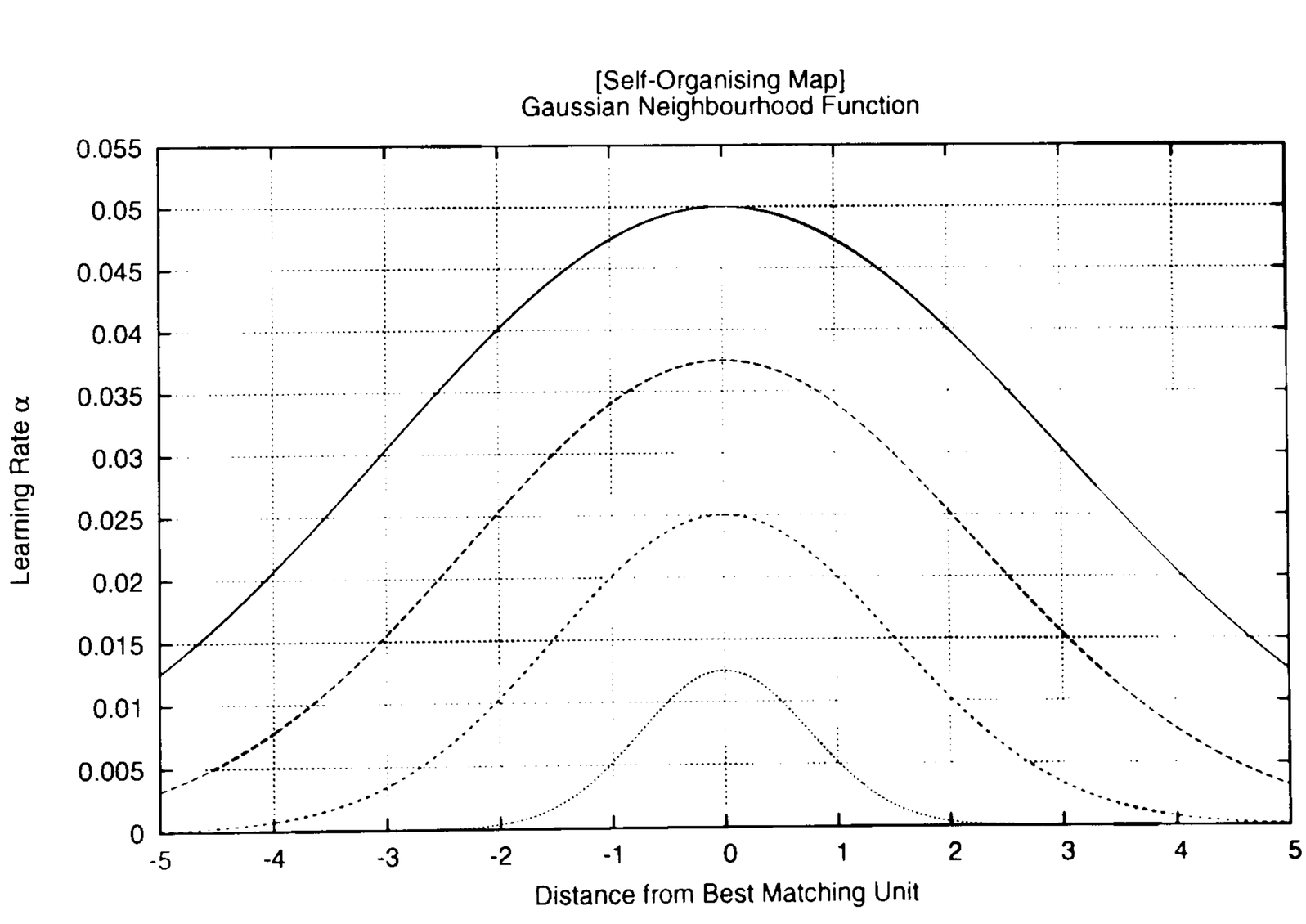

Figure 5.6: Gaussian Neighbourhood Function

The Synaptic Adaptation Algorithm

All the nodes that exist within the neighbourhood of the best matching unit as defined by Equation 5.3.2 are forced to 'learn' from the input data. The manner in which each node i learns from its neighbouring nodes is by changing the weight vector w_j according to:

$$w_j(t+1) = w_j(t) + h_{ij}(t)\Big(x(t) - w_j(t)\Big) \tag{5.3.3}$$

where, j is the index of the node in the neighbourhood h_{ij} of node i. The shape of the neighbourhood function causes the best matching unit to undergo the strongest adaption of its synaptic weights with the node further away from the best matching unit subject to a weaker learning rate. This causes similar nodes to cluster together and, over many iterations, they will expand their knowledge to encompass the whole of the input dimensions.

Figure 5.7 shows an example where the input data consists of a two dimensional vector uniformly distributed between 0,0 and 10,10. Over time, the SOM adapts to represent the uniform distribution of the input data. Specifically, the position vectors represented by the weights w_j spread nearly equidistant over the two-dimensional space.

5.4 Results

The results for the SOM using the features extracted with the method described in Section 5.2 are presented below. Details of training the SOM are provided before the explanation of the results.

Training the SOM

To train the SOM, a set of training data that represents most of the variance of the experimental data is required. It is known from the experimental data that very few fibre failures

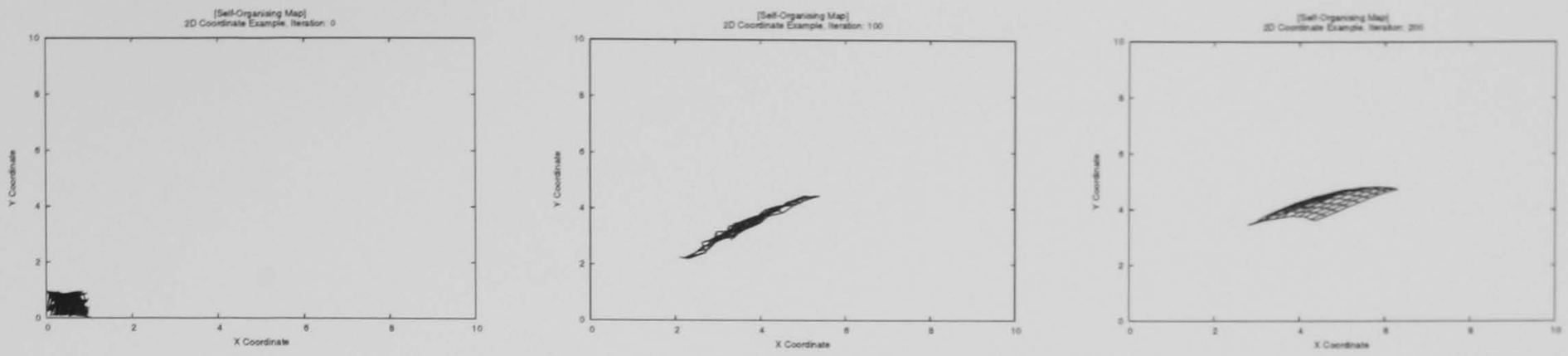

(a) 0 Iterations (b) 100 Iterations (c) 200 Iterations

(d) 300 Iterations (e) 9900 Iterations (f) 110000 Iterations

Figure 5.7: Training of a 10x10 SOM

occur, therefore to accurately classify the fibre failure damage mechanism, this must be adequately represented in the training data. To achieve this, a preliminary visual classification is performed on the experimental data. An index of all the CWTs of the experimental AEs can be found in Appendix B. Table 5.1 shows the rudimentary classification results.

Classification Group	Percentage of AEs	Ratio
Fibre/Fibre Bond Failure	**84.64%**	(551/651)
Fibre Failure	**1.23%**	(8/651)
Erroneous Data	**4.45%**	(29/651)
Both Damage Mechanisms	**9.68%**	(63/651)

Table 5.1: Rudimentary Classification Results

The visual classification has provided four different groups of AEs, covering the two damage mechanisms, erroneous data and AEs with CWTs that exhibit properties of both damage mechanisms. Figure 5.8 shows an example of the CWT of an AE from each of the four visual classification groups.

The fibre/fibre bond failure and fibre failure groups contain AEs that satisfy the criteria set in Sections 4.5.4 and 4.6.4. The erroneous data group contains AEs where a fault has

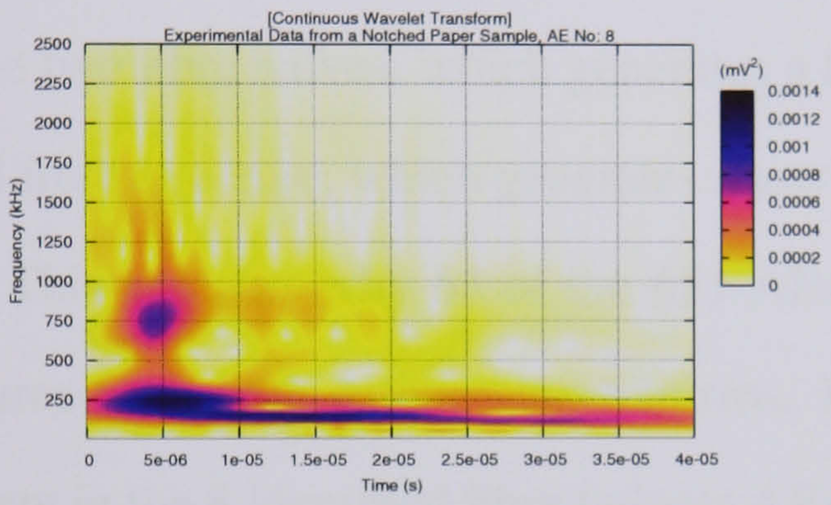

(a) Fibre/Fibre Bond Failure

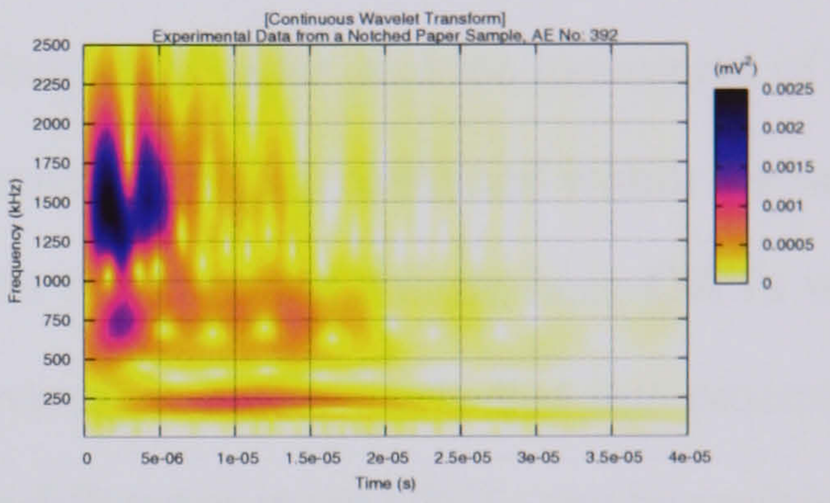

(b) Fibre Failure

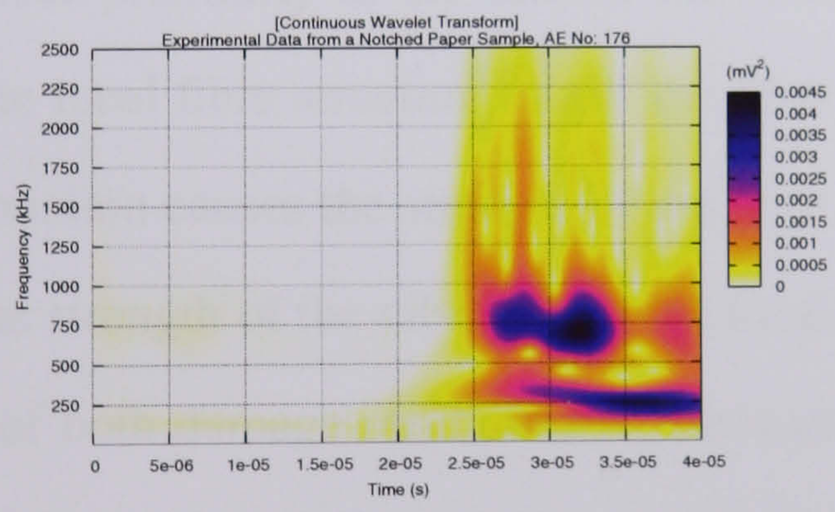

(c) Erroneous Data

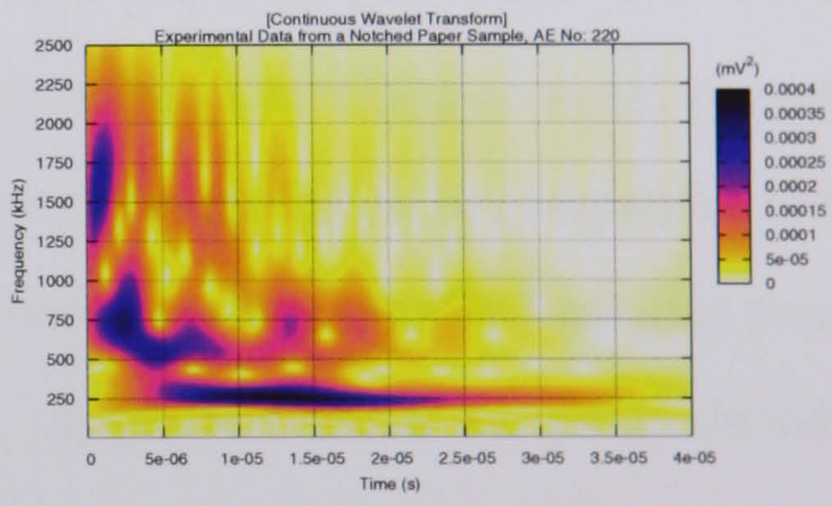

(d) Both Damage Mechanisms

Figure 5.8: Example CWTS of AEs from each Visual Classification Group

occurred in the recording of the AE, such that the general shape of the CWT is incorrect. The example shown in Figure 5.8(c) shows that the hardware used to record the AE was triggered before the front of the AE had reached the sensor. Another common signal acquisition error is when two distinct signals are contained in one AE.

The last group containing AEs that have features from both damage mechanisms is of particular interest. When a fibre fails, the resulting contraction of the two fibre halves causes the local fibre structure to move. As this is almost instantaneous, the contraction of the two fibre halves, which generates a high frequency pulse, and the movement of the local fibre structure, which generates a low frequency wave, are contained within the same AE. This explains why 63 of the 651 AEs in the experimental dataset have CWTs with features from both damage mechanisms. However, it is highly likely that this process is present in the 8 identified fibre failures AEs. The difference in the CWTs can be explained by the strength of the high frequency component in the AEs. For example, if a fibre fails in close proximity to the sensor, the resulting high frequency pulse hides the vibration of the local fibre structure, but if the fibre failure occurs some distance away, geometric attenuation causes the strength of the high frequency component to be comparable to that of the strength of the vibration of the local structure. Therefore the CWT exhibits properties of both damage mechanisms. Theoretically, all the AEs within this group should be classified as fibre failures, but currently there is no obvious method to validate this theory. Therefore, the AEs that contain properties of both damage mechanisms will retain their own classification group.

Having preliminary identified the fibre failures in the experimental data, approximately half of these are selected for use in the training data. If an equal number of bond failures are randomly selected from the data, this will provide a training dataset containing around 8 individual AEs. Having a training dataset of just 8 AEs is insufficient and likely to results in a poorly trained SOM [59]. Therefore, a large training dataset of 64 AEs was

Training Stage	Learning Rate α	Neighbourhood Size σ	Iterations
Ordering Stage	0.05	10	1000
Convergence Stage	0.01	3	10000

Table 5.2: Coefficients for Different Training Stages in the SOM

selected. If the 64 AE training set were chosen at random from the experimental data, the fibre failure damage mechanism would not be adequately represented and the SOM not properly trained. Therefore, the 4 fibre failures chosen at random are repeated 8 times in the training data. The training data is then populated with 32 randomly selected bond failures to provide a training set of 64 AEs, where the experimental data contains 651 AEs.

The SOM is traditionally trained using two stages. The first stage uses a high learning rate α with a large neighbourhood σ over a small number of iterations, to order the nodes in the SOM. The second stage uses a small learning rate with a small neighbourhood over many iterations so that the weight vectors of the nodes converge. Table 5.2 details the values used for the (α, σ) coefficients used in both training stages.

The quantisation error q is the average difference between the input data and its corresponding best matching unit.

$$q = \frac{\sum_{n=1}^{N} ||x(n) - w_i(n)||}{N} \tag{5.4.1}$$

where:

q Quantisation Error

n Iteration Number

N Total Number of Iterations

x Input Data

w_i Best Matching Unit

A perfectly trained map will have a quantisation error of 0. The quantisation error for the AE dataset is 0.044923. This indicates that the SOM is well trained and should show reasonable performance in classifying the AEs.

Performance of the SOM

This section assesses the performance of the SOM in classifying the two types of damage mechanisms. The structure of the SOM can be visualised using the unified distance matrix (u-matrix) method by Ultsch [123]. Figure 5.9 shows the u-matrix representation for the SOM. The light colours highlight areas of the map with similar nodes, with a dark colour showing that a node is unrelated to its neighbours.

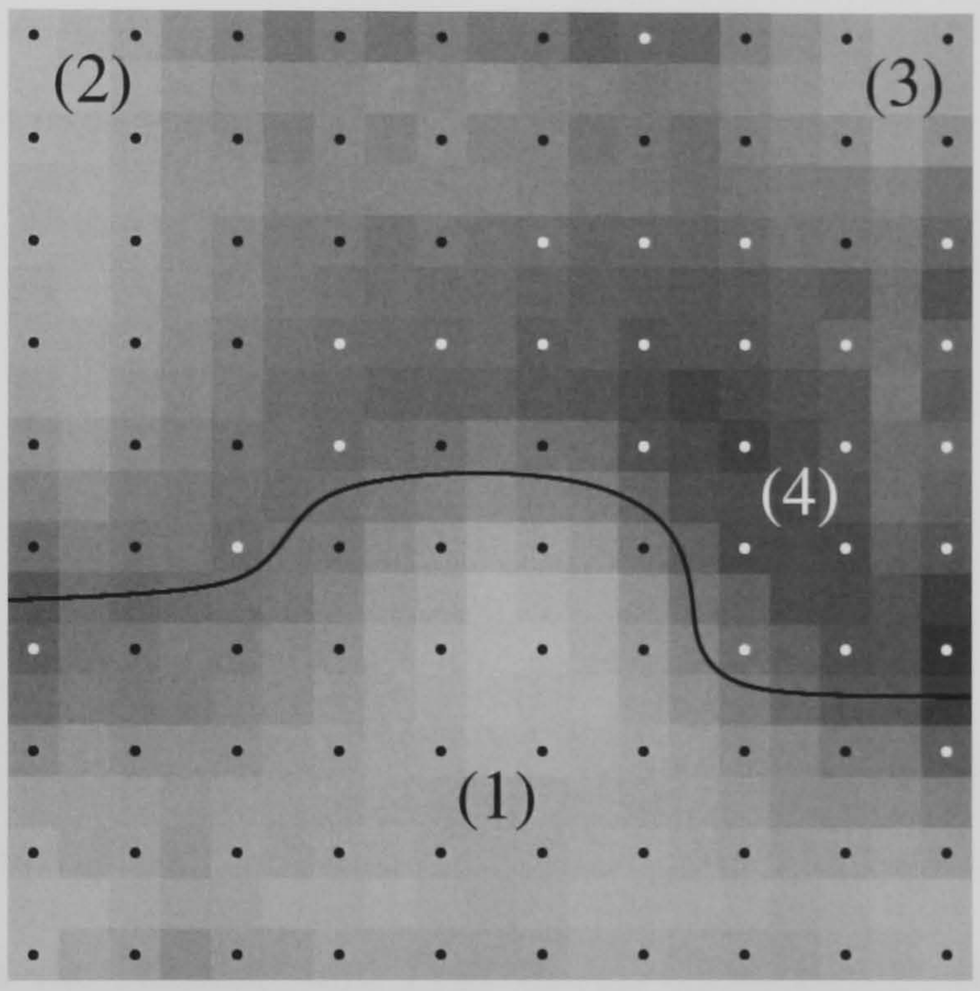

Figure 5.9: The U-Matrix showing the Distances between Weights of Neighbouring Nodes

Figure 5.9 clearly shows a divide between the north half of the map and the south half of the map. The southern half of the map is one large cluster of similar nodes and is denoted by (1). The northern half of the map contains two smaller clusters of similar nodes denoted by (2) and (3) and a small cluster of dissimilar nodes denoted by (4). To understand the nature of areas (1), (2), (3) and (4) the SOM is used to classify the experimental data. Figure 5.10 shows the number of AEs classified by each node for each visual classification group. Figure 5.10(b) shows that area (1) is associated with the fibre failure damage mechanism. Figure 5.10(a) shows that areas (2) and (3) associated with the fibre/fibre bond failure mechanism and Figure 5.10(c) shows that area (4) associated

with the erroneous AEs present in the experimental data.

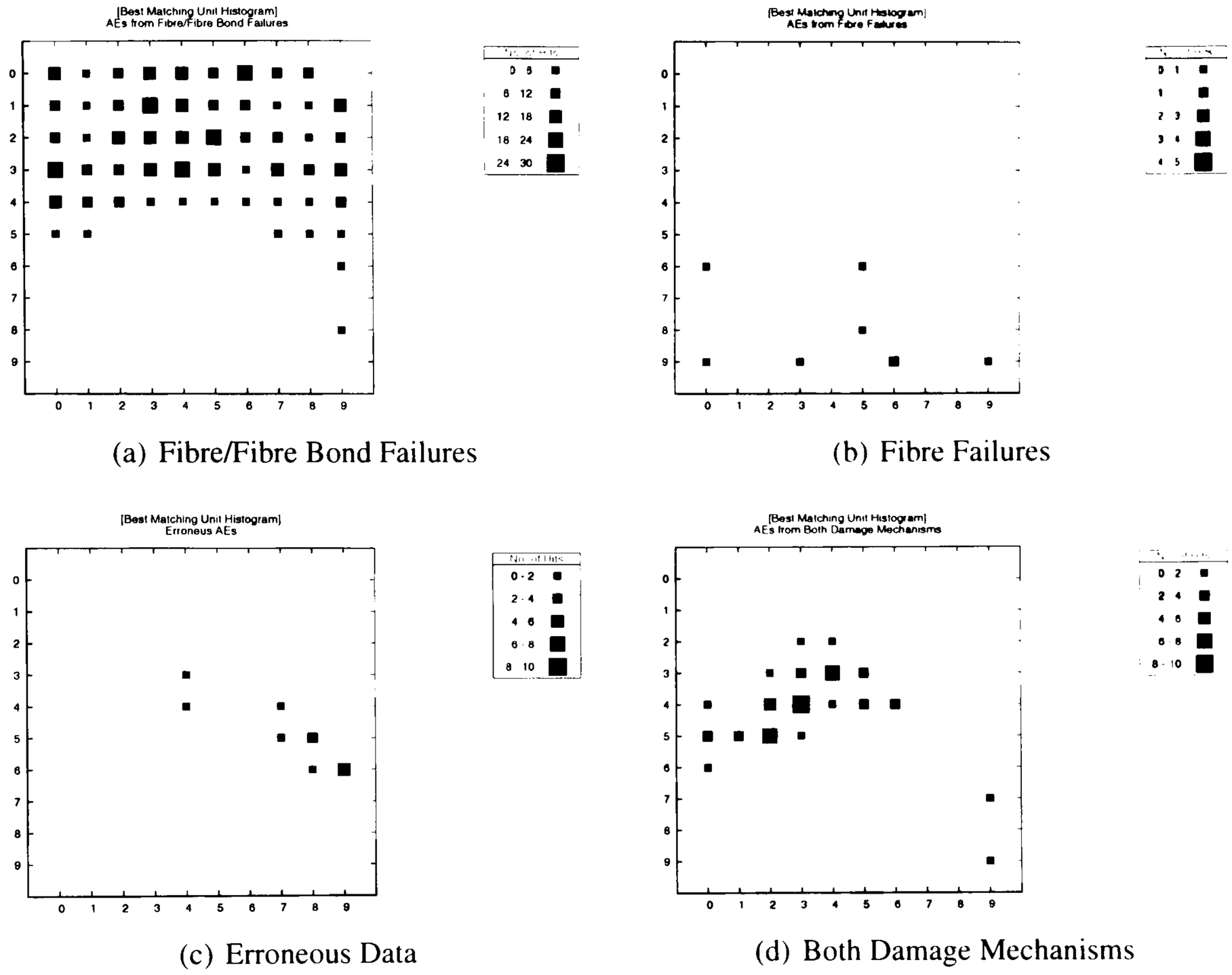

(a) Fibre/Fibre Bond Failures

(b) Fibre Failures

(c) Erroneous Data

(d) Both Damage Mechanisms

Figure 5.10: Number and Type of AE Classified by the SOM

On closer inspection of Figure 5.10, 6 of the AEs that have been classified as fibre failures by the SOM, 5 were visually classified as containing features from both damage mechanisms and 1 AE was visually classified as a fibre/fibre bond failure. Table 5.3 details the discrepancy in classification between the visual inspection approach and the SOM, with Figure 5.11 showing the incorrectly classified AEs.

Area (4) that defines the erroneous AEs within the experimental data contains nodes (7,4), (7,5), (8,5), (9,5), (8,6) and (9,6). These nodes have classified 26 of the 29 erroneous AEs and 13 of the 551 fibre/fibre bond failures. Assuming that the visual classification of the experimental data is correct, Table 5.4 summarises the findings of this preliminary study of the SOM, showing the probability of the AE generated being correctly classified

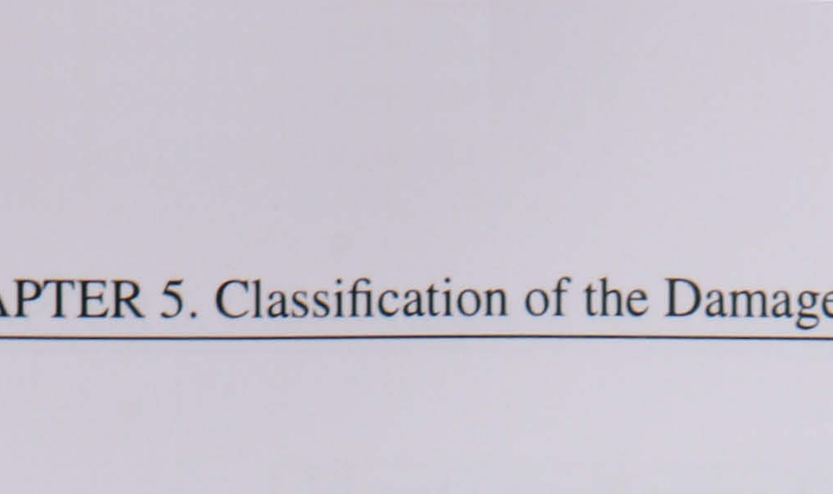

(a) AE No: 571

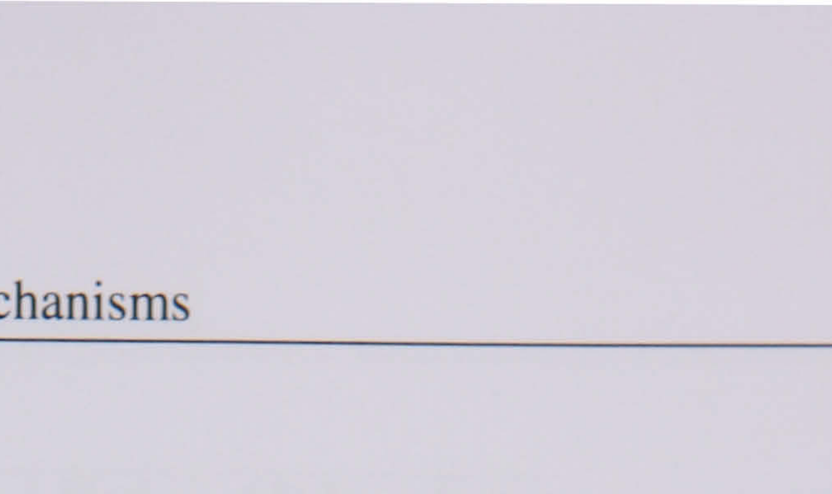

(b) AE No: 111

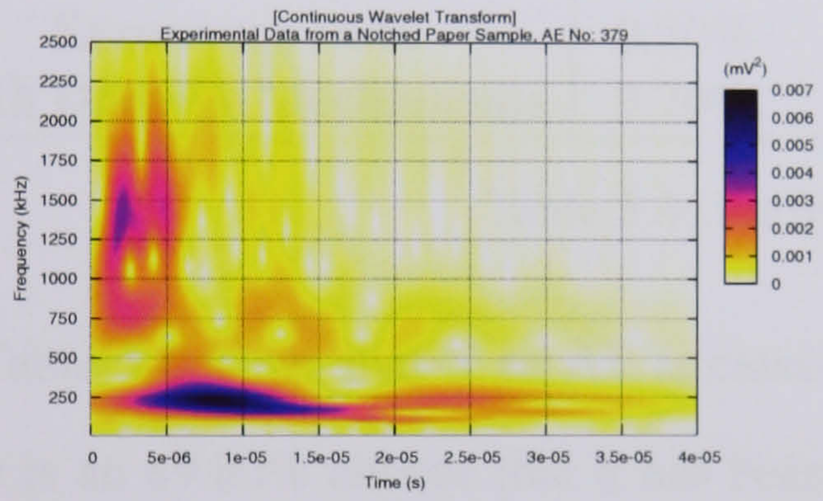

(c) AE No: 379

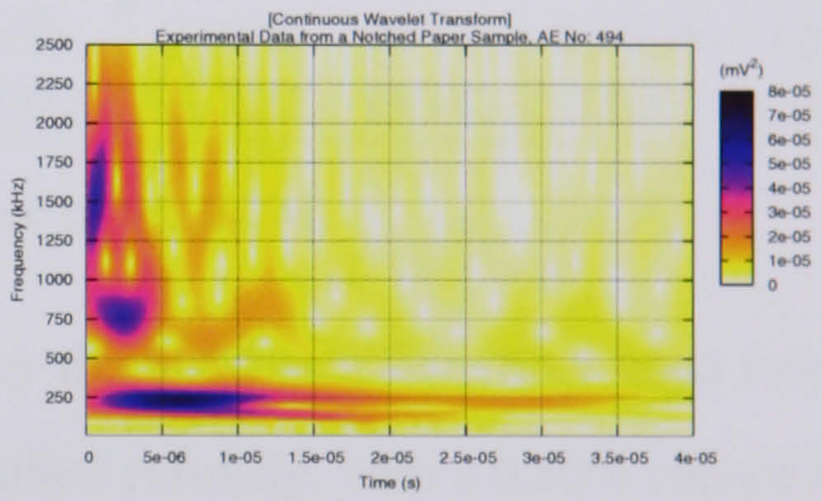

(d) AE No: 494

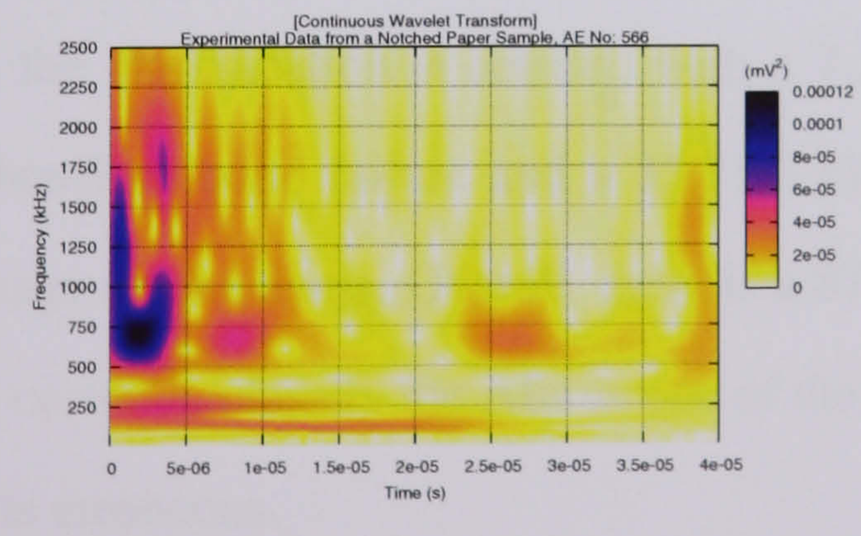

(e) AE No: 566

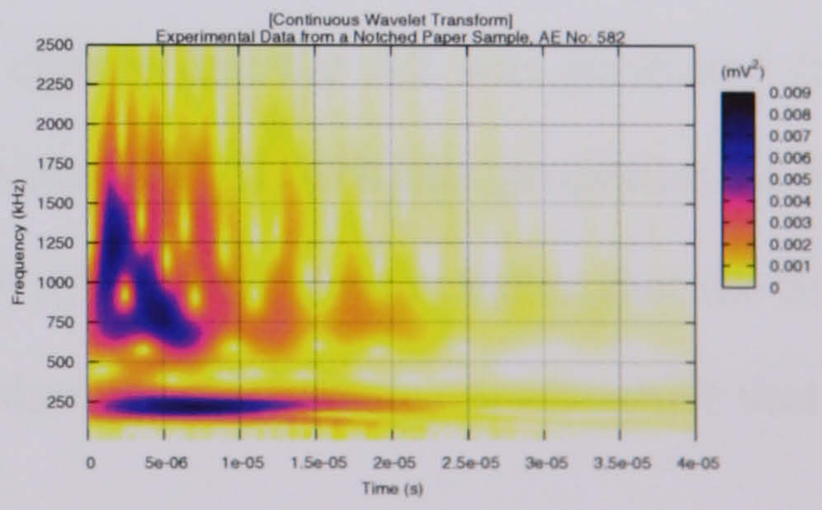

(f) AE No: 582

Figure 5.11: AEs Incorrectly Classified by the SOM

Visual Classification Group	Node	AE Number
Fibre/Fibre Bond Failure	(9,8)	571
Both Damage Mechanisms	(0,6)	111
Both Damage Mechanisms	(9,7)	379
Both Damage Mechanisms	(9,7)	494
Both Damage Mechanisms	(0,6)	566
Both Damage Mechanisms	(9,9)	582

Table 5.3: AEs Incorrectly Classified by the SOM

as a particular damage mechanism.

Damage Mechanism	Fibre/Fibre Bond Failure		Fibre Failure		Erroneous Data	
	%	Ratio	%	Ratio	%	Ratio
Fibre/Fibre Bond Failure	89.80%	(537/598)	7.14%	(1/14)	33.33%	(13/39)
Fibre Failure	0.00%	(0/598)	57.14%	(8/14)	0.00%	(0/39)
Erroneous Data	0.50%	(3/598)	0.00%	(0/14)	66.67%	(26/39)
Both Damage Mechanisms	9.70%	(58/598)	35.71%	(5/14)	0.00%	(0/39)

Table 5.4: Performance of the SOM

Table 5.4 states that if an AE is classified by the SOM as a fibre/fibre bond failure, there is an 89.80% chance that it has been classified correctly, with a 0.50% chance that the AE is erroneous and a 9.70% chance that the AE exhibits features from both damage mechanisms. Similarly, if an AE is classified as a fibre failure, there is a 57.14% chance that the classification is correct, with a 7.14% chance that the AE was generated from a fibre/fibre bond failure and a 35.71% chance that the AE exhibits properties of both damage mechanisms. Overall, there is a 87.71% ((537+8+26)/651) chance that the SOM will correctly classify the AEs as one of the two damage mechanisms or recognise that the AE is erroneous.

5.5 Summary

This chapter has presented a preliminary investigation of the potential of the SOM for use in classifying the damage mechanisms present in paper. The success of the SOM is highly

dependent on the relevance of the features used and the quality of the training data. The feature extraction method employed reduces the resolution of the CWT of each AE, at the same time attempting to preserve the overall shape of the CWT. This method is not ideal, as approximately 25% of the features which are located in the northwest corner of the CWT are effectively redundant as only a small number of AEs carry any information within this time and frequency range. However, the feature extraction method was the simplest way of conserving the basic shape of the CWT.

This chapter has also explained the method for training an unbiased SOM by equitably representing both damage mechanisms in the training data. This process must be applied to any data where there is an abundance of one particular damage mechanism. Failure to do so will produce a SOM that is only able to classify one type of damage mechanism. Having trained the SOM, an initial study was conducted to ascertain the potential of using the SOM as a classification tool for the damage mechanisms in paper.

The SOM is able to distinguish between the two damage mechanisms, but there are a number of AEs exhibiting properties from both damage mechanisms, that the SOM fails to properly classify. However, the SOM is able to provide an initial classification and at the least shows that AEs generated from the fibre failure damage mechanism actually occur. The SOM has definite potential for use as a classification tool and this chapter only addresses the initially steps of developing a SOM for this purpose.

Chapter 6

Conclusions and Future Work

6.1 Conclusions

This research has presented a method for investigating and understanding the micro-mechanics of paper using the AE monitoring technique by bringing together ideas and approaches from several scientific disciplines ranging from paper physics, acoustic emission technology, numerical modelling and neural networks.

The main objective of this research was to answer the following question:

> ***Is it possible to identify the two damage mechanisms present in paper, the fibre/fibre bond failure and the fibre failure, using the acoustic emission monitoring technique?***

The theoretical results from the hybrid vibro-acoustic numerical model developed in Chapter 4 show that the two damage mechanisms can be classified using features from the CWT of the generated AEs. The following criteria characterise a fibre/fibre bond failure:

- The dominant frequency components of the AE is at approximately 250 kHz or 750 kHz.

- The strongest frequency component exists at either approximately 250 kHz or 750 kHz.

- The duration of the frequency component at approximately 250 kHz is longer than that of the frequency component at approximately 750 kHz.

Similarly, the criteria characterising a fibre failure are:

- The dominant frequency component of the AE is greater than 800 kHz.

- The duration of the dominant frequency component is less than 5.00E-06 seconds.

- The dominant frequency component is present at the start of the AE.

Simply put, the fibre/fibre bond failure is represented by a low frequency wave, with the fibre failure represented by a high frequency pulse. In general, the experimental data confirms the findings of the numerical model, however there are a number of AEs with CWTs that fit the criteria of both damage mechanisms. This was highlighted when trying to classify the two damage mechanisms using a SOM in Chapter 5.

The SOM is able to classify the AEs that have distinct properties relating to each damage mechanism, but fails when the AEs appears to exhibit properties of both damage mechanisms. It is important to remember that the AE is a byproduct of the damage mechanism and does not result directly from the failure process. As failure occurs, the tension in the local fibre structure changes, causing a redistribution of the internal stress that in turn causes the local fibre structure to vibrate. It is this vibration that generates the AE. This implies that the properties of the AE are dependent on the state of the local fibre structure.

The failure of a fibre/fibre bond will cause the local fibre structure to vibrate and will produce an AE with a low frequency component. The failure of a fibre causes an instantaneous contraction of the two fibre halves that produces a high frequency pulse. This

contraction of the two fibre halves causes the local fibre structure to vibrate. The fibre failure damage mechanism causes a high frequency pulse immediately followed by the low frequency vibration of the fibre structure. The SOM is able to classify the fibre failures where the high frequency pulse dominates the features of the CWT, but fails when the high frequency pulse has a similar amplitude to that of the low frequency vibration. This is highly dependent on the location of the fibre failure, as a failure closer to the sensor will produce an AE with a CWT that has the characteristics of a fibre failure damage mechanism, whereas a fibre failure occurring at a distance from the sensor exhibits the CWT characteristics of a fibre/fibre bond failure damage mechanism.

Therefore, to answer the research question, it is possible to distinguish between a fibre/fibre bond failure and a fibre failure. However, in practise factors such as the random nature of the microscopic structure of the paper and the attenuation of the acoustic signal complicate the classification process. The following sections will provide more detailed conclusions on the different aspects of this work.

The Numerical Model

The hybrid vibro-acoustic numerical model provides a method for producing and analysing the two damage mechanisms at a level unachievable by experimental techniques. The difficulty of being able to generate experimental data containing AEs of predominantly one type of damage mechanism spawned the development of the numerical model. The model is able to provide a theoretical acoustic fingerprint of the two types of damage mechanisms. In doing so, it has enabled a deeper understanding of the micro-mechanics of the fibre structure and has provided a point of reference to analyse the experimental data.

The hybrid vibro-acoustic model uses the mass/spring paradigm to simulate the movement of the paper fibre structure that in turn generates an AE when coupled with the acoustic wave equation. Most current vibro-acoustic simulations use FEM or BEM as the

modelling technique, which suggests that the hybrid vibro-acoustic model is to some extent novel. The mass/spring model has seen extensive use in the real-time animation of cloth, where accuracy is sacrificed for speed as long as the animation is visually accurate. In this work, the mass/spring model has shown to be able to simulate the vibration of fibres with an accuracy that was adequate to drive the acoustic model, but was primarily chosen for its flexibility in simulating the damage mechanisms in paper. This mass/spring implementation is unique in its simulation of the damage mechanisms present in paper by dynamically manipulating the mass and spring elements as stated in Algorithms 8 and 9.

Acoustic Evidence of the Damage Mechanisms

By developing the hybrid vibro-acoustic numerical model, the author gained a further insight into the physical process involved in the generation of the AE resulting from the two selected damage mechanisms. For instance, Chapter 4 documents how the fibre/fibre bond failure damage mechanism causes a measurable change in the fibre structure such that the average length between two bonds increases as the damage increases. Simply put, the fibre structure before any failure has occurred is well connected and can be thought of as rigid. As the fibre/fibre bonds fail, the fibre structure becomes more flexible as the connectivity within the structure decreases. This can be detected by a decrease in the average frequency of the AE, as shown by the results in Section 4.5.5.

Classification of the Damage Mechanisms

The SOM has provided an insight into the potential of automatic identification of the fibre/fibre bond failure and fibre failure damage mechanisms. The theoretical results highlight the importance of the shape of the CWT for distinguishing between the two damage mechanisms. The feature extraction method was designed to best preserve the shape of the CWT using the least amount of information possible. It was decided to split the CWT into

windows of 5.00E-06s in duration covering a frequency range of 100 kHz. This results in 200 windows. The normalised sound power level of each window is calculated to provide 200 data elements for each AE.

The SOM is then trained using a small subset of the experimental data so that both damage mechanisms are evenly represented in the training dataset. The analysis of the performance of the SOM described in Chapter 5 shows that the SOM has an 87.71% chance of correctly classifying the experimental data. This provides a solid basis for developing a commericially viable classification tool.

6.2 Future Work

This work has provided a solid argument for using numerical modelling techniques in conjunction with experimental data to better understand the micro-mechanics of paper. It would be beneficial to the paper physics community to continue this research using different well defined paper types to expand the knowledge accrued by this work. The numerical model need not be limited to paper and is versatile enough so that its use can be expanded to other types of material, such as cloth and rubber. Essentially, all that would be required is the use of different material properties and an understanding of the damage mechanisms in the material in question.

The hybrid vibro-acoustic numerical model is in its infancy as a tool for the material scientist. The obvious natural progression and most important step for the numerical model would be to expand it to the third dimension. The implementation would require a third coordinate for each node in the input file and an extra dimension to the matrices used in the implicit solver. Once this is completed, the numerical model can be applied to a host of new materials and structures ranging from the microscopic to the macroscopic in scale.

It would also be of interest to employ the numerical model to simulate larger structures

to those presented in this work. However, the computational efficiency of the implicit solver leaves much to be desired when the number of mass/spring elements is greater than 1000. This can be attributed directly to the storage mechanism of the sparse array. The sparsity of the arrays generated from the mass/spring model are dependent on the number of springs connected to each mass and it is difficult to pre-determine the general structure of the matrix. Therefore the most efficient method for populating the sparse array is to use a flexible array which allows the dynamic insertion of data. The JAVA ArrayList has this feature, but is considerably slower than the standard array object. To eliminate the computational cost a standard array could be used or investigate the possibility of using the standard BLAS and LAPACK high performance numerical libraries. It would also be possible to increase the efficiency of the implicit solver by preconditioning the sparse matrix.

The final suggested improvement on the numerical model is to model the fibre as a string instead of a series of masses and springs. This would require a fundamental change in the theory of the model to incorporate the equation of a realistic string as shown below.

$$\frac{\partial^2 y}{\partial t^2} = \frac{\tau}{\mu}\frac{\partial^2 y}{\partial x^2} + \pi\frac{Er^4}{4\mu}\frac{\partial^4 y}{\partial x^4} + \alpha\frac{\partial y}{\partial t} \tag{6.2.1}$$

where:

τ Tension in the String

μ Mass/Unit Length

E Young's Modulus

r Radius of String

α Damping Constant

The last suggestion for future work is to investigate the fracture behaviour of the paper using the experiments presented by this report. It is possible, using the SOM as a classification tool, to label each AE from the experimental data with a damage type. This will

provide the order and type of each recorded AE. Figure 6.1 shows the damage profile of a typical notched paper specimen. A cursory glance shows that the failure of the fibres occur before final fracture, suggesting that the final few AEs are generated by the fibre sliding over one another. Further work is needed to explore the validity of this statement.

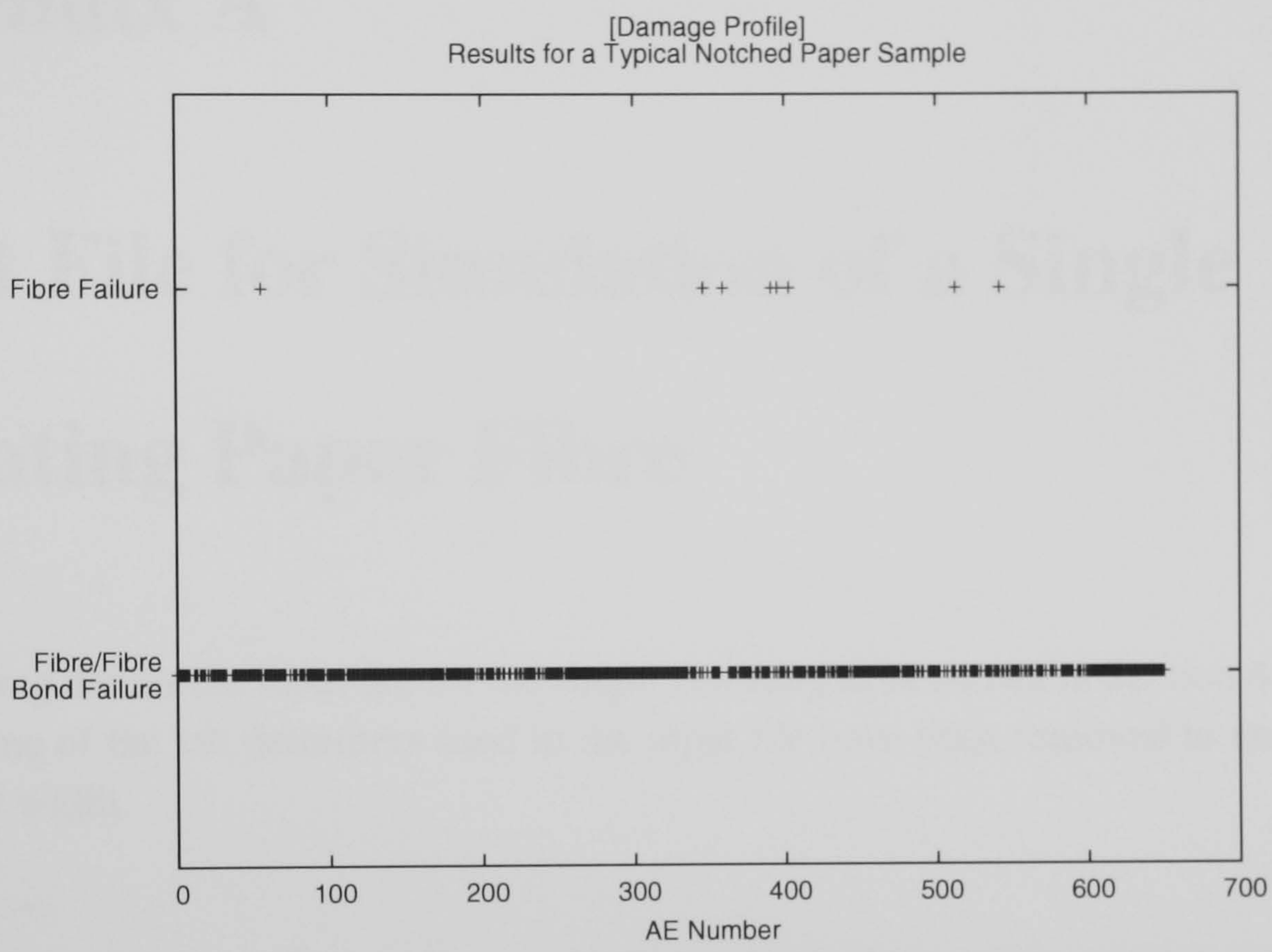

Figure 6.1: Damage Profile of a Typical Notched Paper Sample

Appendix A

Input File for Simulation of a Single Vibrating Paper Fibre

The following details the input file for the single vibrating fibre shown in Section 4.4. Note that the some of the tab delimiters used in the input file have been removed to ensure the correct text width.

```
Section System
x1        x2        y1        y2        dt        damping gravity iters solver runwave stretch
-5.5E-04 5.5E-04 -5.5E-04 5.5E-04 1.0e-08 1.5e-06 0.0     4000  IEuler  false   true
End System
Section Nodes
Node    x         y       type    m
0       -5.0E-04 0.0     1       5.1E-12
1       -4.6E-04 0.0     0       5.1E-12
2       -4.3E-04 0.0     0       5.1E-12
3       -3.9E-04 0.0     0       5.1E-12
4       -3.6E-04 0.0     0       5.1E-12
5       -3.2E-04 0.0     0       5.1E-12
6       -2.9E-04 0.0     0       5.1E-12
7       -2.5E-04 0.0     0       5.1E-12
8       -2.1E-04 0.0     0       5.1E-12
9       -1.8E-04 0.0     0       5.1E-12
10      -1.4E-04 0.0     0       5.1E-12
11      -1.1E-04 0.0     0       5.1E-12
12      -7.1E-05 0.0     0       5.1E-12
```

13	-3.6E-05	0.0	0	5.1E-12
14	0.0	0.0	0	5.1E-12
15	3.6E-05	0.0	0	5.1E-12
16	7.2E-05	0.0	0	5.1E-12
17	1.1E-04	0.0	0	5.1E-12
18	1.4E-04	0.0	0	5.1E-12
19	1.8E-04	0.0	0	5.1E-12
20	2.1E-04	0.0	0	5.1E-12
21	2.5E-04	0.0	0	5.1E-12
22	2.9E-04	0.0	0	5.1E-12
23	3.2E-04	0.0	0	5.1E-12
24	3.6E-04	0.0	0	5.1E-12
25	3.9E-04	0.0	0	5.1E-12
26	4.3E-04	0.0	0	5.1E-12
27	4.6E-04	0.0	0	5.1E-12
28	5.0E-04	0.0	1	5.1E-12

End Nodes

Section Springs

Spring	N1	N2	E	L	t	w	P.Ratio	Fibre	Type
0	0	1	3.5E10	3.6E-05	2.8E-06	3.5E-05	0.28	0	0
1	1	2	3.5E10	3.6E-05	2.8E-06	3.5E-05	0.28	0	0
2	2	3	3.5E10	3.6E-05	2.8E-06	3.5E-05	0.28	0	0
3	3	4	3.5E10	3.6E-05	2.8E-06	3.5E-05	0.28	0	0
4	4	5	3.5E10	3.6E-05	2.8E-06	3.5E-05	0.28	0	0
5	5	6	3.5E10	3.6E-05	2.8E-06	3.5E-05	0.28	0	0
6	6	7	3.5E10	3.6E-05	2.8E-06	3.5E-05	0.28	0	0
7	7	8	3.5E10	3.6E-05	2.8E-06	3.5E-05	0.28	0	0
8	8	9	3.5E10	3.6E-05	2.8E-06	3.5E-05	0.28	0	0
9	9	10	3.5E10	3.6E-05	2.8E-06	3.5E-05	0.28	0	0
10	10	11	3.5E10	3.6E-05	2.8E-06	3.5E-05	0.28	0	0
11	11	12	3.5E10	3.6E-05	2.8E-06	3.5E-05	0.28	0	0
12	12	13	3.5E10	3.6E-05	2.8E-06	3.5E-05	0.28	0	0
13	13	14	3.5E10	3.6E-05	2.8E-06	3.5E-05	0.28	0	0
14	14	15	3.5E10	3.6E-05	2.8E-06	3.5E-05	0.28	0	0
15	15	16	3.5E10	3.6E-05	2.8E-06	3.5E-05	0.28	0	0
16	16	17	3.5E10	3.6E-05	2.8E-06	3.5E-05	0.28	0	0
17	17	18	3.5E10	3.6E-05	2.8E-06	3.5E-05	0.28	0	0
18	18	19	3.5E10	3.6E-05	2.8E-06	3.5E-05	0.28	0	0
19	19	20	3.5E10	3.6E-05	2.8E-06	3.5E-05	0.28	0	0
20	20	21	3.5E10	3.6E-05	2.8E-06	3.5E-05	0.28	0	0

```
21      21      22      3.5E10  3.6E-05 2.8E-06 3.5E-05 0.28    0       0
22      22      23      3.5E10  3.6E-05 2.8E-06 3.5E-05 0.28    0       0
23      23      24      3.5E10  3.6E-05 2.8E-06 3.5E-05 0.28    0       0
24      24      25      3.5E10  3.6E-05 2.8E-06 3.5E-05 0.28    0       0
25      25      26      3.5E10  3.6E-05 2.8E-06 3.5E-05 0.28    0       0
26      26      27      3.5E10  3.6E-05 2.8E-06 3.5E-05 0.28    0       0
27      27      28      3.5E10  3.6E-05 2.8E-06 3.5E-05 0.28    0       0
End Springs
Section Initial
Node    dx          dy          du      dv      type
0       -5.0e-06    0.0         0.0     0.0     1
28       5.0e-06    0.0         0.0     0.0     1
1        0.0        1.1e-06     0.0     0.0     0
2        0.0        2.2e-06     0.0     0.0     0
3        0.0        3.3e-06     0.0     0.0     0
4        0.0        4.3e-06     0.0     0.0     0
5        0.0        5.3e-06     0.0     0.0     0
6        0.0        6.2e-06     0.0     0.0     0
7        0.0        7.1e-06     0.0     0.0     0
8        0.0        7.8e-06     0.0     0.0     0
9        0.0        8.5e-06     0.0     0.0     0
10       0.0        9.0e-06     0.0     0.0     0
11       0.0        9.4e-06     0.0     0.0     0
12       0.0        9.8e-06     0.0     0.0     0
13       0.0        9.9e-06     0.0     0.0     0
14       0.0        1.0e-05     0.0     0.0     0
15       0.0        9.9e-06     0.0     0.0     0
16       0.0        9.8e-06     0.0     0.0     0
17       0.0        9.4e-06     0.0     0.0     0
18       0.0        9.0e-06     0.0     0.0     0
19       0.0        8.5e-06     0.0     0.0     0
20       0.0        7.8e-06     0.0     0.0     0
21       0.0        7.1e-06     0.0     0.0     0
22       0.0        6.2e-06     0.0     0.0     0
23       0.0        5.3e-06     0.0     0.0     0
24       0.0        4.3e-06     0.0     0.0     0
25       0.0        3.3e-06     0.0     0.0     0
26       0.0        2.2e-06     0.0     0.0     0
27       0.0        1.1e-06     0.0     0.0     0
End Initial
```

APPENDIX A. Input File for Simulation of a Single Vibrating Paper Fibre

```
Section Force
Node    Fx      Fy      Start   Finish
End Force
Section NodeDamage
Node    When    Type    Option
End NodeDamage
Section Grid
x1      x2      y1      y2      Nx   Ny     dt      ts      rho    c       Method
-9.0E-03 9.0E-03 -9.0E-03 9.0E-03 250  250    1e-07   1e-07   1.25   350.0   acousticO4
End Grid
Section Storage
NodePos NodeScreen NodeList Spring SpringPos Init  Coeff Tension Energy
np.dat  nsp.dat    nl.dat   s.dat  sp.dat    i.dat c.dat t.dat   e.dat
End Storage
Section Sensor
Sensor  X       Y       File
0       125     100     sensor0.dat
1       125     80      sensor1.dat
2       125     5       sensor2.dat
3       100     125     sensor3.dat
4       80      125     sensor4.dat
5       5       125     sensor5.dat
6       100     100     sensor6.dat
7       80      80      sensor7.dat
8       5       5       sensor8.dat
End Sensor
Section DrawNode
Draw    Width   Height  xMargin yMargin xMass   yMass   Prefix  Every
true    470     330     150     10      5       5       n       100
End DrawNode
Section DrawGrid
Draw    Var     Width   Height  xMargin yMargin dx      dy      Max     Min     Prefix  Every
true    P       640     550     10      10      2       2       6e-2    -6e-2   p       10
End DrawGrid
Section DrawKey
Draw    Width   Height  Colours Levels  stepX   stepY   Scheme
true    10      400     400     10      2       2       redblue
End DrawKey
Section DrawTension
Draw    Width   Height  xMargin yMargin Max     Min     Prefix  Every
```

```
true    470     330     150     10      0       0       t       100
End DrawTension
Section DrawForce
Draw    Width   Height  xMargin yMargin Max     Min     Prefix  Every
true    470     330     150     10      0       0       f       100
End DrawForce
```

Appendix B

CWTs of 651 Experimental AEs

This appendix lists the 651 CWTs of the experimental data used in testing the potential of a SOM for classifying the fibre/fibre bond failure and fibre failure damage mechanisms as seen in Chapter 5.

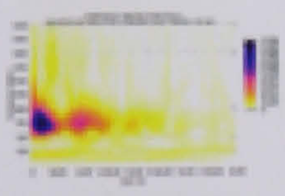

1

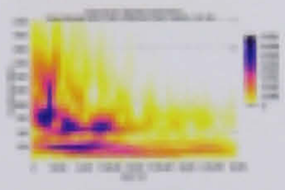

2

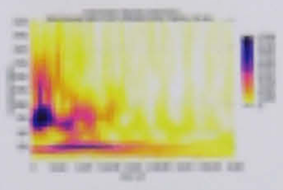

3

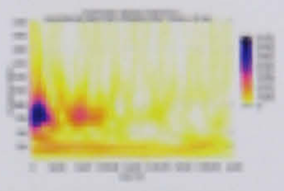

4

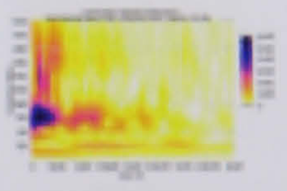

5

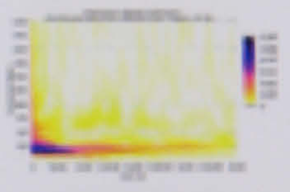

6

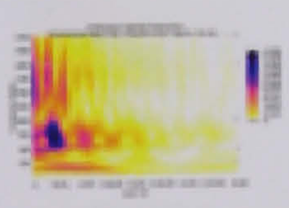

7

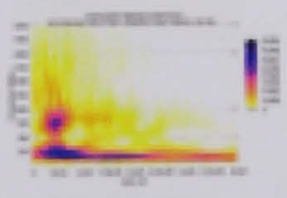

8

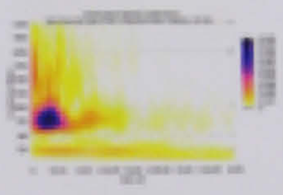

9

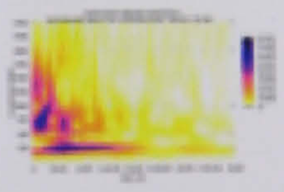

10

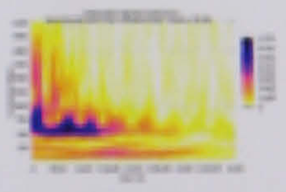

11

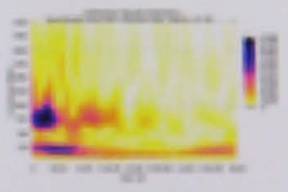

12

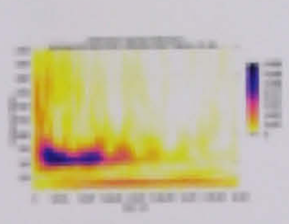

13

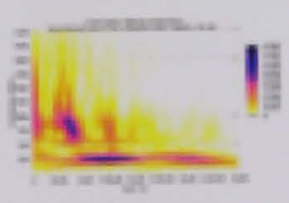

14

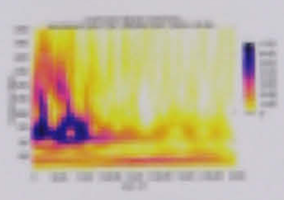

15

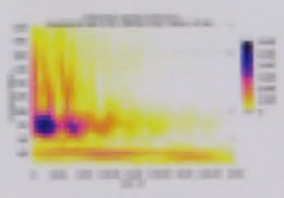

16

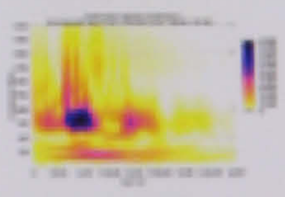

17

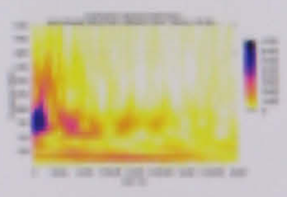

18

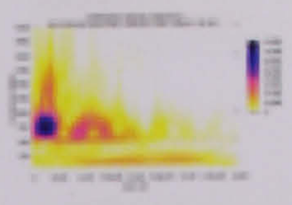

19

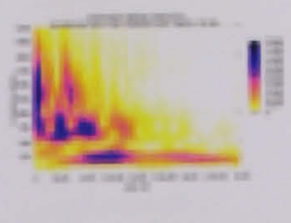

20

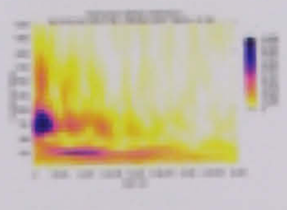

21

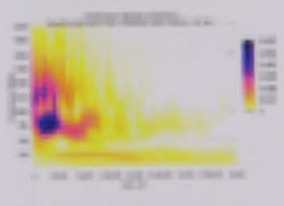

22

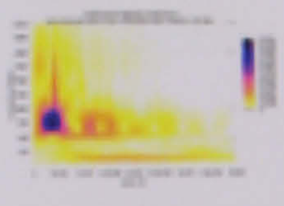

23

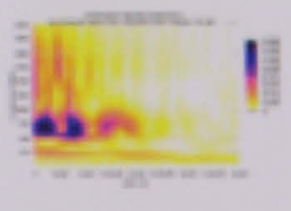

24

25
26
27
28
29
30
31
32
33
34
35
36
37
38
39
40
41
42
43
44
45
46
47
48
49
50
51
52
53
54
55
56
57
58
59
60
61
62
63
64
65
66
67
68
69
70
71
72
73
74
75
76
77
78

79 80 81 82 83 84

85 86 87 88 89 90

91 92 93 94 95 96

97 98 99 100 101 102

103 104 105 106 107 108

109 110 111 112 113 114

115 116 117 118 119 120

121 122 123 124 125 126

127 128 129 130 131 132

133 134 135 136 137 138

139 140 141 142 143 144

145 146 147 148 149 150

151 152 153 154 155 156

157 158 159 160 161 162

163 164 165 166 167 168

169 170 171 172 173 174

175 176 177 178 179 180

181 182 183 184 185 186

187
188
189
190
191
192
193
194
195
196
197
198
199
200
201
202
203
204
205
206
207
208
209
210
211
212
213
214
215
216
217
218
219
220
221
222
223
224
225
226
227
228
229
230
231
232
233
234
235
236
237
238
239
240

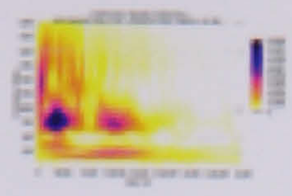
241

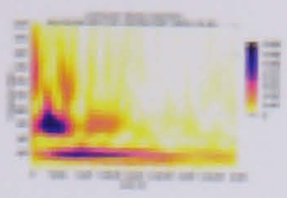
242

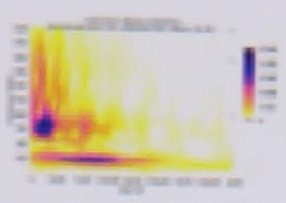
243

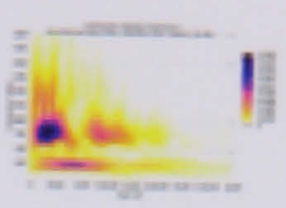
244

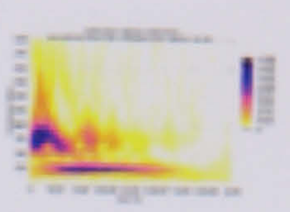
245


246

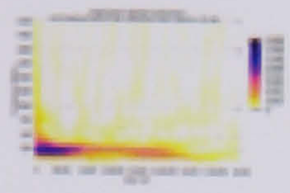
247

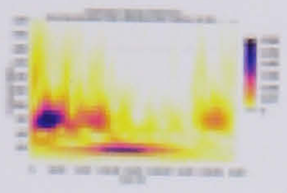
248

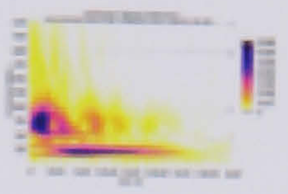
249

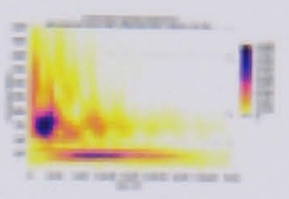
250

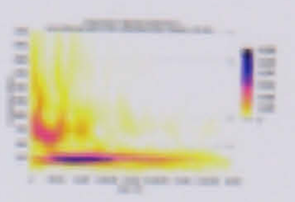
251

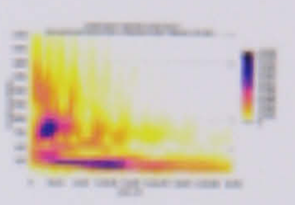
252

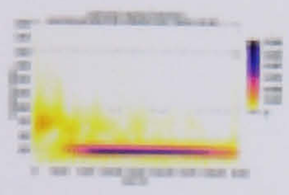
253

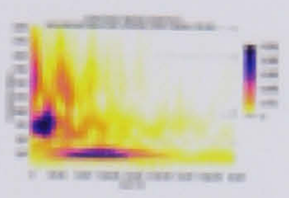
254

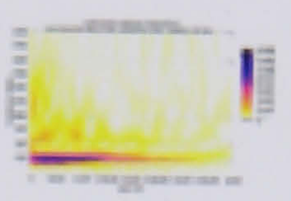
255

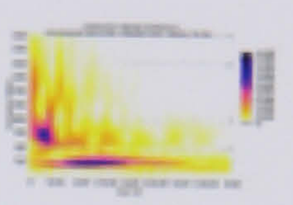
256

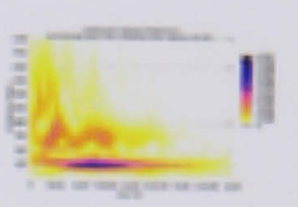
257

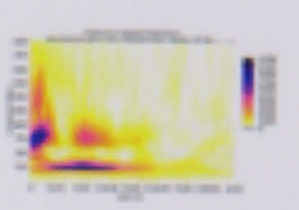
258

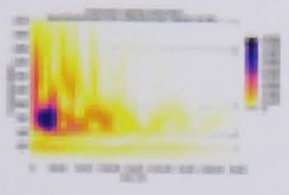
259

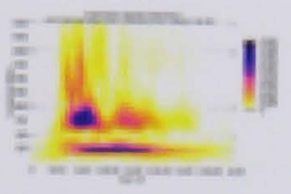
260

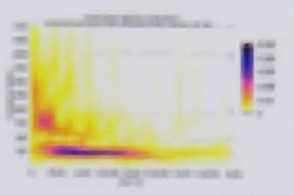
261

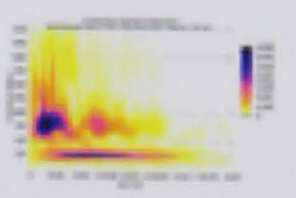
262

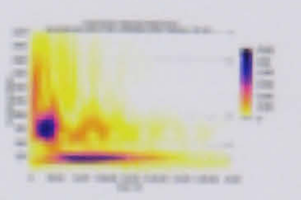
263

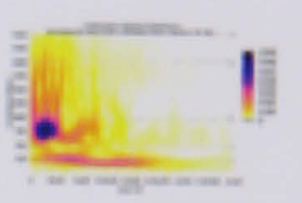
264

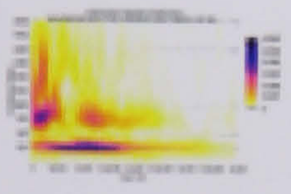
265

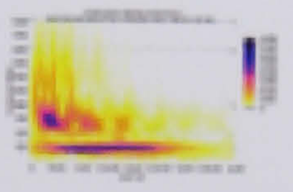
266

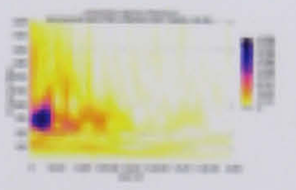
267

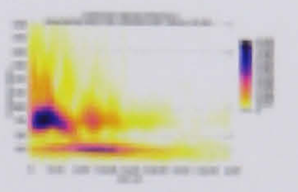
268

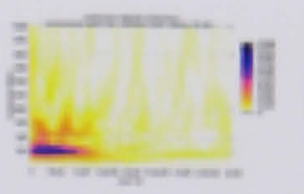
269

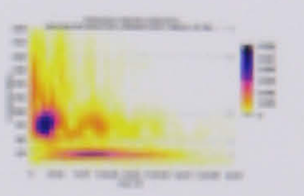
270

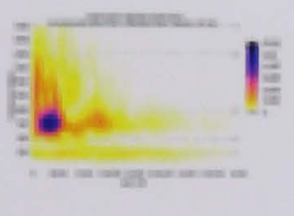
271

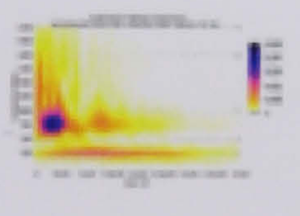
272

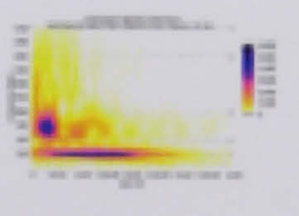
273

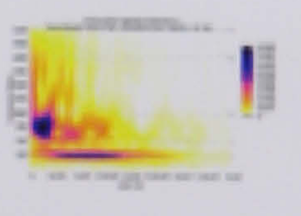
274

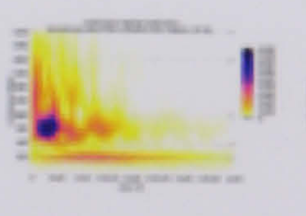
275

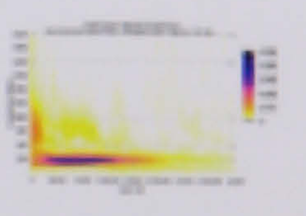
276

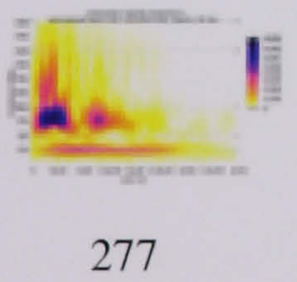
277

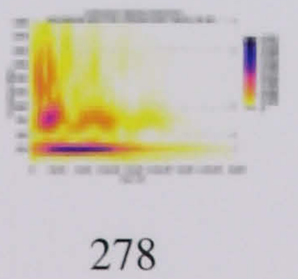
278

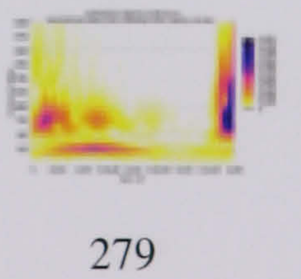
279

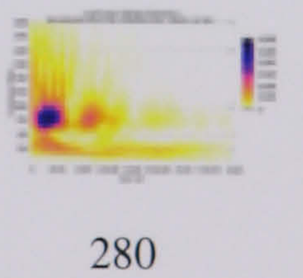
280

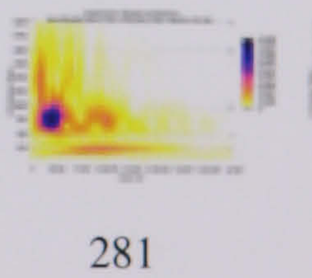
281

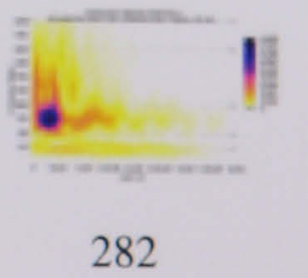
282

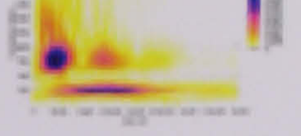
283

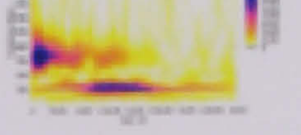
284

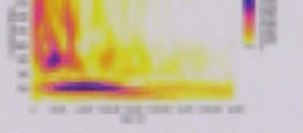
285

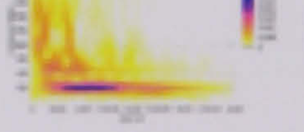
286

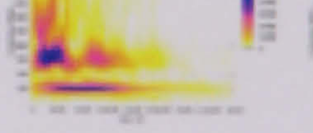
287

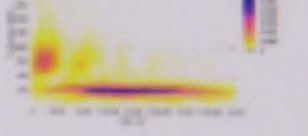
288

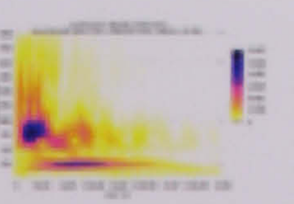
289

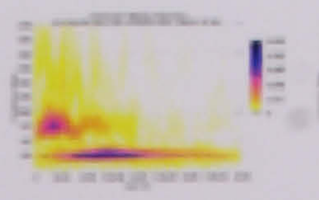
290

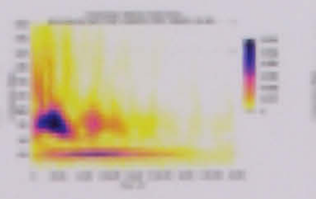
291

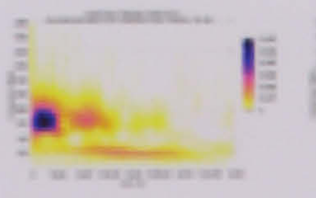
292

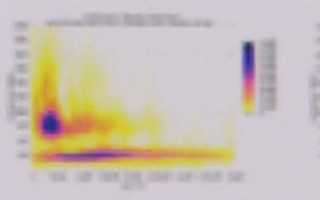
293

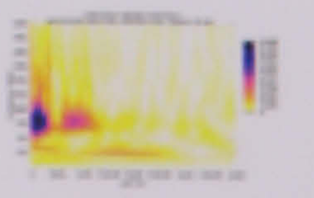
294

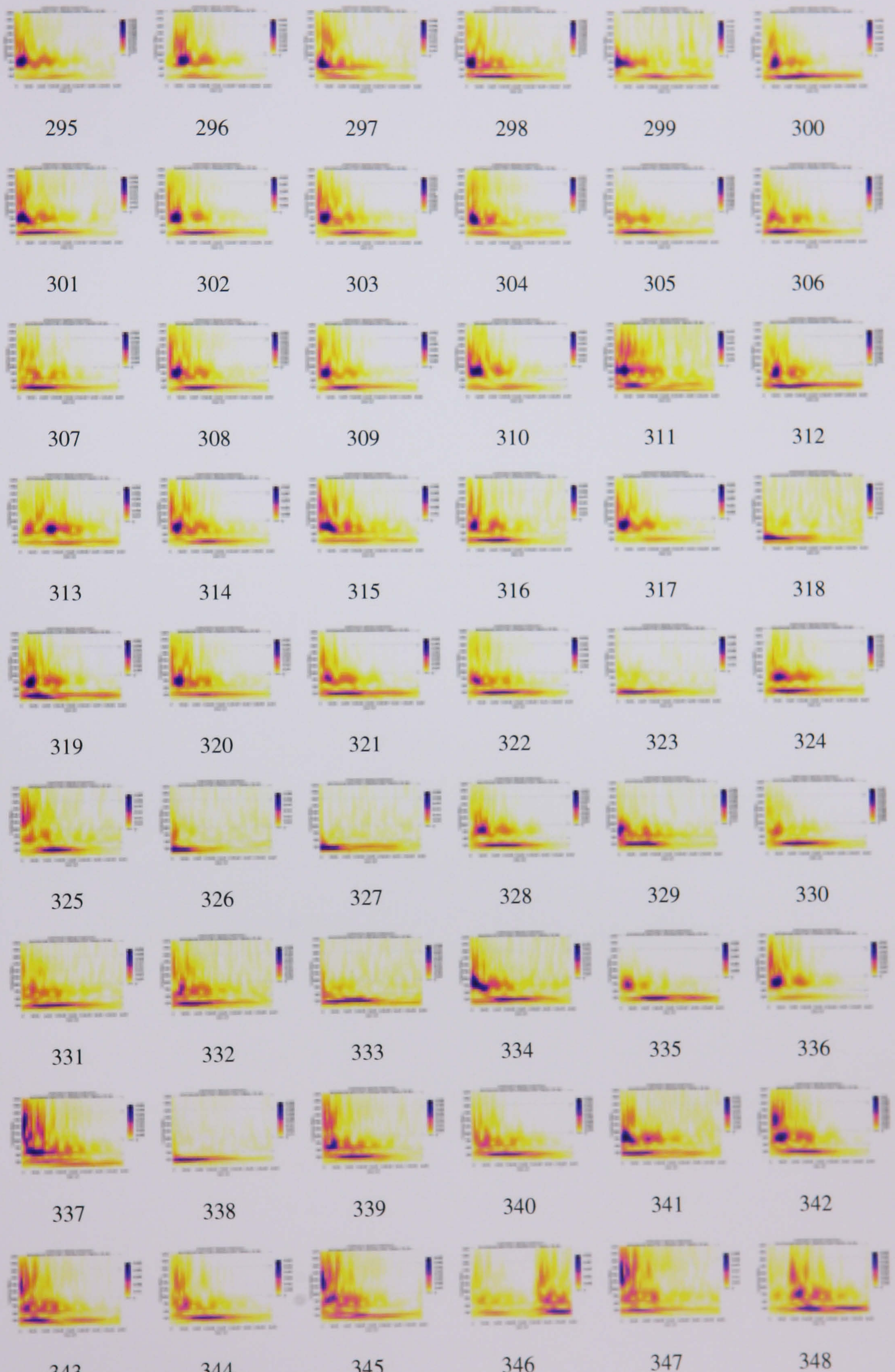

295 296 297 298 299 300

301 302 303 304 305 306

307 308 309 310 311 312

313 314 315 316 317 318

319 320 321 322 323 324

325 326 327 328 329 330

331 332 333 334 335 336

337 338 339 340 341 342

343 344 345 346 347 348

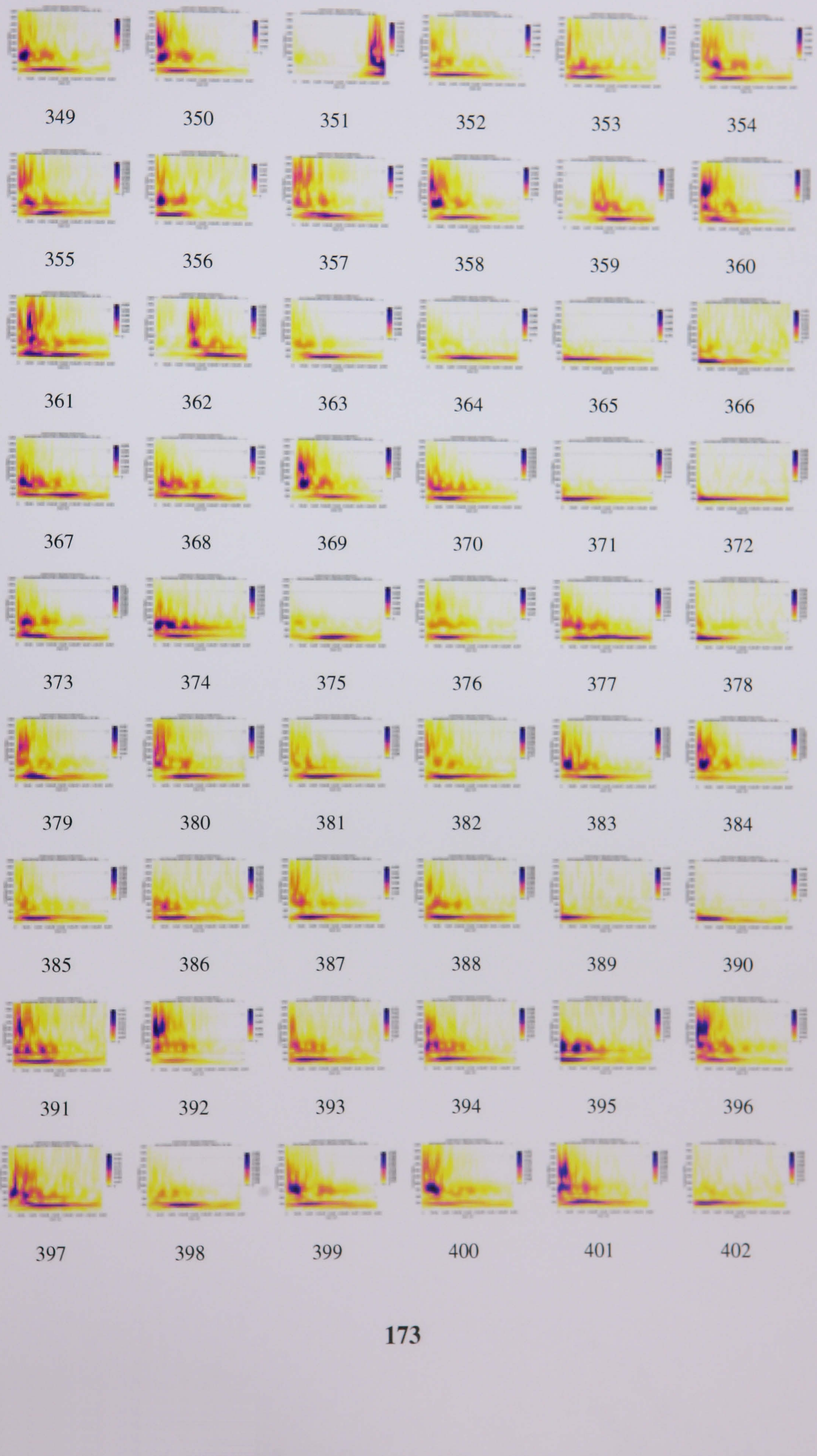

349 350 351 352 353 354

355 356 357 358 359 360

361 362 363 364 365 366

367 368 369 370 371 372

373 374 375 376 377 378

379 380 381 382 383 384

385 386 387 388 389 390

391 392 393 394 395 396

397 398 399 400 401 402

403 404 405 406 407 408

409 410 411 412 413 414

415 416 417 418 419 420

421 422 423 424 425 426

427 428 429 430 431 432

433 434 435 436 437 438

439 440 441 442 443 444

445 446 447 448 449 450

451 452 453 454 455 456

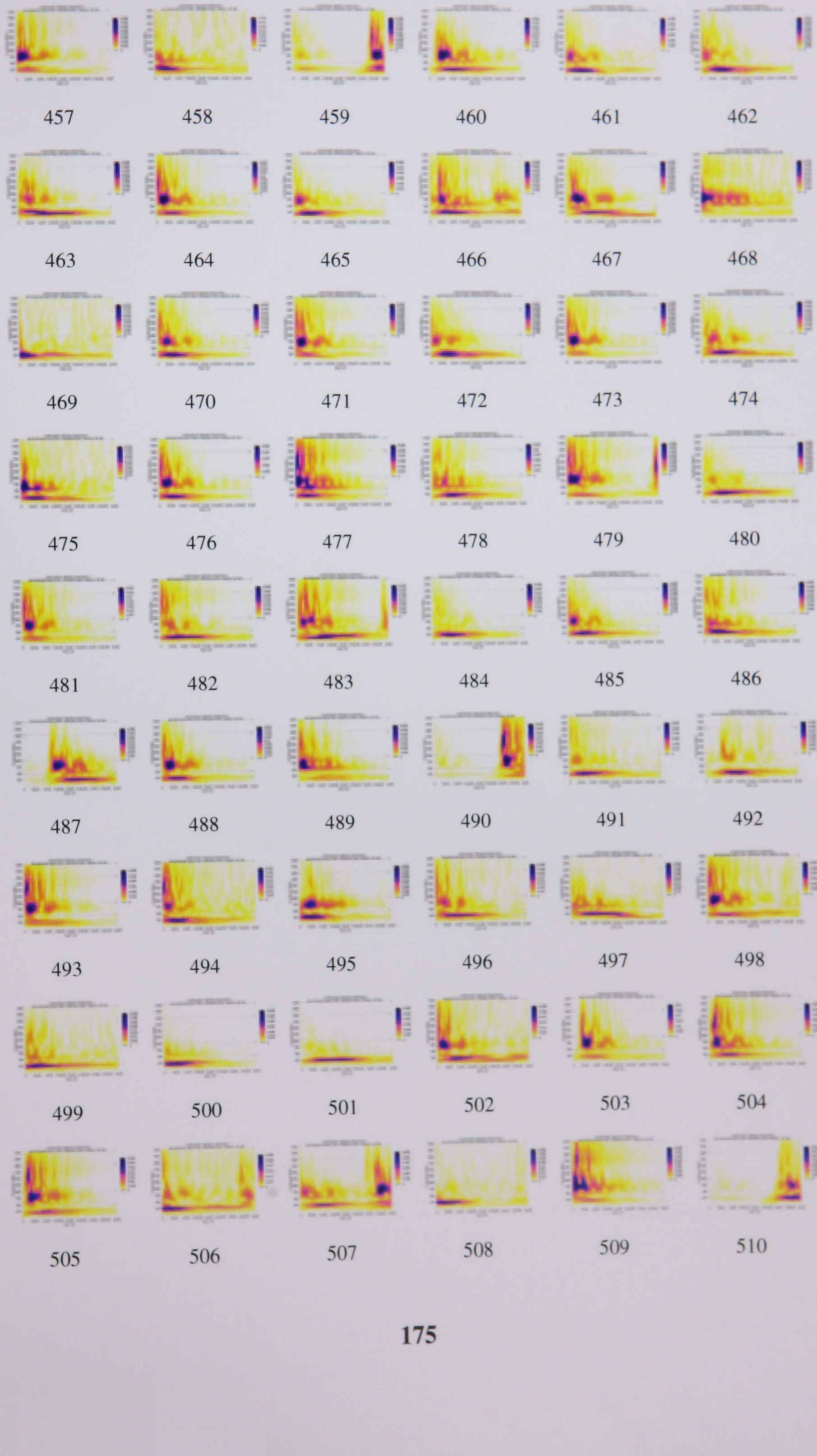

457 458 459 460 461 462

463 464 465 466 467 468

469 470 471 472 473 474

475 476 477 478 479 480

481 482 483 484 485 486

487 488 489 490 491 492

493 494 495 496 497 498

499 500 501 502 503 504

505 506 507 508 509 510

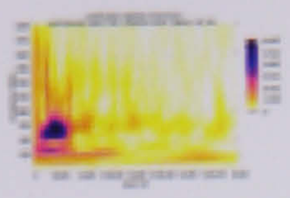

511

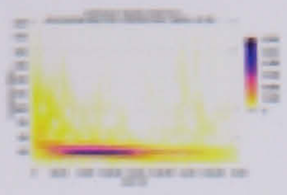

512

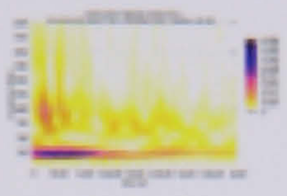

513

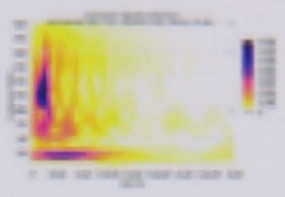

514

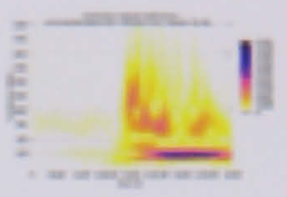

515

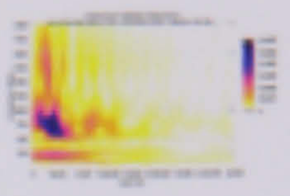

516

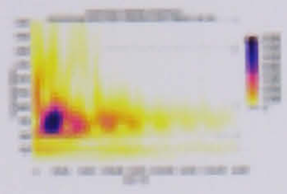

517

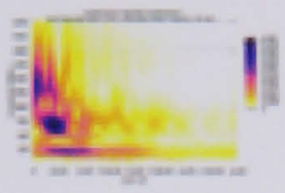

518

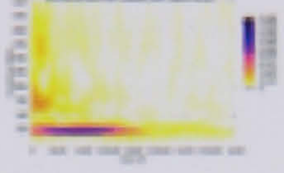

519

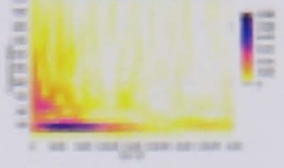

520

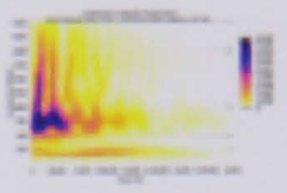

521

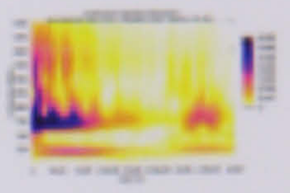

522

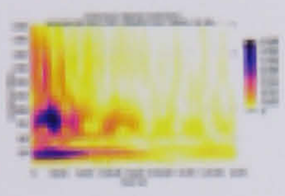

523

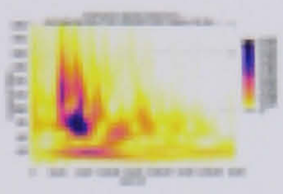

524

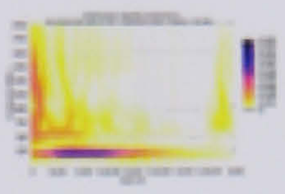

525

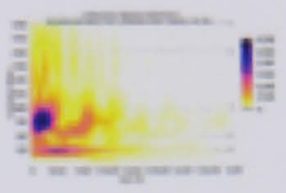

526

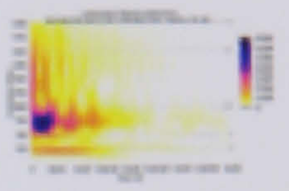

527

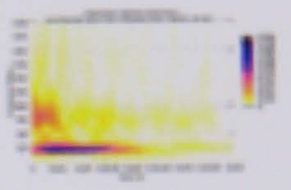

528

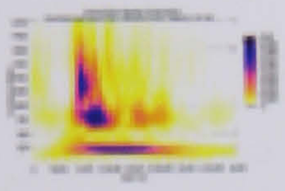

529

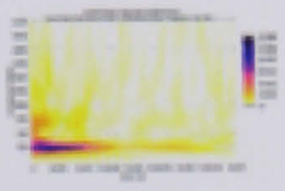

530

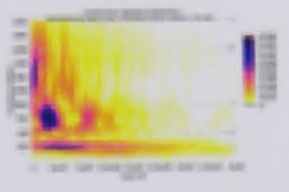

531

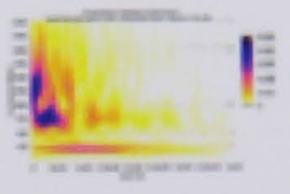

532

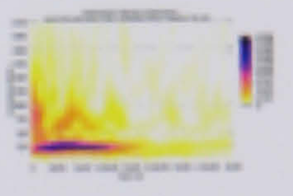

533

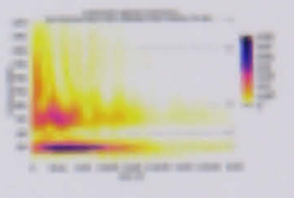

534

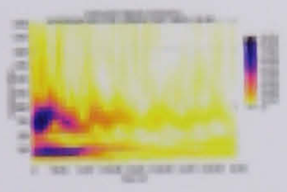

535

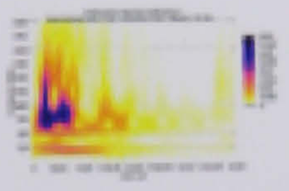

536

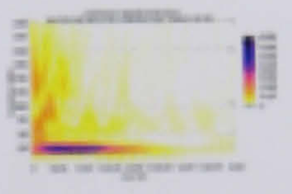

537

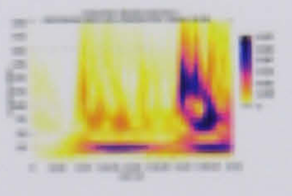

538

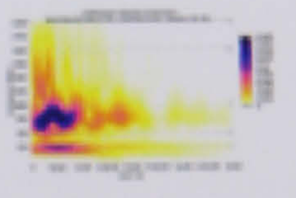

539

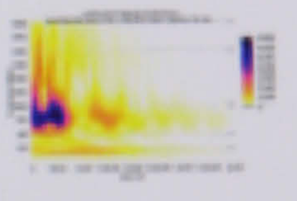

540

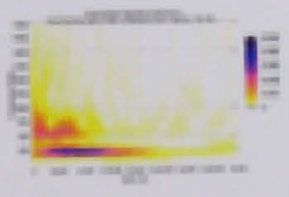

541

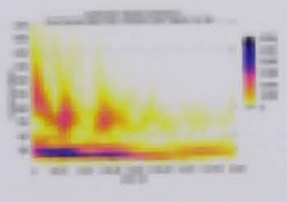

542

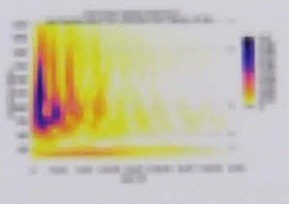

543

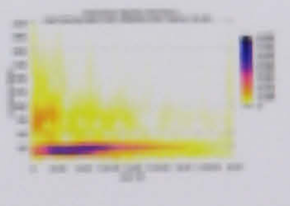

544

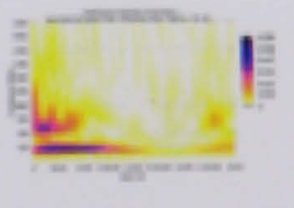

545

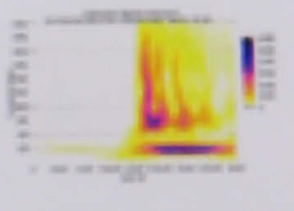

546

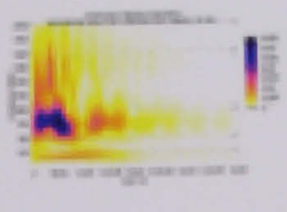

547

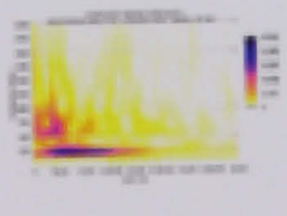

548

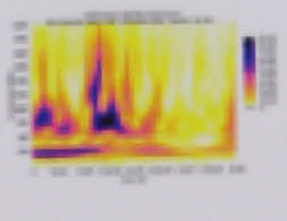

549

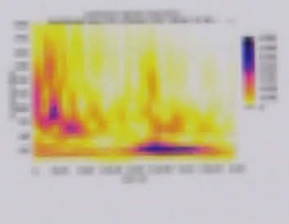

550

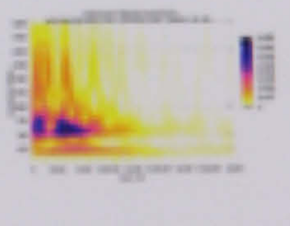

551

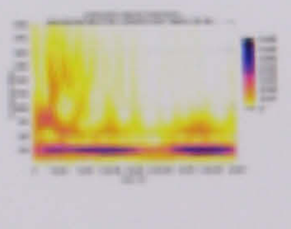

552

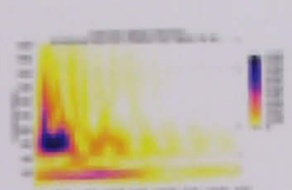

553

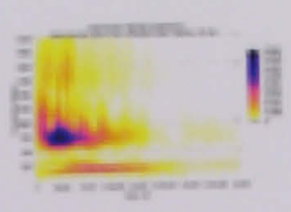

554

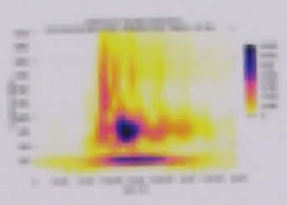

555

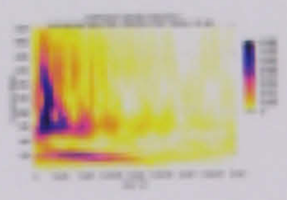

556

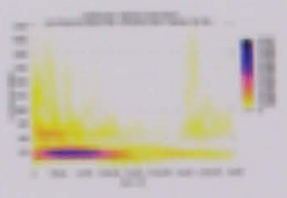

557

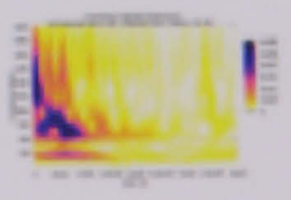

558

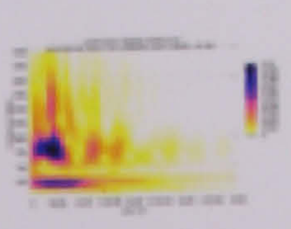

559

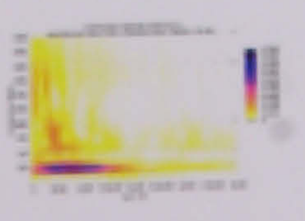

560

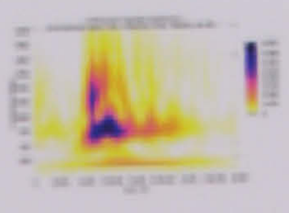

561

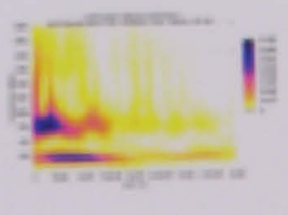

562

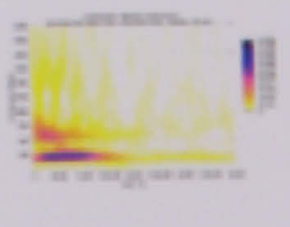

563

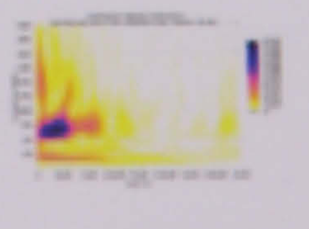

564

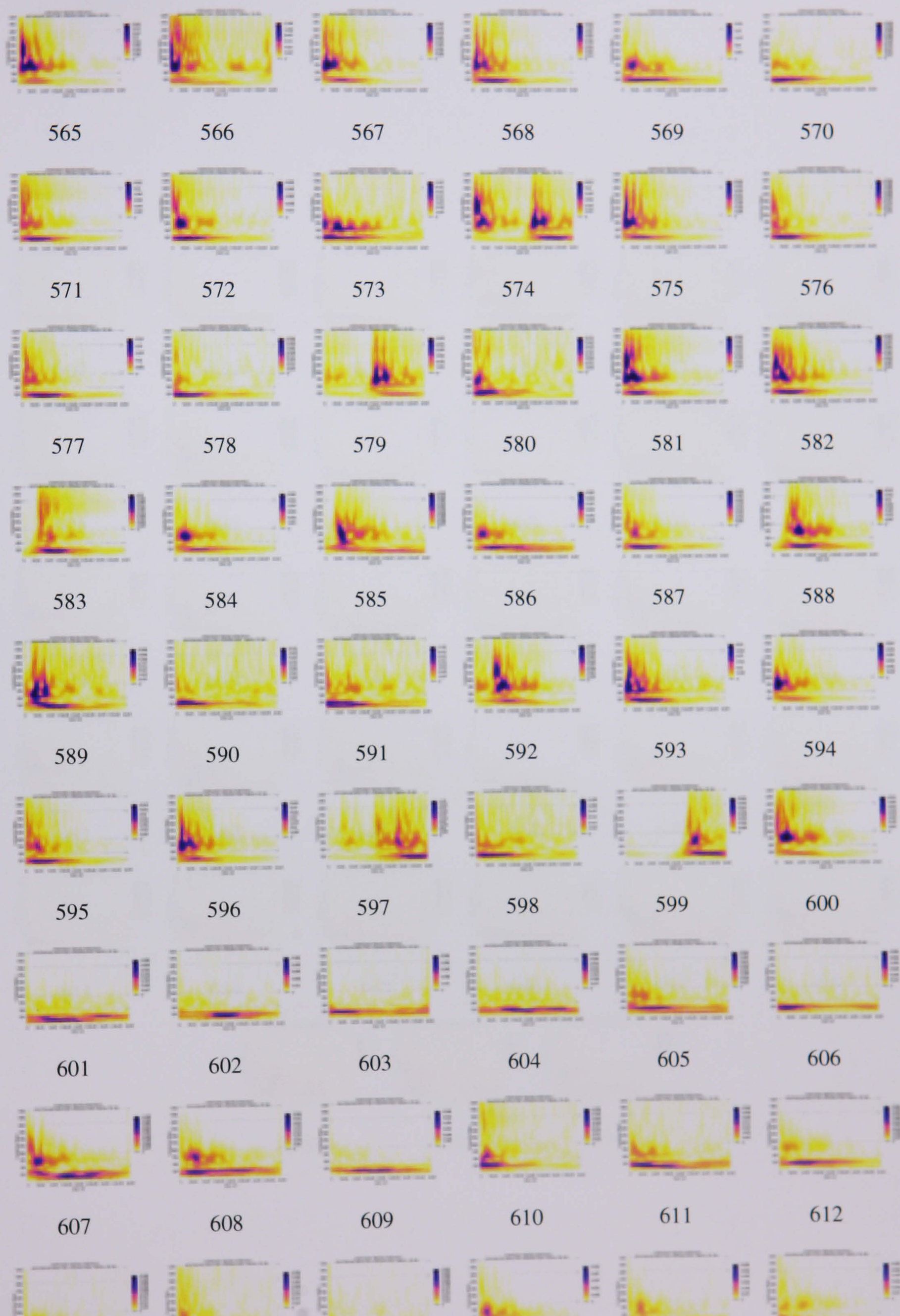

565 566 567 568 569 570

571 572 573 574 575 576

577 578 579 580 581 582

583 584 585 586 587 588

589 590 591 592 593 594

595 596 597 598 599 600

601 602 603 604 605 606

607 608 609 610 611 612

613 614 615 616 617 618

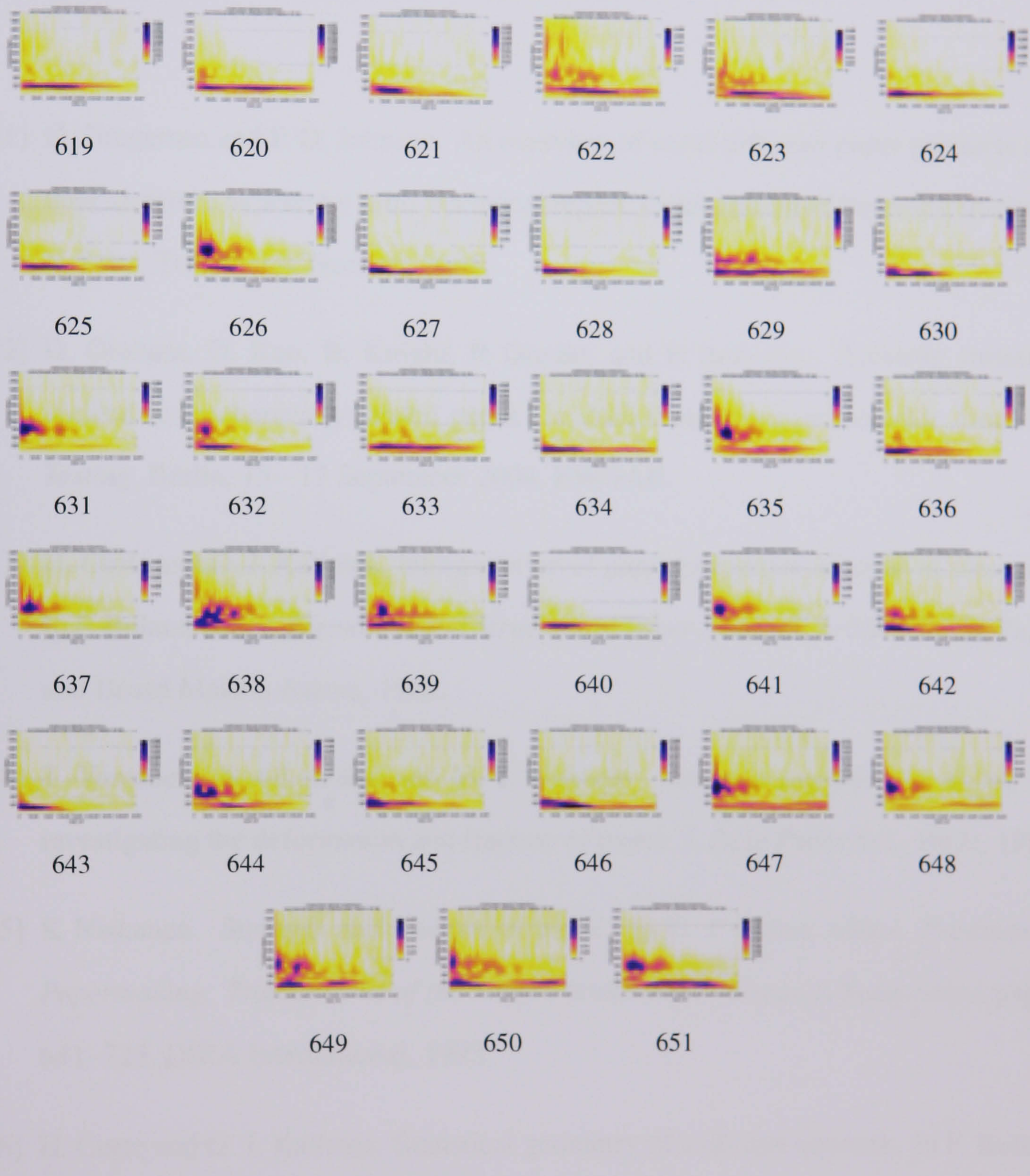

619 620 621 622 623 624

625 626 627 628 629 630

631 632 633 634 635 636

637 638 639 640 641 642

643 644 645 646 647 648

649 650 651

Bibliography

[1] Ø. Gregersen and P. O. Johnsen. An overview of some different paper products and their structure as seen by sem. Technical report, Paper and Fibre Research Institute, N-7491, Trondheim, Norway, 2004.

[2] D. Graham, D. Kao, B. Knight, P. Gradin, and P. Isaksson. Acoustic emission applied to mechanically loaded paper. In *26th Conference on Acoustic Emission Testing*, Berlin, 15 - 17 September 2004. EWGAE.

[3] H. Corte and O. J. Kallmes. Interpretation of paper properties in terms of structure. In F. Bolam, editor, *Formation and Structure of Paper*, pages 352–368. British Paper and Board Makers Assoc., 1962.

[4] T. Yamauchi, S. Okumura, and M. J. Noguchi. Acoustic emission as an aid for investigating the deformation and fracture of paper. *J. Pulp Paper Sci.*, 16(2), 1990.

[5] K Niskanen. Strength and fracture of paper. In C. F. Baker, editor, *Products of Papermaking: Transactions of the Tenth Fundamental Research Symposium*, pages 641–725. DIRA International, 1993.

[6] H. Corte and O. J. Kallmes. Statistical geometry of a fibrous network. In F. Bolam, editor, *Formation and Structure of Paper*, pages 13–46. British Paper and Board Makers Assoc., 1962.

[7] H. Corte, O. J. Kallmes, and D. Jarrot. Mechanical failure of ideal 2-d fibre networks. *Paper Maker*, 142(1):61–68, 1961.

[8] D. H. Page, P. A. Tydeman, and M. Hunt. A study of fibre-to-fibre bonding by direct observation. In F. Bolam, editor, *Formation and Structure of Paper*, pages 171–194. British Paper and Board Makers Assoc., 1962.

[9] D. H. Page, P. A. Tydeman, and M. Hunt. Behaviour of fibre-to-fibre bonds in sheets under dynamic conditions. In F. Bolam, editor, *Formation and Structure of Paper*, pages 249–264. British Paper and Board Makers Assoc., 1962.

[10] T. Uesaka, E Retulainen, L. Paavilainen, R. E. Mark, and D. S Keller. *Handbook of Physical and Mechanical Testing of Paper and Paperboard*, chapter 15 Determination of Fibre-Fiber Bond Properties. Marcel Dekker Inc., 2001.

[11] R. S. Seth and D. H. Page. The stress strain curve of paper. In J. Brander, editor, *The Role of Fundamental Research in Paper Making*, pages 421–454. Mechanical Engineering Publ. Ltd., 1983.

[12] B. A. Jayne. Mechanical properties of wood fibres. *Tappi J.*, 42(6):461–467, 1957.

[13] T. Holroyd. *Acoustic Emission and Ultrasonic Monitoring Handbook*. Coxmoor Publishing Company, 2000.

[14] J. J. Kovecevich, S. P. Nuspl, and M. O. Robertson. Recent advances in the application of acoustic leak detection to process recovery boilers. In *TAPPI Engineering Conference*, 1995.

[15] K. Miller. Tank bottom leak detection in above ground storage tanks using acoustic emission. *Material Evaluation*, 48(6):822–829, 1990.

[16] M. Ge. Analysis of source location algorithms, part 1: Overview and non-iterative methods. *J. Acoustic Emission*, 21:14–28, 2003.

[17] M. Ge. Analysis of source location algorithms, part 2: Iterative methods. *J. Acoustic Emission*, 21:29–51, 2003.

[18] M. A. Hamstad, A. O'Gallagher, and J. Gary. A wavelet transform applied to acoustic emission signals: Part 2: Source location. *J. Acoustic Emission*, 20:62–82, 2002.

[19] L. Gaul, S. Hurlebaus, and L. J. Jacobs. Localization of a 'synthetic' acoustic emission source on the surface of a fatigue specimen. *Res. Nondestr. Eval.*, pages 105–117, 2001.

[20] H. Vallen. Ae testing: Fundamentals, equipment, applications. Technical report, Vallen Systeme, 2002.

[21] T-T. Wu. Elastic wave propagation and nondestructive evaluation of materials. *Proc. Natl. Sci. Counc.*, 23(6):703–715, 1999.

[22] J-E. Berg and P. A. Gradin. Effect of temperature on fracture of spruce in compression, investigated by use of acoustic emission monitoring. *J. Pulp Paper Sci.*, 26(8):294–299, 2000.

[23] P. A. Gradin, S. Nyström, P. Flink, S. Forsberg, and F. Stollmaier. Acoustic emission monitoring of light weight coated paper. *J. Pulp Paper Sci.*, 23(3), 1997.

[24] P. Isaksson, P. A. Gradin, and A. Kulachenko. The onset and progression of damage in isotropic paper sheets. Technical report, Solid Mechanics, Mid Sweden University, 2005.

[25] P. A. Houle and J. P. Sethna. Acoustic emission from crumpling paper. *Phys. Rev. E*, 54(1), 1996.

[26] L. Salminene. *Aspects of Fracture Processes in Paper*. PhD thesis, Laboratory of Physics, Helsinki University of Technology, 2003.

[27] M. Minozzi, G. Caldarelli, L. Pietronero, and S. Zapperi. Dynamic fracture model for acoustic emission. *Eur. Phys. J. B*, 36:203–207, 2003.

[28] M. Johnson. *Acoustic Emission in Composite Laminates - Numerical Simulations and Experimental Characterization*. PhD thesis, Department of Solid Mechanics, KTH, Royal Institute of Technology, 2002.

[29] M. Johnson and P. Gudmundson. Broad-band transient recording and characterization of acoustic emission events in composite laminates. *Composites Science and Technology*, 60:2803–2818, 2000.

[30] M. Johnson and P. Gudmundson. Experimental and theoretical characterization of acoustic emission transients in composite laminates. *Composites Science and Technology*, 61:1367–1378, 2001.

[31] M. Johnson. Ae transients from delaminations in composite laminates - experiments and numerical predictions. Technical report, Department of Solid Mechanics, KTH, Royal Institute of Technology, 2002.

[32] M. Johnson. Waveform based clustering and classification of ae transients in composite laminates using principal component analysis. *NDT&E International*, 35:367–376, 2002.

[33] M. Johnson. Classification of ae transients based on numerical simulations of composite laminates. Technical report, Department of Solid Mechanics, KTH, Royal Institute of Technology, 2002.

[34] M. A. Hamstad, A. O'Gallagher, and J Gary. A wavelet transform applied to acoustic emission signals: Part 1: Source identification. *J. Acoustic Emission*, 20:39–61, 2002.

[35] E. O. Brigham. *The Fast Fourier Transform and Its Applications*. Prentice-Hall Inc., 1988.

[36] I. N. Sneddon. *Fourier Transforms*. Dover Publications, 1995.

[37] W. H. Press, S. A. Teukolsky, W. T. Vetterling, and B. P. Flannery. *Numerical Recipes in C++, The Art of Scientific Computing*. Cambridge University Press, 2002.

[38] L. Cohen. *Time-Frequency Analysis: Theory and Applications*. Prentice Hall, 1994.

[39] T. A. C. M Claasen and W. F. G. Mecklenbrauker. The wigner distribution - a tool for time-frequency signal analysis, part 1: Continuous-time signals. *Philips Journal of Research*, 35(3):217–250, 1980.

[40] T. A. C. M Claasen and W. F. G. Mecklenbrauker. The wigner distribution - a tool for time-frequency signal analysis, part 2: Discrete-time signals. *Philips Journal of Research*, 35(4/5):276–300, 1980.

[41] G. Kaiser. *A Friendly Guide to Wavelets*. Birkhäuser, 1994.

[42] C. K. Chui. *An Introduction to Wavelets*. Academic Press, 1992.

[43] R. K. Young. *Wavelet Theory and its Applications*. Kluwer Academic, 1993.

[44] C. Torrence and G. Compo. A practical guide to wavelet analysis. *Bulletin of the American Meteorological Society*, 79(1), 1998.

[45] C. Torrence and G. Compo. A practical guide to wavelet analysis. Technical report, National Center for Atmospheric Research, University of Colorado, 1998.

[46] H. Vallen and J. Vallen. Free-of-cost software tools generate dispersion curves, perform wavelet transform and help correlate both kinds of information. Technical report, Vallen-Systeme, 2002.

[47] M. Takemoto, H. Nishino, and K. Ono. *Acoustic Emission - Beyond the Millenium*, chapter Wavelet Transform - Applications to AE Signal Analysis. Elsevier, 2000.

[48] H. Suzuki, T. Kinjo, Y. Hayashi, M. Takemoto, and K. Ono. Wavelet transform of acoustic emission signals. *J. Acoustic Emission*, 14(2):69–84, 1996.

[49] M. A. Hamstad. An illustrated overview of the use and value of a wavelet transformation to acoustic emission technology. Technical report, National Institute for Science and Technology, University of Denver, 2003.

[50] Clecom Software Specialists. Autosignal [online]. Available from: `http://www.clecom.co.uk/science/autosignal`.

[51] Mathworks. Wavelet toolbox - matlab [online]. Available from: `http://www.mathworks.com`.

[52] A. Salehian, Z. Hou, and F. G. Yuan. Identification of location of a sudden damage in plates using wavelet approach. In *Proceedings of the 16th ASCE Engineering Mechanics Conference*, University of Washington, Seattle, 2003. 16th ASCE Engineering Mechanics Conference.

[53] A. Salehian. Identifying the location of a sudden damage in composite laminates using wavelet approach. Master's thesis, Worcester Polytechnic Institute, 2003.

[54] K. Kabeya. Structural health monitoring using multiple piezoelectric sensors and actuators. Master's thesis, Department of Mechanical Engineering, Virginia Tech, 1998.

[55] C-C. Chang and Z. Sun. Locating and quantifying structure damage using spatial wavelet packet signature. In S-C. Liu, editor, *Smart Structures and Materials 2003: Smart Systems and Nondestructive Evaluation for Civil Infrastructures*, 2003.

[56] S. Pittner and S. V. Kamarthi. Feature extraction from wavelet coefficients for pattern recognition tasks. *IEEE Trans. Pattern Analysis and Machine Intelligence*, 21(1):83–88, 1999.

[57] C-H. Chen, J-D. Lee, and M-C. Lin. Classification of underwater signals using neural networks. *Tamkang Journal of Science and Engineering*, 3(1):31–48, 2000.

[58] J. Lattin, J. D. Carrol, and P. E. Green. *Analyzing Multivariate Data*. Brooks/Cole, 2003.

[59] T. Kohonen. *Self-Organizing Maps*. Springer, 2001.

[60] R. Ohayon and C. Soize. *Structural Acoustics and Vibration*. Academic Press Ltd, 1998.

[61] F. Grosveld, R. Buehrle, and J. Robinson. Structural and acoustic numerical modelling of a curved composite honeycomb panel. *AIAA*, 2277, 2001.

[62] A. Jarvinen. Vibro-acoustic modelling of a loudspeaker. In *NAM*, Stockholm, 7 - 9 September 1998.

[63] ESI Group. Rayon [online]. Available from: `http://www.esi-group.com`.

[64] LMS. Sysnoise [online]. Available from: `http://www.lmsintl.com`.

[65] ABAQUS Inc. Abaqus [online]. Available from: `http://www.hks.com`.

[66] D. Bourguignon and M-P. Cani. Controlling anisotropy in mass-spring systems. In *Eurographics Workshop on Computer Animation and Simulation (EGCAS)*, pages 113–123, August 2000.

[67] X. Provot. Deformation constraints in a mass-spring model to describe rigid cloth behaviour. *Proceedings of Graphics Interface*, pages 141–155, 1995.

[68] D. Baraff and A. Witkin. Large steps in cloth simulation. In *Computer Graphics*, pages 43–45. SIGGRAPH, 1998.

[69] K-J. Choi and H-S. Ko. Stable but respnsive cloth. In *ACM Transactions on Graphics*, pages 604–611. SIGGRAPH, 2002.

[70] D. H. House and D. E. Breen. *Cloth Modeling and Animation*. A. K. Peters, Ltd., 2000.

[71] D. H. House, R. W. DeVaul, and D. E. Breen. Towards simulating cloth dynamics using interacting particles. *International Journal of Clothing Science and Technology*, 8(3):75–94, 1996.

[72] D. E. Breen, D. H. House, and M. J. Wozny. A particle-based model for simulating the draping behaviour of woven cloth. *Textile Research Journal*, 64(11):663–685, 1994.

[73] J. Lander. Devil in the blue faceted dress: Real-time cloth animation. *Game Developer Magazine*, May 1999.

[74] A. Fuhrmann, C. Groß, and V. Luckas. Interactive animation of cloth including self collision detection. *Journal of WSCG*, 11(1), 2003.

[75] R. Rosenblum, W. Carlson, and Tripp E. Simulating the structure and dynamics of human hair: Modeling, rendering and animation. *Journal of Visualization and Computer Animation*, 2:141–148, June 1991.

[76] H. D. Taskiran and U. Güdükbay. Physically-based simulation of hair strips in real-time. In *Proceedings of the 13th International Conference in Central Europe on*

Computer Graphics, Visualization and Computer Vision, pages 153–156. WSCG, February 2005.

[77] K. Pallister. *Game Programming Gems 5*. Charles River Media, 2005.

[78] D. Eberly. *Game Physics*. Elsevier, 2004.

[79] M. Benvegnu. Clothsim [online]. Available from: `http://www.benve.org/ClothSim/indexeng.htm`.

[80] Alias. Maya [online]. Available from: `http://www.alias.com`.

[81] Autodesk. 3d studio max [online]. Available from: `http://www.autodesk.com`.

[82] W. Cheney and D. Kincaid. *Numerical Mathematics and Computing*. Brooks/Cole Publishing Company, 1999.

[83] P. R. Cook. *Real Sound Synthesis for Interactive Applications*. AK Peters, Ltd., 2002.

[84] University of York. Cymatic [online]. Available from: `http://www-users.york.ac.uk/~dmh8/cymatic/cymatic.htm`.

[85] M. Pearson. Tao [online]. Available from: `http://web.ukonline.co.uk/taosynth`.

[86] C. H. Taal. The mass-spring paradigm for physical modelling of drums. Technical report, Media Engineering Research Group, Dept. of Electronics, University of York, 2003.

[87] W. F. Ames. *Numerical Methods for Partial Differential Equations*. Academic Press Inc., 1992.

[88] G. K. Batchelor. *An Introduction to Fluid Dynamics*. Cambride University Press, 2000.

[89] W. F. Hughes and J. A. Brighton. *Schaum's Outlines of Fluid Dynamics*. McGraw-Hill, 1999.

[90] R. T. Fenner. *Finite Element Methods for Engineers*. Imperial College Press, 1996.

[91] K. Koketsu. Finite-element simulation of seismic wave propagation with a voxel grid. In A. Donnellan, editor, *3rd ACES Workshop Proceedings*, 2002.

[92] M. Hofer, R. Lerch, N. Finger, G. Kovacs, J. Schöberl, S. Zaglmayr, and U. Langer. Finite element calculation of wave propagation and excitation in periodic piezoelectric systems. In H. A. Mang and F. G. Rammerstorfer, editors, *Proceedings of the Fifth World Congress on Computational Mechanics*, 2002.

[93] H. K. Versteeg and W. Malalasekera. *An Introduction to Computational Fluid Dynamics - The Finite Volume Method*. Prentice Hall, 1995.

[94] A. Zakaria, J. Penrose, F. Thomas, and X. Wang. The two dimensional numerical modelling of acoustic wave propagation in shallow water. *Acoustics*, 2000.

[95] ANSYS Inc. Ansys [online]. Available from: `http://www.ansys.com`.

[96] CD-adapco Group. Star cd [online]. Available from: `http://www.cd-adapco.com`.

[97] CHAM. Phoenics [online]. Available from: `http://www.cham.co.uk`.

[98] J. Lighthill. On sound generated aerodynamically, I. General Theory. *Proceedings of the Royal Society of London*, A211:564–587, 1952.

[99] A. C. Reynold. Boundary conditions for the numerical solution of wave propagation problems. *Geophysics*, 43:1099–1110, 1978.

[100] M. B. Giles. Non-reflecting boundary conditions for euler equation calculation. *AIAA J*, 28(12):2050 – 2058, 1990.

[101] J. B. Freund. Proposed inflow/outflow boundary condition for direct computation of aerodynamic sound. *AIAA J*, 35(4):740–742, 1997.

[102] T. Colonius. Numerically nonreflecting boundary and interface conditions for compressible flow and aeroacoustic computations. *AIAA J*, 35(7):1126–1133, 1997.

[103] N. Corle. The influence of solid boundaries upon aerodynamic sound. *Proceedings of the Royal Society of London*, A216(1127):412–424, 1953.

[104] T. D. Rossing and N. H. Fletcher. *Principles of Sound and Vibration*. Springer-Verlag, 1995.

[105] D. V. Hutton. *Fundamentals of Finite Element Analysis*. McGraw-Hill, 2003.

[106] C. Felippa. Introduction to stability analysis. Technical Report ASEN 5519-006, Aerospace Engineering Sciences, University of Colorado at Boulder, 2004.

[107] P. Henrici. *Discrete Variable Methods in Ordinary Differential Equations*. Wiley, 1962.

[108] A. Ralston. *A First Course in Numerical Analysis*. McGraw-Hill, 1965.

[109] F. Ercolessi. *A Molecular Dynamics Primer*. http://www.fisica.uniud.it/ ercolessi/, 1997.

[110] L. Verlet. Computer experiments on classical fluids. i. thermodynamical properties of lennard-jones molecules. *Phys. Rev.*, 159:98–103, 1967.

[111] J. H. E. Cartwright and O. Piro. The dynamics of runge-kutta methods. *Int. J. Bifurcation and Chaos*, 2:427–449, 1992.

[112] R. M. Alford, K. R. Kelly, and D. M. Boore. Accuracy of finite-difference modelling of acoustic wave propagation. *Geophysics*, 39(6):834–842, 1974.

[113] F. J. Fahy. *Sound Intensity*. E & F N Spon, 1995.

[114] H. Vallen. Sampling rate of ae aquisition system. Personal Communication, February 2005.

[115] H. Vallen. Sensor prototypes 409 (#1-2) and 410 (#3-7) frequency-response curves & capacity. Technical Report AEP-4015, Vallen Systeme GmbH, 2004.

[116] Ø. Gregersen. Material properties of paper. Personal Communication, February 2005.

[117] G. Allan. *Elementary Statistics - A Step by Step Approach*. Wm. C. Brown Publishers, 1992.

[118] R. J. Harris. *A Primer of Multivariate Statistics*. Lawrence Erlbaum Associates, 2001.

[119] PFI. Partner 3 presentation of work. 30 Month AEP Project Meeting, September 2005.

[120] T. Kohonen, J. Hynninen, J. Kangas, and J. Laaksonen. Som_pak: The self-organizing map program package. Technical Report A31, Helsinki University of Technology, Laboratory of Computer and Information Science, FIN-02150 Espoo, Finland, 1996.

[121] E. Alhoniemi, J. Hollmén, O. Simula, and J. Vesanto. Process monitoring and modeling using the self-organizing map. *Integrated Computer Aided Engineering*, 6(1):3–14, 1999.

[122] T. Honkela, I. Koskinen, I. Koskenniemi. and Sakari. Karvonen. Kohonen's self-organizing map in contextual analysis of data. In K. Tanaka and S. Ghandeharizadeh, editors, *Information Organization and Databases: Foundations of Data Organization*, pages 135–148. Kluwer, 2000.

[123] A. Ultsch. Self organized feature maps for monitoring and knowledge aquisition of a chemical process. In S. Gielen and B. Kappen, editors, *Proceedings of the International Conference on Artificial Neural Networks (ICANN93)*, pages 864–867. Springer-Verlag, 1993.